Norwegian University of Life Sciences
Faculty of Environmental Sciences
and Natural Resource Management

Philosophiae Doctor (PhD)
Thesis 2018:55

An experimental study on rotor-wake interactions of wind turbines

Eksperimentelle undersøkelser av den turbulente vakestrømningen bak vindturbiner

Franz Volker Mühle

An experimental study on rotor-wake interactions of wind turbines

Eksperimentelle undersøkelser av den turbulente vakestrømningen bak vindturbiner

Philosophiae Doctor (PhD) Thesis

Franz Volker Mühle

Norwegian University of Life Sciences
Faculty of Environmental Sciences and Natural Resource Management

Ås 2018

Thesis number 2018:55
ISSN 1894-6402
ISBN 978-82-575-1762-5

PhD supervisors

Professor Muyiwa Samuel Adaramola
Faculty of Environmental Science and Natural Resource Management
Norwegian University of Life Sciences
Ås, Norway

Professor Lars Roar Sætran
Department of Energy and Process Engineering
Norwegian University of Life Sciences
Trondheim, Norway

Associate Professor Arne Reidar Gravdahl
Faculty of Environmental Science and Natural Resource Management
Norwegian University of Life Sciences
Ås, Norway

Evaluation committee

Professor Sandrine Aubrun-Sanches
Research Department
Centrale Nantes
Nantes, France

Professor Alberto Zasso
Department of Mechanical Engineering
Politecnico di Milano
Milan, Italy

Professor Erik Trømborg
Faculty of Environmental Science and Natural Resource Management
Norwegian University of Life Sciences
Ås, Norway

To my Mother

Acknowledgements

Many people have been involved in supervising and supporting this thesis, who I would like to express my gratitude to.

First of all I would like to thank my supervisors, Sam Adaramola Lars Sætran and Arne Gravdahl. Thank you, Sam for giving me the opportunity to work on this project and for providing me the freedom I needed to be creative. I always felt taken care of and knew your office door was open for any kind of discussion. Thank you, Lars for giving me the possibility to work at the place I enjoyed most during my PhD, the fluid mechanics laboratory at NTNU, and for welcoming me from the very beginning on as part of your team. It was always nice coming to your office and leaving with new ideas and questions to solve. Thank you, Arne for always showing interest in my work and your support when needed. I always knew that I had someone to support me if things would not work out.

I would like to thank the colleagues I collaborated with: Jan, Jannik and Thomas, without you the thesis would not have been possible in the way it is now. My special thanks go to Jan, there are so many things that come in my mind to thank you for that I cannot name all of them here. It was a great pleasure teaming up with you.

I would like to thank everyone at the Department of Energy and Process Engineering at NTNU for your hospitality. It was a great research stay with many enriching experiences.

I had a great time working at MINA and EPT, thanks to my office mates, my fellow PhD students and my colleagues. Thank you for brightening my life, also outside of work. Many thanks also tho the administrative staff at NMBU and NTNU for all their support.

A special thank goes to my family, for all the support you gave me in all kind of ways. It is important to know that there are people who will be always on you side, no matter what happens.

Finally, I would like to thank all my friends in Germany, Norway and all around the world. I am very lucky to have so many good friends. You all had your contribution to the thesis and it is most likely bigger as you would think. I would like to name all of

you here, but I am scared I would miss out half of the people after this whole thesis writing. But now that I am finished I will have more time and I am sure we will have the possibility to meet some time and I can thank you personally.

Ås, May 2018
Franz Mühle

Abstract

Interactions of wind turbine wakes with downstream turbines can reduce a wind farm's power production and increase loads on the individual turbines. For the purpose of wind farm optimization, different aerodynamic approaches to modify the performance and wake flow of one or two model wind turbines have been tested in a number of wind tunnel experiments.

In a first set of measurements, different modifications of the rotor design to limit wake effects are studied. Herein, the effect of the blade number on the wake development is studied by comparing the wake properties behind 2- and 3-bladed model wind turbines. Also, the influence of the rotational direction is investigated by comparing the performance of an aligned two-turbine array with co- and counter-rotating rotors. Moreover, the effect of winglets on the performance and vortex interaction in the wake is assessed. For this purpose, a new rotor with aerodynamically optimized winglets has been designed. The performance of the rotor is compared to a reference rotor without winglets and effects on the vortex interaction and velocity recovery in the wake are investigated.

The second set of measurements investigated the control of the model wind turbines by intentional yaw misalignment. Therefore, the wake flow behind a yawed turbine exposed to different inflow conditions is measured, while also the power and loads on a two-turbine array are analyzed for varying separation distances, lateral offsets and yaw angles. Selected test cases are furthermore provided for validation purposes of CFD codes. In a Blind test experiment, performance and wake data are compared to computational results from external groups.

All the experiments have been carried out in the closed-loop wind tunnel at NTNU in Trondheim. The wakes were investigated for uniformly distributed and sheared inflow velocity profiles with different turbulence intensities ranging from 0.23% to 10.0%. During the project different rotor designs from 2- to 3-bladed rotors, all with a diameter of $D = 0.9$ m, are investigated. The velocities in the wake are measured using a 2-component laser Doppler velocimetry system or a Cobra probe, which is used to extract phase-averaged information from the wake flow.

The potential of the blade number and opposite rotational directions in turbine array are found not to have a significant potential for the optimization of a wind farm. While not affecting the mean velocity distribution, the blade number is observed to influence to turbulence peak levels in the wake. An opposite rotation of the downstream turbine is assessed only to be effective for very small turbine separation distances, where the energy contained in the wake swirl of the upstream turbine can be extracted. The design of aerodynamically optimized winglets could rise the power coefficient C_P of a single rotor by 8.9%, whereas the thrust coefficient C_T only increased by 7.4%. Winglets are furthermore found to accelerate the tip vortex interaction in the wake, leading to a local shear layer enlargement and earlier wake recovery. In a wind farm, rotors with winglets extract more energy and leave a similar amount of kinetic energy in the wake for potential downstream turbines. Yaw control is found to have the largest potential for the optimization of wind farms. The total power of an aligned two-turbine array is assessed to increase up to 11% by deflecting the upstream turbine's wake laterally though an intentional yaw misalignment. However, yaw moments on yawed turbines and turbines operating in a partial wake are observed to increase, showing the importance of considering loads for yaw control. Finally, the comparison of experimental data to numerical predictions in the Blind test confirmed the strength of codes based on Large-Eddy Simulations (LES) in predicting mean velocity and turbulent kinetic energy levels in the wake precisely.

Table of contents

List of figures

List of tables

List of papers

Paper I

The effect of the number of blades on wind turbine wake – a comparison between 2-and 3-bladed rotors

Mühle F, Adaramola MS and Sætran L

Published in Journal of Physics, Conference Series, vol. 753 (2016) 032017

doi: 10.1088/1742-6596/753/3/032017

The author's contribution: The rotors were designed and constructed by Mühle. The experimental work and the analysis of the data were performed by Mühle. The manuscript was written by Mühle and reviewed by Adaramola and Sætran. The project was supervised by Adaramola and Sætran. The paper was presented by Mühle at the Torque conference 2016 in Munich.

Paper II

The effect of rotational direction on the wake of a wind turbine rotor – an experimental comparison study of aligned co- and counter rotating turbine arrays

Mühle F, Adaramola MS and Sætran L

Published in Energy Procedia, vol. 137 (2017), pp. 238-245

doi: 10.1016/j.egypro.2017.10.346

The author's contribution: The experimental work and the analysis of the data were performed by Mühle. The manuscript was written by Mühle and reviewed by Adaramola and Sætran. The project was supervised by Adaramola and Sætran. The paper was presented by Mühle at the DeepWind conference 2017 in Trondheim.

Paper III

An experimental study on the effect of winglets on the tip vortex interaction in the near wake of a model wind turbine

Mühle F, Bartl J, Hansen T, Adaramola M S and Sætran L

Manuscript

The author's contribution: The rotor was designed by Mühle and Hansen and the winglet design was optimized by Hansen. The experiment was planned and performed by Mühle. The data was evaluated, analyzed and discussed by Mühle and Bartl. The manuscript was written by Mühle and Bartl and reviewed by Hansen. The project was supervised by Adaramola and Sætran.

Paper IV

Winglet Shape Optimisation for a Model-Scale Wind Turbine

Hansen T and Mühle F

Published in Wind Energy, vol. (2018), pp. 1-17

doi: 10.1002/we.2183

The author's contribution: The optimization and computational analysis was performed by Hansen. The rotor blade was designed by Hansen and Mühle. The construction of the wind tunnel models and the experimental testing was performed by Mühle. The evaluation and validation of the numerical results was performed by Hansen. The article was written by Hansen and reviewed by Mühle.

Paper V

Wind tunnel experiments on wind turbine wakes in yaw: Effects of inflow turbulence and shear

Bartl J, Mühle F, Schottler J, Sætran L, Peinke J, Adaramola M S and Hölling M

Accepted for publication in Wind Energy Science, 2018

doi: 10.5194/wes-2017-59

The author's contribution: The experiment was planned and performed by Bartl and Mühle. The data was evaluated, analyzed and discussed by Bartl, Mühle and Schottler. The manuscript was written by Bartl and reviewed by Mühle and Schottler. The project was supervised by Peinke, Hölling, Adaramola and Sætran.

Paper VI

Wind tunnel study on power and loads optimization of two yaw-controlled model wind turbines

Bartl J, Mühle F and Sætran L

In review in Wind Energy Science

doi: 10.5194/wes-2018-24

The author's contribution: The experiment was planned and performed by Bartl and Mühle. The data was evaluated, analyzed and discussed by Bartl and Mühle. The manuscript was written by Bartl and reviewed by Mühle. The project was supervised by Sætran.

Paper VII

Blind test 5 – the wake behind a yawed wind turbine

Mühle F, Schottler J, Bartl J, Futrzynski R, Evans S, Bernini L, Schito P, Draper M, Guggeri A, Kleusberg E, Henningson D, Hölling M, Peinke J, Adaramola M S and Sætran L

In review in Wind Energy Science

doi: 10.5194/wes-2018-30

The author's contribution: The experiments were planned and performed by Mühle, Bartl and Schottler. The data was evaluated, analyzed and discussed by Mühle, Bartl and Schottler. The numerical data was provided by co-authors Futrzynski, Evans, Bernini, Schito, Draper, Guggeri, Kleusberg and Henningson. The Blind test workshop was organized by Mühle and Bartl. The manuscript was written by Mühle and reviewed by Bartl and Schottler. The project was supervised by Peinke, Hölling, Adaramola and Sætran.

Additional papers

Paper VIII

Lidars for Wind Tunnels - an IRPWind Joint Experiment Project

Sjöholm M, Vignaroli A, Agelou N, Nielsen M B, Mann J, Mikkelsen T, Bolstad H C, Merz K O, Sætran L, Mühle F, Tiihonen M and Lehtomäki V

Published in Energy Procedia, vol. 137 (2017), pp. 339-345

doi: 10.1016/j.egypro.2017.10.358

Paper IX

Experiments in the wind turbine far wake for the evaluation of an analytical wake model

García L, Vatn M, Mühle F and Sætran L

Published in Journal of Physics, Conference Series, vol. 854 (2017) 012015

doi: 10.1088/1742-6596/854/1/012015

Paper X

Comparative study on the wake deflection behind yawed wind turbine models

Schottler J, Mühle F, Bartl J, Peinke J, Adaramola M S, Sætran L and Hölling M
Published in Journal of Physics, Conference Series, vol. 854 (2017) 012032
doi: 10.1088/1742-6596/854/1/012032

Paper XI

Wind tunnel experiments on wind turbine wakes in yaw: Redefining the wake width

Schottler J, Bartl J, Mühle F, Sætran L, Peinke J and Hölling M
Accepted for publication in Wind Energy Science, 2018
doi: 10.5194/wes-2017-58

Paper XII

A Detached-Eddy-Simulation study: Proper-Orthogonal-Decomposition of the wake flow behind a model wind turbine

Göing J, Bartl J, Mühle F, Sætran L, and Thamsen P U
Submitted to Journal of Physics, Conference Series, DeepWind 2018

Paper XIII

Experimental validation of analytical wake and downstream turbine performance modeling

Polster F, Bartl J, Mühle F, Thamsen P U and Sætran L
Submitted to Journal of Physics, Conference Series, DeepWind 2018

Paper XIV

Validation of the real-time-response ProCap measurement system for full field wake scans behind a yawed model-scale wind turbine

Bartl J, Müller A, Landolt A, Mühle F, Vatn M, Oggiano L and Sætran L
Submitted to Journal of Physics, Conference Series, DeepWind 2018

Nomenclature

Roman Symbols

A_{in}	Inlet area of the contraction nozzle
A_{out}	Outlet area of the contraction nozzle
A_R	Rotor swept area
a	Axial induction factor
a'	Tangential induction factor
B	Number of rotor blades
C_P	Power coefficient
C_T	Thrust coefficient
C_L	Lift coefficient
C_D	Drag coefficient
c	Chord length
D	Rotor diameter wind turbine
F	Prandtl's tip loss factor
f_D	Doppler frequency
M	Torque
n	Number of measurements
P	Power
p_{amb}	Ambient pressure

Δp	Pressure difference
R	Rotor radius wind turbine
Re	Reynolds number
B_R	Random uncertainty
r	Radial position
P_R	Systematic uncertainty
Δr	Radial blade element length
C_T	Thrust force
TI	Turbulence intensity
t	Student's t
$Temp$	Temperature
U_∞	Inlet velocity
U_∞^*	Normalized inlet velocity
$\bar{u}$	Time averaged velocity
u'	Turbulent velocity component
U_{ref}	Reference velocity
Δx	Fringe spacing interval
y_{ref}	Reference height

Greek Symbols

α	Power law coefficient
α_a	Angle of attack
β	Blade pitch angle
γ	Yaw angle
λ	Tip speed ratio
λ_{loc}	Local tip speed ratio

λ_{LDV}	Wave length laser beams LDV
ω	Rotational speed of the rotor
ω_R	Total uncertainty
φ	Flow angle
ρ	Air density
σ	Standard deviation
ν	Kinematic viscosity
σ_s	Solidity, fraction of blade covered area
θ	Blade twist angle

Superscripts

$*$	Normalized values

Acronyms / Abbreviations

BEM	Blade element momentum
CFD	Computational fluid dynamics
DAQ	Data acquisition
FFT	Fast Fourier Transformation
LiDAR	Light detection and ranging
LES	Large-eddy simulation
PIV	Particle image velocimetry
RANS	Reynolds-Averaged-Navier-Stokes
TKI	Turbulent kinetic energy

Chapter 1

Introduction

This section introduces the topic of wind energy and rotor wake interactions and explains the motivation for the PhD thesis. The important contribution of wind energy development to achieve the climate goals and to limit global warming is explained. Furthermore, the historic development of wind energy, which resulted in large turbines, which are clustered in wind farms onshore and offshore is summarized to show the success of previous research. Next, wind farm interactions, which affect the overall efficiency and increased turbine loading are explained to show the potential for wind farm optimization. Thereafter the turbine wake, which causes these interactions and is characterized by low velocities and increased turbulence is introduced. Then the measures, wind farm layout, rotor design and turbine control, which can be optimized to limit such wake effects are presented. The motivation is concluded with an introduction of the wake investigation techniques, wind tunnel tests, numerical simulations and measurements of full-scale wind turbines, which all have some limitations, but complement each other to provide accurate wake data. After the motivation, the objectives of the PhD thesis are explained. The main goal of the PhD thesis is to enhance the current knowledge of the physics of rotor wake interactions to improve wind farm efficiency. Finally, the thesis structure will be presented and the different papers are classified and connected.

1.1 Motivation

The consequences of the climate change are one of the major topics human kind is likely to face in future. Herein, the largest single source of global greenhouse gas emissions is the utilization of fossil fuels for the generation of electricity and heat (IPCC, 2014). Although the energy sector is already a major contributor to global warming, the world wide energy demand is expected to further increase in the next decades (IEA, 2017).

The political will to limit global warming has resulted in the Paris Agreement that was adopted in 2015. The agreement has the goal of saving the climate and limiting the increase in global average temperature below 2 °C compared to pre-industrial levels (UNFCCC, 2015). To achieve this two-degree goal the transition from fossil fuels to renewable energy sources is of major importance (IEA, 2016).

1.1.1 Historic summary of wind turbine development

Within the renewable energies, wind energy, with its vast potential plays a fundamental role in the energy transition. Wind energy has also a long history, which will be presented in the following overview that is adopted from Hau (2013) and Manwell et al. (2010). The first historical source goes back to the 7th century and tells of vertical axis wind mills that were used in Persia for milling grain. But also in China wind mills were already used for the irrigation of rice fields. The horizontal axis wind turbine, which is the common type today, is assumed to be invented in Europe in the 12th century. It was used all over Europe up into the 20th century mainly for milling, but with further development also for sawing wood and machining metal. The power generation with wind turbines began already in the end of the 19th century. The Danish professor Paul La Cour built a wind turbine driving a dynamo as early as 1891, this concept was further developed and utilized until the middle of the 20th century. Furthermore, La Cour is assumed to be the first researcher to carry out wind tunnel experiments on wind turbines in a self constructed facility. Until the 17th century, wind turbine development was no result of systematic research, but then physical and mathematical thinking became more established and scientists drafted the first works on wind mills. In the 1920's the aerodynamicist Albert Betz formulated the modern physical principles of wind energy conversion, he published his research in 1926 and provided basis for the aerodynamically design of wind turbine blades (Betz, 1926).

In the first part of the 20th century different turbine concepts were developed in Europe and the United States ranging from small turbines that where produced in a large quantity to experimental turbines with big rotors. The rotors had different number of blades ranging from 2-bladed to multiple bladed rotors and were manufactured from various materials like fabric, aluminum, stainless steel laminated wood and even glass-fiber composites. However, the low price of fossil fuels lead to decreasing interest in further development of windmills for energy generation. Consequently, most of the turbines where decommissioned in the 1960's as they where economically unprofitable.

However, the oil crisis in the 1970's changed the perspective on energy generation, as the price for fossil fuels increased and western countries wanted to become more independent from oil exports. Consequently, renewable energy sources became interesting for electricity generation again. Therefore, the US government and European governments, especially Denmark, Sweden and Germany initialized various research programs to further develop wind power. In the 1980's, the focus was set primarily on large experimental turbines, which were mostly developed by well known industrial companies. The turbines were tested intensively the first years and were even kept running into the 1990's. Even though the large turbines were not very successful and thus the research focus on them came too early, they provided the technical foundation for modern wind turbine technology. Simultaneously, an interest in clustering wind turbines arose and as a result the first wind farms were built in California in the beginning of the 1980's. A large number of turbines in these wind farms were imported from Denmark, where companies started to build small 3-bladed turbines, after the energy crisis. These turbines were economically sustainable and were manufactured in a large number. Together with the first law supporting renewable energies in Germany, wind power became more and more important.

In the following decades, those turbines were further developed from a diameter of 15 m and a rated power of 50 kW to turbines with a diameter of up to 180 m and a rated power of up to 9.5 MW, which are actually used today (Windpowermonthly, 2017). Wind turbines are also not only installed on land but also more and more offshore. Between 2011 and 2017 the globally installed offshore capacity increased from around 4.000 MW to 18.000 MW (GWEC, 2017). The offshore wind marked is expected to further grow and with the successful development of floating wind turbines, high wind locations in deep water can be utilized for wind farm installations in the future. The successful history of wind energy for generating electricity and the importance of wind power can be seen in the globally installed wind power capacity, which is distributed to 90 countries and increased from 24.000 MW in 2001 to around 540.000 MW in 2017. Today, wind power is effectively competing with traditional energy sources and thus a further increase of installed capacity of over 800.000 MW globally is expected until 2021 (GWEC, 2017).

1.1.2 Wind turbine interactions

Most wind turbines today are installed in wind farms as the installation and maintenance costs are lower compared to a single turbine operation. However, the turbines cannot be arranged randomly and too close to each other. This is because the flow downstream of a wind turbine is characterized by a reduced mean flow velocity and an increased turbulence level. This flow field, behind the wind turbine, is called the wind turbine wake.

Experimental and numerical studies show that the velocity deficit in the wake is only minor after a separation distance of $10D$ (D is the rotor diameter) (Ammara et al., 2002). The higher turbulence however, is still present at a distance of $15D$ downstream of the rotor (Højstrup, 1999). In most wind farms, the typical spacing for turbines is between 4 - $8D$, as the installation costs would be too high for larger separation distances (Barthelmie et al., 2006). Consequently, the turbines are usually installed close enough that they interact with each other and the wake of the upstream turbine influences the downstream turbine's power production. Barthelmie et al. (2009) reported average losses of 10 - 20% between the first and second turbine row in a offshore installation and a maximum power drop of up to 35% in the extreme case when the turbines are aligned with the wind direction. In another study, Thomsen and Sørensen (1999) investigated fatigue loads in an offshore wind farm and found an increase of 5 - 15% for the whole wind farm compared to the free flow situation. Furthermore, Sanderse (2009) stated an increase of up to 80% in fatigue loading for turbines that were aligned with the wind direction. Because of this influence on wind farm performance and the large potential of wind farm optimization, the European Academy of Wind Energy (EAWE) listed wake investigations as one of the research challenges in their long-term wind energy research agenda (van Kuik et al., 2016).

1.1.3 An introduction into the wind turbine wake

The wake of a wind turbine is schematically depictured in Figure 1.1. It can be mainly divided into two different sections, the near wake and the far wake (S. Lissaman, 1979). The complex near wake region is characterized by pressure equalization of the low pressure, resulting from extracting energy by the rotor and the ambient air. As a result, the wake widens and the center line velocity decreases until it reaches its minimum (when the pressure in the wake is similar to the ambient pressure) at around 1 - $2D$ downstream (Ainslie, 1988). From there, fluid mixing dominates the wake flow, the high turbulence in the boundary layer that is caused by blade tip vortices, mixes with the higher velocity in the ambient flow, generating a shear layer that expands outwards and inwards until it reaches the center line at around 2 - $5D$. This point is defined as the end of the near wake (Crespo et al., 1999).

After the transition region where the wake velocity is further increasing and the tip vortices decay due to interaction with the ambient turbulence, the far wake begins at around $5D$. In the far wake the wake is fully developed and the velocity deficit in the center decays with a rate that is dependent on the ambient turbulence (Ainslie, 1988). In a hypothetical case with an uniform inflow, the velocity and turbulence profiles in the far wake are axissymmetric and distributed self similar (Crespo et al., 1999).

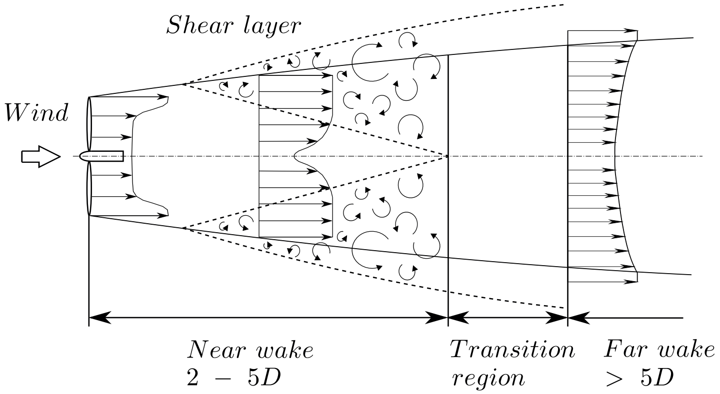

Figure 1.1: Schematic wake flow, adapted from (Hau, 2013; S. Lissaman, 1979).

1.1.4 Wind farm optimization approaches

Research on wind turbine wakes already started in the 1970's and since then several studies, investigating the wind turbine wake and its implication have been conducted. Detailed reviews about these studies and the wind turbine wake research can be found from Vermeer et al. (2003) and Sanderse (2009).

Understanding wakes and their structure in detail is important for the optimization of wind farms. Wake effects have to be considered when planning the arrangement of wind turbines and the operation of a wind farm can be optimized by taking turbine interactions into account. There are different approaches for optimizing the performance of a wind farm. These are mainly the wind farm layout, the turbine/rotor design and the wind farm control during operation. For the optimization of wind farms not every single turbine is optimized but the whole arrangement has to be as effective as possible. Thus, a single turbine might operate at a less efficient state and not extract the maximum energy from the wind, leaving more energy for downstream turbines, so that the whole farm can be more efficient.

The wind farm layout is offering a large potential for increasing overall performance. In a complex terrain it is determined mainly by the site's topography and the wind regime. Flat terrain and especially offshore sites offer better possibilities for a customized farm layout. Based on the layout, the wake impact on the downstream turbines could be improved using different approaches. Firstly, the separation distances among the turbines could be increased until the wake effects decayed before reaching the downstream turbine. The demand for land however would be very high and also installation and infrastructure would increase costs dramatically. Secondly, the turbine configuration can be varied by different approaches like an aligned array or structured and unstructured grids. Consequently, many factors have to be taken into account finding the most efficient layout. Therefore, several studies optimizing the wind farm layout have been conducted. An initial optimization study on wind farm layout was conducted by Mosetti et al. (1994). The authors used the Jensen wake model to simulate a wind farm and optimized it for maximum energy and minimum installation cost. Since then, many studies using different approaches to optimize wind turbine arrays have been conducted. An overview of these approaches is given in the review by Shakoor et al. (2016).

The rotor design is another possibility to optimize a wind farm in the design process. Usually wind turbine rotors are designed to extract as much energy from the wind as possible. However, if they could be designed to leave more energy in the flow, the overall performance of a wind farm could benefit from that, because more energy would be available for downstream turbines operating in the wake. An example for such a rotor concept is the low-induction rotor, which is working at non optimal induction and thus has a lower efficiency. Such a rotor is mainly designed for load reduction but is also reducing wake effects (Quinn et al., 2016). Designing a rotor with the focus on limiting wake losses was not yet considered a lot within wind farm optimization. The overall performance of a wind farm could also be increased by a rotor design with an improved efficiency that has no implications on the velocity deficit in the wake. Thus, the energy content in the wake of such a rotor is similar to the energy content of a wake forming behind rotor without improved efficiency.

The wind farm control offers large potential for the optimization of wind farms. There are mainly two approaches for wind farm control optimization, the induction based and the wake redirection control (Raach et al., 2016). A preliminary study on this topic was conducted by (Steinbuch et al., 1988) who showed that by applying control strategies the interactions between turbines can be limited and thus the energy output is maximized. A survey summarizing literature on wake farm control can be found in Knudsen et al. (2014). In a recent study Bartl and Sætran (2016) investigated the induction based control methods tip speed variation and pitch angle variation and showed that both techniques only have minor potential for wind farm optimization. Wake redirection is considered to have a bigger potential for control optimization. Fleming et al. (2015, 2014) tested the three redirection strategies yaw angle variation, tilt variation and individual pitch control. They showed good wake redirection with performance increase and load reduction for yaw and tilt variation, whereas individual pitch control resulted only in little wake redirection but an increase in blade loading. This was confirmed by Gebraad et al. (2014) who used the FLORIS model to evaluate yaw control for a small wind farm and also found a performance increase and load reduction.

In a study investigating different approaches for wind farm optimization, Fleming et al. (2016b) combined wind farm layout and wind farm control and showed that the best improvement was reached by applying a coupled control and layout optimization. This suggests, that all approaches have to be taken into account and combined to further optimize the wind farm performance. Consequently, further studies investigating wind farm layout, rotor design and wind farm control are needed.

1.1.5 Wake investigation techniques

There are mainly three techniques to investigate wind turbine wake investigations, full-scale measurements, computational fluid mechanics (CFD) simulations and wind tunnel experiments.

Full-scale experiments are widely conducted for the investigation of single turbines and wind farms. However, the measurements of full-scale wake data are rather complex, because substantial measurement equipment is needed. Nevertheless, many studies present velocity profiles measured with met masts (Barthelmie et al., 2007; Hansen et al., 2012). The installation of such met masts is expensive and thus the costs are rather high. In the last few years the development of the remote sensing technique LiDAR (laser detection and ranging) has made significant progress and LiDAR instruments have been used in several studies for wake measurements behind full-scale turbines (Kumer et al., 2015; Trujillo et al., 2016). LiDAR instruments can also be installed on the nacelle of a wind turbine to track the wake (Raach et al., 2017). However, the costs of full-scale experiments could be decreased by new full-scale measurement techniques. Such a technique was developed by Reuder et al. (2016), who equipped a drone with velocity measurement technique and used it to fly into the wake to directly measure flow properties. Notwithstanding, the biggest drawback of full-scale measurements are the uncontrollable boundary conditions. The inflow and the flow regime cannot be controlled and are constantly changing, which makes it hard to measure at defined boundary conditions and get reliable wake data. Consequently, other wake investigation techniques are needed to draw reliable conclusions on the wind turbine wake.

A 'somewhat' cheaper technique for wake investigations are numerical CFD simulations. This technique was developed intensively in the last decades and several different models were established. A state-of-the-art review on the calculation of wind turbine wake aerodynamics is presented by Sanderse et al. (2011). With computer simulations it is possible to extract detailed information of the wind turbine wake and multiple wake properties. Even though this technique is already very advanced, there are some limitations to it. Because direct numerical simulations still require too much computational capacity, small turbulent structures cannot be simulated and numerical models are depended on different turbulence models resolving turbulence in the flow. Furthermore, boundary conditions have to be defined and the grid has to be generated. Consequently, CFD simulations are depended on various input parameters, which influence the results and thus make them unreliable. As a consequence numerical models have to be validated against reliable data obtained by measurements.

Experimental wind tunnel tests under controlled boundary conditions are good techniques to deliver reliable results for CFD validation. In the last decades several experimental studies on the wind turbine wake have been conducted. These scaled model experiments helped to better understand the wake of wind turbines and to investigate different design and operation parameters and their influence on the wake development. The wake of single turbines was investigated in detail using different measurement technique (e.g. Chamorro and Porté-Agel 2009; Medici and Alfredsson 2006). Furthermore, numerous experiments of multiple aligned turbine arrays were conducted for a better comprehension of wake interactions see amongst others (Schottler et al., 2017; Schreiber et al., 2017). Moreover, whole wind farms consisting of multiple turbine rows were investigated in the wind tunnel to better understand wind farm behavior see for example Corten et al. (2004). Even though wind tunnel experiments provide actual measurement results, there are limitations to such measurements. One disadvantage is the influence of the wind tunnel walls, which can block the flow and limit it from expanding freely. This effect gets stronger with an increasing blockage ratio, which is defined as the ratio of the wind turbine rotor and the cross-section of the wind tunnel. The biggest limitation of wind tunnel experiments is achieving scaling similarity. While it is no problem to match the tip speed ratio of a full-scale turbine it is very hard to achieve Reynolds number similarity between wind tunnel tests and full-scale applications. Only few studies, which used advanced pressurized wind tunnels, were able to achieve model Reynolds numbers, which are similar to those occurring at full-scale turbines see for example (Miller et al., 2016). Nevertheless, as pictured in Figure 1.2 low Reynolds number wind tunnel experiments provide precise measurement data, which can be used for the validation and calibration of numerical CFD simulations. The validated CFD codes in turn can then be used to predict what is happening in full-scale applications. Consequently, experimental wind tunnel studies are not only important to understand the wake structure but also to provide reference data for the validation of CFD codes.

1.2 Objective

The existing literature on wind turbine wakes indicates that a lot of studies including experimental models in wind tunnel tests, numerical simulations and measurements of

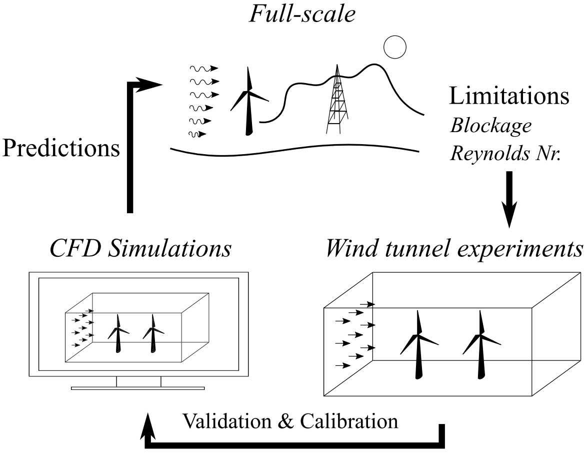

Figure 1.2: The importance of wind tunnel experiments and the connection between the three wake measurement techniques.

full-scale wind turbines have already been carried out to understand the characteristics and the behavior of wind turbine wakes. Nevertheless, there is still need for further investigation to fully understand the wake of wind turbines and thus the interaction between wind turbines.

For this PhD thesis, experimental studies were carried out to investigate the performance characteristics and the wake structures of single model wind turbines and multiple turbine arrays under various operating conditions and for different parameters that could have an effect on the wind turbine wake. The knowledge gained from this study will provide better understanding of the overall flow structure around wind turbines and the physics of rotor wake interactions and therefore help in proper planning and designing of wind farms. In addition, the generated data is used as reference for the validation of CFD codes and thus helps to improve numerical tools that are used for the simulation of wind farms.

In *Paper I*, *Paper II* and *Paper III* the focus is on rotor design and how it affects the wake development. Thus, these papers give insight on the potential of adopting the rotor design in order to improve the overall performance of a wind farm. *Paper I* focuses on how the rotor blade number is influencing the wake structure of a single wind turbine. The study should show if it could be beneficial to consider other concepts than the common three bladed turbine rotor to better account for losses due to turbine interactions. *Paper II* investigates the potential of opposite rotating rotors. Detailed measurements of the wake structure as well as the overall performance of an aligned turbine array are considered to show if different rotational directions in a wind farm could have the potential to improve the wind farm efficiency. In *Paper III* the wake of a rotor with winglets and thus an improved efficiency is compared to that of a base line rotor. The study shall give information if a rotor, that is equipped with winglets, is changing the wake structure, and thus improving or deteriorating the performance of a wind farm.

The rotor design and winglet optimization for the winglet wake experiment in *Paper III* are presented in *Paper IV*. The goal of the study is not only the design of a rotor for the wake investigations, but also the analysis of the potential of adding winglets at the blade tips for power optimization of a single wind turbine and providing basic design instructions for further winglet concepts. Furthermore, a detailed analysis of the blade flow shall show the difference of a winglet and a baseline rotor and explain why a winglet rotor can be beneficial. Together with *Paper III* it is investigated if winglets can not only improve the efficiency of a single turbine but also a complete wind farm.

Optimizing the wind farm control by redirecting the wake with intentional yaw misalignment is the topic of *Paper V* and *Paper VI*. These studies shall help to evaluate the potential of yaw control strategies for the optimization of wind farms. Thereby, the focus of *Paper V* is on the wake structure behind yawed turbines. The paper provides detailed information about the wake structure and how it is affected by varying inflow conditions. Consequently, it provides information that is needed for the development of advanced wind farm control algorithms. *Paper VI* is focusing on the power production and loads of a turbine operating in the wake of a yawed turbine at various inflow conditions and array configurations. Together with *Paper V* this study completes the link between detailed wake flow characteristics and the performance and loads of a turbine operated in the wake.

Paper VII compares detailed experimental measurement results of complex wakes behind yawed wind turbines to numerical predictions, obtained by various CFD simulations of the same wake flow. The comparison and the analysis of discrepancies of the CFD results should help code developers to see how well their simulations perform and thus provide information for further development of CFD solvers. Furthermore, the data is published and made available to CFD developers as validation reference for CFD codes.

1.3 Thesis outline

After the introduction given in this chapter, chapter 2 describes the methods applied in the PhD thesis. Firstly, the experimental facilities and the model wind turbines that were used to study rotor wake interactions are specified. After that the different rotor designs that were developed are introduced. The blade element momentum (BEM) code that was used for the rotor evaluation and design will be described and the 3D printing production technique, that was applied for the rotor concepts will be introduced and evaluated by comparing performance and wake measurements of aluminum and 3D printed rotors. At the end of chapter 2 the employed measurement technique and the method determining the measurement uncertainty will be explained.

In chapter 3 the results are summarized and the outcome of the articles are linked and brought in an overall perspective. A schematic summary and connection of all papers is presented in Figure 1.3. All articles can be assigned to the overall topic of the project, rotor-wake interactions. However, they are divided into the subtopics wind farm optimization and reference data for CFD validation. Whereat the major part is on the optimization of wind farms, which is again divided into the two categories rotor design and control strategies. Within the topic of rotor design the three topics, which are, comparison 2-3-bladed rotors (*Paper I*), counter rotating wind turbine rotors (*Paper II*) and winglet rotors (*Paper III* and *Paper IV*) are discussed. Within control strategies the focus is on intentional yaw misalignment (*Paper V* and *Paper VI*). The topic reference data for CFD validation is represented by *Paper VII*, which is based on the wind turbine wakes in yaw measurement campaign. This article is complementing the studies for wind farm optimization by comparing the experimental results to numerical CFD predictions and providing detailed data that can be used by CFD developers for the validation of their numerical wake simulation codes. The motivation for all investigated topics will be summarized, before the literature will be briefly reviewed. Furthermore, the major results of each study will be summarized and a conclusion on their potential for wind farm optimization will be given.

The introductory chapters of the PhD thesis will be completed by the conclusions, in which the potential for wind farm optimization of the different approaches will be analyzed. Furthermore, recommendations for future research work on the promising methods for wind farm optimization will be given.

After the introductory chapters, all the papers that are part of the PhD project will be provided. The seven articles are ordered regarding the research topics and will not be assorted in a chronological order.

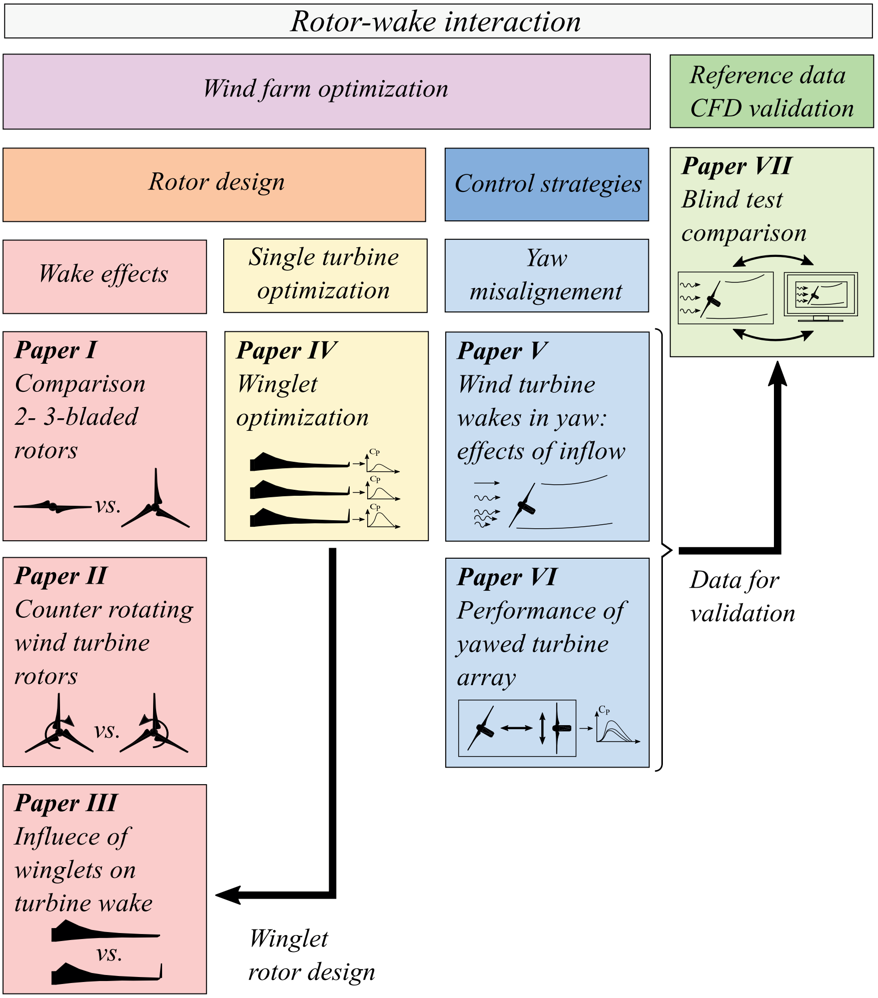

Figure 1.3: Summary and connection of all papers in the thesis.

Chapter 2

Methodology

This chapter introduces the methodologies applied in the PhD study. First the wind tunnel is described and different inflow conditions with varying velocity distribution and turbulence levels are introduced. Then the three model wind turbines used for the experiments are presented. Next the focus is on the design of the different model rotors. The blade element momentum (BEM) method, which was used for the design of the blades and the numerical investigation of the rotors, will be briefly summarized. Furthermore, the different rotor concepts, used in the various experiments will be presented. Because the new rotors were manufactured with the 3D printing technique, it will be analyzed whether 3D printed rotors are applicable in wind tunnel tests. Then the measurement technique, which was used to measure the power, force and wake properties is introduced. The chapter is concluded with a description of the method that was used to quantify the measurement uncertainty and presentation of typical measurement uncertainties occurring during the project.

2.1 Wind tunnel

All the experimental studies were conducted in the closed-loop wind tunnel in the Fluid Mechanics Laboratory at the Norwegian University of Science and Technology (NTNU). The test section of the wind tunnel has a length of 11.15 m and a width of 2.71 m, it is depicted in Figure 2.1. The roof of the wind tunnel was adjusted for zero pressure gradient and thus the height increased from 1.80 m at the inlet to 1.85 m at the outlet. The tunnel is driven by a radial fan with a power of 220 kW, at the end of the test section. The test section inlet is formed as a contraction nozzle with static pressure taps all around the circumference of the nozzle inlet and outlet cross-section measuring the pressure difference Δp. Applying the continuity equation and Bernoulli's law, Δp can be used for calculating the inlet velocity of the wind tunnel with:

$$U_\infty = \sqrt{\frac{2\Delta p}{\rho\left(1 - \frac{A_{out}^2}{A_{in}^2}\right)}}, \tag{2.1}$$

where ρ is the air density, A_{in} the area of the nozzle inlet and A_{out} the area of the nozzle outlet. The advantage of this measurement technique is, that no device is blocking the flow and thus the inlet velocity U_∞ can be obtained without disturbing the flow. In all experiments conducted for the seven papers the inlet velocity of the wind tunnel was adjusted to $U_\infty = 10.0$ m/s.

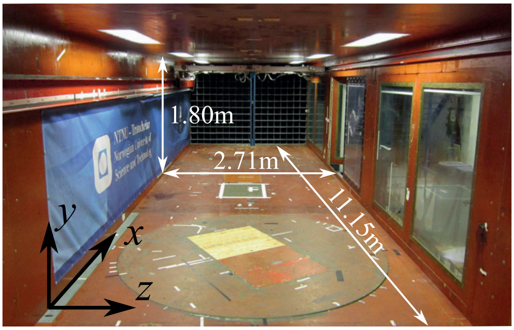

Figure 2.1: Test section of the wind tunnel with dimensions and coordinate system, looking in flow direction.

2.1.1 Inflow conditions

During the experiments three different inflow conditions were investigated: low-turbulence uniform, high-turbulence uniform and high-turbulence shear. The higher turbulence was generated by passive grids at the test section inlet. Figure 4 shows the grid setting at the inlet and the normalized velocity $U_\infty^* = {}^{\bar{u}}/_{U_{ref}}$ and turbulence intensity $TI = {}^{u'}/_{U_{ref}}$ at the turbine position, which is $2D$ behind the grid. Where U_{ref} is the reference velocity at hub height, $\bar{u}$ is the time averaged velocity and u' the turbulent velocity component.

Low-turbulence inflow

The low-turbulence inflow was applied in most studies and was therefore investigated in all Papers except *Paper VII*. As pictured in Figure 4a there was no grid installed at the inlet of the test sections resulting in a flow with only marginal turbulence intensity of $TI = 0.23\%$. TI and U_∞ are uniformly distributed in the empty wind tunnel

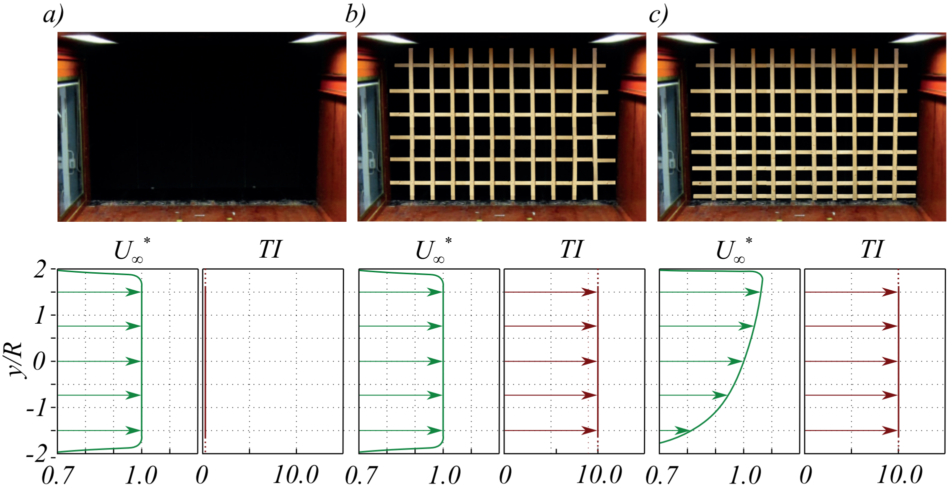

Figure 2.2: Different inlet configurations and resulting $U_\infty{}^*$ and TI in [%] at the turbine position for (a) low-turbulence uniform, (b) high-turbulence uniform and (c) high-turbulence shear inflow.

and the mean velocity over the rotor swept area is found to deviate by ±0.8% for $U_\infty = 10.0$ m/s.

High-turbulence inflow

The high-turbulence inflow was used in *Paper IV*, *Paper V*, *Paper VI* and *Paper VII*. In order to get a uniform high-turbulent flow the inlet was equipped with a turbulence grid as shown in Figure 4b. The grid is fabricated from evenly spaced wooden bars with a clearance of 0.24 m resulting in a solidity of 35%. The grid generates a turbulence intensity of $TI = 10.0\%$ at the turbine position ($0D$). However, because the turbulence is only generated at the inlet it decays with increasing distance resulting in $TI = 5.5\%$ $3D$ and $TI = 4.1\%$ $6D$ behind the turbine position, detailed measurements of U_∞ and TI are presented in *Paper V*. The grid structure can still be observed in the flow at the turbine position, resulting in a spatial variation of U_∞ over the rotor area of ±2.5% at the turbine position. However this variation is found to be only ±1.0%, $3D$ behind the turbine.

High-turbulence shear inflow

The third inflow condition is a high-turbulence shear flow that was used in *Paper V* and *Paper VII*. The grid generating the turbulent shear flow is shown in Figure 4c. It has a solidity of 38% and is also made of wooden bars that are distributed evenly in horizontal direction with a clearance of 0.24 m. In vertical direction however, the distance between the bars is increasing from 0.016 m at the wind tunnel floor to 0.30 m at the ceiling. This arrangement is resulting in a velocity shear in which the normalized velocity is 1.0 at hub height, see Figure 4c. The shear profile can be described with the power law:

$$\frac{\bar{u}}{U_{ref}} = \left(\frac{y}{y_{ref}}\right)^{\alpha}. \tag{2.2}$$

Equation (2.2) describes the mean wind speed $\bar{u}$ as a function of height y provided that U_{ref} is known at a reference height y_{ref}. The power law coefficient α determines the strength of the shear. The described grid was designed to obtain a α of 0.11, which corresponds to a neutral atmospheric boundary layer (Wharton and Lundquist, 2012). The turbulence intensity at the turbine position is $TI = 10.0\%$ at hub height and with increasing distance it decays similar to that of the high-turbulence grid, the detailed streamwise evolution is shown in *Paper V*.

2.1.2 Wind tunnel blockage

As already mentioned in Chapter 1, a limitation in wind tunnel experiments is the blockage effect. The model wind turbines are an obstacle in the flow, consequently part of the flow is evading the rotor and expanding around the turbine. If the cross-section fraction that is blocked by the wind turbine rotor is too large, the expansion is limited by the wind tunnel boundaries and the flow hitting the turbine is influenced, resulting in higher velocities at the turbine. The model rotors used in the study have a blockage ratio of approximately 13% in the NTNU wind tunnel. Sarlak et al. (2016) showed in their study that a blockage ratio of this size has already an influence on the power and thrust measurements of the turbine. There exist different methods correcting for the wind tunnel blockage, see for example (Chen and Liou, 2011; Ryi et al., 2015). Nevertheless, they are also based on different assumptions. Consequently, analyzing the results of wind tunnel experiments it has to be kept in mind that the power and forces of a turbine could be higher in comparison with the free flow condition.

2.2 Model wind turbines

The three model turbines Turbine 1 (T1), Turbine 2 (T2) and Laterally Angled Rotating System 1 (LARS1), which were used in the wind tunnel experiments, are shown in Figure 1. Detailed technical drawings of the model turbines are attached in Appendix A. The turbines were already used for various studies at NTNU. Krogstad and Lund

(2012) designed the standard NTNU rotor and measured power and thrust for the single turbine T2. This study was extended by Adaramola and Krogstad (2011) who investigated the performance of an aligned turbine array with turbines T1 and T2 at various separation distances, yaw angles and blade pitch angles. The first wind turbine wake measurements at NTNU were conducted by Krogstad and Adaramola (2012) who investigated the near wake of the single turbine T2 at different tip speed ratios and yaw angles. Moreover, measurements of the wake formed behind a turbine array of T1 and T2 were conducted by Bartl et al. (2012) and Schümann et al. (2013). A recent study by Pierella and Sætran (2017) examined the influence of the tower structure on the wake development behind the single turbine T2 and an aligned array with T1 and T2. Furthermore, an elaborated analysis, providing detailed information about the wake behind single turbine T2 was performed by Eriksen and Krogstad (2017a,b).

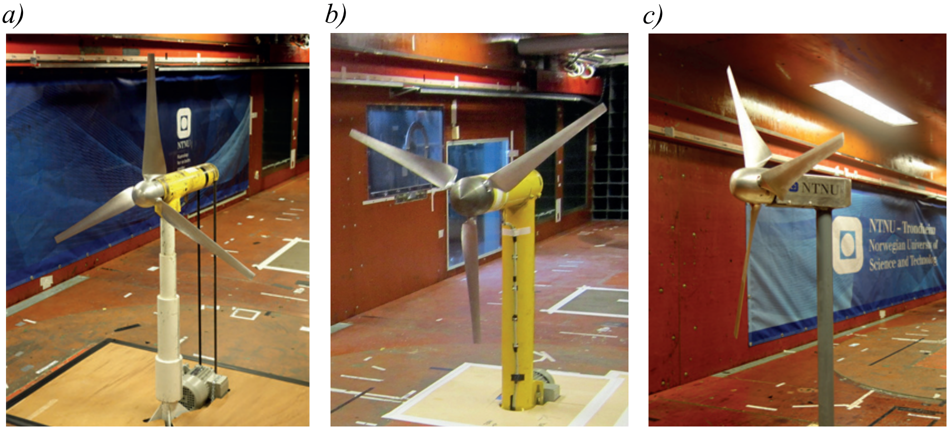

Figure 2.3: Model wind turbines (a) T2, (b) T1 and (c) LARS1, all equipped with the standard 3-bladed NTNU rotor.

The turbines T1 and T2 are driven by an asynchronous motor that is located at the base of the turbine tower and controlled by a frequency converter. This configuration enables an adjustment of the turbines rotational speed, independent from the flow regime in the wind tunnel. Consequently, the turbines can be operated at a wide range of tip speed ratios even though they operate in stall. Model turbine T2 was the most common turbine in the PhD study and was used in all papers except *Paper V*. On the contrary T1 was only used as a downstream turbine in *Paper II*. Model turbine LARS1 was designed for the yaw experiments and is employed in *Paper V*, *Paper VI* and *Paper VII*. It has a slimmer tower and a smaller nacelle as turbines T1 and T2 to limit blockage of the wake flow when the turbine is yawed. It is driven by a servo motor that is installed inside the turbine nacelle. The motor is also frequency-controlled enabling operation at a constant rotational speed. The three turbines have a similar hub structure so that all different rotors can be installed on all turbines. During the yaw experiments another model wind turbine, from ForWind in Oldenburg (Germany) was used. The turbine is somewhat smaller than the NTNU turbines. A detailed description is presented in (Schottler et al., 2016a). Wake measurements behind this turbine are part of *Paper VII*.

2.3 Model rotor design

For the PhD work the existing rotors at NTNU were used in addition to a new set of model rotors, which were designed in the course of this study. The two parameters that have to be determined in the blade design are the span-wise chord length c and twist angle θ distribution. The determination of these parameters is based on different approaches for the diverse blade designs. The classical blade element momentum (BEM) theory was applied to evaluate the rotor designs. Furthermore, it was used in the rotor design process together with another technique, which is based on the modification of existing rotor designs. In the following sub-chapters, the BEM method is explained, the different rotors are described and their design and production process are discussed.

2.3.1 Blade element momentum method

For the evaluation of the different rotors and the blade design, a classical BEM code was developed, which is described below based on (Hansen, 2015). Furthermore, non-dimensional numbers, which are important for the evaluation of wind turbine rotors will be explained.

The available energy for a wind turbine is defined by the kinetic energy of the wind. It is given by:

$$P_{avl} = \frac{1}{2}\rho A_R U_\infty^3, \tag{2.3}$$

where A_R is the rotor swept area However, the turbine cannot extract all the available power from the wind. The power coefficient C_P is a dimensionless number, which describes the aerodynamic efficiency of a wind turbine and thus, the amount of energy it is extracting from the flow:

$$C_P = \frac{P}{0.5\rho A_R U_\infty^3}. \tag{2.4}$$

P denotes the power extracted by the rotor. The maximum aerodynamic efficiency of a wind turbine according to Betz is $C_{P,Betz} = \frac{16}{27}$. Similar to the power coefficient another dimensionless number, the thrust coefficient C_T can be calculated with:

$$C_T = \frac{T}{0.5\rho A_R U_\infty^2}, \tag{2.5}$$

where T is the thrust force acting on the rotor. C_T is not directly related to the aerodynamic efficiency. However, it is an indication on how much the flow is affected by the wind turbine. Another important non-dimensional parameter is the tip speed ratio λ, which is defined as the ratio of the blade tip speed and the inflow velocity,

$$\lambda = \frac{\omega R}{U_\infty}, \tag{2.6}$$

where ω is the rotational speed and R is the rotor radius.

Flow around wind turbine

The stream tube, pictured in Figure 2.4 is a common one-dimensional approach to describe the flow around a wind turbine. It can be seen, that the velocity is already decreasing before hitting the turbine. This reduction in velocity can be described by a rotor induced axial velocity component acting in opposite flow direction, which is defined by the axial induction factor a. With the axial induction factor, the axial velocity u_1 at the rotor plane can be expressed with the known inflow velocity U_∞, which becomes important when calculating the aerodynamics at the rotor blades:

$$u_1 = (1 - a)U_\infty. \tag{2.7}$$

Considering the three-dimensionality of the flow, the rotating rotor blades cause wake rotation behind the wind turbine, which induces additional tangential velocity. This additional tangential velocity component in the wake can be specified with the tangential induction factor *a'*. Similar to the axial velocity, the tangential velocity at the rotor plane can be calculated by:

$$u_t = (1 + a')\omega r. \tag{2.8}$$

where r is the radial position of the blade element. Opposite to the axially induced velocity the tangentially induced velocity is added to the rotational component as the flow is accelerated in tangential direction.

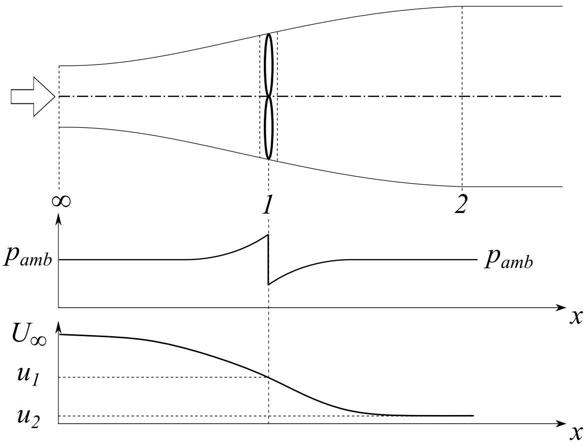

Figure 2.4: Schematic stream tube describing the one-dimensional flow passing a wind turbine, with the corresponding pressure and velocity distribution.

Rotor evaluation with BEM method

In the blade element momentum method, the stream tube, presented in Figure 2.4 is divided into several rings. As a result the flow regime at each blade element can be analyzed (see Figure 2.5) and the steady-state power and thrust of the rotor can be calculated. The BEM method is a two-dimensional approach, consequently the span wise velocity component is not considered and thus each element is independent and there is no lateral transfer between the elements, which depicts a limitation of the method.

The flow regime on a blade element and the resulting forces are pictured in Figure 2.5. It can be seen that the velocity acting on the blade element V_{rel} is the resulting velocity from the axial and tangential velocity component, which stem from the wind speed and the rotor rotation respectively. The flow angle φ is defined as the angle included between V_{rel} and the rotor plane, it can be calculated along with the induction factors by applying:

$$\varphi = \tan^{-1}\left(\frac{(1-a)U_\infty}{(1+a')\omega r}\right). \tag{2.9}$$

The flow angle is split into the twist angle of the blade θ and the angle of attack α_a, resulting in:

$$\alpha_a = \varphi - \theta. \tag{2.10}$$

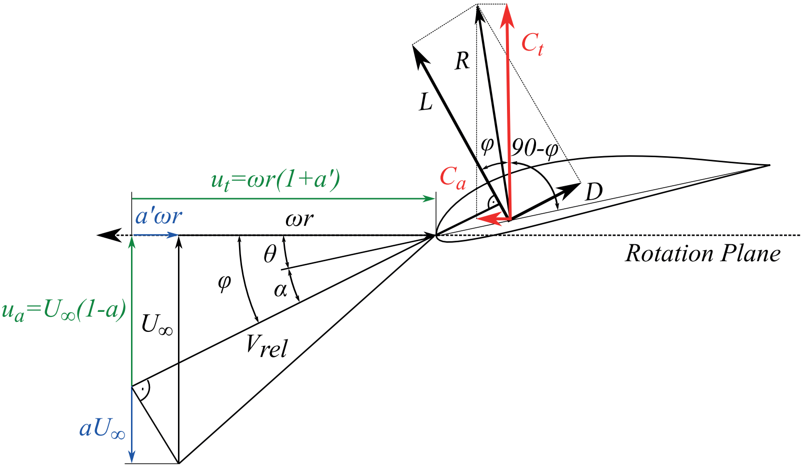

Figure 2.5: Blade element with velocity triangle at the rotor plane and the resulting force R, with components for lift L and drag D and the load coefficients in axial and tangential direction.

The lift and drag coefficients C_L and C_D, which are non-dimensional coefficients representing the lift and drag force acting on the blade element, can be found in look up tables, simulated or obtained through experiments. In this study C_L and C_D were calculated using the program XFOIL (Drela, 1989). With this two dimensionless parameters the axial and tangential load coefficients C_a and C_t can be calculated according to:

$$C_a = C_L \cos\varphi + C_D \sin\varphi, \tag{2.11}$$

and

$$C_t = C_L \sin\varphi - C_D \cos\varphi. \tag{2.12}$$

The evaluation process with the BEM code is iterative as the induction factors are unknown in the beginning. So, in the BEM analysis initial values for the induction factors a and a' need to be guessed, as they are necessary to calculate the flow angle. After the load coefficients are obtained, the actual induction factors can be calculated according to:

$$a = \frac{1}{\frac{4F\sin^2\varphi}{\sigma_s C_a} + 1}, \tag{2.13}$$

and

$$a' = \frac{1}{\frac{4F\sin\varphi\cos\varphi}{\sigma_s C_t} - 1}. \tag{2.14}$$

F denotes the Prandtl's tip loss factor, which corrects the induction factors for a finite blade number and the spanwise flow, limiting the loads at the tip, consequently, its effect is increasing with increasing radial position r. σ_s is the solidity, which is defined as the fraction of the annular area that is covered by the blades. Furthermore, in the BEM code values of $a > 0.2$ need to be corrected according to Glauert to account for the fact that the thrust forces can be bigger as the static pressure in the flow. If the initial induction factors and the actual induction factors are within a defined tolerance level, the iteration is stopped and the thrust and torque of each blade element are calculated with:

$$T_{(r)} = \frac{1}{2}\rho B \frac{U_\infty^2 (1-a)^2}{\sin^2\varphi} c C_t \Delta r, \tag{2.15}$$

and

$$M_{(r)} = \frac{1}{2}\rho B \frac{U_\infty (1-a)\omega r(1+a')}{\sin\varphi\cos\varphi} c C_t r \Delta r, \tag{2.16}$$

where, c is the chord length of the blade element B is the number of rotor blades and Δr is the blade element length in radial direction. The total power of the rotor P is the sum of the shaft torques from all annual sections:

$$P = \sum M_{(r)} \omega r. \tag{2.17}$$

Similar to the torque the thrust force acting on the rotors is the sum of the thrust forces of all blade elements:

$$P = \sum T_{(r)}. \tag{2.18}$$

BEM for blade design

For the blade design the chord length and twist angle were determined for each blade element. Therefore, the axial induction factor was optimized according to:

$$16a^3 - 24a^2 + a(9 - 3x^2) - 1 + \lambda_{loc}^2 = 0, \tag{2.19}$$

where $\lambda_{loc} = \frac{\omega r}{U_\infty}$ is the local tip speed ratio. The corresponding tangential induction factor is dependent on the axial induction factor and could thus be calculated by:

$$a' = \frac{1-3a}{4a-1}. \tag{2.20}$$

The flow angle was obtained by solving Equation (2.9) and together with the optimum angle of attack of the used airfoil $\alpha_{a,opt}$ the twist angle was calculated according to:

$$\theta = \varphi - \alpha_{a,opt}. \tag{2.21}$$

The chord length for each blade element could then be obtained by:

$$c = \frac{8\pi a \lambda_{loc} \sin^2\theta R}{(1-a)BC_a\lambda}. \tag{2.22}$$

The results for the separate blade elements together with the radial position resulted in the chord length and twist angle distribution of the new blade.

2.3.2 Rotors

In order to investigate the influence of the rotor design on the wake development, several rotors were tested in the wind tunnel experiments. The chord and twist distribution of these rotors is presented in Figure 2.6 and the key parameters are summarized in Table 2.1.

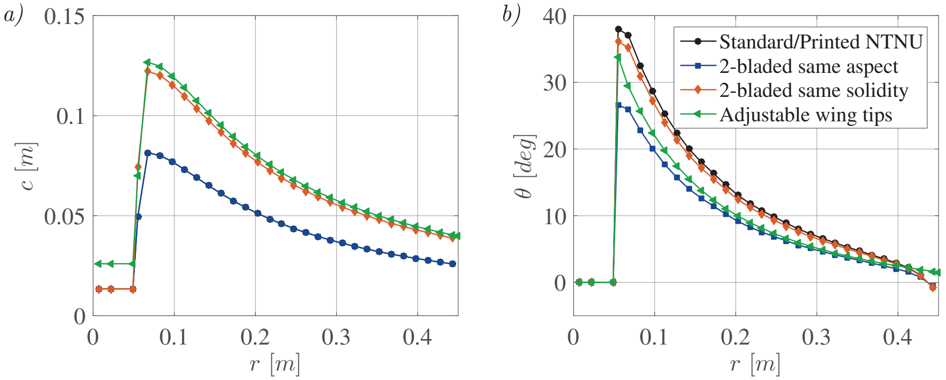

Figure 2.6: Span-wise (a) chord length c and (b) twist angle θ distribution for the rotors used in the PhD study (r is the radial position).

The existing rotors at NTNU were milled from an aluminum alloy. Such rotors are very precise and sturdy and are suited very well for wind tunnel experiments.

Table 2.1: Key parameters of the rotors used in the PhD study, (tip speed ratio (λ) clock-wise (CW) and counter-clock-wise (CCW) rotation).

Rotor	Number blades	opt. λ	C_P	C_T	Rotational direction	Airfoil	Material	Papers
Standard NTNU	3	6	0.46	0.90	CCW	S826	Aluminum	*II*, *V*, *VI*, *VII*
Printed NTNU	3	6	0.48	1.00	CW	S826	VeroGray	*I*, *II*
2-bladed same solidity	2	6	0.45	0.98	CW	S826	VeroGray	*I*
2-bladed same aspect	2	7	0.45	1.03	CW	S826	VeroGray	*I*
Adjustable wing tips	2	6	0.47-0.52	0.97-1.08	CCW	R-opt	VeroGray	*III*, *IV*

However, this production technique is very costly and could therefore not be considered as production method for the various model rotors. Therefore, another technique was selected and the rotors were produced using a considerably more reasonable manufacturing option of rapid prototyping using a 3D printer. The printer used for the blade fabrication is a Objet Eden 500V that works based on the Multi-Jet Modeling technique. This technique enables the production of very detailed parts with a high accuracy and smooth surfaces. Accordingly the fabricated blades are of high quality and their appearance is similar to the milled aluminum blades. Nevertheless, they were manufactured from a material called VeroGray, which has worse performance than aluminum regarding tensile strength and modulus of elasticity (Ver, 2016). Accordingly, they act different in the wind tunnel test. Therefore, their applicability in wind tunnel tests was verified and evaluated in 2.3.3.

Standard NTNU rotor

The standard NTNU rotor (see Figure 1) was used in most studies of the PhD study and it additionally served as reference for all the other rotor designs. The blades for the rotor were designed using BEM theory, the design and the rotor are described in detail in (Krogstad and Lund, 2012). The rotor has a diameter of $D = 0.984$ m and has three blades, which are fabricated from aluminum. Therefore, it is well suited for wind tunnel experiments as the blades do not deflect and thus have a defined geometry even when operated under heavy load. The rotor is based on the NREL S826 airfoil from root to tip. The shape of the airfoil is pictured in Figure 2.7 and its polars for $Re = 1.0{\cdot}10^5$ are presented in Figure 2.8. A detailed description of the airfoil can be found in (Somers, 2005).

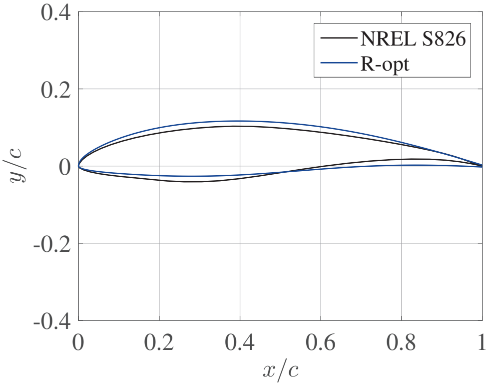

Figure 2.7: Airfoil shapes used for the model rotors.

The airfoil was originally developed as tip airfoil for full-scale wind turbines, hence it was designed for Reynolds numbers of $Re \approx 1.0{\cdot}10^6$. This is approximately one magnitude higher as the chord based Reynolds number at the blade tip in the experiments, which is approximately $Re_{c,tip} = 1.1{\cdot}10^5$ at the optimal tip speed ratio of the rotor ($\lambda = 6$) and the inlet velocity of $U_\infty = 10.0\,\mathrm{m/s}$. However, Krogstad and Lund (2012) performed a Re dependence test and found a performance independence for $U_\infty > 9.0\,\mathrm{m/s}$. Consequently, the airfoil performs already decently at lower Re. The airfoil polars for $Re = 1.0{\cdot}10^5$ generated by XFoil are presented in Figure 2.8 . This rotor was used in the experiments for *Paper II Paper V Paper VI* and *Paper VII.*

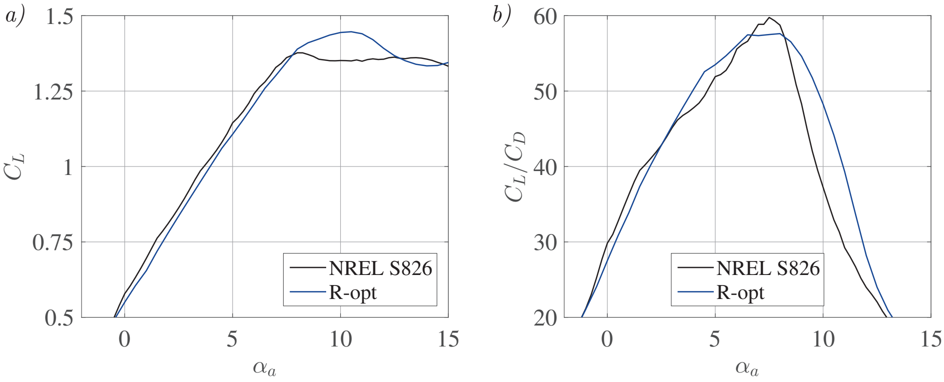

Figure 2.8: Predicted airfoil polars at $Re = 1.0{\cdot}10^5$ using XFOIL.

2-bladed rotors

For *Paper I* the effect of the blade number on the wake development was investigated. Accordingly new 2-bladed rotors were designed, they can be seen in Figure 2.9. The goal of the design was to obtain 2-bladed rotors that have similar performance as the 3-bladed reference rotor, which is the standard NTNU rotor. To get rotors with similar C_P and C_T, the chord and twist distribution of the blades from the standard NTNU rotor were modified. To find designs with matching C_P and C_T, the newly designed blades were evaluated with a BEM code .

Figure 2.9: Model rotors for the experiment comparing the effect of the blade number on the wake development, mounted on model turbine T2 (taken from *Paper I*).

For the 2-bladed rotors, two design approaches, which have the same aspect ratio and same solidity were considered. For the rotor with the same blade aspect ratio the chord length distribution is similar to the 3-bladed rotor and the twist distribution was modified until the maximum C_P's of the 2-bladed rotors match that of the 3-bladed reference rotor. This results in a rotor blade that has twist angles that are 70% of those of the reference blades (see Figure 2.6). The 2-bladed rotor with the same solidity as the 3-bladed rotor, has blades with chord lengths that are 1.5 times greater as those of the reference blade. Moreover, the BEM analysis yielded in a slightly modified twist distribution that is 95% of those of the reference blade (see Figure 2.6). The three rotors that were manufactured with the 3D printing technology and tested in the study are shown in Figure 2.9. Because they all rotate in clockwise direction, the printed 3-bladed rotor together with the standard NTNU rotor were also used for the counter rotation experiment investigated for *Paper II*.

Rotor with adjustable wing tips

In *Paper III* and *Paper IV*, the effect of winglets on the rotor performance and the wake are investigated. Therefore, a new rotor with exchangeable wingtips was developed. As it can be seen in Figure 2.10, the last 0.05 m of the blade tip can be changed. In this way different tip winglet shapes can be investigated with the model rotor. The rotor has two blades because the chord length and thus the thickness of the profile could be designed bigger than for a 3-bladed rotor. This thicker profile was needed because of constructional constraints, as the wing tip needs to be attached to the blade with a threaded rod that runs through the whole blade. Furthermore, the stability of the blade could be increased by thicker profiles and thus the deflection of the blade tips under operation would be limited. This was considered to be very important, since the experimental measurement results were used for validation of a CFD code for the winglet optimization.

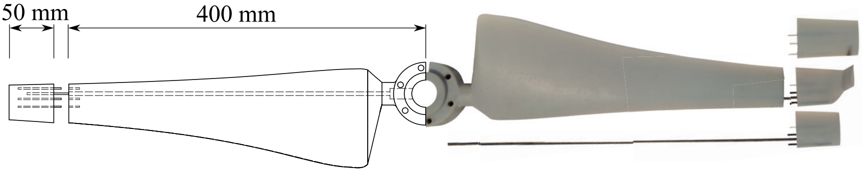

Figure 2.10: Model wind turbine rotor with exchangeable blade tips.

To further increase the stability of the blade in the tip region a new airfoil named R-opt was designed. As it can be seen in Figure 2.7, the R-opt profile is thicker than the S826 in the trailing edge region to limit torsion of the blade. The airfoil was optimized for $Re = 1.0 \cdot 10^5$ and therefore has a better performance at this Reynolds number as the S826 airfoil (see Figure 2.8).

2.3.3 3D printed blades for wind tunnel tests

The milled NTNU rotors and the 3D printed rotors used in the PhD study are fabricated from different materials with diverse properties, see Table 2.2. Therefore, they perform slightly different in the wind tunnel tests. While the Aluminum rotor is stiff and not deforming at all, the 3D printed blades deflect with increasing aerodynamic forces. To quantify this effect and to see if the 3D printed blades are applicable in the wind tunnel test, the performance and rotor forces of two identical 3-bladed rotors, one milled from Aluminum and one 3D printed in VeroGray were investigated and compared.

The power coefficient C_P over a range of λ is pictured in Figure 2.11a. It can be seen that the two curves slightly diverge and the printed rotor has a somewhat better performance. However, the differences up to $\lambda = 7.0$ are only insignificant and are

Table 2.2: Relevant mechanical properties of blade materials Aluminum and VeroGray.

Material	Tensile strength [N/mm^2]	Modulus of Elasticity [N/mm^2]	Density [kg/m^3]
Aluminum	∼250	70,000	2.7
VeroGray	60	3,000	1.17

within the measurement uncertainty. However, when $\lambda > 7.0$ the discrepancy of the graphs is increasing, resulting in a higher run-off tip speed ratio for the 3D printed rotor.

A similar trend can be observed for the thrust coefficient C_T, shown in Figure 2.11b. Whereas the graphs for C_T are almost identical until $\lambda = 7.0$, they start diverging from there increasingly. While the forces on the Aluminum rotor are getting bigger with increasing λ, the forces on the 3D printed rotor are not increasing as strongly and even start to decrease from $\lambda = 10.0$.

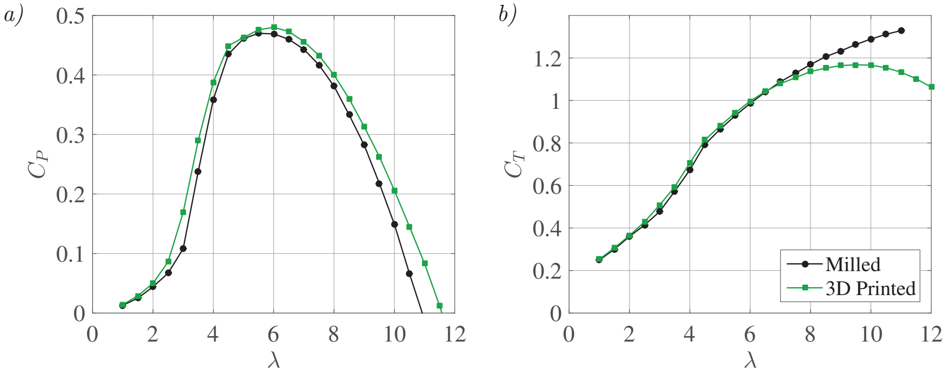

Figure 2.11: (a) C_P and (b) C_T for the 3-bladed rotor milled from Aluminum and 3D printed in VeroGray.

The difference in performance can be explained by the blade deformation of the 3D printed rotor, which is pictured for $\lambda = 6.0$ and $\lambda = 10.0$ in Figure 2.12. The blade deformation was determined with an optical method. The blade tip was illuminated by a stroboscopic flash light that was synchronized with the rotational speed of the turbine. Using this method the airfoil shape could be frozen and pictures of the deformed blade were recorded with a camera on a fixed tripod. An computational evaluation of the images resulted in the values for the deflection and twist of the blade at the tip. At the optimal tip speed ratio of $\lambda = 6.0$, the blade tip is clearly deflected backwards. However, the blade is just shifted backwards, which is expected to have no decisive influence on the rotor performance, as C_P and C_T are alike at $\lambda = 6.0$. A different deformation can be observed at $\lambda = 10.0$, where the printed blades are not only deflected backward but also slightly twisted in clock-wise direction. This additional twist angle changes the flow regime over the blade and thus, has a significant influence on the rotor performance, which is due to the strongly decreasing C_L/C_D for low α_a (see Figure 2.8a). The effect can be seen in the distinct differences in C_P and C_T between the Aluminum and 3D printed rotor at $\lambda = 10.0$.

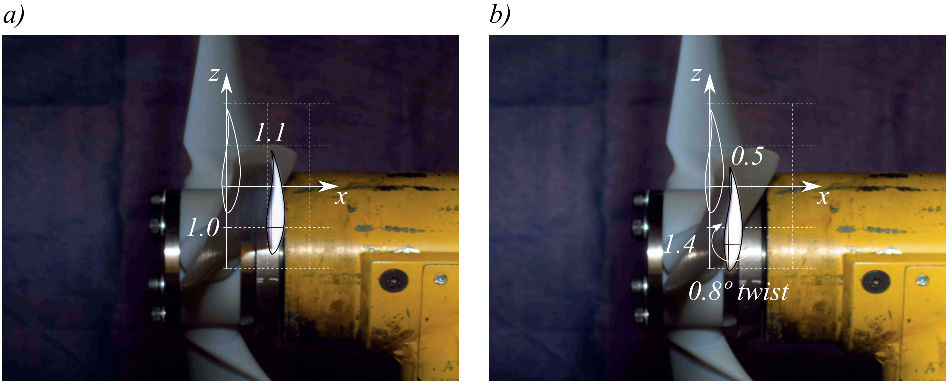

Figure 2.12: Deformation of the blade tip of the 3D printed 3-bladed rotor for $U_\infty = 10.0$ m/s at (a) $\lambda = 6$ and (b) $\lambda = 10$. With the blade deflection in x- and y-direction given in cm.

The significant differences between the two rotors are caused by a twist of the blade tip that occurs at tip speed ratios, which are beyond the optimum tip speed ratio. Therefore, it can be concluded that the printed rotors are well suited for wake investigations carried out at the optimum tip speed ratio of the rotor. However, measurement results at high tip speed ratios have to be treated with special caution. This also applies for results that should be used as reference data for CFD validation. For such experiments Aluminum rotors are favored as they do not deform and have defined geometrical properties, also at high tip speed ratios.

2.3.4 Scaling effects

The scaling of the model rotors is another limitation of wind tunnel tests. Whereas the model turbines are operated to match tip speed ratios of full scale turbines, it is almost impossible to match the chord based Reynolds number at the tip, which is calculated by:

$$\mathrm{Re} = \frac{V_{rel} c}{\nu}, \tag{2.23}$$

where ν is the kinematic viscosity of air. The viscosity and and the relative velocity V_{rel} in the model-scale and in full-scale are identical, but the chord length c is significantly different resulting in model Reynolds numbers which are around one magnitude lower as those appearing on full-scale turbines.

Even though, the the Reynolds number cannot be matched, the polars of the used airfoil should be stable in the operational range of the rotor. This is important because the Reynolds number is not a constant value, but can change along the blade in the course of one rotation. Consequently, if the airfoil polars are not stable for the occurring *Re*, the axial and tangential blade forces can alter for parts of the blade where extreme Reynolds numbers occur.

As discussed in section 2.3.2, the NTNU rotor was tested for Reynolds number dependence and was found to be independent for the boundary conditions tested in the Phd study. Also the new airfoil R-opt, which was developed for the rotor with the exchangeable tips, was optimized to operate stable at low Reynolds numbers. Nevertheless, it should be kept in mind that the wind tunnel experiments are affected by scaling effects and do not represent the full-scale exactly.

2.4 Measurement technique

In the experiments carried out in this study, different measurement techniques were used to study turbine power, forces acting on the turbine and various wake properties. Most of the measurement devices provided analog signals, which were transformed to digital signals and conditioned using DAQ (data acquisition) system devices from National Instruments. Before transforming the analog signals to digital signals, they were amplified by in-house amplifiers in order to be able to use the whole measurement range from -10 V to +10 V of the 16-bit DAQ systems and thus limit discretization errors. The digital voltage signals were analyzed and recorded using a computer with a LabView routine. The transformation of the voltage data to the desired variables and the evaluation of this properties was conducted with MATLAB.

2.4.1 Power measurement technique

The hub of the model wind turbines T1 and T2 is equipped with measurement technique to determine the rotor power. In Figure 2.13, the hub of T2 and a sketch of its cross-section are pictured. It can be seen that the hub is equipped with a torque transducer to measure the shaft torque M and an optical RPM sensor to determine the rotational speed of the rotor. With these two parameters the rotor power can be calculated according to $P = M \cdot \omega$.

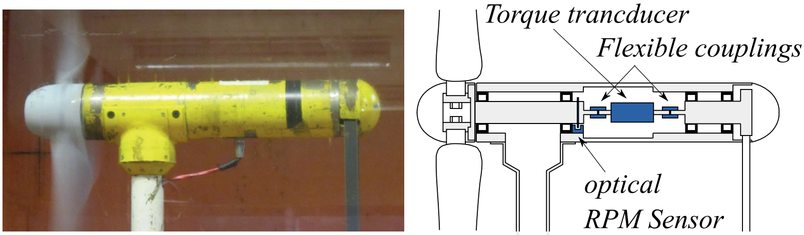

Figure 2.13: Picture of the turbine hub of T2 and a sketch of its cross-section showing the setting with the installed measurement technique (blue) inside the hub.

The Hottinger 2 N torque transducer is located to the rotor as close as possible. With this setting only the roller bearings are located between the rotor and the transducer and thus the shaft friction losses are limited. Furthermore, flexible couplings before and after the transducer secure this highly sensitive measuring device from load peaks. The transducer was calibrated prior to all the measurements by applying a range of reference weights at the blade tips (see Figure 2.14). The calibration process resulted in a linear relation between the rotor torque and the voltage signal. Furthermore, the calibration factor was observed to be stable throughout all experiments and only varied insignificantly.

Figure 2.14: Calibration process of torque transducer.

The optical RPM sensor provides a signal amplitude at a fixed rotor position for every revolution of the turbine rotor. With the time span between the signals the rotational velocity of the rotor can be calculated. Furthermore, the RPM signal was synchronized with the other measured signals to determine the rotor position were the other measurands were obtained. Due to this arrangement, the data could be analyzed in relation to the rotor position to get phase-locked information. Such phase-locked data was generated and investigated in the wake experiments of the winglet rotor for *Paper III*.

2.4.2 Force measurement technique

For the force measurements the model turbines were installed on a aerodynamic balance, which is located under the wind tunnel floor. With the six-component force balance from the Carl Schenck AG, it is possible to measure all force components acting on the model turbines and calculate the aerodynamic moments with the accompanying lever arms. For the experiments, only the three horizontal load cells were used and in most experiments, only the component in flow direction was considered to obtain the thrust force acting on the turbine and rotor assembly. All three components were recorded in the experiments for *Paper VI* and *Paper VII* in which - in addition to the thrust force - the yaw moments were analyzed. In some studies the solely rotor thrust was of interest. Therefore, the thrust force acting on the turbine rig without the rotor was measured separately and subtracted from the total thrust. All load cells were calibrated separately prior to every measurement by applying defined reference weights on the load cells. Similar to the torque transducer, a linear relation between the force and voltage was obtain in the measurement range. Furthermore, the aerodynamic balance served as a rotating table for the turbine models. This enabled a control of the yaw angle from outside the wind tunnel.

2.4.3 Wake measurement technique

For measuring the wake flow mainly two measurement techniques were used. In the experiments for *Paper I*, *Paper II*, *Paper V*, *Paper VI* and *Paper VII*, the wake properties were measured with a LDV (Laser-Doppler velocimetry) system. Only in *Paper III*, where phase-locked data was acquired, a Cobra probe was used for the velocity measurements. This technique was chosen because it could be synchronized with the other measurement devices and the data could be obtained at a defined rotor position with a fixed sampling frequency. The measurement devices were mounted on a traverse system in the wind tunnel that was controlled from outside with a LabView routine. With this setting, the wake measurement devices could be traversed in the wake flow.

Laser Doppler velocimetry

The most applied velocity measurement technique in the PhD study was LDV. All the measurements were conducted using a 2-component Dantec FiberFlow LDV system, which is shown in Figure 2.15. With the LDV technique, it is possible to measure flow velocities with a high temporal resolution and thus get not only time-averaged mean velocities, but also time-independed flow information.

LDV is an optical measurement technique, which is non-intrusive and does not need calibration. Furthermore, the velocities do not need to be transferred from voltages but are provided directly and in real time. Therefore, the voltage signals are processed by so called burst spectrum analyzer (BSA) and analyzed by the accompanying BSA flow software. The laser beam is generated by a air-cooled Argon-ion laser with up to 300 mW per wavelength. In the transmitter, the laser beam is split into two beams by a bragg cell and each of these beams is separated into the two colors green ($\lambda_{\mathrm{LDV}} = 514.5$ nm) and blue ($\lambda_{\mathrm{LDV}} = 488$ nm). With the four manipulators, the lasers are adjusted so that the maximum amount of light is linked to the fibers directing the beams into the probe, from where they are transmitted and the back scattered light is received.

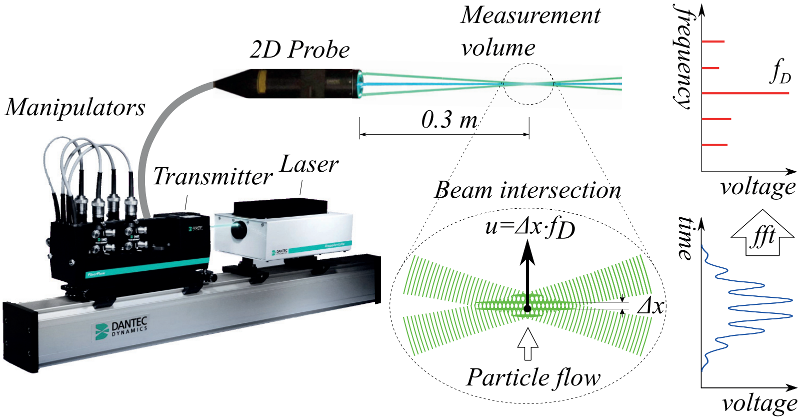

Figure 2.15: Picture of the turbine hub and sketch of the setting with the installed measurement technique (blue) insight the hub.

The measurement principle of the LDV system is briefly sketched in Figure 2.15. It can be seen that with the LDV technique, the velocity of the airflow is not measured directly, but the velocity of particles moving in the flow. The measurement volume is formed by two laser beams of similar intensity, which are transmitted from the LDV probe, where they are focused to intersect and form a fringe pattern with the known interval Δx. When a particle is passing through the fringe pattern it scatters light back to a receiver in the probe. This back scattered light contains a frequency shift entailed by the Doppler frequency f_D of the moving particle, which is proportional to the velocity of the particle passing through the fringe pattern. This optical signal is converted to a voltage signal, which is filtered and amplified and then transformed to the frequency domain by a Fast Fourier Transformation (FFT) in order to determine

f_D. As the distance traveled by the particle is given by Δx and the time of this travel is contained in f_D the velocity of the particle can be calculated by $u = \Delta x \cdot f_D$.

The LDV probe was installed on the wind tunnel traverse and adjusted by leveling the reflections on the wind tunnel wall or floor and aligning them with the probe. The LDV system was adjusted to only take samples into account that were recorded by the lasers in both measurement directions. In the experiments $5.0{\cdot}10^5$ samples were recorded for every measurement point. The acquisition data rate was adjusted by controlling the particles in the flow. Throughout the measurements the acquisition data rate was between 1 500 Hz and 2 500 Hz what resulted in a measurement time between 20 s and 35 s. The particles with a size between 0.5 μm and 2.0 μm were created with a thermal smoke generator that was located at the end of the test section. In that way the particles traveled through the whole wind tunnel where they distributed evenly before entering the test section.

Cobra probe

For the investigation of the wake flow of the rotor equipped with winglets in *Paper III* a Series 100 Cobra probe from TFI (TurbulentFlow Instrumentation) was used. This measurement technique was selected, because with this device it is possible to synchronize the turbine rotation and the velocity measurements and allocate measurants to an exact turbine position to obtain phase-locked wake data.

The Cobra probe, which is shown in Figure 2.16, is a 4-hole Pitot tube in which the pressure transducers are located directly in the probe body. The short tubing between the pressure tabs together with a linearisation process, correcting for pressure fluctuations in the tubing, enables the Cobra probe to measure not only time-averaged mean velocities but also time-varying turbulent velocity components (Hooper and Musgrove, 1997).

The Cobra probe does not require extensive calibration, as the probe head has a defined geometry (see Figure 2.16) and the calibration process is performed by the manufacturer who provides calibration tables for the individual probes. The pressure regime at the probe head, which is determined by the four pressure values measured at the tabs, can be assigned to the three velocity components u, v and w as well as the static pressure at the tip of the device by applying the calibration tables. Detailed information of the calibration process and the transformation from the pressures to the velocities is provided by Shepherd (1981)

In the PhD study, the four voltage signals provided by the Cobra probe were evaluated by a MATLAB routine with implemented interfaces of the manufacturer TFI providing the calibration tables. The analysis resulted in the time-varying velocities

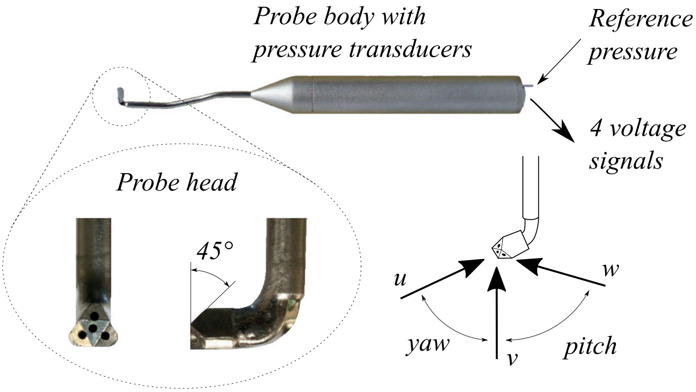

Figure 2.16: Series 100 Cobra probe, with detailed probe head geometry and the flow axis system.

of the three components, which were used to calculate the other flow properties like the time-averaged velocities, the flow angles and the turbulent kinetic energy (TKI). In order to obtain accurate results, the flow angles must be within 45°. Therefore, all measurements in which one of the flow angles was bigger than 45° were excluded from the analysis.

The Series 100 Cobra probes used for the study have a frequency response of 600 Hz. In order to obtain phase-locked data one rotor revolution was divided in 120 section, each of 3°. With a rotational speed of 1 280 RPM this resulted in a required frequency response of at least 2 560 Hz in order to get information for every rotor position per revolution. In order to sample the data with a frequency response of 2 560 Hz, the usable frequency range was extended by changing the transfer function cut-off amplitude for the linearization process. With this measure the response of the probe was extended to over 3 000 Hz. Nevertheless, the disadvantage of this method is, that signals with frequencies >1 000 Hz need to be amplified, because such signals appear too weak at the transducers. Consequently, also noise is amplified, which increases the measurement error. In order to avoid aliasing, the data acquisition rate was 10 240 Hz resulting in an over-sampling ratio of 4.

For the experiments, two Cobra probes were used simultaneously, to reduce the time for the measurements. Therefore they were installed in a support, carrying them with a defined distance of separation. One of the biggest challenges is to install the probes straight in the wind tunnel. In order to achieve this, the velocities were measured with the LDV probe and the Cobra probe at the same position. The direction of the Cobra probes was adjusted until the measurement devices measured the same velocity components, resulting in identical flow angles. The procedure is pictured in Figure 2.17.

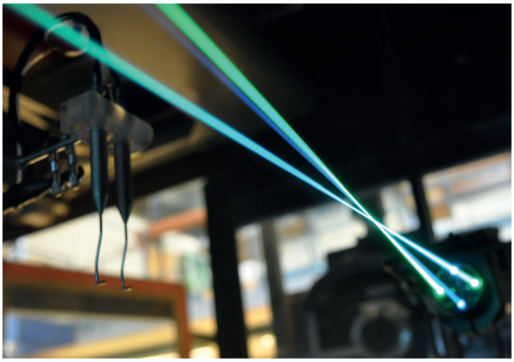

Figure 2.17: Simultaneous measurements with LDV and Cobra probe for adjustment of Cobra probe head.

2.5 Measurement uncertainty

Experimental measurements are not perfect. They are always afflicted with some deviation between the true value and the measured value. This error has various sources and can typically be divided into the two categories systematic and random errors, see Figure 2.18.

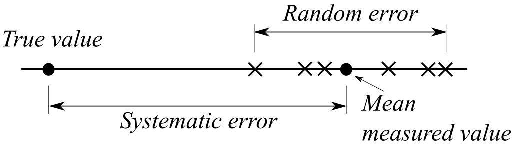

Figure 2.18: Explanation of systematic and random error.

Systematic errors can be described as repeatable and consistent, meaning that they are not changing during the experiment. Random errors are caused by unpredictable changes in the experiment, which are not known and thus can not be repeated. Usually, the real error of a measurement is unknown and cannot be determined. A method to evaluate how accurate an experiment was and to quantify the error, is to calculate the uncertainty of a measurement. The measurement uncertainty is an estimated range, in which the error will be arranged based on a confidence interval.

Measurements of all individual parameters are afflicted with uncertainties that propagate to a total uncertainty of the final result. For example, the measured quantities temperature $Temp$, ambient pressure p_{amb}, inlet velocity U_∞, rotational speed of the rotor ω and shaft torque M are needed to calculate C_P (Equation (2.4)) and each parameter features an inaccuracy that will affect the total uncertainty of the final result for C_P.

To obtain the total uncertainties of the investigated parameters in this work the procedure described by Wheeler and Ganji (2010) was applied. Therefore, the measurement process was outlined in the beginning and the relation between the final result and all depended parameters was defined. For all the parameters possible error sources containing errors due to calibration, data acquisition, data reduction methods and other sources were listed. For each individual source, the errors were determined. The systematic errors were estimated based on manufacturers specifications or from previous studies and observations. For the random errors the standard deviation of the measured parameters was calculated. To get the standard deviation of the turbulence properties the standard deviation was calculated based on the technique described in (Benedict and Gould, 1996). With all the individual error terms the total systematic uncertainty was calculated using a root of the sum of the squares:

$$B_R = \left\{ \sum_{i=1}^{n} \left(B_i \frac{\partial R}{\partial x_i} \right)^2 \right\}^{1/2}, \tag{2.24}$$

where B_i is the systematic error of the individual parameter and and $\frac{\partial R}{\partial x_i}$ is the derivative of the overall parameter with respect to the individual parameter. The random uncertainty for every measurement point is calculated with:

$$P_R = \pm t \frac{\sigma}{\sqrt{n}}, \tag{2.25}$$

where t is the value of the Student's t, σ is the standard deviation and n is the number of measurements. The resulting individual error terms are combined to the total uncertainty by the root of the sum of the squares, similar to that of the systematic uncertainty. The total uncertainty is calculated by a combination of both uncertainties:

$$\varpi_R = \sqrt{B_R^2 + P_R^2}. \tag{2.26}$$

In this study, all uncertainties were estimated based on an 95%-confidence level. The analysis of the uncertainties for the different investigated quantities suggested that systematic errors had the largest contribution to the total uncertainty. Nevertheless, also random uncertainties were distinguished, which could be seen in higher levels of uncertainty in turbulent flows.

Typical uncertainties for mean velocities measured with the LDV system were around 1% whereas the turbulence from these measurements featured slightly higher uncertainties around 2%. The measurements with the Cobra probe featured higher uncertainties, which were typically up to 5% for the velocity and 8% for the turbulence.

Typical uncertainties of the power coefficient C_P were found to be approximately 3% around the optimum tip speed ratio of the rotor. Outside this region the results were affected by less inaccuracy. For the thrust coefficient C_T, the uncertainty was observed to rise with increasing tip speed ratios reaching uncertainties of up to around 2%.

Chapter 3

Summary of main results

This chapter summarizes the main results of the PhD study and the main findings of the papers will be presented. The contribution to the field of wind farm optimization will be discussed in beginning. Within this field, the study comparing the wake of 2- and 3-balded wind turbine rotors will be presented. Afterwards, the main findings of the project analyzing counter rotating wind turbine rotors will be shown. The third rotor modification concept that will be presented examines the effect of winglets on wind turbine blades, in which the design of the winglets and their influence on the wake development will be discussed. The wind farm optimization will be finalized by presenting the results of the wind turbine wakes in yaw project, where the potential of intentional yaw misalignment for wind farm control optimization will be shown. The summary of the main results will be completed by presenting the findings of the Blind test comparison, where reference data was provided for CFD validation.

3.1 Wind farm optimization

For the main part of the PhD thesis rotor-wake interactions were investigated to evaluate different methods, which were deemed to have the potential to optimize the power output of wind farms. Firstly the approach of modifying the rotor design to limit wake effects was studied. Within this technique the effect of the blade number on the wake development was studied by comparing wake properties of 2- and 3-bladed model wind turbines in *Paper I*. Furthermore, the influence of the rotational direction of the wind turbine rotors in a wind farm was investigated in *Paper II* by comparing the performance of an aligned turbine array with co- and counter-rotating rotors. The third rotor design modification that was studied, was a rotor equipped with winglets. For this study, a new rotor was designed and winglets for this rotor were optimized before comparing the performance of the rotor with and without winglets in *Paper IV*. The winglet rotor's effect on the wake was investigated in *Paper III*, where wakes of rotors with and without winglets were compared. The second approach for wind farm optimization that was considered in the project was improving the turbine control by intentional yaw misalignment. In order to apply yaw control it is important to know how the wake flow of a yawed turbine. To provide more information about the wake structure *Paper V* investigates the influence of different inflow conditions on the wake shape and development. The power and loads of a turbine array in various yaw configurations are discussed in *Paper VI*.

3.1.1 Comparison of 2- and 3-bladed rotors

The costs of a wind turbine can be reduced if 2-bladed rotors instead of common 3-bladed rotors are used. However, using 2-bladed rotors is accompanied by several disadvantages like higher noise emissions, distracting visual effects and unfavorable dynamic behavior (Hau, 2013). Those disadvantages are deemed to be the reason why the research effort on the wake development of 2-bladed rotors was limited and only few studies on this topic exist.

In an experimental study, Newman et al. (2015) investigated wake effects in scaled down wind farms consisting of 12 small model wind turbines with 2- and 3-bladed rotors with similar C_P. They found large differences of mean streamwise velocities in the near wake of the array, where the wake of the 2-bladed rotors showed higher mean velocities. However, in the far wake the differences between the two rotor concepts for the mean velocities where only insignificant. Furthermore, the streamwise Reynolds stresses were observed to be higher in the wake of the 3-bladed turbines leading to higher fatigue loading on the downstream turbines.

Analytical wake models suggest that the blade number does not have an influence on the velocity in the wake as they do not take the blade number into account (Polster et al., 2017). The main parameter determining the wake flow in the models is the thrust coefficient C_T, which was similar for the tested rotors in the study. However, there might be differences in the wake flow as already suggested in the study by Newman et al. (2015). Especially the turbulence intensity is expected to be different in the wake behind the 2- and 3-bladed rotors, as the stronger tip vortices of the rotors with only two blades are deemed to increase the turbulence levels behind the rotor edge. Therefore, the wake of 2- and 3- bladed turbines were compared in *Paper I*.

The differences of the wake properties between the 2- and 3-blade rotors from the line wakes of *Paper I* are summarized in Table 3.1. The available power in the wake ($P_{ava} = 0.5\rho A_R U_\infty^3$). was calculated in order to compare the velocities in the wake. It can be seen that the differences in the available power and thus the mean streamwise velocities are only minor. This is confirmed by similar wake recovery rates for all three rotor concepts. Furthermore, full wake scans of the mean streamwise velocity at $5D$ reveal no major differences and thus verify these observations. Comparing the turbulence in the wake there also is no indication of big differences between the wakes of the three rotors. Nevertheless, it can be seen that the turbulence levels in the wake behind the 2-bladed rotors are higher than those of the 3-bladed rotor at all investigated distances, whereas the differences become smaller with increasing distance. The major discrepancies in TI occur mainly behind the tip region and are caused by the stronger tip vortices of the 2-bladed rotors, which decay with increasing distance.

Table 3.1: Summary of differences in available power (P_{ava}) and turbulence intensity (TI) in the wake behind the 3-bladed rotor (Rotor1), the 2-bladed rotor with the same aspect ratio (Rotor2) and the 2-bladed rotor with the same solidity (Rotor3).

		Rotor1 - Rotor2	Rotor1 - Rotor3
3D	P_{ava}	1,3%	0.2%
	TI	-0.5%	-1.9%
5D	P_{ava}	1,0%	-3.0%
	TI	-0.5%	-1.2%
7D	P_{ava}	1,1%	-3.2%
	TI	-0.2%	-0.2%

It can be concluded from the study that the wakes of 2- and 3-bladed rotors are similar. The differences in mean streamwise velocity are minor and the turbulence intensity is only varying for the blade number at small distances and is equalized at typical separation distances of wind turbines. As a result, using turbines with 2-bladed instead of 3-bladed rotors does not improve the power output of a wind farm. Nevertheless, 2-bladed rotors do not have a negative influence on wake interactions and can therefore be used in wind farms to decrease installation costs, without affecting the overall power.

A weakness of the study is displayed by the circumstance, that the C_P's of the 2- and 3-bladed rotors do not match at the tip speed ratios where the turbines were operated. The 2.7% higher C_P of the 3-bladed rotor makes it difficult to draw reliable conclusions about the overall performance of a wind farm. To solve this problem, new 2-bladed rotors with higher C_P's that exactly match that of the 3-bladed rotor need to be designed and the wake of these rotors need to be compared to the 3-bladed rotor. Furthermore, an experiment investigating the overall performance of an aligned

2-turbine array would be necessary to draw a reliable conclusion about the different energy content in the wake of 2- and 3-bladed turbines.

3.1.2 Counter rotating wind turbine rotors

From Figure 3.1 can be seen, that the wake behind a clockwise rotating wind turbine is rotating counter-clockwise and thus opposite to the turbine rotor. Consequently, the inflow of a downstream turbine operating in the wake of an upstream turbine contains a tangential velocity component in opposite direction to the rotor rotation. This additional velocity component is changing the velocities at the rotor plane, which could affect the performance of the rotor. It might have a positive effect on the rotor performance if this additional velocity component is orientated in opposite direction and thus in the direction of the rotor rotation. Consequently, it might be beneficial to use a mirrored rotor design for the upstream turbine to get an array with counter rotating turbines. However, only little attention has been paid to this topic and only few studies, which investigate the effect of alternating rotational direction in a wind farm, exist.

An experimental study on this topic was conducted by Yuan et al. (2013, 2014), who investigated an aligned tandem turbine array with co- and counter rotating rotors. They showed that the counter-rotating array was more efficient as the co-rotating array in extracting power. The performance increase was found to be up to 20% at a separation distance of $0.7D$, but decreased with increasing distance and was found to be negligible from $6.5D$ on. Nevertheless, the study showed the potential of counter-rotating turbines for the optimization of wind farms. Therefore, the effect of the rotational direction on the wake of a wind turbine rotor was investigated in *Paper II*.

In the study for *Paper II* the wake was analyzed with special focus on the tangential velocity component. Furthermore, the performance of a two-turbine array with co- and counter-rotating rotors was compared. In addition to the experiments, a BEM code was used to study the effect of the additional tangential velocity component on the blade loads and the performance of the aligned turbine array.

The BEM analysis of the flow around the blade showed that the additional tangential component in the inflow changes the flow angle. As a result, the angle of attack on the downstream rotor decreased in the co-rotating array, whereas it increased in the counter-rotating array. The performance comparison of the tandem turbine arrays showed no big differences between the co- and counter-rotating array. However, the counter-rotating array had a slightly better performance at all investigated turbine separation distances. At $2.00D$ the combined C_P was 1.2% higher, at $3.50D$ and

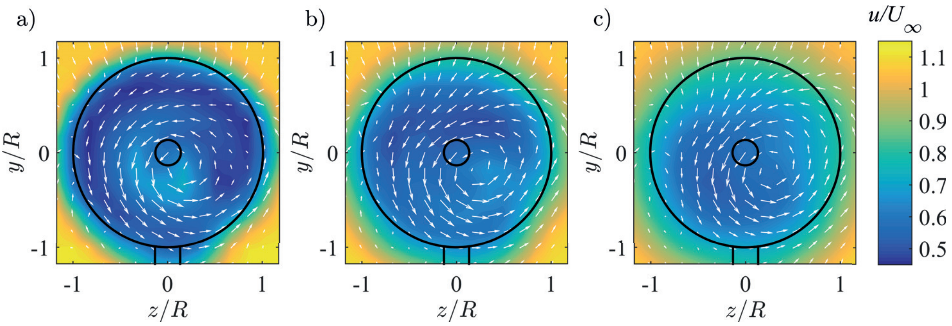

Figure 3.1: Contour plots of normalized streamwise mean velocity, with arrows representing the resultant of the vertical and horizontal velocity component, in the wake (a) $2.00D$, (b) $3.50D$ and (c) $5.15D$ behind the clock-wise rotating 3-bladed rotor mounted on turbine T2, the black lines represent the turbine rotor, nacelle and tower, locking in flow direction.

$5.15D$ the difference was 2.0% and 0.6%, respectively. This was confirmed by the BEM calculations, which were generally between 5% and 7% lower as the experimental results, but showed the same trends.

However, as the performance improvement stems from a increased flow angle, the same effect could be generated by changing the pitch angle of the blade. This observation is confirmed by Bartl and Sætran (2016), who investigated the C_P of the same rotor for a variation of pitch angles and found a higher C_P if the twist angle was greater than the one applied in the study for the counter rotating wind turbine rotors.

From this observation and the small differences in C_P of the co- and counter-rotating turbine array can be concluded, that the optimization potential of alternating rotational directions in a wind farm is insignificant.

3.1.3 Winglet rotor

Most modern airplanes are equipped with winglets to improve their efficiency (Figure 3.2). The additional winglets reduce the fuel consumption by around 4-5% for transport airplanes (Freitag and Schulze, 2009). Winglets improve the performance of a wing by reducing the induced drag, which is generated at the blade tip where the pressure difference between the pressure and suction side of the blade is equalized and a vortex is formed. The resulting span wise flow from the pressure to the suction side influences the lift and drag at the tip and further inwards and the lift of the wing is reduced (see Figure 3.3). A winglet reduces this span wise flow and consequently helps to limit the reduction of lift.

Figure 3.2: Winglet on the wing tip of a transport airplane.

From the performance enhancement achieved in aviation it can be concluded, that winglets might also have the potential to improve the performance of a wind turbine. Consequently, several studies investigating the effect of winglets on wind turbine rotors have been conducted.

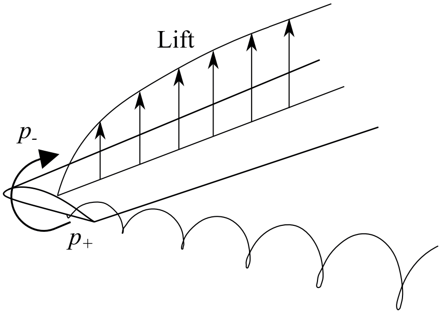

Figure 3.3: Pressure equalization at the blade tip and the resulting tip vortex and lift distribution.

Johansen and Sørensen (2006) designed six winglet shapes, and analyzed them with the EllipSys3D solver. They showed that winglets can improve the performance, but also worsen it if not properly designed. Their best design increased C_P by around 1.0%, which was accompanied by an increase in C_T of 1.6%. In a further study, they used the same CFD solver to perform a parameter study changing the height, curvature radius, sweep angle and twist angle of a winglet (Johansen and Sørensen, 2007). They designed and investigated 10 winglet concepts and their results show that the winglet height has the biggest influence on the C_P and C_T. Whereupon a winglet with a height of 4% of the rotor radius had the highest C_P and C_T increase of 2.6% and 3.6%, respectively. Gaunaa and Johansen (2007) also used the EllipSys3D solver to investigate winglets, which they designed with a self-developed free wake lifting line code. They showed that downwind winglets are more effective than upwind winglets. Maniaci and Maughmer (2012) designed downwind winglets with the height of 8%

rotor radius for a model-scale wind turbine (D = 3.3 m). Results of wind tunnel experiments with this rotor showed an increase in C_P of 9% and confirmed the large influence of winglet height on the performance. The same rotor was used by (Gertz et al., 2012, 2014) who tested different winglet designs and found performance increases between 5% and 8%. The wake formed behind a rotor with downwind winglets was experimentally studied by (Tobin et al., 2015). They found an increased velocity deficit in the wake of the winglet rotor. However, they predicted that this deficit could be evened by the higher C_P of the winglet rotor and increase the total C_P of a turbine array. Furthermore, they found similar tip vortex strength for the winglet and baseline rotor. In his PhD thesis Ostovan (2017) investigated the performance of an aligned turbine array operating with and without down-facing winglets and found an increase in overall efficiency if winglets were installed on the upstream turbine. Furthermore, he measured the tip vortices in the very near wake and estimated an induced drag reduction of around 15%.

All these studies show that additional winglets on wind turbine rotors have the potential to increase the performance of a single turbine and turbine array. To further investigate this promising technique, in *Paper IV* a new rotor was designed and winglets for this rotor were optimized for an increased C_P. Furthermore, the growth in C_T was limited in the optimization to reduce wake effects. In *Paper III* the wake behind this new rotor was investigated experimentally and compared to the baseline rotor without winglets.

During the optimization process the six design parameters span, sweep, angle of attack, radius, root chord and tip chord were varied and over 100 different designs were investigated numerically. The optimal winglet for the rotor in the design framework was found to have a span of 10.8% of the rotor radius. According to the CFD simulations the winglet increased the rotor power by 7.8% and the thrust by 6.3%. This was confirmed by the experiments, which showed an increase of C_P and C_T of 8.9% and 7.4%, respectively. The same increase in C_P was achieved by increasing the blade radius by 3.6%. Analyzing the rotor blade flow showed that the winglet improves the rotor performance mainly by increasing the lift in the tip region of the blade. In this region the induced drag is reduced because the pressure difference is shifted from the blade tip to the winglet.

The experimental wake study showed that up to $4.0D$ downstream the differences in mean streamwise velocity between the winglet and baseline rotor are small, suggesting a minor effect of blade tip extensions on the combined efficiency of a wind farm. The investigation of total kinetic energy, revealed slightly higher initial energy peaks in the tip region, when winglets were attached to the rotor tips. Starting from a dwonstream distance of approximately $2.0D$, the shear layer behind the tip region was observed to be significantly broader for the wingletted configuration. An analysis of the out-of-plane vorticity showed that the tip vortices of the wingletet rotor were breaking around $1.0D$ earlier as those of the rotor without winglets. Furthermore, higher absolute vorticity was found when winglets where mounted on the rotor.

The winglet study showed that it is possible to design winglets, which increase the wind turbine performance with a moderate growth of rotor thrust. Furthermore, it confirmed the findings from literature that winglets can help to improve not only the performance of a single turbine but also those of a turbine array consisting of multiple turbines.

However, the investigation of the blade extension showed, that a by 3.6% increased rotor radius has the same effect on the C_P as the winglet with a span of 10.8% of the radius. In conclusion, winglets make most sense if the rotor diameter is limited, which can be the case for offshore applications, where the costs of the tower can be reduced if its height is limited. Nevertheless, winglets are deemed to be a good possibility to optimize a wind farm by a modified rotor design.

3.1.4 Yaw wake control

Usually a wind turbine is aligned with the flow to extract most energy possible from the wind. However, if the rotor is not perpendicular to the wind direction, the velocity experienced by the rotor decreases with the cosine of the yaw angle γ (see Figure 3.4). As a result, the power of the rotor reduces. Moreover, the thrust force of the rotor T contains a streamwise and lateral force component. The resulting lateral force component introduced by the yawed rotor F_z deflects the wake sideways. As a result, the wake trajectory can be controlled by intentionally yawing the rotor. Even though such a yaw misalignment would decrease the turbine performance. The overall efficiency of a wind farm could be increased if the wake is directed away from a downstream turbine leaving more energy in its inflow. Such wake redirection is considered to be a promising technique to improve wind farm control (Gebraad et al., 2016).

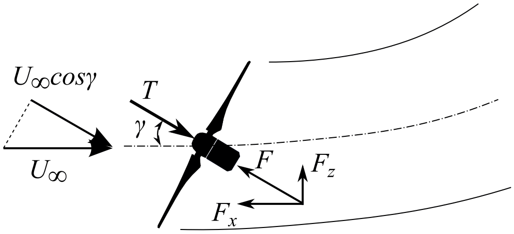

Figure 3.4: Sketch of forces induced by a yawed wind turbine and the resulting lateral wake deflection.

Among wake redirection techniques, yaw misalignment is deemed to have the largest potential for increasing the farm efficiency (Fleming et al., 2014). Therefore, several studies investigating the wake development behind a yawed turbine have been conducted. In an experimental study Medici and Alfredsson (2006) analyzed the wake behind a small yawed model turbine of $D = 0.18$ m. They investigated a yaw range from $\gamma = 0° - 20°$ and found a distinct deflection of the wake, caused by a clear cross-stream flow component. Krogstad and Adaramola (2012) used a larger turbine of $D = 0.9$ m, on which they showed that the power output decreased proportional to $cos^3\gamma$. They furthermore investigated the near wake and found a dependency of the wake deflection and structure on the turbine's tip speed ratio. Bastankhah and Porté-Agel (2016) performed an extensive experimental particle image velocimetry (PIV) study on the wake of a yawed model wind turbine of $D = 0.15$ m. Their results confirm the wake's dependency on factors like wake rotation and tip speed ratio. A combined experimental and numerical study was performed by Howland et al. (2016) who investigated the wake behind a small drag disc of $D = 0.03$ m. They show that the yawed non-rotating disc has a realistic wake deflection. In their analysis of the wake shape, they found an asymmetric so-called curled wake shape, which is created by a counter-rotating vortex pair. In another experimental study, Schottler et al. (2016b) investigated the performance of an aligned turbine array and showed an asymmetric power output depending on the upstream turbines yaw angle. This asymmetric behavior was also observed by Fleming et al. (2014), who performed a numerical study based on Large-eddy simulations (LES) and found a slightly different wake deflection depending on the yaw direction. Gebraad et al. (2016) performed another CFD study using the SOWFA solver and confirmed the large potential of intentional yaw misalignment for wind farm control optimization. The influence of atmospheric stability on the wake of yawed turbines was numerically investigated by Vollmer et al. (2016). They show that the wake shape and skew is highly depended on the atmospheric stability. In a recent CFD LES study Wang et al. (2017) showed the importance of including tower and nacelle in the simulations. Moreover, also full-scale experiments investigating the effect of yaw were carried out. Trujillo et al. (2016) used LiDAR to track the near wake behind a 5 MW offshore wind turbine for a yaw range from $\gamma = -10.5° – 10.5°$. In another full-scale study Fleming et al. (2016a) applied a yaw wake-steering open-loop controller to a wind turbine array. Their study showed that the power output of two turbines was improved by yaw based wake steering. Jiménez et al. (2010) used the experimental results from Medici and Alfredsson (2006) to verify LES simulations around a yawed actuator disc. From the numerical results they derived an analytical momentum conservation based wake model for predictions of the velocity deficit and wake trajectory of a yawed wind turbine. Bastankhah and Porté-Agel (2016) used the results of their extensive experimental and numerical studies to develop another analytical model for the far wake of a yawed wind turbine, which also accounts for inflow turbulence.

Despite the large potential of yaw control for wind farm optimization found in the literature, the existing studies point out the need for detailed wake measurements of yawed turbines. In order to provide such data a collaborative project on wind turbine wakes in yaw was initialized between NBMU, NTNU and ForWind in Oldenburg. The wakes behind two yawed wind turbine models of different design, were investigated extensively under various inflow conditions in the NTNU wind tunnel. The experimental results of the project are the basis of *Paper V*, which investigates the influence of inflow turbulence and shear on the wake structure and *Paper VII*, which compared the experimental results to numerical predictions. Furthermore, the measurements were used for the additional *Papers X* and *XI*, where the wake of the two model turbines was compared. The detailed data sets from the wind turbine wakes in yaw project are published by Schottler, Bartl, and Mühle (2018). Additional to the wake experiments, a two-turbine array was investigated at various differing yaw and lateral offset configurations. With the results of this experiment the potential of power and load optimization of yawed wind turbines was discussed in *Paper VI*. Furthermore, the far wake of a smaller yawed turbine rotor of $D = 0.45$ m was experimentally investigated and analyzed in the additional *Paper XIV*.

The analysis in *Paper V* revealed minor asymmetries in the wake between positively and negatively yawed rotors, which stem from tower wake interactions. The asymmetries were found to be larger for the lower inflow turbulence. The inflow turbulence also influenced the shape of the wake, which had a clear kidney shape for all inflow conditions, whereas it was more distinct at larger downstream distances. Moreover, the wake deflection was observed to be slightly different for the two investigated levels of inflow turbulence. Furthermore, the moderate shear in the inflow was found to have little influence on the wake properties. The study shows, that the turbulent kinetic energy in the wake is deflected to the same degree as the mean streamwise velocity profiles, while its expansion is slightly wider. Furthermore, it was shown that the levels of peak turbulence decreased similarly to the rotor thrust if a yaw angle is applied.

The power and load optimization study in *Paper VI* showed that the combined power of a two-turbine array could be increased by intentional yaw misalignment of the upstream turbine. The largest improvements for a yaw angle of $\gamma = 30°$were found at a separation distance of $6D$. For this arrangement, the total performance increased up to 11% for the low-turbulence and 8% for the high turbulence inflow. This discrepancy confirms the strong influence of inflow turbulence on power gains if yaw control is applied. Furthermore, the power gains were found to be asymmetric due to the different wake shape and deflection for positive and negative yaw angles. Although, the total power could be increased by yawing the upstream turbine, the yaw moments for the upstream and downstream turbine both increased. By applying a lateral offset of $0.5D$ most of the wake could be steered away from the downstream turbine, which resulted in an increased total power and reduced yaw moments. Furthermore, it was demonstrated that yawing the downstream turbine opposite to the upstream turbine mitigated the yaw moments and increased the total power.

The wind turbine wakes in yaw project resulted in more publications, which are not included in the thesis. The main findings of these articles are described below. In the additional *Paper X* the available power method, which was used for the quantification of the wake deflection in wind turbine wakes in yaw study is established. Two-point statistics of the wake properties are investigated in the additional *Paper XI*. The results reveal a ring of strongly intermittent flow around the mean velocity deficit, in the wake of the yawed turbine, resulting in a wider wake expansion as if only considering the mean velocity. The findings show the importance of considering non-Gaussian distributions of velocity increments for wind farm control optimization. In the additional *Paper XIV* the focus is on the far wake trajectory. The results of this paper show that the wake deflection has an asymptotic behavior and the skew angle is almost zero in the far wake.

The study on wind turbine wakes in yaw confirmed that intentional yaw misalignment is an effective method to laterally deflect the wake and thus has large potential for the power optimization of wind farms. However, the rotor blades of a yawed rotor experience unsteady flow conditions in the course of one rotation which resulted in increased loads on the yawed turbine. The same applies for turbines operating in a partial wake of a yawed turbine. Consequently, loads have to be taken into account when optimizing the wind farm control. A possibility for load reduction is yaw control of the downstream turbine. By yawing the downstream turbine opposite to the upstream turbine not only the loads can be reduced, but also the power can be increased.

3.2 Reference data for CFD validation

CFD simulations are a good technique to study rotor-wake interactions of wind turbines. However, as mentioned in Section 1.1.5, CFD codes and the applied turbulence models need to be validated with actual measurement data in order to determine their accuracy. To help with the validation and the further development of CFD codes, selected results of the experiments with the yawed turbines were compared to computational results in *Paper VII*. Furthermore, the data sets were published so that they can be used as reference data for the validation of new CFD simulations.

3.2.1 Blind test comparison

In the Blind test series, which was initiated by NTNU in 2011, experimental data of turbine performance and wake flow is compared to numerical predictions. In each Blind test, specific test cases for turbine arrangement and operation in the wind tunnel are defined and the turbine performance and wake properties are measured according to the description of these test cases. All the information, which is needed to reconstruct the test cases in a CFD domain, including boundary conditions as well as turbine and wind tunnel geometry, are published in detail and institutions, which develop or work with CFD simulations are invited to predict the test cases without knowing the results. The blindly submitted numerical predictions are compared to the experimental results to analyze the accuracy of the simulations and to identify sources for deviations among the different techniques.

The first Blind test focused on a single turbine and modelers were asked to predict its performance as well as the mean streamwise velocity and turbulent kinetic energy in the wake for distances from $1D$ to $5D$ behind the turbine. The Blind test attracted eight different research groups who submitted simulations of various types ranging from Reynolds-Averaged-Navier-Stokes (RANS) simulations to Large-eddy simulations. The simulation results deviated significantly from the experimental results as reported by Krogstad and Eriksen (2013). Whereas the spread in performance around the experimental results were considerable, the predictions of wake turbulence were scattered by several orders of magnitude. In the next Blind test a second turbine, operating in the wake of the first turbine, was added to increase the test complexity. The participants were asked to simulate the performance of both turbines with the focus on the downstream turbine operating in the wake. Furthermore, the modelers were asked to simulate the wake formed behind the downstream turbine. For this Blind test nine predictions were submitted. The results reported by Pierella et al. (2014) show a large spread in the performance of the downstream turbine and the predictions of the wake properties varied significantly for the different simulations. In the third Blind test the complexity was again increased by applying a lateral offset of half a rotor diameter to the same turbine array as in Blind test 2. The results reported in Krogstad et al. (2015) show an improvement in the performance predictions, which contained only a small scatter around the experimental result. However, the simulations of the asymmetric wake still contained large uncertainties in predicting turbulence. The fourth Blind test focused on the influence of different inflow conditions. Therefore, the wake behind a single turbine was investigated up to $9D$ behind the upstream turbine for low-turbulent, high-turbulent and turbulent shear inflow. Furthermore, the performance of an aligned turbine array was investigated. The five research groups, which submitted numerical results for this Blind test, managed to predict the performance of the upstream turbine fairly well. However, the more complicated predictions of the downstream turbine's performance still contained a significant scatter. The results presented by Bartl and Sætran (2017) show that the mean wake properties were generally predicted well. Nevertheless, the turbulence predictions still showed a large discrepancy between experimental and numerical results.

In the fifth Blind test, which is presented in *Paper VII* the performance and the wake flow of two different single yawed turbines and a turbine array with a yawed upstream turbine were compared in three test cases. In the first test case the modelers were asked to predict power, thrust and yaw moments of the yawed NTNU turbine LARS1 and the wake flow at $3D$ and $6D$ behind the turbine. For the second test case the non-yawed NTNU turbine T2 was placed $3D$ behind the yawed turbine and the power, thrust and yaw moments of the downstream turbine as well as the wake flow $3D$ behind the turbine were investigated. The third test case was similar to the first test case. Only the NTNU turbine was replaced by the ForWind turbine, which has a somewhat smaller rotor diameter and a different rotor design. The modelers were asked to provide predictions for the streamwise and vertical velocity component as well as the turbulent kinetic energy, at the defined downstream distances in full wake planes. The numerical and experimental results were compared visually and also by applying different statistical methods to get quantitative information about the deviations.

The Blind test attracted four institutions who submitted results for the three test cases. The predictions for the power, thrust and yaw moments show significant deviations from the experimental results. The scatter was larger than observed in previous Blind tests, suggesting that the simulations had problems with the increased complexity of unsteady blade loading due to the yawed turbine operation. The comparison of the wake flow generally showed very good agreement between the experimental data and the numerical predictions. The general features such as the wake shape and deflection were predicted well by all the simulations. Also the streamwise velocity in the wake was predicted fairly accurate by all simulations. Even though it is difficult to predict the flow in vertical direction because of its low magnitude, the complex patterns of the vertical velocity component were accurately predicted by all simulations in general. The same applies for the turbulent kinetic energy in the wake behind the single turbine and the two-turbine array. Whereas previous Blind tests showed that it is difficult to predict the wake turbulence, all simulations managed to predict the turbulent kinetic energy accurately.

The results of this Blind test comparison confirmed the continuous improvement in performance and wake flow predictions from Blind test 1 to Blind test 5. Furthermore, they showed that the different simulation techniques were able to perform accurate predictions, also for complex setups featuring highly unsteady flow in yawed and partial wake operation.

Chapter 4

Conclusions

The present PhD thesis investigated rotor-wake interactions and analyzed the potential of different concepts for the optimization of wind farms. For this purpose, performance and loads of model wind turbines as well as their wake characteristics were measured in a number of experimental wind tunnel studies. In the scope of the thesis, the wake flows behind rotors of different number of blades, different rotational direction and additional winglets on the wing tips were investigated to investigate how the different rotor designs could affect the wake characteristics and effects on turbines operated in the wake. In the second part of the thesis, the wake behind a yawed turbine was investigated for different inflow conditions and yaw angles. The potential of intentional yaw misalignment for wind farm control optimization was thereafter analyzed for a setup of two aligned and laterally offset turbines. The wake flow data was furthermore used as reference data in a blind test experiment, to which numerical predictions were compared and deficits in the CFD codes identified. The comparison of wakes behind a 2- and 3-bladed rotor of the same thrust loading showed a minor difference in the mean streamwise velocity development. The peak levels of rotor-generated turbulence were, however, observed to be lower for a three-bladed rotor in the near wake. In general, it could be concluded, that the blade number of similar rotor designs did not noticeably affect the wake flow and thus would not have any significantly influence the overall wind farm power.

An investigation of a counter-rotating array of two turbines showed only a small potential for power optimization. A slightly improved combined performance was attributed to higher angles of attack on the counter-rotating downstream turbine. Therefore, similar performance increases could be potentially obtained by downstream turbine pitch control.

An attachment of optimized winglets on the blade tips of a two-bladed rotor could raise the power coefficient C_P by 8.9%, while the thrust coefficient C_T was observed to increase only moderately by 7.4% at the same time. Moreover, an analysis of the wake behind a wingletted rotor showed a significant influence on the tip region, while the energy content in the wake was almost identical for the two rotor concepts. The total kinetic energy was found to be initially higher in the tip region, when winglets were attached to the rotor tips. An analysis of the phase-averaged vorticity in the tip region disclosed an earlier interaction of the tip vortices behind the wingletted rotor. The vortex pairing caused an earlier expansion of the shear layer in the tip region, leading to a slightly faster wake recovery.

The second part of this thesis, confirmed that intentional yaw misalignment of a turbine laterally deflects the wake downstream of the rotor due to a lateral component of the thrust vector. Furthermore, it was shown that the level of inflow turbulence affected the curled shape and also the overall deflection of the wake. Moreover, the wake shape was found to be significantly asymmetric for positive and negative yaw angles of the upstream rotor. By steering the wake away from a downstream turbine the performance of a turbine array could be increased by up to 11%. However, the yaw moments acting on the yawed turbine and the downstream turbine operating in a partial wake were observed to increase, which emphasized the importance of also considering loads when applying yaw control for the power optimization of wind farms. A possibility to reduce loads with yaw control was demonstrated to be an opposite yawing of the downstream turbine operated in a partial wake. This strategy was found to decrease loads on the downstream turbine while the total power output was slightly increased. In conclusion, the study showed a large potential of intentional yaw misalignment for optimizing wind farm control.

A comparison of numerical predictions to experimental reference data in the Blind test confirmed the ability of Large-Eddy based CFD codes to predict mean velocities and turbulent kinetic energy levels in the wake accurately.

Future work

As highlighted above, yaw control was seen to be a very promising method for the power optimization of wind farms. For this reason, it is recommended that further research should focus on this topic. As accurate numerical predictions were obtained in the Blind test experiment, further quantities could be extracted from these simulations. An investigation of the detailed rotor loads acting on a turbine in different yaw configurations is recommended. Furthermore, the loads acting on a downstream turbine operated in a partial wake are deemed to be crucial to be assessed for a holistic optimization of a yaw-controlled wind farm.

Furthermore, the effects of winglets on the individual blade loads could be investigated in more detail. It is expected that the loads in the blade tip region rise and consequently increase the blade root bending moments. This is of importance for an optimization process of a rotor, in which a trade-off between power gains and increased structural loads must be achieved.

References

Verogray RGD850, Stratasys, safety data sheet, revision A, 2nd March 2016, 2016.

Adaramola, M. and Krogstad, P.-Å.: Experimental investigation of wake effects on wind turbine performance, Renewable Energy, 36, 2078–2086, doi:10.1016/j.renene.2011.01.024, 2011.

Ainslie, J.: Calculating the flowfield in the wake of wind turbines, Journal of Wind Engineering and Industrial Aerodynamics, 27, 213 – 224, doi:doi.org/10.1016/0167-6105(88)90037-2, 1988.

Ammara, I., Leclerc, C., and Masson, C.: A viscous three-dimensional differential/actuator-disk method for the aerodynamic analysis of wind farms, Journal of Solar Energy Engineering, 124, 345–356, doi:10.1115/1.1510870, 2002.

Barthelmie, R. J., Larsen, G. C., Frandsen, S. T., Folkerts, L., Rados, K., Pryor, S. C., Lange, B., and Schepers, G.: Comparison of Wake Model Simulations with Offshore Wind Turbine Wake Profiles Measured by Sodar, Journal of Atmospheric and Oceanic Technology, 23, 888–901, doi:10.1175/JTECH1886.1, 2006.

Barthelmie, R. J., Frandsen, S. T., Nielsen, M. N., Pryor, S. C., Rethore, P.-E., and Jørgensen, H. E.: Modelling and measurements of power losses and turbulence intensity in wind turbine wakes at Middelgrunden offshore wind farm, Wind Energy, 10, 517–528, doi:10.1002/we.238, 2007.

Barthelmie, R. J., Hansen, K., Frandsen, S. T., Rathmann, O., Schepers, J. G., Schlez, W., Phillips, J., Rados, K., Zervos, a., Politis, E. S., and Chaviaropoulos, P. K.: Modelling and measuring flow and wind turbine wakes in large wind farms offshore, Wind Energy, 12, 431–444, doi:10.1002/we.348, 2009.

Bartl, J. and Sætran, L.: Blind test comparison of the performance and wake flow between two in-line wind turbines exposed to different turbulent inflow conditions, Wind Energy Science, 2, 55–76, doi:10.5194/wes-2-55-2017, 2017.

Bartl, J. and Sætran, L.: Experimental testing of axial induction based control strategies for wake control and wind farm optimization, Journal of Physics: Conference Series, 753, 032 035, doi:10.1088/1742-6596/753/3/032035, 2016.

Bartl, J., Pierella, F., and Sætrana, L.: Wake Measurements Behind an Array of Two Model Wind Turbines, Energy Procedia, 24, 305 – 312, doi:10.1016/j.egypro.2012.06.113, 2012.

Bastankhah, M. and Porté-Agel, F.: Experimental and theoretical study of wind turbine wakes in yawed conditions, Journal of Fluid Mechanics, 806, 506–541, doi:10.1017/jfm.2016.595, 2016.

Benedict, L. H. and Gould, R. D.: Towards better uncertainty estimates for turbulence statistics, Experiments in Fluids, 22, 129–136, doi:10.1007/s003480050030, 1996.

Betz, A.: Wind-Energie und ihre Ausnutzung durch Windmühlen, Vandenhoeck, 1926.

Chamorro, L. P. and Porté-Agel, F.: A Wind-Tunnel Investigation of Wind-Turbine Wakes: Boundary-Layer Turbulence Effects, Boundary-Layer Meteorology, 132, 129–149, doi:10.1007/s10546-009-9380-8, 2009.

Chen, T. and Liou, L.: Blockage corrections in wind tunnel tests of small horizontal-axis wind turbines, Experimental Thermal and Fluid Science, 35, 565 – 569, doi: 10.1016/j.expthermflusci.2010.12.005, 2011.

Corten, G., Schaak, P., and Hegberg, T.: Turbine Interaction in Large Offshore Wind Farms; Wind Tunnel Measurements, ECN Wind Energy, ECN-C–04-048, 2004.

Crespo, A., Hernández, J., and Frandsen, S.: Survey of modelling methods for wind turbine wakes and wind farms, Wind Energy, 2, 1–24, doi:10.1002/(SICI) 1099-1824(199901/03)2:1<1::AID-WE16>3.0.CO;2-7, 1999.

Drela, M.: XFOIL: An Analysis and Design System for Low Reynolds Number Airfoils. Low Reynolds Number Aerodynamics, Springer-Verlag, lecture notes in Eng. 54., 1989.

Eriksen, P. E. and Krogstad, P.: An experimental study of the wake of a model wind turbine using phase-averaging, International Journal of Heat and Fluid Flow, 67, 52 – 62, doi:10.1016/j.ijheatfluidflow.2017.05.002, 2017a.

Eriksen, P. E. and Krogstad, P.-Å.: Development of coherent motion in the wake of a model wind turbine, Renewable Energy, 108, 449 – 460, doi:10.1016/j.renene.2017.02.031, 2017b.

Fleming, P., Gebraad, P. M., Lee, S., van Wingerden, J.-W., Johnson, K., Churchfield, M., Michalakes, J., Spalart, P., and Moriarty, P.: Simulation comparison of wake mitigation control strategies for a two-turbine case, Wind Energy, 18, 2135–2143, doi:10.1002/we.1810, 2015.

Fleming, P., Churchfield, M., Scholbrock, A., Clifton, A., Schreck, S., Johnson, K., Wright, A., Gebraad, P., Annoni, J., Naughton, B., Berg, J., Herges, T., White, J., Mikkelsen, T., Sjöholm, M., and Angelou, N.: Detailed field test of yaw-based wake steering, Journal of Physics: Conference Series, 753, 052 003, doi:10.1088/1742-6596/753/5/052003, 2016a.

Fleming, P. a., Gebraad, P. M. O., Lee, S., van Wingerden, J. W., Johnson, K., Churchfield, M., Michalakes, J., Spalart, P., and Moriarty, P.: Evaluating techniques for redirecting turbine wakes using SOWFA, Renewable Energy, 70, 211–218, doi: 10.1016/j.renene.2014.02.015, 2014.

Fleming, P. A., Ning, A., Gebraad, P. M. O., and Dykes, K.: Wind plant system engineering through optimization of layout and yaw control, Wind Energy, 19, 329–344, doi:10.1002/we.1836, 2016b.

Freitag, W. and Schulze, E. T.: Blended Winglets Improve Performance, AERO-MAGAZINE, 35, 2009.

Gaunaa, M. and Johansen, J.: Determination of the Maximum Aerodynamic Efficiency of Wind Turbine Rotors with Winglets, Journal of Physics: Conference Series, 75, 012 006, doi:10.1088/1742-6596/75/1/012006, 2007.

Gebraad, P. M. O., Teeuwisse, F. W., van Wingerden, J. W., Fleming, P. A., Ruben, S. D., Marden, J. R., and Pao, L. Y.: Wind plant power optimization through yaw control using a parametric model for wake effects—a CFD simulation study, Wind Energy, 19, 95–114, doi:10.1002/we.1822, 2014.

Gebraad, P. M. O., Teeuwisse, F. W., van Wingerden, J. W., Fleming, P. A., Ruben, S. D., Marden, J. R., and Pao, L. Y.: Wind plant power optimization through yaw control using a parametric model for wake effects—a CFD simulation study, Wind Energy, 19, 95–114, doi:10.1002/we.1822, 2016.

Gertz, D., Johnson, D. A., and Swytink-Binnema, N.: An Evaluation Testbed for Wind Turbine Blade Tip Designs—Winglet Results, Wind Engineering, 36, 389–410, 2012.

Gertz, D., Johnson, D. A., and Swytink-Binnema, N.: Comparative Measurements of the Effect of a Winglet on a Wind Turbine, in: Wind Energy - Impact of Turbulence, edited by Hölling, M., Peinke, J., and Ivanell, S., pp. 121–126, Springer Berlin Heidelberg, Berlin, Heidelberg, 2014.

GWEC: Global Wind Report 2016-Annual Market Update. 2016, 2017.

Hansen, K. S., Barthelmie, R. J., Jensen, L. E., and Sommer, A.: The impact of turbulence intensity and atmospheric stability on power deficits due to wind turbine wakes at Horns Rev wind farm, Wind Energy, 15, 183–196, doi:10.1002/we.512, 2012.

Hansen, M. O.: Aerodynamics of wind turbines, Routledge, 2015.

Hau, E.: Wind turbines: fundamentals, technologies, application, economics, Springer-Verlag Berlin Heidelberg, 3 edn., doi:10.1007/978-3-642-27151-9, 2013.

Højstrup, J.: Spectral coherence in wind turbine wakes, Journal of Wind Engineering and Industrial Aerodynamics, 80, 137 – 146, doi:https://doi.org/10.1016/S0167-6105(98)00198-6, 1999.

Hooper, J. and Musgrove, A.: Reynolds stress, mean velocity, and dynamic static pressure measurement by a four-hole pressure probe, Experimental Thermal and Fluid Science, 15, 375 – 383, doi:10.1016/S0894-1777(97)00005-8, 1997.

Howland, M. F., Bossuyt, J., Martínez-Tossas, L. A., Meyers, J., and Meneveau, C.: Wake structure in actuator disk models of wind turbines in yaw under uniform inflow conditions, Journal of Renewable and Sustainable Energy, 8, 043 301, doi:10.1063/1.4955091, 2016.

IEA: Energy, climate change and environment 2016 insights, IEA Publications, Paris,France, 2016.

IEA: World Energy Outlook 2017, Organisation for Economic Co-operation and Development, OECD, 2017.

IPCC: Climate change 2014: mitigation of climate change. Contribution of Working Group III to the Fifth Assessment Report of the Intergovernmental Panel on Climate Change [Edenhofer, O., R. Pichs-Madruga, Y. Sokona, E. Farahani, S. Kadner, K. Seyboth, A. Adler, I. Baum, S. Brunner, P. Eickemeier, B. Kriemann, J. Savolainen, S. Schlömer, C. von Stechow, T. Zwickel and J.C. Minx (eds.)]., Cambridge University Press, Cambridge, United Kingdom and New York, NY, USA, 2014.

Jiménez, n., Crespo, A., and Migoya, E.: Application of a LES technique to characterize the wake deflection of a wind turbine in yaw, Wind Energy, 13, 559–572, doi: 10.1002/we.380, 2010.

Johansen, J. and Sørensen, N. N.: Aerodynamic investigation of winglets on wind turbine blades using CFD, Denmark. Forskningscenter Risoe. Risoe-R, no. 1543(EN), iSSN 0106-2840, 2006.

Johansen, J. and Sørensen, N. N.: Numerical analysis of winglets on wind turbine blades using CFD, in: European Wind Energy Congress, Citeseer, 2007.

Knudsen, T., Bak, T., and Svenstrup, M.: Survey of wind farm control—power and fatigue optimization, Wind Energy, 18, 1333–1351, doi:10.1002/we.1760, 2014.

Krogstad, P.-Å. and Adaramola, M. S.: Performance and near wake measurements of a model horizontal axis wind turbine, Wind Energy, 15, 743–756, doi:10.1002/we.502, 2012.

Krogstad, P.-Å. and Eriksen, P. E.: “Blind test” calculations of the performance and wake development for a model wind turbine, Renewable Energy, 50, 325 – 333, doi:10.1016/j.renene.2012.06.044, 2013.

Krogstad, P. Å. and Lund, J.: An experimental and numerical study of the performance of a model turbine, Wind Energy, 15, 443–457, doi:10.1002/we.482, 2012.

Krogstad, P.-Å., Sætran, L., and Adaramola, M. S.: “Blind Test 3” calculations of the performance and wake development behind two in-line and offset model wind turbines, Journal of Fluids and Structures, 52, 65–80, doi:10.1016/j.jfluidstructs.2014.10.002, 2015.

Kumer, V.-M., Reuder, J., Svardal, B., Sætre, C., and Eecen, P.: Characterisation of Single Wind Turbine Wakes with Static and Scanning WINTWEX-W LiDAR Data, Energy Procedia, 80, 245 – 254, doi:10.1016/j.egypro.2015.11.428, 2015.

Maniaci, D. and Maughmer, M.: Winglet design for wind turbines using a free-wake vortex analysis method, in: 50th AIAA Aerospace Sciences Meeting including the New Horizons Forum and Aerospace Exposition, p. 1158, doi:10.2514/6.2012-1158, 2012.

Manwell, J. F., McGowan, J. G., and Rogers, A. L.: Wind energy explained: theory, design and application, John Wiley & Sons, 2 edn., 2010.

Medici, D. and Alfredsson, P. H.: Measurements on a wind turbine wake: 3D effects and bluff body vortex shedding, Wind Energy, 9, 219–236, doi:10.1002/we.156, 2006.

Miller, M., Kiefer, J., Westergaard, C., and Hultmark, M.: Model Wind Turbines Tested at Full-Scale Similarity, Journal of Physics: Conference Series, 753, 032 018, doi:10.1088/1742-6596/753/3/032018, 2016.

Mosetti, G., Poloni, C., and Diviacco, B.: Optimization of wind turbine positioning in large windfarms by means of a genetic algorithm, Journal of Wind Engineering and Industrial Aerodynamics, 51, 105 – 116, doi:https://doi.org/10.1016/0167-6105(94) 90080-9, 1994.

Newman, A. J., Cal, R. B., and Castillo, L.: Blade number effects in a scaled down wind farm, Renewable Energy, 81, 472 – 481, doi:10.1016/j.renene.2015.03.013, 2015.

Ostovan, Y.: Winglets for wind turbines: An experimental study on aerodynamic performance and tip vortex behavior, Ph.D. thesis, Middle East Technical University, 2017.

Pierella, F. and Sætran, L.: Wind tunnel investigation on the effect of the turbine tower on wind turbines wake symmetry, Wind Energy, 20, 1753–1769, doi:10.1002/we.2120, 2017.

Pierella, F., Krogstad, P.-Å., and Sætran, L.: Blind Test 2 calculations for two in-line model wind turbines where the downstream turbine operates at various rotational speeds, Renewable Energy, 70, 62 – 77, doi:10.1016/j.renene.2014.03.034, special issue on aerodynamics of offshore wind energy systems and wakes, 2014.

Polster, F., Bartl, J., Mühle, F., Thamsen, P. U., and Sætran, L.: Experimental validation of analytical wake and downstream turbine performance modelling, Journal of Physics: Conference Series, manuscript submitted for publication, 2017.

Quinn, R., Schepers, G., and Bulder, B.: A Parametric Investigation Into the Effect of Low Induction Rotor (LIR) Wind Turbines on the Levelised Cost of Electricity for a 1 GW Offshore Wind Farm in a North Sea Wind Climate, Energy Procedia, 94, 164 – 172, doi:10.1016/j.egypro.2016.09.213, 2016.

Raach, S., Schlipf, D., Borisade, F., and Cheng, P. W.: Wake redirecting using feedback control to improve the power output of wind farms, in: 2016 American Control Conference (ACC), pp. 1387–1392, doi:10.1109/ACC.2016.7525111, 2016.

Raach, S., Schlipf, D., and Cheng, P. W.: Lidar-based wake tracking for closed-loop wind farm control, Wind Energy Science, 2, 257–267, doi:10.5194/wes-2-257-2017, 2017.

Reuder, J., Båserud, L., Kral, S., Kumer, V., Wagenaar, J. W., and Knauer, A.: Proof of Concept for Wind Turbine Wake Investigations with the RPAS SUMO, Energy Procedia, 94, 452 – 461, doi:10.1016/j.egypro.2016.09.215, 2016.

Ryi, J., Rhee, W., Hwang, U. C., and Choi, J.-S.: Blockage effect correction for a scaled wind turbine rotor by using wind tunnel test data, Renewable Energy, 79, 227 – 235, doi:10.1016/j.renene.2014.11.057, selected Papers on Renewable Energy: AFORE 2013, 2015.

S. Lissaman, P.: Energy effectiveness of arbitrary arrays of wind turbines, Journal of Energy, 3, 323–328, doi:10.2514/3.62441, 1979.

Sanderse, B.: Aerodynamics of Wind Turbine Wakes: Literature Review, vol. ECN-E–09-016 of *ECN.: E-series*, ECN Wind Energy, 2009.

Sanderse, B., van der Pijl, S., and Koren, B.: Review of computational fluid dynamics for wind turbine wake aerodynamics, Wind Energy, 14, 799–819, doi:10.1002/we.458, 2011.

Sarlak, H., Nishino, T., Martínez-Tossas, L., Meneveau, C., and Sørensen, J.: Assessment of blockage effects on the wake characteristics and power of wind turbines, Renewable Energy, 93, 340 – 352, doi:10.1016/j.renene.2016.01.101, 2016.

Schottler, J., Hölling, A., Peinke, J., and Hölling, M.: Design and implementation of a controllable model wind turbine for experimental studies, Journal of Physics: Conference Series, 753, 072 030, doi:10.1088/1742-6596/753/7/072030, 2016a.

Schottler, J., Hölling, A., Peinke, J., and Hölling, M.: Wind tunnel tests on controllable model wind turbines in yaw, AIAA 34th Wind Energy Symposium, doi:10.2514/6.2016-1523, 2016b.

Schottler, J., Hölling, A., Peinke, J., and Hölling, M.: Brief communication: On the influence of vertical wind shear on the combined power output of two model wind turbines in yaw, Wind Energy Science, 2, 439–442, doi:10.5194/wes-2-439-2017, 2017.

Schottler, J., Bartl, J., and Mühle, F.: Wind tunnel experiments on wind turbine wakes in yaw, doi:10.5281/zenodo.1193656, 2018.

Schreiber, J., Nanos, E. M., Campagnolo, F., and Bottasso, C. L.: Verification and Calibration of a Reduced Order Wind Farm Model by Wind Tunnel Experiments, Journal of Physics: Conference Series, 854, 012 041, doi:10.1088/1742-6596/854/1/012041, 2017.

Schümann, H., Pierella, F., and Sætran, L.: Experimental Investigation of Wind Turbine Wakes in the Wind Tunnel, Energy Procedia, 35, 285 – 296, doi:10.1016/j.egypro.2013.07.181, 2013.

Shakoor, R., Hassan, M. Y., Raheem, A., and Wu, Y.-K.: Wake effect modeling: A review of wind farm layout optimization using Jense's model, Renewable and Sustainable Energy Reviews, 58, 1048 – 1059, doi:https://doi.org/10.1016/j.rser.2015.12.229, 2016.

Shepherd, I. C.: A four hole pressure probe for fluid flow measurements in three dimensions, Journal of Fluids Engineering, 103, 590–594, doi:10.1115/1.3241774, 1981.

Somers, D. M.: The S825 and S826 airfoils, National Renewable Energy Laboratory, Subcontractor Report, last access 03.11.2017, 2005.

Steinbuch, M., de Boer, W., Bosgra, O., Peters, S., and Ploeg, J.: Optimal control of wind power plants, Journal of Wind Engineering and Industrial Aerodynamics, 27, 237 – 246, doi:https://doi.org/10.1016/0167-6105(88)90039-6, 1988.

Thomsen, K. and Sørensen, P.: Fatigue loads for wind turbines operating in wakes, Journal of Wind Engineering and Industrial Aerodynamics, 80, 121 – 136, doi:10.1016/S0167-6105(98)00194-9, 1999.

Tobin, N., Hamed, A. M., and Chamorro, L. P.: An Experimental Study on the Effects ofWinglets on the Wake and Performance of a ModelWind Turbine, Energies, 8, 11 955–11 972, doi:doi:10.3390/en81011955, 2015.

Trujillo, J. J., Seifert, J. K., Würth, I., Schlipf, D., and Kühn, M.: Full-field assessment of wind turbine near-wake deviation in relation to yaw misalignment, Wind Energy Science, 1, 41–53, doi:10.5194/wes-1-41-2016, 2016.

UNFCCC: Adoption of the Paris Agreement. Proposal by the President, United Nations Office at Geneva, Geneva, Switzerland, 2015.

van Kuik, G. A. M., Peinke, J., Nijssen, R., Lekou, D., Mann, J., Sørensen, J. N., Ferreira, C., van Wingerden, J. W., Schlipf, D., Gebraad, P., Polinder, H., Abrahamsen, A., van Bussel, G. J. W., Sørensen, J. D., Tavner, P., Bottasso, C. L., Muskulus, M., Matha, D., Lindeboom, H. J., Degraer, S., Kramer, O., Lehnhoff, S., Sonnenschein, M., Sørensen, P. E., Künneke, R. W., Morthorst, P. E., and Skytte, K.: Long-term research challenges in wind energy - a research agenda by the European Academy of Wind Energy, Wind Energy Science, 1, 1–39, doi:10.5194/wes-1-1-2016, 2016.

Vermeer, L. J., Sørensen, J. N., and Crespo, a.: Wind turbine wake aerodynamics, Progress in Aerospace Sciences, 39, 467–510, doi:10.1016/S0376-0421(03)00078-2, 2003.

Vollmer, L., Steinfeld, G., Heinemann, D., and Kühn, M.: Estimating the wake deflection downstream of a wind turbine in different atmospheric stabilities: an LES study, Wind Energy Science, 1, 129–141, doi:10.5194/wes-1-129-2016, 2016.

Wang, J., Foley, S., Nanos, E. M., Yu, T., Campagnolo, F., Bottasso, C. L., Zanotti, A., and Croce, A.: Numerical and experimental study of wake redirection techniques in a boundary layer wind tunnel, Journal of Physics: Conference Series, 854, 012 048, doi:10.1088/1742-6596/854/1/012048, 2017.

Wharton, S. and Lundquist, J. K.: Assessing atmospheric stability and its impacts on rotor-disk wind characteristics at an onshore wind farm, Wind Energy, 15, 525–546, doi:10.1002/we.483, 2012.

Wheeler, A. and Ganji, A.: Introduction to Engineering Experimentation, Pearson Education, Upper Saddle River, New Jersey, USA, third edition edn., 2010.

Windpowermonthly: Ten of the biggest turbines, URL https://www.windpowermonthly.com/10-biggest-turbines, accessed: 2018-02-09, 2017.

Yuan, W., Ozbay, A., Tian, W., and Hu, H.: An experimental investigation on the effects of turbine rotation directions on the wake interference of wind turbines, in: 51st AIAA Aerospace Sciences Meeting including the New Horizons Forum and Aerospace Exposition, p. 607, doi:10.2514/6.2013-607, 2013.

Yuan, W., Tian, W., Ozbay, A., and Hu, H.: An experimental study on the effects of relative rotation direction on the wake interferences among tandem wind turbines, Science China Physics, Mechanics & Astronomy, 57, 935–949, doi:10.1007/s11433-014-5429-x, 2014.

Appendix A

Technical drawings

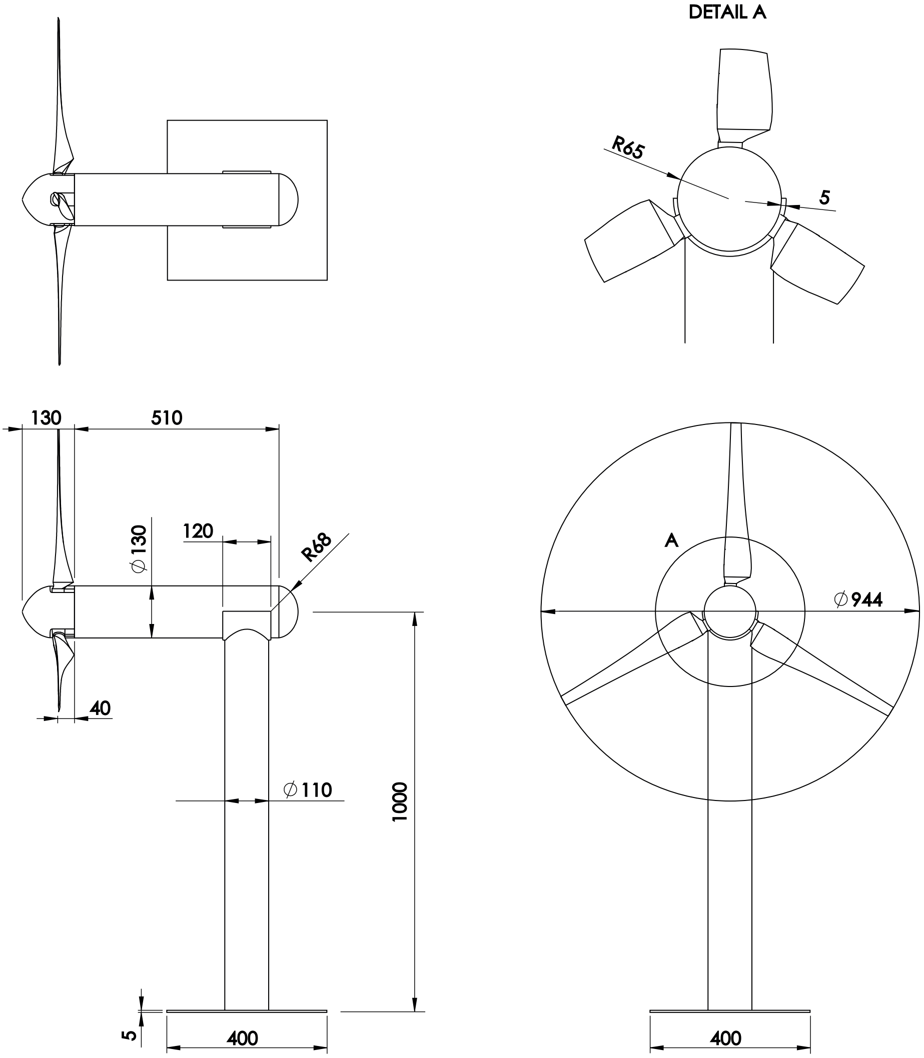

Figure A.1: Technical drawing of NTNU model wind turbine T1.

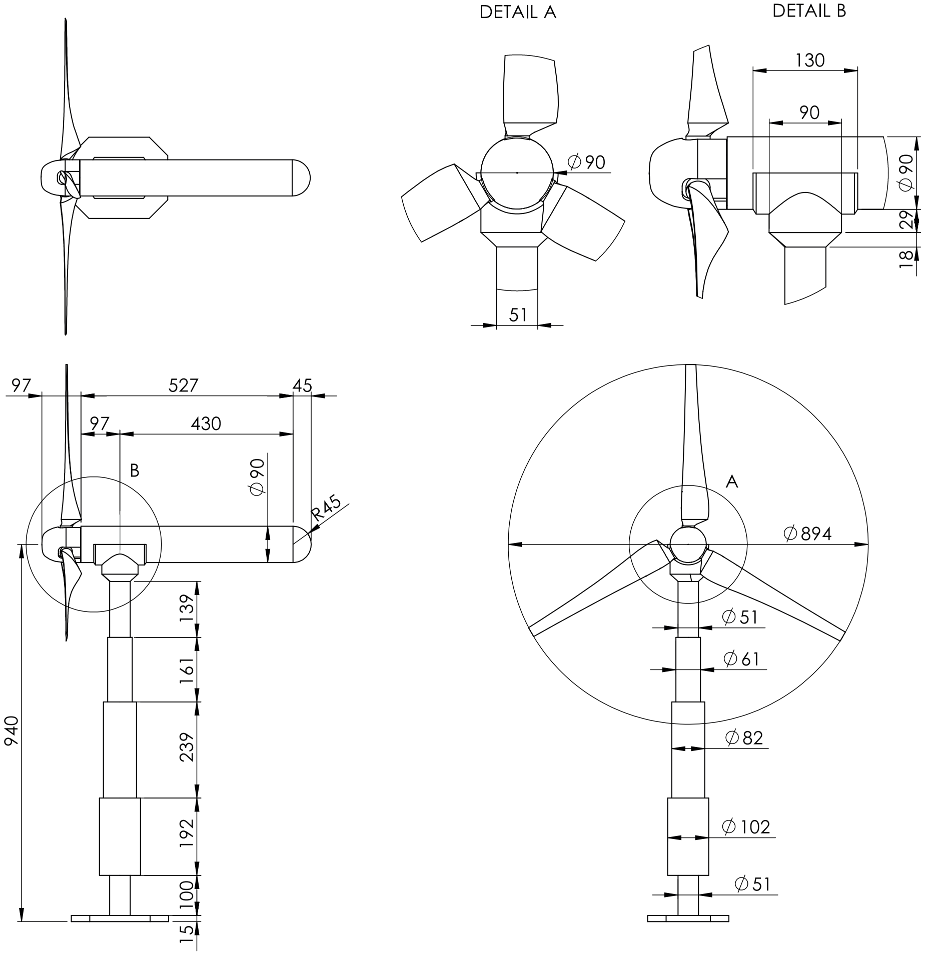

Figure A.2: Technical drawing of NTNU model wind turbine T2.

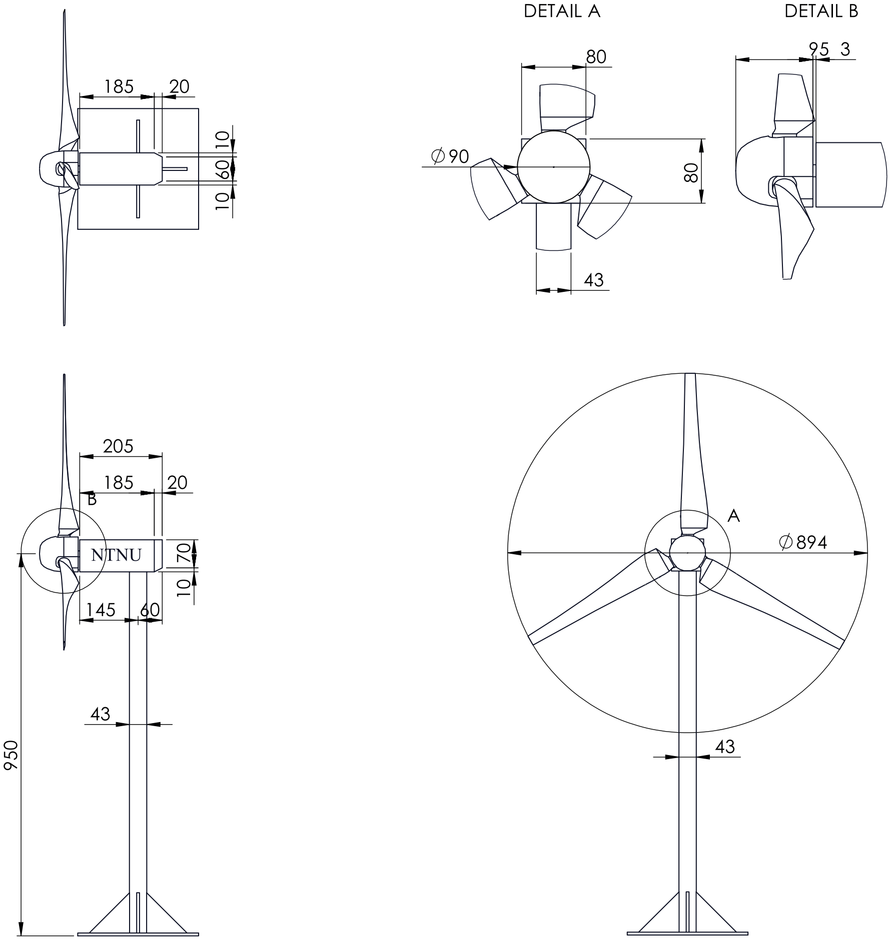

Figure A.3: Technical drawing of NTNU model wind turbine LARS1.

PAPER I

The effect of the number of blades on wind turbine wake – a comparison between 2-and 3-bladed rotors

Franz Mühle[1], **Muyiwa S Adaramola**[1] **and Lars Sætran**[2]

[1] Department of Ecology and Natural Resource Management, Norwegian University of Life Science (NMBU), 1430 Ås, Norway

[2] Department of Energy and Process Engineering, Norwegian University of Science and Technology (NTNU), 7491 Trondheim, Norway

Corresponding Author: Franz Mühle (franz.muhle@nmbu.no)

Abstract. Due to cost benefit and weight reduction, 2-bladed wind turbines have the potential to become more important for offshore wind applications. In order to optimize the arrangement of wind turbines in wind farms and for accurate forecasts of the power production, a detailed knowledge of the wake flow is needed. In this study, three different rotors with varying number of blades and similar performance behaviour have been designed and manufactured using the 3-dimensional (3D) printing technology. The performance characteristics of these rotors as well as their wake features are measured experimentally in wind tunnel tests and compared. The velocity deficit is seen to vary only insignificantly for the wakes in distances of 3D (where D is the rotor diameter), 5D and 7D behind the turbine. However, higher turbulence intensity levels are recorded in the wake of the 2-bladed rotors. This could have potential for a faster wake recovery and thus a narrower turbine spacing.

1 Introduction

In the wind power industry the development and research in the last decades focused mostly on 3-bladed turbines. Whereas in the 1970's and 1980's 2-bladed turbines were still investigated and considered in turbine development, the research effort in 2-bladed turbines was only minor in the last years. This is due to the disadvantages of 2-bladed rotors compared to 3-bladed rotors, such as the higher noise emissions, the distracting visual effects and the unfavorable dynamic behavior. However, as the offshore wind energy market is gaining importance, the 2-bladed turbines are getting more significant again. This is due to the fact, that the drawbacks are not so much relevant offshore and the big advantage of one less rotor is strongly decreasing the costs (Hau, 2013). Nevertheless the maximum theoretical attainable performance is increasing with increasing blades number because of reduced tip vortices, which is also a drawback for 2-bladed rotors when comparing them to the established 3-bladed rotors. This fact should also be considered when looking at the economic potential of the rotor blade number. Moreover, in a wind farm set-up, wake effects are especially of interest to evaluate how the turbines interact and hence, their implication on wind farm design and power production.

There are several structural issues with wind turbines with 2-bladed rotor. One of the main issue is the unsteady loading of the blades. Whereas a 3-bladed rotor has a constant inertia about the yaw axis, which is independent of the azimuthal position of the rotor hub. However, the rotational inertia of a 2-bladed rotor is periodic, with the maximum at the horizontal position and the minimum at the vertical position and consequently, 2-bladed turbines have higher cyclic loads relative to 3-bladed rotor (Jamieson, 2011). It is also unfavorable that when one blade is in the tower shadow the other one is pointing straight up and is thus exposed to the strongest winds under atmospheric inflow conditions. There are some strategies how to solve these problems and reduce the turbine loadings. However, the presented article will only focus on the aerodynamic performance and the wake effects of wind turbines with 2- and 3-bladed rotors.

The influence of the number of blades on the performance of a wind turbine was discussed by Wilson, Lissaman, and Walker (1976). They showed that the power coefficient of a wind turbine approaches Betz limit as number of blade increases. However, using a computational fluid dynamics (CFD) analysis, Newbauer and Kupathy obtained opposite results when they investigated 2-, 3- and 4- bladed rotors and observed an increasing power coefficient with decreasing number of blades (Newbauer and Kumpaty, 2012). The same trend was observed by Duquette, Swanson, and Visser (2003) who performed experimental and numerical studies on blade number effects, but only for three and more blades. McTavish, Feszty, and Nitzsche (2013) looked at the wake expansion of a 2- and a 3- bladed turbine experimentally. However, they used two completely different turbine concepts and therefore their results are not suited for comparison of blade number effects. In a recent study, Newman, Cal, and Castillo (2015) investigated wake effects of a wind turbine arrangement with varying number of blades experimentally with particle image velocimetry (PIV). In their experiment, they identified the wakes of two 3 x 4 turbine arrangements adjusting the same power output, one array consisting only of 3- bladed and one only of 2- bladed turbines. They found velocity differences of up to 10% in the near wake and subtle distinctions in the far wake. Furthermore, they showed that 3-bladed turbines cause 25% higher fatigue loads than 2-bladed ones for the second turbine row.

The main objective of this present work is to show how rotors, with the same maximum power coefficient, but different number of blades influencing the wake characteristics of a wind turbine. The focus here is on the difference between 2- and

3- bladed rotors. As 2-bladed rotors are considered to become significant in offshore wind application, it is important to understand how turbines with such rotors affect one another in a wind farm arrangement. As turbines with 3-bladed rotors have been investigated closely in the past and a lot information about their wakes is available, the wakes of 2-bladed rotors are compared with those of a 3-bladed rotor to find the main distinctions between them. In addition, effect of number of blades on the inflow conditions and consequently the power output of a downstream turbine is presented. Furthermore, the turbulence characteristics of the wake are investigated to quantify wake recovery rates and the resulting fatigue loads on the downwind turbine.

2 Methods

2.1 Experimental setup

The experiments were conducted in a closed-return wind tunnel located at the Department of Energy and Process Engineering, Norwegian University of Science and Technology (NTNU), Trondheim, Norway. The wind tunnel has a test section of 2.7m x 1.8m x 11.0m. The rotors were mounted on the model turbine as described in (Krogstad and Lund, 2012). The blockage ratio of the turbine in the wind tunnel is 11.8% (Adaramola and Krogstad, 2011). The wind tunnel was operated at low inlet turbulence intensity of 0.23% and the inlet velocity U_∞ of 10.0m/s for all experiments. The torque was measured with a torque transducer installed inside the hub of the model wind turbine and the thrust force was measured with a 6-component force balance. The measurements with these devices resulted in uncertainties of about ±3% for the maximum power coefficient (C_P) and ±2% for the thrust coefficient (C_T) at the optimum tip speed ratio (TSR). A sketch of the experimental setup is shown in Figure 1.

Wake velocity measurements were carried out at downstream distances of 3D, 5D and 7D (where D is the rotor diameter) and at the wind turbines' hub-height. This distances where chosen to examine the wake development as well as the main wake features, which were expected to be significant at 3D, whereas distances of 5D and 7D are considered to be more relevant for full scale applications. Moreover, in order to get a clear understanding of the inflow conditions of the downstream turbine, full two-dimensional wake measurements for all three rotors were conducted at 5D. All the wake measurements were performed when the wind turbines were operating at their respective optimum tip speed ratio. The velocity measurements were conducted using a 2-component Laser Doppler velocimetry (LDV) instrument. The uncertainty of the mean velocities are lower than ±0.5% of the mean velocity considering a 95%

confidence interval whereas the uncertainty of the turbulence intensities are calculated to be lower than ±2% of the mean velocity with a confidence level of 95%.

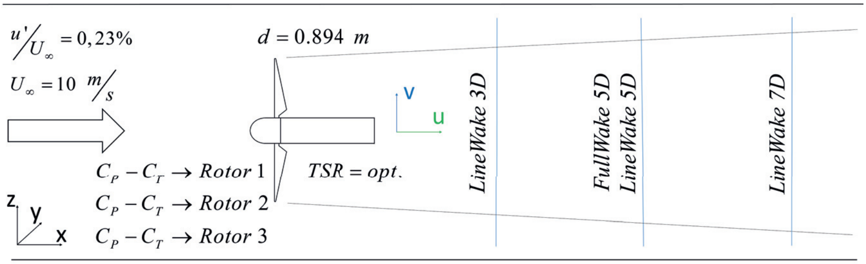

Figure 1: Sketch of the experimental setup.

2.2 Rotor design

The rotor design is based on the rotor developed at the Department of Energy and Process Engineering (at NTNU Trondheim), which is described in (Krogstad and Lund, 2012) based on the NREL S826 airfoil. This rotor is a 3-bladed rotor milled from an aluminum alloy and it was used in the study as reference rotor. The purpose of the rotor design process is to produce 2-bladed rotors that have the same maximum power coefficients (C_P) as the reference rotor and design parameters, which are based on the 3-bladed rotor (NTNU rotor). When the number of blades is changed, other blade parameters are adjusted so the rotors would have similar performance behavior. The two main parameters which were adjusted in the blade design process in this study are the chord length and the twist angle. Consequently, two new rotors were designed, one with the same aspect ratio (rotor 2) and another one with the same solidity (rotor 1) as the reference rotor. The 2-bladed rotor with the same aspect ratio as the 3-bladed rotor needs to have a higher tip speed ratio (TSR) to achieve a similar C_P as the 3-bladed rotor, which involved a change of the twist angle to take the higher circumferential velocities into account. The other 2-bladed rotor with the same solidity requires a modified chord length distribution to change the blocked area of the rotor and the TSR for this rotor concept was expected to be the same.

To stay as close as possible to the reference case, the twist angle distribution was related to that of the reference rotor. Thus, the twist angles where reduced proportionately to the original twist angle distribution. The performances of the resulting rotor were determined with a blade element momentum (BEM) code and compared the results to that of the reference rotor. The twist angles were adjusted until the same maximum C_P value was achieved. For the rotor with the same solidity the reference chord length was multiplied by 1.5 to take the area of the one dropped blade into account. Calculations with the BEM code showed that the twist angle had to be also modified slightly for this rotor to reach the same maximum C_P value as for the reference rotor. The resulted rotor properties of the three rotors, which were manufactured and used in the study are presented in Table 1. All rotors are rotating in clockwise direction.

Table 1: Properties of tested rotors.

	Description	Chord length [%]	Twist angle [%]	Opt. TSR
Rotor 1	3-bladed rotor	100	100	6
Rotor 2	2-bladed rotor same aspect ratio	100	70	7
Rotor 3	2-bladed rotor same solidity	150	95	6

All three rotors were manufactured using a 3D printer based on the multi-jet modeling technology. In a preliminary study, it was checked if this fabrication technique is suited to produce accurate blades that can be used in wind tunnel experiments. The results of this preliminary study showed that with the selected 3D printing technology, it is possible to produce blades with fine features in a high quality and with a good accuracy. Therefore, the printed blades are suited for the application in wind tunnel tests. The three rotors, which were fabricated for the wind tunnel experiments for this article are depictured in Figure 2.

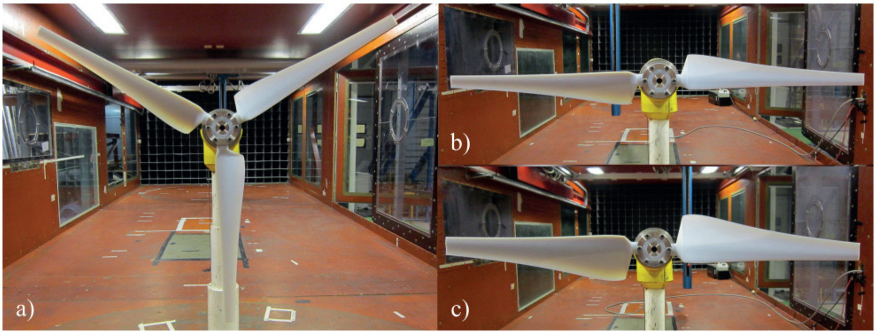

Figure 2: Printed rotors for experiment: (a) Rotor 1, (b) Rotor 2 and (c) Rotor 3.

2.3 Rotor performance

The purpose of the rotor design process was to match the maximum power coefficients of the three different rotor concepts. Therefore, preliminary calculations were undertaken using a BEM code. The results of these calculations showed that the maximum C_P values were identical for the three designed rotors. In order to validate the results of the preliminary calculations, the power coefficient and thrust coefficient were determined experimentally as a function of TSR. Figure 3 present the experimentally measured C_P and C_T profiles for the three rotor concepts. It can be seen, that the maximum C_P values differ slightly, thus the predictions with the BEM code where not precise as the blades were designed to have exactly the same maximum C_P. In Figure 3, it can be seen that the two 2-bladed rotors have maximum values, which are slightly lower than that for the 3-bladed rotor. While rotor 1 (3-bladed rotor) has the maximum C_P of 0.480 at TSR 6, rotor 2 has a maximum C_P of 0.452 at TSR 7 and rotor 3 has maximum C_P of 0.453 at TSR 6. Consequently, the maximum C_P's of Rotor 1 is 2.7% larger than the maximum C_P's of rotor 2 and rotor 3.

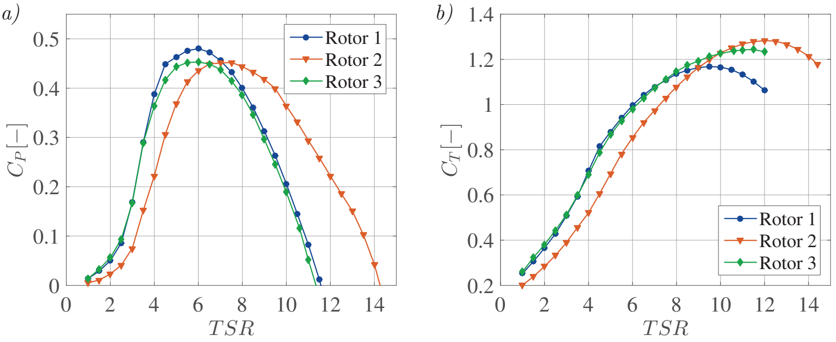

Figure 3: (a) Power coefficient and (b) thrust coefficient, as a function of the tip speed ratio for the three investigated rotors.

From Figure 3b, it can be observed that rotor 1 and rotor 3, which have the same solidity, have similar C_T profiles for TSR ≤ 8, and thereafter, the two profiles are diverged. On the other hand, rotor 2 has a slightly lower C_T which is on an average 18% lower when compared with the other two rotor concepts within the $1 < \text{TSR} < 8$. From TSR > 8, the C_T for rotor 2 is observed to continue increase whereas the C_T for the other two rotor concepts start to decrease. However, at the respective optimum TSR ($\text{TSR}_{\text{max}} = 6$ for rotor 1 and rotor 3 and, $\text{TSR}_{\text{max}} = 7$ for rotor 2), the C_T values are very similar and all three lie in the range of 1.0.

3 Results and discussion

3.1 Kinetic energy in the wake

The wake of a wind turbine is characterized by a velocity deficit and a higher turbulence level behind the turbine. The velocity deficit in the wake is important to know, as this gives information about the energy that is available for a wind turbine operating downstream and thus, in the wake of an upstream wind turbine. In the presented study the effects of blade number of a wind turbine rotor on the wake is investigated. Therefore, the wake velocities for the three different rotors concepts were measured at 3D, 5D and 7D behind the model turbine. At these distances line wakes at turbine hub height where measured in a wind tunnel width range of -2.57z/R to+ 2.57z/R (wind tunnel width (z) position divided by rotor radius (R), with an interval of 50 mm. The results of these measurements are shown in Figure 4. In this figure, the downstream velocity (u) is normalized by the inflow freestream velocity (U_∞). It can be seen from this that the mean velocities differ slightly for the different rotors. Slight variations are observed mainly in the area directly behind the rotors, whereas in the boundary area of the wake the velocity deficit is mostly similar for all three rotors at the investigated distances. As the velocity in the wake relates to the available power for a downwind turbine, the measured velocities were integrated over the rotor area to estimate available power in the wake. Using this information, the rotors were compared according to the energy they left in the flow for a downwind rotor. However, for all the observations should be kept in mind, that the C_P for rotor 1 is about 2.7% larger than the C_P for the other two rotors at their maximum TSR.

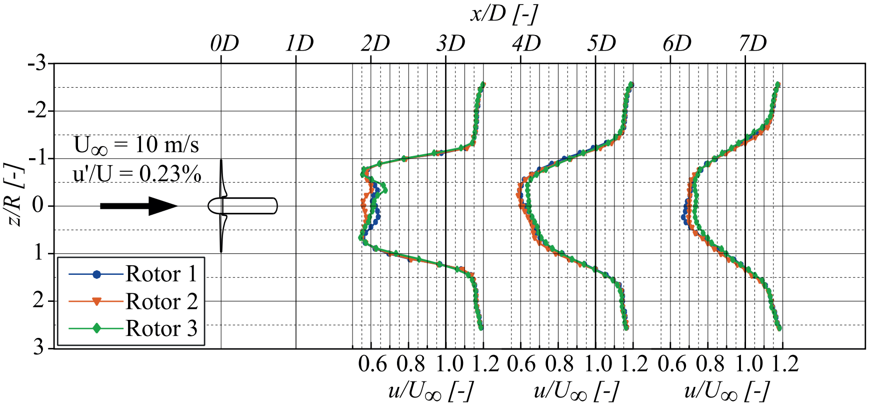

Figure 4: Velocity deficit in the wake for the three rotor concepts, normalized by the inflow velocity, at different downstream distances (3D, 5D and 7D) in the wind tunnel.

The estimated available power at downstream distance of 3D indicated that both the 2-bladed rotors have less energy in the wake compared with the 3-bladed rotor. However, the difference in the available power is not substantial, relatively to rotor 1, rotor 2 has 1.3% less available power in the wake and rotor 3 has only 0.2% less available power in the wake. At 5D, however, whereas rotor 2 has 1.1% less available power, rotor 3 has 3.2% more available power in the wake than rotor 1. The differences in kinetic energy for the three rotor concepts increases with increasing distance, thus the clearest distinctions can be observed at 7D. Accordingly at this distance the wake of rotor 2 has 1.1% less energy and rotor 3 has 3.2% more available energy in the wake than rotor 1. The trend that in the distinctions in the velocity deficit increases with increasing distance is obvious when comparing rotor 2 and rotor 3. Rotor 3 has always more energy in the wake than rotor 2, small difference of 1.1% at 3D but 4.0% at 5D and 4.3% at 7D. However, the differences in the velocities in the wake of the three rotors is insignificant and the velocity profiles are alike. Thus, it can be assumed, that an aligned arrangement consisting of two 3-bladed rotors has the potential to be more efficient compared with a similar turbine arrangement using rotor 2 and rotor 3, because the C_P of rotor 1 is 2.7% larger.

To examine how the wake is changing with increasing distance the wake recovery rate is calculated. This is done by dividing the percentage change in available energy for the different downstream distances by the rotor diameter. Between 3D and 5D it is clear that rotor 3 with 7.7 %/D has the highest recovery rate whereas rotor 1 with 6.1 %/D and rotor 2 with 6.3 %/D having similar recovery rates. This trend cannot be seen for the recovery rates between 5D and 7D, where rotor 1, rotor 2 and rotor 3 have similar recovery rate of 5.4 %/D, 5.3 %/D and 5.5 %/D, respectively. Therefore, it becomes obvious that the wakes for all three rotors recover faster for the closer distances than in the region further down of the rotor.

The velocity profiles at the hub-height are very alike and thus, the difference in the wake kinetic energy fields at turbine hub height are obscured. To check if the distinctions are minor across the entire height of the rotors and check for asymmetry effects for the different rotors, full two-dimensional wake for the three rotors were measured at a distance of 5D in a width range from -1.5z/R to 1.5 z/R and height range from -1.5y/R to 1.5 y/R with an increment of 75 mm in y-direction and z-direction. The results of the full-wake measurement for the kinetic energy is shown in Figure 5.

Looking at the contour plots it can be observed that for all three rotors the wake maximum velocity deficit is displaced below hub height and shifted to negative y- and z- half plane. In addition, on the outer edges of the rotors it can be observed that the wake is shifted towards the negative z-direction. This asymmetry effects are expected, which is due to tower interactions with the wake as show by Pirella (Pierella, 2014).

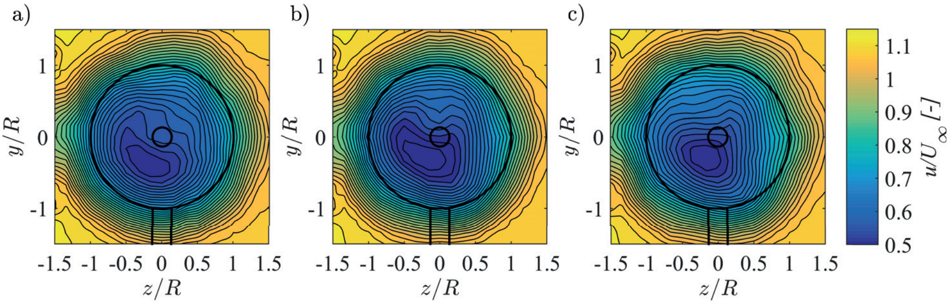

Figure 5: Contour plots for velocity deficit in the wake, normalized by the inflow velocity, at downstream distance 5D: (a) rotor 1, (b) rotor 2 and (c) rotor 3. (The thick black line represent the turbine rotor outline, looking in flow direction)

However, it can be seen that this maximum velocity deficits change slightly for the three rotors. Whereas for rotor 2, the area with the high deficits is largest but it is slightly smaller for rotor 1 and rotor 3. When comparing the available energy at the rotor plane similarly as for the line wakes the same trends become obvious at a distance of 5D. Here, rotor 1 has 0.8% more energy than rotor 2 with difference of 0.2% compared to the line wakes. The energy difference between rotor 1 and rotor 3 shows 2.6% more energy for rotor 3 almost the same results as for the line wakes. Larger differences can be observed when looking at the share of energy on left-side of the wake than the right-side. For the energy calculations based on the full wakes, the theoretical power is around 10% lower than the theoretical power calculation based on the wake profiles at the hub-height. Consequently, the analysis based on the line wakes the power in the wake is somewhat underestimated. However, the results show, that there are no major differences in the kinetic energy in the wake at 5D for the three rotor concepts in altitudinal direction.

To examine where the 3- and 2-bladed rotor concepts diverge from each other, the energy density at every measurement point was calculated for all three rotor concepts and the energy densities of the 2-bladed rotors were subtracted from the energy density of the 3-bladed rotor. The results of these calculations are shown in Figure 6. This figure show that the major differences in energy density between the 2- and 3-bladed rotors occur in the area outside of the rotor where they are up to -20% in positive z-direction and +20% in negative z-direction. Within, the rotor area of the turbine the distinctions are only minor, where the differences from rotor 1 and rotor 2 are in the area between -5 and 5% while the differences from rotor 1 and rotor 3 are between -9 and 3%. However, it can be seen that rotor 1 has a higher energy density in its wake at 5D as rotor 2, considering the rotor area of a potential downwind turbine. Rotor 3, on the other side, has a higher energy density in the wake as rotor 1 considering the same observation area. Moreover, the larger differences can be observed in the outer part of the wake, here the 3-bladed rotor has a higher energy density as both 2-bladed rotors in negative z-direction and vice versa in positive z-direction. This is due to the differential symmetry behavior for the different blade number of the rotors.

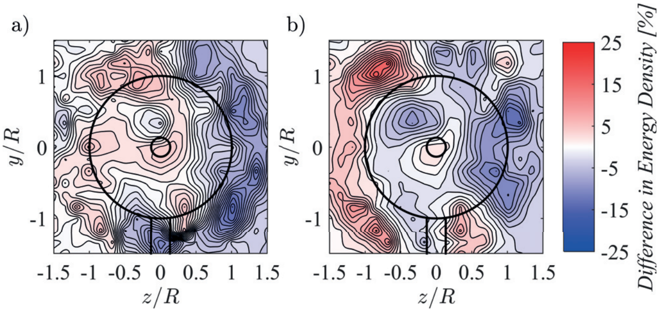

Figure 6: Difference in energy density in the wake in share of theoretical power at 0D, at downstream distance 5D in y- and z-direction normalized by the rotor radius (looking in main flow direction): (a) rotor 1 – rotor 2 and (b) rotor 1 – rotor 3.

3.2 Turbulence intensity in the wake

The second wake feature which is of interest is the turbulence intensity and thus, the turbulent energy in the wake. As the LDV measurement system measures velocities in 2 directions the combined turbulence intensity for the x- and z-direction was calculated according to Equation (1).

$$TI = \frac{\sqrt{1/2({u'_x}^2 + {u'_z}^2)}}{\sqrt{U_{\infty,x}^2 + U_{\infty,z}^2}} * 100 \ [\%] \tag{1}$$

Figure 7 shows that the turbulence intensities obtained from 2 directional components at the distances 3D, 5D and 7D, have significant variations among the three sets of rotors considered in this study. These differences occurring mostly in the area behind the rotor and at the turbine rotor edge where the intensity peaks occur. In the outer wake region, the three wakes are almost identical. When comparing the rotor concepts, the 2-bladed rotors produce higher turbulence in the wake at all three distances investigated. At a distance of 3D the integral of the turbulence intensity of the investigated wake section is 0.5% higher in the wake of rotor 2 as those of rotor 1 and rotor 3 has even a 2.0% higher overall turbulence intensity as rotor 1. At the distance of 5D, the same trend can be observed, the difference between rotor 3 and rotor 1 is only 1.2%. Even though the total turbulent energy in the measured section of the wake is only changing marginally at all three investigated distances, the differences in turbulent energy between the three rotor concepts are decreases with increasing distance. This is due to the fact that the overall turbulence intensity increased by around 1% between 3D and 7D for rotor 1 and rotor 3 whereas it decreased by 0.5% in the same section for rotor 3. Consequently, at the downstream distance of 7D, the differences for the three rotors are only minor and in the range of 0.2%. The profiles in the diagram in Figure 7 at 7D are almost overlapped in the outer part of the wake as well as in the area behind the rotor. Furthermore, the turbulent intensity profiles even out with increasing distance. Whereas at the distance of 3D the turbulent intensity profiles have high peak values between 17 and 22% at the rotor edge and peak values of up to 10% at the inner rotor area. These extreme values reduce with increasing distance due to turbulent mixing within the wake. Consequently, at 7D the turbulence intensity varies approximately 2% between the center (10%) and the rotor edge (12%).

The higher turbulence levels at distances at 3D and 5D indicate that the wake of the 2-bladed rotors recovers faster in that area. This becomes obvious especially when looking at rotor 3 that has the highest turbulent levels. The faster wake recovery rate was already observed in the kinetic energy analysis where the wake of the 2-bladed rotors especially for rotor 3, recovered faster than the wake formed behind the 3-bladed rotor. The higher turbulence levels can be beneficial in a wind farm arrangement as the wakes, especially at low distances of separation, recover faster, the turbine spacing can be reduced and thus, more wind turbines can be installed in a smaller area. This can reduce the total land rental fee costs and increase the wind farm energy yield per unit area of land. However, the fatigue loads on a turbine operating in the wake of a 2-bladed turbine are increased due to the higher turbulence level.

In order to examine how the turbulent energy differs across within swept area of the wind turbine and to investigate the asymmetry effects for the different rotors, the turbulence intensity was measured in full two-dimensional for the three rotors at a distance of 5D within a width range of -1.5z/R to 1.5z/R and a height range of -1.5y/R to 1.5y/R with an interval of 75mm along both directions. Figure 8 shows the contour plots for the turbulent intensity obtained from the x- and the z-direction. The 2-dimensional wakes confirm the observations made from the line wakes. It can be clearly seen, that the 2-bladed rotors (Figure 8b,c) have higher turbulent levels than the 3-bladed rotor (Figure 8a) and especially, the rotor 3 shows very high turbulence intensity (Figure 8c). The contour plots show clearly that the intensity peaks are at the edge of the rotors, which indicates that the largest turbulence is induced by the tip vortices. Consequently, the 2-bladed rotors generating stronger tip vortices than the 3-bladed rotors. Furthermore, the wakes of all three rotors are slightly shifted towards

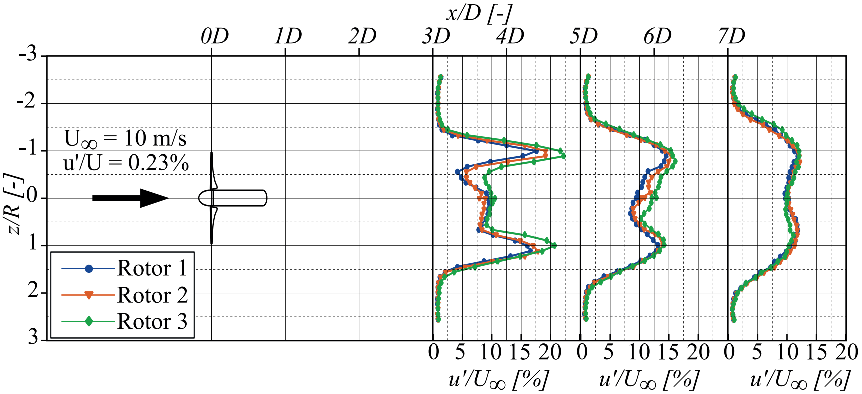

Figure 7: Wake turbulent energy obtained from 2 directional components for the three rotor concepts, at different downstream distances (3D, 5D and 7D) in the wind tunnel.

positive z-direction whereas this effect is more obvious for the 2-bladed turbines and especially rotor 3. In addition, the maxima of turbulent intensity for all three rotors occur at the rotor edge at the positive z- and negative y half. This is opposite to the asymmetry observed for the wake velocities where the highest deficit was at the negative z- and y-direction. Nevertheless, this asymmetry is expected to be caused by interferences of the wake with the turbine tower. The evaluation of the turbulence intensity in y- and z- direction reinforce the observations made from the turbulent intensity profiles at hub-height of the rotor and thus, the higher turbulence of the 2-bladed rotor concepts especially in the tip region.

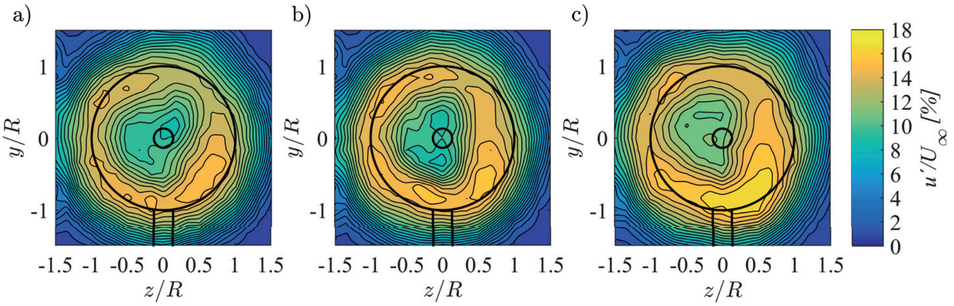

Figure 8: Contour plots for turbulent intensity obtained from 2 directional components, at downstream distance 5D (looking in flow direction): (a) rotor 1, (b) rotor 2 and (c) rotor 3.

4 Conclusions

The comparison between the wakes of one 3- bladed and two 2-bladed rotor concepts with similar maximum C_P values have been presented and discussed in this paper. The results show that the wakes formed behind rotors with different blade number are have minor distinctions and the thrust force acting on the rotors is similar for the optimal operation range of the rotors.

The velocity deficit in the wake formed behind the three different rotors is offers no major deviations between the tested rotors. Thus, from a power optimization point of view, the mean wake velocities provide only a minor potential for improvement. Consequently, it can be concluded that the number of blades is not influencing the velocity deficit in wake and thus, the potential inflow velocities of a downwind turbine strongly. Nevertheless, in future investigations it would be of interest to test turbines with rotors with varying blade number in an experiment with an aligned turbine array to confirm the observations made by investigating the wakes and if there is a possible potential for improvement by adjusting control strategies.

However, the turbulent intensities show higher variation for the 2-bladed rotors. Especially at the tip region, the turbulent intensities are higher, which is caused by the stronger tip vortices generated of the 2- bladed turbines. This higher turbulence levels in the wake support a higher wake recovery rate of the 2- bladed rotors when compared with the 3- bladed rotor, especially in closer distance behind the turbine. This faster wake recovery offers the potential for a narrower turbine spacing and thus a higher power density per unit land area in a wind farm plant. However, from a structural point of view, the downstream turbine operating in the wake of a 2-bladed turbine experiences higher turbulence levels, which could increase fatigue loads.

References

Adaramola, M. and Krogstad, P.-Å.: Experimental investigation of wake effects on wind turbine performance, Renewable Energy, 36, 2078–2086, doi:10.1016/j.renene.2011.01.024, 2011.

Duquette, M. M., Swanson, J., and Visser, K. D.: Solidity and Blade Number Effects on a Fixed Pitch, 50 W Horizontal Axis Wind Turbine, Wind Engineering, 27, 299–316, doi:10.1260/030952403322665271, 2003.

Hau, E.: Wind turbines: fundamentals, technologies, application, economics, Springer-Verlag Berlin Heidelberg, 3 edn., doi:10.1007/978-3-642-27151-9, 2013.

Jamieson, P.: Innovation in Wind Turbine Design, John Wiley & Sons, Ltd, doi:10.1002/9781119975441, 2011.

Krogstad, P. Å. and Lund, J.: An experimental and numerical study of the performance of a model turbine, Wind Energy, 15, 443–457, doi:10.1002/we.482, 2012.

McTavish, S., Feszty, D., and Nitzsche, F.: Evaluating Reynolds number effects in small-scale wind turbine experiments, Journal of Wind Engineering and Industrial Aerodynamics, 120, 81 – 90, doi:10.1016/j.jweia.2013.07.006, 2013.

Newbauer, S. and Kumpaty, S.: Computational Fluid Dynamics of Aerodynamic Effects for Optimum Number of Wind Turbine Blades, in: ASME 2012 International Mechanical Engineering Congress and Exposition, pp. 3123–3129, American Society of Mechanical Engineers, doi:10.1115/IMECE2012-85557, 2012.

Newman, A. J., Cal, R. B., and Castillo, L.: Blade number effects in a scaled down wind farm, Renewable Energy, 81, 472 – 481, doi:10.1016/j.renene.2015.03.013, 2015.

Pierella, F.: Experimental investigation of wind turbine wakes and their interaction, 2014.

Wilson, R. E., Lissaman, P. B., and Walker, S. N.: Aerodynamic performance of wind turbines, Oregon State University Corvallis, Oregon, 1976.

PAPER II

The effect of rotational direction on the wake of a wind turbine rotor – a comparison study of aligned co- and counter rotating turbine arrays

Franz Mühle[1], **Muyiwa S Adaramola**[1] **and Lars Sætran**[2]

[1] Faculty of Environmental Sciences and Natural Resource Management, Norwegian University of Life Science (NMBU), N-1433 Ås, Norway

[2] Department of Energy and Process Engineering, Norwegian University of Science and Technology (NTNU), N-7491 Trondheim, Norway

Corresponding Author: Franz Mühle (franz.muhle@nmbu.no)

Abstract. Various concepts have been investigated in wind turbine research to improve the productivity of wind farms. However, there are some strategies, which offer further potential for improvement. One of these concepts is the rotational direction of a wind turbine, which has influence on its wake characteristics and development. In this study the effect of rotor rotational direction of an upwind turbine on the performance of another wind turbine operating in its wake was investigated. Two model wind turbines with the same rotor diameter, in-line arrangement, are used for this study. The upstream wind turbine was operated either co-rotating or counter-rotating with respect to the downstream wind turbine and the distance between the turbines was varied between 2.0D and 5.15D (where D is the rotor diameter). The performance and wake measurements of the turbine arrays were investigated using both numerical and experimental approaches. By operating the upstream turbine in counter-rotating direction with respect to the downstream turbine, the combined productivity of the two turbines was found to have improved. This improvement is significant at 3.5D, where the productivity was observed to increase by 2.0%.

Nomenclature

C_P	power coefficient	L	lift force
C_T	thrust coefficient	D	drag force
D	turbine rotor diameter	R	resulting force
TSR	tip speed ratio	C_a	axial load coefficient
U_∞	inflow velocity	C_t	tangential load coefficient
ω	angular velocity of rotor	θ	twist angle
v_θ	extra angular velocity component	α	angle of attack
u	axial velocity	φ	flow angle
v	angular velocity		

1 Introduction

Due to increasing awareness of the environmental impacts of development and the utilization of fossil fuels and nuclear energy, use of renewable energy sources for electricity generation have significantly increased globally in recent years. Herein wind energy, with a huge global potential, is playing a major role. In the last few years, a considerable part of wind energy research have been focused on offshore wind energy resources assessment and development. The interest in offshore wind resource is due to relative better wind speed and more environmental friendly nature of wind turbine in the offshore region, when compared with onshore installations. One of the main factors affecting the overall productivity of a wind farm is the wind turbine wake. The characteristics and development of a wind turbine wake depends on factors such as the operating conditions of the turbine, freestream wind conditions and site topology. The goal of the wind turbine wake study is to improve the arrangement and overall performance of a wind farm. Barthelmie et al. (2009) investigated the performance of an offshore wind farm at different wind conditions. In their study, they showed that the performance between the first and second turbine row drops by about 37% at the worst case when the downstream turbine operates completely in the wake of the upstream turbine and the distance of separation between the turbines is 7D (where D is the rotor diameter). Sanderse (2009) and Vermeer, Sørensen, and Crespo (2003) reviewed research work in wind turbine wake aerodynamics. Their reviews show that different control mechanisms have been considered to optimize the operation of a wind farm. Nevertheless, there are still some concepts of wind turbine operating conditions, which have not been thoroughly investigated and that could offer further potential for the optimization of wind farms.

One of these concepts is the application of turbine rotors rotating in opposite directions. Due to the aerodynamics of the wind turbine blade, the wake of a wind turbine rotates in opposite direction as the wind turbine rotor. By operating the two or more wind turbines in counter-rotating direction in wind farm set-up, the wind turbine wakes could be affected and hence, leads to improved performance of the wind farm. However, little attention has been given to this topic. The literature provides a few articles about small wind turbines having two rotors, which are rotating in opposite directions. Shen, Zakkam, Sørensen, and Appa (2007) used DTUs EllipSys3D solver to investigate a wind turbine with such a rotor. They investigated power coefficient (C_P) and thrust coefficient (C_T) for different separation distances of the rotors. They stated that C_P is almost independent of separation distance. However, in their study distance between turbines was limited to 1D. This small distances of separation offers not enough information about the effect of counter rotating rotors in a wind farm application. The same applies for the more recent study by Santhana Kumar, Abraham, Joseph Bensingh, and Ilangovan (2013). They performed numerical and experimental investigations varying the distance of separation between 0.25D and 0.75D. They reported that the power increase of such a rotor is best at a separation of 0.65D. Two experimental studies investigating the effects of different rotational direction for a wind farm application were also conducted by Yuan et al. (2013, 2014). They investigated turbine arrays with co- and counter- rotating rotors to find effects of the turbine rotation on the wake. In their paper, they show that the rotation direction can have a positive influence on the aligned turbine arrangement and that the power output from the downstream turbine can be increased by up to 20% for very small distances of separation (0.7D) compared to the case where the rotors are co-rotating. However, in this study, small model wind turbines with a rotor diameter of 127 mm were used and thus, their Reynolds numbers at the blade chord are in the range of around 8000 which is very low when compared with commercial wind turbine Reynolds number. Thus, the performance of the turbine could be influenced by these low Reynolds numbers. Another possible shortcoming of their study is the low optimum tip speed ratio (TSR) of the model wind turbines used in their experiment, which is 3.7 and thus, smaller than TSR for commercial wind turbines, which is around 6. Nevertheless, the studies of Yuan et al. provides good insight into the effects of the rotational direction of wind turbine rotors and show that this concept could improve a wind farms power output. However, the counter- rotating turbine rotor concept may be limited to offshore applications, as the disturbing visual effects may obstacle their uses in onshore applications. Therefore, it can be beneficial for offshore wind farm arrays with small turbines' separation distance.

The aim of this present study is to investigate the effect of operating the upstream wind turbine in counter-rotating direction on the performance as well as wake characteristics of a wind farm, which comprises of a two wind turbine experimentally approach. Unlike previous similar studies, the wind turbines used in this study provide higher Reynolds numbers at the chord and an optimum TSR, which is similar to that of modern and commercial three-bladed wind turbine. Furthermore, a simple blade element momentum (BEM) code, taking also angular inflow velocities into account, was developed to investigate the flow around at the rotor blade. This code can be applied to evaluate the concept of counter rotating wind turbine rotors for wind farm efficiency improvement estimations.

2 Two dimensional blade aerodynamics

The rotational direction of the wake, that is the inflow for a downstream turbine, influences the performance and thus, the aerodynamics at the rotor blades of a downstream wind turbine. To understand the flow around the blade, due to a change of the rotational direction of an upwind rotor, two dimensional aerodynamics at blade element are a simple way to interpret the flow changes at the blade. The explanation in the following is based on Hansens Aerodynamics of Wind Turbines (Hansen, 2015).

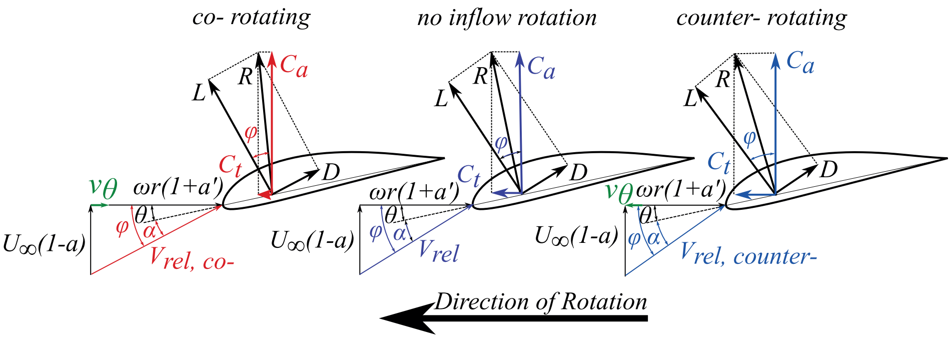

Figure 1: Velocities and resulting forces at the rotor plane for (a) co- rotating turbines with a positive angular velocity component in the inflow (b) no angular component in the inflow and (c) counter- rotating turbines with a negative angular velocity component in the inflow.

In Figure 1 the velocity triangles and resulting forces for the inflow of a downstream turbine operating in the wake of an upstream turbine of a co- and a counter-rotating turbine array as well as the case with no inflow rotation are depictured. These figures of the blade element show the changes for the three inflow conditions. For the co-rotating turbine array (Figure 1a), which is the usual case in wind farm applications, the angular component of the inflow adds to the angular component resulting from the rotor rotation. Whereas for the counter- rotating array (Figure 1c), the angular component is opposite to that of the rotor rotation. Accordingly the relative velocity for the co-rotating array is increased and the one for the counter- rotating array is decreased. On a first sight this might look as a degradation of the performance of the counter- rotating array, however the flow angle also and thus the angle of attack are changed, more precisely they decreases for the co- rotating and increases for the counter rotating array. Also the forces acting on the blade element are changing with a changing flow angle. Here the special interest is on the tangential load coefficient C_t, which determines the torque provided by each blade element and thus the power produced by the turbine. Looking at the tangential load coefficient for the three cases, it is obvious that the counter- rotating array has the highest C_t whereas the co- rotating array has the lowest C_t. This clarifies why a downstream rotor in a counter- rotating turbine array may have a better performance when compared with a downstream turbine in a co- rotating turbine array.

To get a better idea of the proportions of the changes in the flow angle and the relative velocity, a BEM analysis (see section 3.2), was performed. The flow angle φ, the relative velocity and the tangential load coefficient C_t. were determined for 20 blade elements along the span of a wind turbine rotor blade. In this analysis, the three inflow conditions, positive, negative and no wake rotation were investigated. The results of this analysis for the reference case (3.5D, TSR=4.5) are depictured in Figure 2.

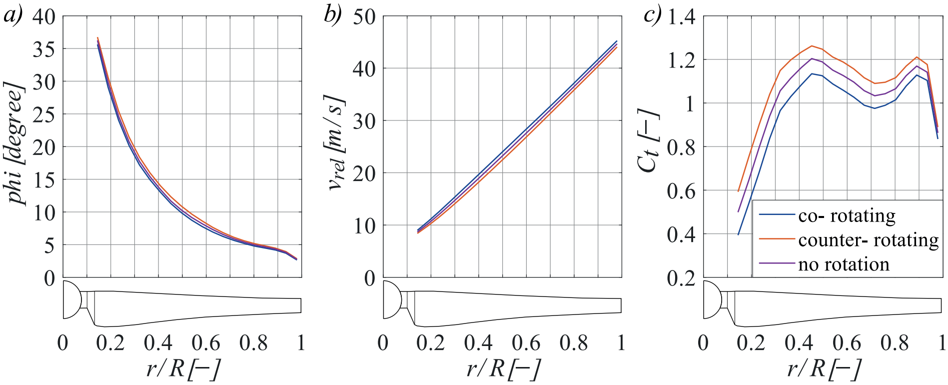

Figure 2: Calculated blade parameters from BEM simulation at a downstream distance of 3.5 D and TSR 4.5 (a) flow angle φ along the blade span (b) relative velocity along the blade span and (c) tangential load coefficient along the blade span.

In Figure 2a, the flow angle for the three investigated cases along the blade is shown, it can be seen that the differences for the three investigated cases are very small and mainly observable in the middle of the blade. As shown in Figure 1, the flow angle is largest for the counter- rotating case and smallest for the co- rotating case. When observing the relative velocities along the blade in Figure 2b, it can be seen that the alterations are small as well and that, as expected, the velocities for the co- rotating array are biggest and smallest for the counter- rotating array. Clearer differences can be observed in Figure 2c, where the tangential load coefficient is plotted along the blade span. Especially around the central part of the blade, the alterations are large where C_t for the counter- rotating array is bigger than C_t for the co-rotating array. This trend is the same along the blade span, whereas differences are decreasing towards the tip where they are only minor.

3 Methods

In this work study the influence of the rotational direction of an upwind turbine in a co- and a counter- rotating array, which consist of two turbines is investigated. Both experimental and numerical methods were used. For the numerical studies, a BEM code, taking the extra rotational velocity component into account, was developed. The possibility of working with both techniques allows a comparison of their results. Furthermore, the BEM code can be validated with experimental results, so it can be applied in later studies. In addition, using the BEM code, different blade parameters such as flow angle the relative velocity and C_t, which were discussed in section 2, can be calculated. Consequently these results are important to understand the flow conditions around the blade and to identify the changes for the different rotational directions of the upwind rotor.

3.1 Experimental setup

The experiments were conducted in the closed-return wind tunnel of the Department of Energy and Process Engineering at NTNU with a test section of 2.7 x 1.8 x 11.0 m. For the tests, the model turbines described in (Krogstad et al., 2015) were used where the rotors were changed for the upwind turbine to get a co- and a counter- rotating configuration. The turbine arrangement in the wind tunnel can be seen in Figure 3.

Figure 3: Turbine array with counter- rotating rotors in NTNUs wind tunnel at a separation distance of 3.5D

The wind tunnel was operated at low inlet turbulence intensity of 0.23% and the inlet velocity U_∞ was adjusted to 10.0 m/s at the position of the upwind turbine. The torque for both turbines was measured with a torque transducer placed inside of each turbine's hub. Line-wake velocity measurements were carried out at three different downstream distances of 2D, 3.5D and 5.15D at the wind turbine's hub-height using a 2-component Laser Doppler velocimetry (LDV) instrument. The wake measurements were performed when the upwind wind turbine was operated at its respective optimum tip speed ratio (TSR). A summary of the variables changed during the experiment and the measurands are given in Table 1.

Table 1: Variables and measurands in the experiment.

Separation distance	Rotational direction upwind	Rotational direction downwind	Measurands
2.00D	counter-clockwise	counter-clockwise	C_P
	clockwise	counter-clockwise	C_P, wake
3.50D	counter-clockwise	counter-clockwise	C_P
	clockwise	counter-clockwise	C_P, wake
5.15D	counter-clockwise	counter-clockwise	C_P
	clockwise	counter-clockwise	C_P, wake

The design of the rotors used in the study is based on the rotor developed at the Department of Energy and Process Engineering at NTNU Trondheim, which is described in detail in (Krogstad and Lund, 2012) and it is based on the NREL S826 airfoil. The two counter-clockwise rotating rotors are milled from an aluminum alloy and the rotor, rotating in clockwise direction was manufactured using a 3D printer based on the PolyJet technology. In a preliminary study, it was checked if this fabrication technique is suited to produce accurate blades that can be used in wind tunnel experiments and if the performance and wake characteristics are similar to the aluminum rotors. The results of this preliminary study showed that with the 3D printed and the aluminum rotors have similar performance and produce similar wakes.

3.2 Blade Element Momentum (BEM) code

To evaluate the rotational effect in the inflow of a wind turbine the classical BEM method described by Hansen (2015) was modified. Two main modifications were carried out. As the inflow velocity field for the downstream turbine is the flow field of the wake of an upstream turbine with different velocities in the rotor area, a single inflow velocity is not enough input information. To take all the velocities in the rotor area into account, each blade element is characterized by a separate inflow velocity established using wake measurement data. Furthermore, the additional angular component was simply added for the co- rotating case and, subtracted for the counter- rotating case, from the rotational velocity component generated from rotor rotation. With these two modifications, a ring velocity inflow representing both the axial and the angular velocity component was generated. As the classical method often struggles with convergence problems, the approach of Ning (2014) was implemented in the code. Applying this method and the two modifications, an efficient and reliable modified BEM code was developed, which is useful to analyze the effect of the rotational direction in the inflow of a wind turbine.

4 Results and discussion

4.1 Velocities in the wake

For the BEM code described in section 3, line wakes with the axial and angular component are needed as input information. Therefore, and also, to quantify the development of the wake, velocity measurements for these two velocity components were conducted at three distances behind the upwind turbine. In Figure 4, the angular velocity components resulting from the measurements are depicted.

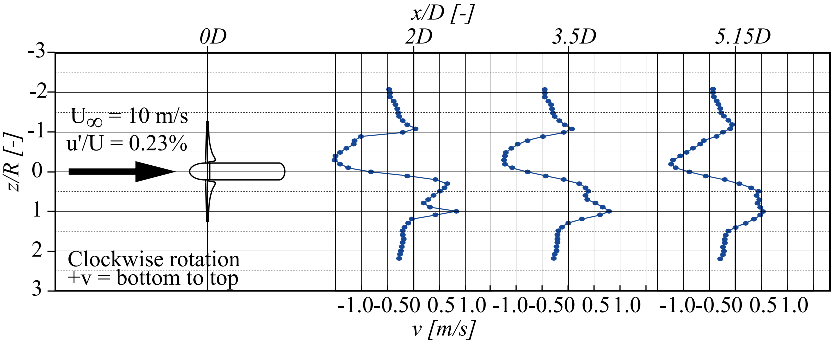

Figure 4: Angular velocity component (v), in the wake of a clockwise rotating turbine at three distances (2.0D, 3.5D and 5.15D).

Analyzing the wake development in Figure 4, it can be clearly seen that the angular velocity component decreases with increasing distance. This is due to turbulent mixing within the wake and it gives rise to the assumption that the effect of rotational direction of the upstream turbine decreases with increasing distance as well. Furthermore, it can be seen that the wakes are asymmetrical and the wake center is slightly shifted to the positive z-direction. This observation is due to interferences between the wake and the turbine tower. However, this effect is mirrored if the turbine rotor is rotating in the opposite direction.

The angular velocity components range between -1.5 m/s and 1.0 m/s at 2D. This corresponds to 15% and 10% of the inflow velocity, thus the angular component is decisive for the inflow and is expected to influence the performance of the rotor significantly. As the magnitudes of the angular velocity component decreases in axial direction, its significance decreases as well. Nevertheless, it is still corresponding to 13% and 5% of the inflow velocity at 5.15D. Consequently, the angular component is expected to have an influence on the turbine performance at all investigated downstream distances.

4.2 Performance of turbine arrays

For the performance study based on the power coefficient, the results of the experiments and the BEM calculations are depictured in Figure 5. For the BEM simulations, identical rotors were used for both the upwind and the downwind turbine. However, in the case of the experiments, the upwind turbine (T2) has a slightly different C_P curve when compared with the downwind turbine (T1) as can be seen in Figure 5a. Nevertheless, the C_P's for the two wind turbines used in the experiment are similar at their optimum power coefficients. The slight bump for the downwind rotor power curve at TSR = 5 is due to Reynolds number effect caused by blade imperfection, which is not occurred for the upwind rotor blades. To estimate the combined power coefficient (see Figure 5b-d) of the aligned two turbine array and two wind turbines operating in an undisturbed flow, the power coefficient of each wind turbine at each measurement point were added together. In the aligned operation of the turbines, the upwind turbine was always operated at its optimum TSR of 6 while the TSR of the downstream turbine was varied from TSR 1 until runaway TSR. Calculating the TSR for the downstream turbine also the inlet velocity of the upstream turbine ($U_\infty = 10.0$ m/s) was considered.

Examining the C_P curves from the experiments and the BEM calculations in Figure 5 the differences between the results of these two methods become clear. In all the cases presented, the power coefficient obtained by experiments is higher than that obtained through the BEM calculations. Nevertheless, the differences between the co- and the counter- rotating array show the same trends. The difference between the two methods were discussed in section 4.3. The purple C_P curves in Figure 5 represent the power coefficients of an imaginary turbine array in which both turbines operate in undisturbed flow conditions and the straight purple lines represents the C_P of the upwind turbine, which operates at a constant TSR and thus has a constant C_P for all investigated points. The diagrams for the three distances show that the combined power coefficient (that is power output) of the turbine array increases with

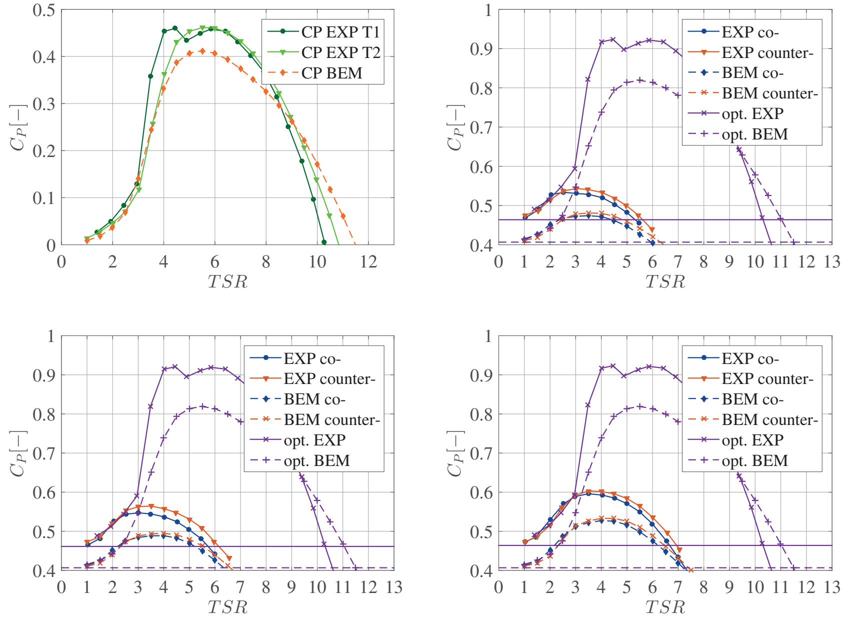

Figure 5: Performance plots for CP from experiments (solid lines) and CP from BEM calculations (dashed lines) for (a) independent operating rotors (b) turbine array at 2.0D (c) turbine array at 3.5D and (d) turbine array at 5.15D

increasing distance for both rotational directions. This is because the velocity deficit decreases due to turbulent mixing effect within the wake. For all three distances the counter-rotating turbine array has a better performance compared with the co- rotating array around the peak of the C_P curves. At 2D, the C_P of the counter rotating array at the maximum TSR of 3 is 1.2% higher than the co-rotating one. At 3.5D, where the biggest difference between the two rotational directions occur, the counter-rotating array has a 2.0% higher efficiency at TSR of 3.5 with respect to co-rotating. At 5.15D, the C_P of the co-rotating array is 0.6% smaller at TSR 4 in comparison with counter-rotating array. Overall, it can be concluded that the counter-rotating turbine array has better performance as the co- rotating turbine array at all investigated cases.

4.3 Differences between Experiments and BEM calculations

In general the results of the BEM calculations, at the optimum TSR range, are around 5-7% lower as those of the experiments. This difference may be due to blockage effects in the wind tunnel as the flow is shrouded and cannot expand freely as in an undisturbed environment. This problem could be solved by correcting the inflow velocity for a wind tunnel application. Irrespective of this shortcoming in the experimental results, the trends for different between the co- and counter-rotating array are the same for the methods.

5 Conclusion

The influence of the rotational direction of an upwind turbine in an aligned two turbine array has been presented and discussed in this paper. The findings from this study show that the rotational direction of an upwind turbine has an effect on the performance of a downstream turbine. In all cases investigated, the overall performance of the counter- rotating turbine array is better than those of the co-rotating turbine array. The observed increase in performance in the counter-rotating array is due to different direction of the angular component in the wake and an accompanying change of the angle of attack. As the angular velocity component in the wake decreases with increasing distance, the smallest impact of the investigated concept is observed at the largest distance considered. The results of developed BEM code for the study were in all cases, in the range of 5 to 7% lower than the experimental results but both methods show the same trends. The developed BEM code can be used to analyze effects of an angular component in the upwind turbine wake flow field

References

Barthelmie, R. J., Hansen, K., Frandsen, S. T., Rathmann, O., Schepers, J. G., Schlez, W., Phillips, J., Rados, K., Zervos, a., Politis, E. S., and Chaviaropoulos, P. K.: Modelling and measuring flow and wind turbine wakes in large wind farms offshore, Wind Energy, 12, 431–444, doi:10.1002/we.348, 2009.

Hansen, M. O.: Aerodynamics of wind turbines, Routledge, 2015.

Krogstad, P. Å. and Lund, J.: An experimental and numerical study of the performance of a model turbine, Wind Energy, 15, 443–457, doi:10.1002/we.482, 2012.

Krogstad, P.-Å., Sætran, L., and Adaramola, M. S.: “Blind Test 3” calculations of the performance and wake development behind two in-line and offset model wind turbines, Journal of Fluids and Structures, 52, 65–80, doi:10.1016/j.jfluidstructs.2014.10.002, 2015.

Ning, S. A.: A simple solution method for the blade element momentum equations with guaranteed convergence, Wind Energy, 17, 1327–1345, doi:10.1002/we.1636, 2014.

Sanderse, B.: Aerodynamics of Wind Turbine Wakes: Literature Review, vol. ECN-E–09-016 of *ECN.: E-series*, ECN Wind Energy, 2009.

Santhana Kumar, P., Abraham, A., Joseph Bensingh, R., and Ilangovan, S.: Computational and Experimental analysis of a Counter-Rotating Wind Turbine system, 72, 300–306, 2013.

Shen, W. Z., Zakkam, V. A. K., Sørensen, J. N., and Appa, K.: Analysis of Counter-Rotating Wind Turbines, Journal of Physics: Conference Series, 75, 012 003, doi: 10.1088/1742-6596/75/1/012003, 2007.

Vermeer, L. J., Sørensen, J. N., and Crespo, a.: Wind turbine wake aerodynamics, Progress in Aerospace Sciences, 39, 467–510, doi:10.1016/S0376-0421(03)00078-2, 2003.

Yuan, W., Ozbay, A., Tian, W., and Hu, H.: An experimental investigation on the effects of turbine rotation directions on the wake interference of wind turbines, in: 51st AIAA Aerospace Sciences Meeting including the New Horizons Forum and Aerospace Exposition, p. 607, doi:10.2514/6.2013-607, 2013.

Yuan, W., Tian, W., Ozbay, A., and Hu, H.: An experimental study on the effects of relative rotation direction on the wake interferences among tandem wind turbines, Science China Physics, Mechanics & Astronomy, 57, 935–949, doi:10.1007/s11433-014-5429-x, 2014.

PAPER III

An experimental study on the effect of winglets on the tip vortex interaction in the near wake of a model wind turbine

Franz Mühle[1], **Jan Bartl**[2], **Thomas H Hansen**[3], **Muyiwa S Adaramola**[1], **Lars Sætran**[2]

[1] Faculty of Environmental Sciences and Natural Resource Management, Norwegian University of Life Sciences, Ås, Norway

[2] Department of Energy and Process Engineering, Norwegian University of Science and Technology, Trondheim, Norway

[3] CMR Prototech, Bergen, Norway

Corresponding Author: Franz Mühle (franz.muhle@nmbu.no)

Abstract. An experimental study on the near wake up to four rotor diameters behind a model wind turbine rotor in two different wing tip configurations is performed. A straight-cut wing tip and a downstream-facing winglet shape are compared on the same rotor. The measurements are performed at the two-bladed rotors' design conditions at a tip speed ratio of $\lambda = 6$, using a setup of two cobra probes resolving all three components of the velocity vector in the wake. Phase-locked flow measurements synchronized with the rotor position at a high spatial and temporal resolution allow to compare the location and strength of the shed tip vortices for the two different rotor tip configurations.

The mean streamwise velocity is found not to be strongly affected by the presence of wing tip extensions, suggesting an insignificant effect of winglets on the inflow conditions of a possible downstream wind turbine. However, the winglets are seen to generate higher total kinetic energy peaks behind blade tips in the very near wake up to two rotor dimaters. Thereafter, an instability is observed leading to an earlier interaction of the tip vortices for the wingletted rotor compared to the reference rotor. The mutual vortex interaction causes the shear layer to broaden, which reflects in bimodal peaks in the turbulent stresses in this downstream region. In contradistinction, the tip vortices formed behind the reference rotor are assessed to be more stable and start merging into larger turbulent structures significantly further downstream.

1 Introduction

Winglets are small extensions at the tip of any kind of lift-generating wing of finite length. Best known from their widespread application in modern aviation, winglets are recognized to reduce induced drag in the tip regions of an aircraft's wings. Several studies confirmed a reduction in induced drag leading to a significant decrease in fuel consumption of modern transportation airplanes (e.g.(van Dam et al., 1981), (Eppler, 1997), (Faye et al., 2002)). The formation of a tip vortex occurs at any kind of wing tip shape of a loaded wing, due to a secondary flow around the tip of the wing's pressure to the suction side. The spanwise flow in the tip region reduces the local angle of attack and induces additional drag near the tip (Giuni and Green, 2013). Although winglets cannot suppress the formation of a tip vortex, they might be able to modifiy the strength and shape of the tip vortex. For an application of winglets on a wind turbine rotor, positive effects on the rotor's performance as well as the break up mechanisms of the tip vortices in the wake are desirable.

Most of the research related to the application of winglets on wind turbines focused on the optimization of an individual rotor's performance. Johansen and Sørensen (2006) designed six different winglet shapes for wind turbine rotors and simulated the flow around the blade tips. Their results confirmed that good winglet designs are able to improve a rotor's power coefficient by around 1.0%, but also can decrease its performance if poorly designed. In a follow up study, Johansen and Sørensen (2007) optimized the winglet's geometry parameters and found a rotor power increase of 2.6%. Another study by Gaunaa and Johansen (2007) showed a stronger positive effect on the power coefficient for downstream-facing winglets than for upstream-facing winglets. Experiments on a model-scale wind turbine of a rotor diameter of $D = 3.3$ m were performed by Maniaci and Maughmer (2012), who designed rather large downstrean-facing winglets with a height of 8% of the rotor radius. They measured an increase in power coefficent of 9% and thus confirmed the large influence of the winglet's height on the performance. The same rotor was also used by Gertz et al. (2012), who experimentally tested different winglet designs and found performance increases between 5% and 8%. An optimization algorithm was used by Hansen and Mühle (2018) to design the winglets for the model scale turbine, which is also investigated in the present study. Numerical predictions and a wind tunnel validation of the rotor performance found a power increase of 7.8% and 8.9%, respectively, compared to a non-wingletted reference rotor.

A smaller number of recent studies also focused on the wake flow behind a wingletted wind turbine, investigating which effect the tip extensions could have on a cluster of multiple turbines. A recent experiment by Ostovan and Uzol (2016) compared the performance of a two-turbine array with and without winglets attached to the blade tips of the upstream turbine ($D = 0.90$ m). They measured an increase of about 2.5% in the upstream turbine's power production. Although winglets attached to the upstream turbine caused a smaller energy production on an aligned downstream turbine, the combined efficiency of both turbines was still found to increase for the wingletted configuration. The focus was shifted on the very near wake behind the rotor in a follow-up study by Ostovan et al. (2017), in which they used Particle-Image-Velocimetry

(PIV) to measure the tip vortex strength in the near wake for a wingletted and a straight-cut blade tip configuration. It was shown that the core vorticity levels were significantly smaller for the winglet case, while the vortex core diameter was measured to be larger. The mixing layer thickness was observed to be higher for the winglet case. An analysis of the streamwise velocity showed a wider wake extension for the winglet case. Anther PIV study of the wake up to $x/D = 5$ behind a significantly smaller rotor of $D = 0.12$ m with and without winglets was conducted by Tobin et al. (2015). Their PIV study indicated an increased velocity deficit in the wake of the wingletted rotor. Although another turbine operated in the wake was found produce less power, the combined power of the two-turbine array could be increased by the use of winglets. Interestingly, their results furthermore indicated a similar level of tip vortex circulation for the wingletted and baseline rotor. Although both instantaneous and phase-averaged quantities were measured by Tobin et al. (2015), no deeper analysis on the effect of winglets on the break-up mechanisms of the tip vortices was presented.

The stability of the tip vortices in the wake of a wind turbine rotor is currently a widely discussed research topic (Sarmast et al., 2014; Sørensen, 2011). The vortices shed from the blade tips form a helical vortex system in the near-wake behind a rotor. At some point, the individual vortex spirals start to interact, break up and merge into turbulent structures. The vortex stability in the near wake determines the initial conditions for the far wake behind a wind turbine, which is again important to correctly predict wake-turbine interactions in wind farms. An experimental PIV study of the vortex interaction in the wake up to $x/D = 5$ behind a two-bladed model turbine of $D = 0.60$ m was performed by Lignarolo et al. (2014). Their results emphasized the importance of the wake instability caused by a pair-wise interaction of the tip vortices on the momentum deficit in the wake, which was shown to be strongly dependent on the turbine's tip speed ratio. An analysis of the development of the turbulent stresses in the wake demonstrated a strong influence of the vortex interaction on a more effective wake mixing after the location of the initial instability. A further experimental study on the transition from coherent to turbulent motions in the wake of a three-bladed model wind turbine was performed by Eriksen and Krogstad (2017). Using phase-averaging on the three-dimensional velocity vector acquired from hot-wire anemometry, they found that the wake is dominated by coherent motions up to $x/D = 1$ before the vortices start to interact. The mutual induction of two of the three tip vortices was observed to be finished by $x/D = 2$, merging into larger turbulent structures. By $x/D = 3$, the flow field was seen to be dominated by turbulent motions. Another extensive PIV study of the wake behind a small rotor of $D = 0.12$ m with straight wing tips was reported by Bastankhah and Porté-Agel (2017) for different turbine tip speed ratios. They found stronger and more stable tip vortices for the optimal tip speed ratio than for the significantly higher run-away tip speed ratio. Due the small size of the rotor with respect to turbulent length scales in the inflow, meandering motions of the wake were observed in this experiment, not making it possible to use phase-averaged wake properties to identify the locations of tip vortex break up.

The objective of the present study is to investigate in detail, how optimized winglets attached to the blade tips affect the interaction mechanisms of the tip vortices in the wake up to $x/D = 4$. For this purpose, highly resolved flow measurements are performed in the wake behind a two-bladed rotor with winglets and the same two-bladed rotor with straigt-cut blade tips. By an analysis of the phase-averaged quantities we investigate, if winglets enhance the break-up of the tip vortices and possibly promote the recovery process of the wake velocity deficit. A decomposition of the time-averaged turbulent stresses in the wake will furthermore describe, how the production of turbulence is modified by the presence of winglets on the blade tips.

2 Setup and methods

2.1 Model wind turbine rotor

As shown in Figure 1, a two-bladed rotor with a total diameter of $D = 0.90$ m with attachable blade tips is applied for the experiments. A custom designed airfoil *R-opt* is used along the entire blade span, while another optimized airfoil shape *W-opt* is used for the winglets (Hansen and Mühle, 2018). The blade tips are exchangeable through a seamless joint located 50 mm from the tip. Two sets of blade tips can be attached, the first of which is a straight-cut blade tip (reference configuration) with a tip chord length of $L_{c,tip} = 39.7$ mm. The second tip configuration is a downstream-facing winglet, the main geometry parameters of which are summarized in Table 1. The exact rotor and airfoil geometry as well as the design optimization is described in detail by Hansen

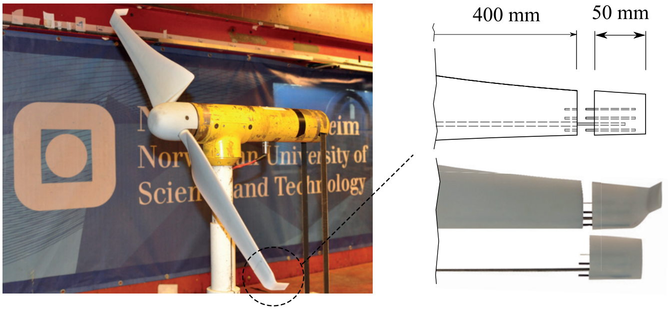

Figure 1: Rotor with exchangeable wingtips.

and Mühle (2018).

The operational characteristics of both rotor configurations are illustrated in Figure 2. Both rotor configurations have an optimum tip speed ratio around $\lambda = 6.0$, while the wingletted rotor produces significantly more power and experiences higher thrust forces at the design point. The reference rotor has a power coefficient of $C_{P,ref} = 0.468$, which rises to $C_{P,winglets} = 0.518$ for the wingletted tip configuration. Simultaneously, the rotor's thrust coefficient at $\lambda = 6.0$ increases from $C_{T,ref} = 0.870$ to $C_{T,winglets} = 0.980$, when winglets are attached to the blade tips. These values might appear very high compared to full-scale wind turbines, which is mainly due to a rather high blockage by the wind tunnel boundaries. The rotor swept area blocks about 12.8% of the wind tunnel's cross-sectional area, which affects the flow expansion around the rotor. The measured power and thrust coefficients have been corrected by Hansen and Mühle (2018), applying a blockage correction suggested by Sarlak et al. (2016). The tip speed ratio is fixed to $\lambda = 6.0$ during the entire experiment for both configurations.

2.2 Wind tunnel and measurement grid

The experiments are performed in the closed-loop wind tunnel at the Norwegian University of Science and Technology (NTNU) in Trondheim, Norway. It has a cross-section of 2.71 m (width) × 1.81 m (height) and measures 11.0 m in length. The inflow is spatially uniform and features a turbulence intensity of $TI = 0.23\%$ for an inflow velocity of $U_\infty = 10.0$ m/s, which is chosen for all presented measurements.

The wake flow is measured at 18 streamwise measurement locations ranging from $x/D = 0.1$ to $x/D = 4.0$ in the wake downstream of both rotor configurations as shown in Figure 3. At each of those locations, a horizontal line at the turbine's hub height is measured from $z/D = 0$ to $z/D = 0.85$. A total of 76 measurement points is scanned

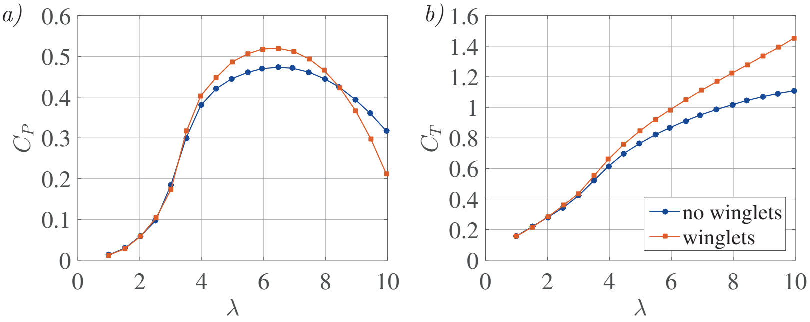

Figure 2: Power coefficient C_P (a) and thrust coefficient C_T (b) of the non-wingletted reference rotor (blue) and wingletted rotor (red).

Table 1: Winglet design variables.

Parameters	Value	Reference
Span	10.76%	Rotor span
Sweep	17.86°	-
AoA	-1.17°	-
Radius	3.09%	Rotor span
Root chord	58%	Rotor tip chord
Tip chord	88%	Winglet root chord

in lateral direction with a varying spatial resolution in the different regions of the wake. In the region around the path of the tip vortex, from $z/D = 0.45$ to $z/D = 0.75$, a very high spatial resolution of Δz=5 mm is scanned.

2.3 Flow measurement techniques

For the measurement of the wake flow, two Cobra probes of the type *Series 100* manufactured by TFI (Turbulent Flow Instrumentation) are applied. A Cobra probe is a four-hole pressure probe, which is able to resolve all three components of the velocity vector. In the presented set of experiments, two Cobra probes are used simultaneously in a parallel setup, significantly reducing the measurement time. Four individual pressure transducers are installed inside the probe, which are pre-calibrated by the manufacturer. Detailed information of the calibration process and the transformation from the pressures to the velocities is provided by Shepherd (1981). A major experimental challenge Cobra probe measurements is a perfectly horizontal installation of the probes in the wind tunnel. This is achieved by an additional validation of the flow velocities measured in the empty wind tunnel by a simultaneous measurement with a two-component Laser-Doppler Anemometer (LDA) at the same location. Thus, the inclination of the Cobra probes can be manually adjusted until both velocity components feature the smallest deviations.

The probe is usually able to resolve high frequencies over 2000 Hz, making it possible to also measure time-varying turbulent velocity components (Hooper and Musgrove, 1997). In this experiment, over-sampling is applied to reach a time-resolution of 10000 Hz, which is necessary to also extract phase-averaged turbulent quantities from the flow. The over-sampled time series are adequately filtered for noise during the post-processing of the data. The Cobra probe allows to synchronize the flow measurement with the rotor position, which is employed for the measurement of phase-averaged data in the rotor wake. Each measurement point was sampled for $t = 40$ s, which covers approximately 5000 full rotations of the rotor and therefore is considered to be sufficiently long for

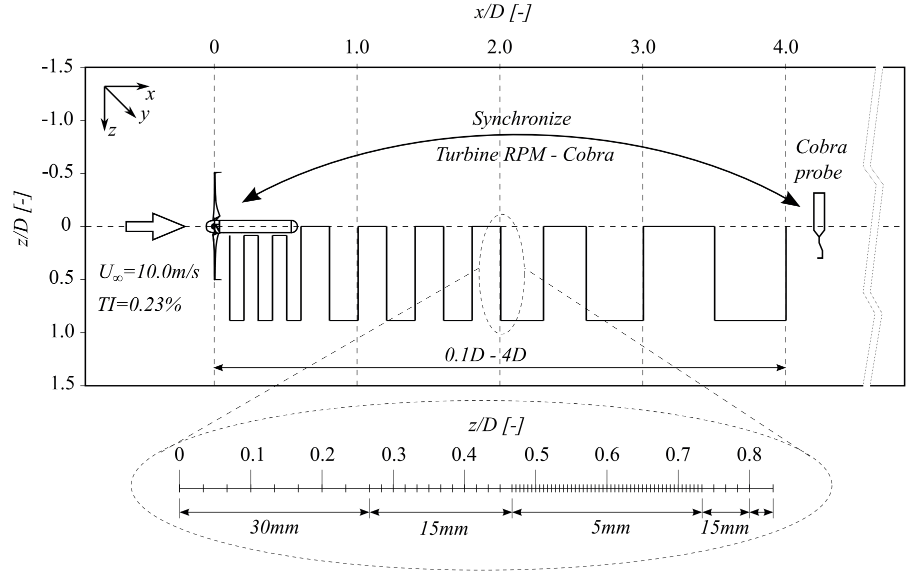

Figure 3: Top view of the experimental setup, reference coordinate system and measurement grid in the wake behind the rotor. The single measurement locations in the zoomed area are representative for all 18 line measurements in the wake.

the extraction of phase averaged data. Four voltage signals corresponding to pressures are acquired from the Cobra probe, which then are evaluated by a MATLAB routine resorting to the calibration tables provided by the manufacturer. Velocity time-series of all three components are obtained after calibration, which are then used to calculate time-averaged velocity components, flow angles and the turbulent normal and shear stress components.

For the calculation of the phase-averaged quantities in the wake, one full rotor revolution is divided in 120 sectors, each of which covers a sector size of 3°. This sector size was previously successfully applied by Eriksen and Krogstad (2017) for a phase-averaged evaluation of the tip vortices behind another rotor of the same diameter.

The Cobra probe is able to measure flow angles up to $\theta = 45°$. Therefore, all measurement samples, in which one of the flow angles is $\theta > 45°$ are excluded from the analysis. The percentages of dismissed data points at the different downstream measurement locations in the wake are listed for both rotor configurations in Table 2. Flow angles $\theta > 45°$ are specifically observed in the very near wake up to $x/D = 1.0$ in the tip vortex region, with a significantly higher percentage for phase-averaged data.

Table 2: Percentages of dismissed data samples due to flow angles $\theta > 45°$ for all downstream measurement locations x/D = 0.1 - 4.0. Four cases are distinguished: time-average vs. phase-averaged flow measurements, as well as the non wingletted reference case (**no WL**) and the wingletted rotor configuration (**WL**).

Dist.	time-averaged		phase-averaged		Dist.	time-averaged		phase-averaged	
x/D	no WL	WL	no WL	WL	x/D	no WL	WL	no WL	WL
0.1	16%	24%	53%	52%	1.4	3%	5%	5%	8%
0.2	11%	26%	51%	54%	1.6	2%	3%	5%	6%
0.3	9%	17%	50%	30%	1.8	1%	3%	3%	6%
0.4	9%	15%	50%	61%	2.0	$< 1\%$	$< 1\%$	2%	3%
0.5	10%	14%	25%	50%	2.3	$< 1\%$	$< 1\%$	2%	2%
0.6	10%	15%	15%	43%	2.6	$< 1\%$	$< 1\%$	2%	2%
0.8	8%	14%	15%	37%	3.0	$< 1\%$	$< 1\%$	1%	2%
1.0	7%	14%	8%	40%	3.5	$< 1\%$	$< 1\%$	3%	1%
1.2	6%	8%	10%	23%	4.0	$< 1\%$	$< 1\%$	3%	4%

2.4 Measurement uncertainty

The measurement uncertainty of the mean velocity components is obtained for every measurement point by the means of a combination of precision error and systematic error as proposed by Wheeler and Ganji (2004). For this purpose, a systematic error for the Cobra probe of ±1.9% (1.2% calibration plus 1.5% pressure measurement) is taken into account (Shepherd, 1981). The maximum total error in the mean streamwise flow component was obtained at $x/D = 0.1$, amounting 4.5% of the absolute velocity values. Further downstream, the total error was found to be between 1% and 2%, with slightly higher values in the tip vortex region. The uncertainty in the turbulent quantities measured in the wake is calculated according to the procedures proposed by Benedict and Gould (1996). The uncertainties in the turbulent stresses are found to be higher than the mean flow components, typically ranging between 5% and 8%.

3 Results

3.1 Mean streamwise velocity

The near wake behind the model wind turbine is scanned in the xz-plane, acquiring all three components of the velocity vector. The time-averaged mean streamwise velocity field in the wake $\overline{U_x}/U_\infty$ behind the two rotors is compared in Figure 4 (a) and (b). The red lines in both plots mark the wake boundaries defined as locations, where $\overline{U_x} = U_\infty = 10$ m/s. Dashed vertical lines indicate the downstream measurement locations, while all other values are interpolated. The wake velocity deficit is assessed to have a very similar magnitude for both configurations. The lateral wake extension, however, is seen to be slightly wider for the wingletted configuration. This is illustrated in Figure 4 (c), showing the mean velocity difference of (a)-(b). The red area behind the rotor tip indicates higher velocities for the reference configuration in this area. This is mainly due to a generally wider wake behind the wingletted rotor. For the downstream distances x/D = 2.0 - 3.0, however, an additional red area is detected further inside. This is due to a local enlargement of the shear layer for the wingletted configuration in this region, as will be explained in more detail in the following sections. Furthermore, a slight increase in mean velocity is observed for the wingletted configuration in the light blue area at the downstream distances x/D = 3.5 and 4.0 and spanwise positions z/D = 0.5 - 0.6. The difference in lateral wake extension is additionally analyzed by the means of a flow visualization around the tip regions as shown in Figure 5. For this purpose, smoke is injected into the flow upstream of the blade tip, which is illuminated by a stroboscopic light synchronized with the turbine RPM, visualizing the formation of the tip vortices downstream of the rotor for both tip configurations. It can be observed that the winglet in Figure 5 (b) is slightly bent outwards due to the centrifugal forces acting on it. The vortex formation is therefore assumed to take place at a location slightly further outside, explaining the wider wake for the wingletted configuration. Apart from this slight spanwise dislocation of the vortex formation, the street of tip vortices shead in both tip configurations seem very similar in the visualized near wake up to x/D = 1.3. This observation is supported by an analysis of the available power of an imaginary downstream rotor. By integrating the velocity profiles at the different downstream distances x/D over an circular cross-section of $r = 0.5D$, significantly less power is available for the wingletted configuration for x/D = 0.5 - 3.5 as shown in Figure 6. This corresponds well with the higher energy extraction of the wingletted rotor as previously shown in Figure 2. At a downstream distance of x/D = 4.0, however, the available power in the wake of the wingletted rotor is measured to surpass the kinetic power contained in the wake of the reference rotor. For a better understanding of these effects, the total kinetic energy contained in the shed tip vortices is analyzed in more detail.

3.2 Total kinetic energy

The total kinetic energy is the sum of the energy contained in the periodic motions of tip vortices and the random turbulent fluctuations $k_{total} = \frac{1}{2}(\overline{\tilde{u}_i\tilde{u}_i}+\overline{u_i u_i})$. The contours of the total kinetic energy in the wake flow are compared for both tip configurations in Figure 7.

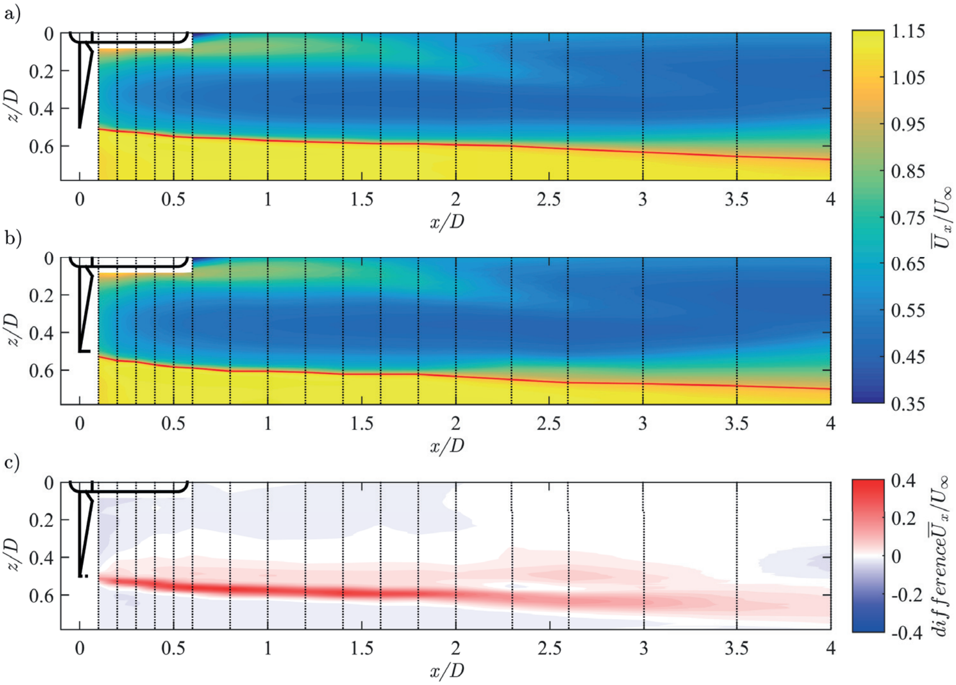

Figure 4: Normalized streamwise velocity (a) rotor without winglets, (b) rotor with winglets and (c) difference between the two rotor concepts (rotor with winglets - rotor without winglets).

The total kinetic energy is assessed to be strongest in a small region behind the blade tips in both cases. Directly downstream of the rotor, the tip vortices have not yet interacted and therefore form a path of concentrated kinetic energy up to about $x/D = 2.0$ in both cases. Further peaks in total kinetic energy are observed behind the blade roots and in the wake of the turbine nacelle. The kinetic energy in these relatively small regions is, however, seen to quickly decay and the energy levels are small compared to the tip vortex shear layers in the outer part of the wake.

The initial width of the tip vortex paths is measured to be similar for both tip configurations, expanding over $\Delta z/D \approx 0.06$ corresponding to an approximated vortex diameter of about $d \approx 0.05$ m. The white lines in Figure 7 (a) and (b) indicate locations, at which the mean streamwise velocity is equal to the incoming reference velocity $U_\infty = 10.0$ m/s. For both tip configurations, these locations correspond well with the tip vortex paths. The tip vortex trajectories create a shear layer between the freestream and the wake flow.

At a downstream distance between $x/D = 2.0$ - 3.0 some deviations are detected

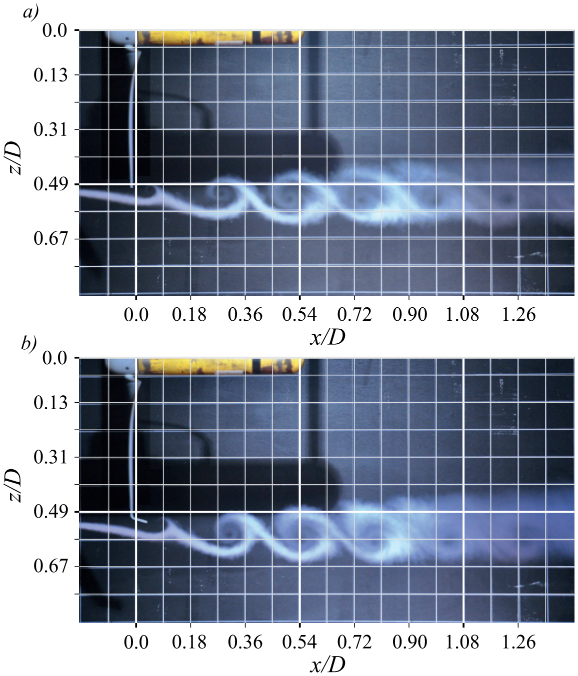

Figure 5: Tip vortex (a) rotor without winglets and (b) rotor with winglets.

in the width of the shear layer between the two cases. The shear layer is seen to be significantly broader for the wingletted configuration as depicted in Figure 7 (b). The peak levels of total kinetic energy between $x/D = 0.3$ - 2.0 are assessed to be of comparable magnitude for both cases. A slightly higher total kinetic energy measured for the wingletted configuration indicates an insignificantly stronger tip vortex in this case. As previously observed in the evaluation of the mean streamwise velocity, the wake seems to be slightly broader for the wingletted case, which is confirmed by a slight lateral offset in z-direction of the kinetic energy peaks.

At the downstream distances $x/D = 2.3$ and 2.6, however, the total kinetic energy peak shape significantly deviates. While the total kinetic energy seems to be concentrated in a smooth Gaussian peak for the non-wingletted reference case, a significantly broader double peak develops for the wingletted configuration at these two downstream distances. The peak levels are seen to be smaller for the winglet case, while the energy seems to be distributed in a broader peak. At even higher downstream distances $x/D = 3.0$ - 4.0, the two peaks melt into a single peak again, showing a very similar distribution as measured for the reference case again. The levels of total kinetic energy, are measured to be comparable for the both configurations at these higher downstream distances.

For a better understanding of the underlying mechanisms, the streamwise development of the three normal stresses $\overline{u_x u_x}$, $\overline{u_y u_y}$ and $\overline{u_z u_z}$ is further analyzed in Figure 8. Note that the scale changes between the single measurement stations. Directly behind the rotor at $x/D = 0.6$, the normal stresses are concentrated to a narrow region around $z/D = 0.50$ and $z/D = 0.55$ for the wingletted configuration, respectively. Up to a downstream distance of about $x/D = 1.0$, the vertical normal stress $\overline{u_y u_y}$ is dominant, featuring about twice the magnitude of the streamwise stress $\overline{u_x u_x}$. For both tip configurations, the spanwise normal stress $\overline{u_z u_z}$ initially has the lowest magnitude, reaching a similar magnitude as the streamwise stress at $x/D = 1.0$. The bimodal peak in the streamwise stress $\overline{u_x u_x}$ is assessed to merge into a single peak at about $x/D = 1.6$ for both configurations, while its magnitude is gradually adjusting to that of $\overline{u_y u_y}$.

As observed in the analysis of the total kinetic energy already, significant deviations between the two rotor tip configurations are taking place around $x/D = 2.3$ - 2.6. While the peaks of the reference configuration approximately keep their width compared to $x/D = 2.0$, the all three peaks of the wingletted configuration become significantly broader at $x/D = 2.3$. A bimodal peak for the vertical and spanwise normal stresses $\overline{u_y u_y}$ and $\overline{u_z u_z}$ is found, while the streamwise stress $\overline{u_x u_x}$ continues to feature one distinct peak only. The bimodal peak shape is due to the two tip vortices interacting in this region, as an analysis of the phase-averaged quantities in the next chapter will reveal. At the same time, the vortex centers are slightly displaced in spanwise direction. The bimodal peak is then merging into a single peak at $x/D = 3.0$ - 4.0 again, while the peaks for all three components are seen to be broader than for the reference configuration. In this region the vortices begin to break up into turbulence as will be explained in the next chapter. In the wake behind non-wingletted reference rotor, no mutual interaction of the tip vortices is detected in the region between $x/D = 2.3$ - 2.6,

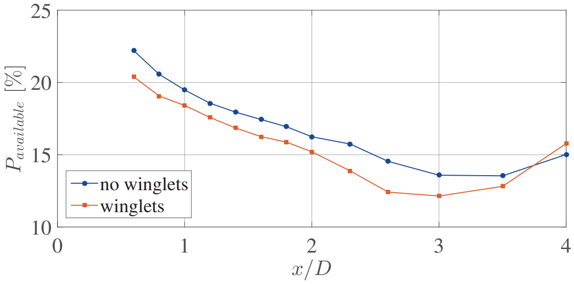

Figure 6: Available power for an imaginary downstream rotor in the wake in percent of total available energy.

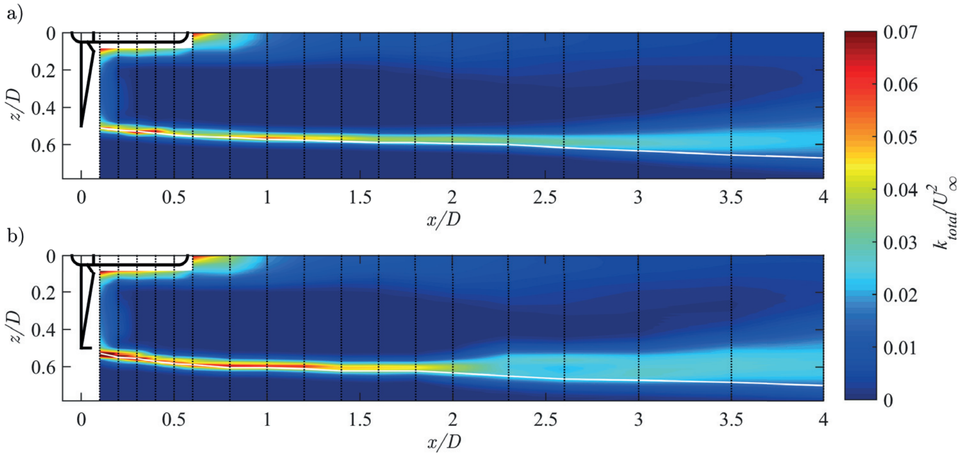

Figure 7: Total kinetic energy (a) rotor without winglets and (b) rotor with winglets.

while the kinetic energy is gradually transferred from the vertical stress $\overline{u_y u_y}$ to the streamwise $\overline{u_x u_x}$ and spanwise stresses $\overline{u_z u_z}$.
For both rotor configurations, the vertical stresses $\overline{u_y u_y}$ dominate the tip region of the wake up until $x/D = 2.6$. At $x/D = 3.0$ already, the streamwise stresses $\overline{u_x u_x}$ contain just as much energy as the vertical ones. At $x/D = 4.0$ the streamwise and spanwise stresses $\overline{u_x u_x}$ and $\overline{u_z u_z}$ are very similar, while the earlier dominating vertical stresses contain less energy. From $x/D = 4.0$ the shear layer seems to be dominated by diffusive mechanisms for both blade tip configurations. The total kinetic energy is not observed to be isotropically distributed at any downstream location in the wake.

Similarly, increased shear stresses are found in the shear layer generated by the path of the tip vortices (Figure 9). These shear stresses $\overline{u_i u_j}$ play a dominant role in the production of the turbulent kinetic energy as they are directly coupled to the production terms $(\partial u_i/\partial x_j + \partial u_j/\partial x_i)$ of the Reynolds averaged Navier Stokes equations.
In the near wake up to $x/D = 1.6$ the $\overline{u_x u_z}$ term is the dominating shear stress in the shear layer for both rotor tip configurations. The same spanwise displacement as for the normal stresses is assessed for the wingletted configuration. The first significant differences between the two configurations can be detected at $x/D = 2.0$. Both $\overline{u_x u_y}$ and $\overline{u_x u_z}$ have a purely positive contribution for the wingletted case, while both shear stresses feature a change of sign from negative to positive around the vortex core for the straight wing tip configuration. The interaction of two tip vortices behind the winglet blade tip is again detected in a bimodal peak of the $\overline{u_x u_y}$ term at $x/D = 2.3$, which then transforms into a bimodal negative peak of the $\overline{u_x u_z}$ term at $x/D = 2.6$.

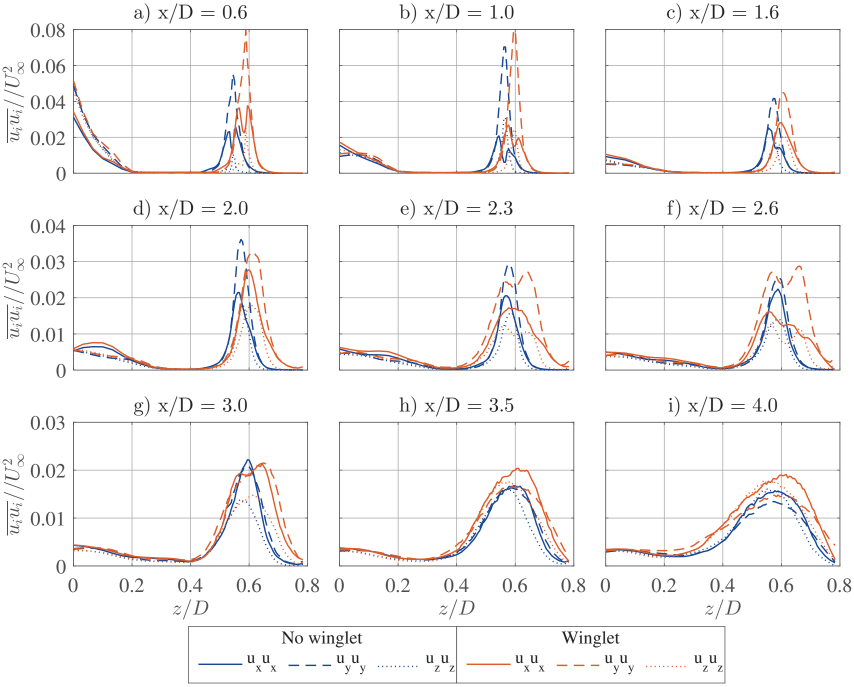

Figure 8: Horizontal profiles of the normal stresses $\overline{u_i u_i}/U_\infty^2$ at selected downstream distances x/D for a non-wingletted and wingletted configuration. Note that the scale of the normal stress range changes.

The vortex interaction behind the wingletted rotor seems to be completed at $x/D = 3.0$, while the strong vortex cores behind the straight wing tip simply seem to have decayed at this downstream distance. In both cases, the shear layer is now dominated by the $\overline{u_x u_y}$ stress, while the other shear stresses are seen to flatten out. The shear layers are observed to broaden out at $x/D = 4.0$ as previously seen for the normal stresses.

3.3 Phase-averaged kinetic energy

Up until now, we have discussed time-averaged quantities allowing to describe the mean flow conditions. As the sampling of the wake flow was synchronized with the rotor position, conditional averaging allows us to assign the measured values to a rotor phase. Thus, we can identify the turbulent kinetic energy and vorticity contained in the individual vortical structures at the different downstream locations for both rotor configurations.

At first, the phase-averaged turbulent kinetic energy in the wake behind the two rotor configurations is compared in Figure 10 for $x/D = 1.0$ - 2.3 and Figure 11 for $x/D = 2.6$ -

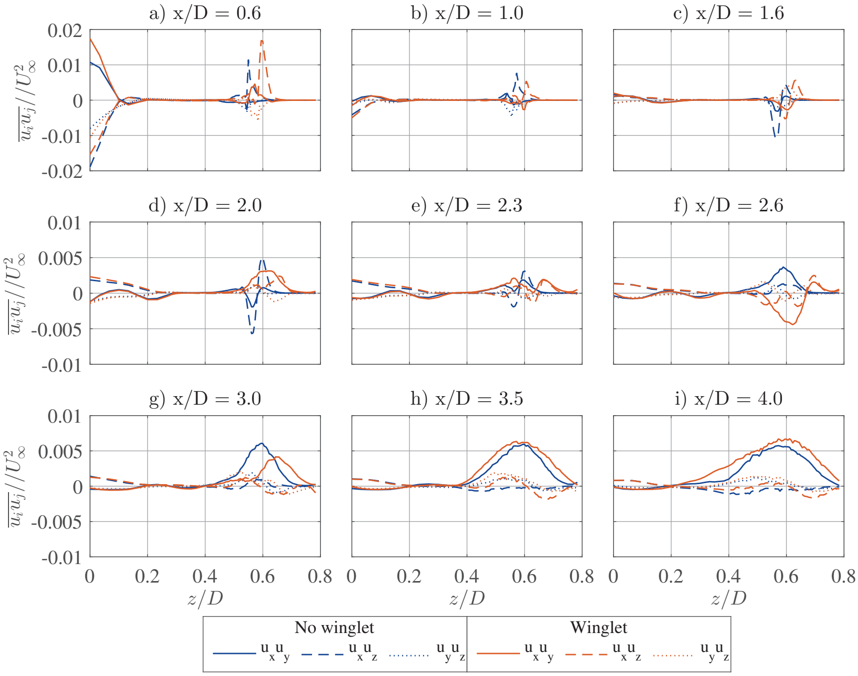

Figure 9: Horizontal profiles of the shear stresses $\overline{u_i u_j}/U_\infty^2$ at selected downstream distances x/D for a non-wingletted and wingletted configuration. Note that the scale of the shear stress range changes.

4.0, respectively. In case of the non-wingletted reference configuration, as depicted in the upper row, the vortex cores are gradually moving outwards to higher z/D with increasing downstream distance x/D. A similar trend is observed for the wingletted configuration depicted in the lower rows of Figures 10 and 11. At about $x/D = 1.6$, the vortices behind the wingletted rotor are assessed to grow significantly stronger than the vortices behind the non-wingletted reference rotor. Between $x/D = 2.0$ and $x/D = 2.3$ the two tip vortices start interacting behind the wingletted rotor configuration, while no interaction is seen for the vortices behind the non-wingletted rotor. At $x/D = 2.6$ the one of the two vortex cores behind the wingletted configuration is seen to transport significantly less turbulent kinetic energy than the other vortex core. The weaker vortex is deflected inwards and wrapped around the stronger vortex core. At $x/D = 3.0$, no explicit vortex cores can be detected anymore, while the turbulent kinetic energy is more evenly distributed over the whole range of rotor positions. In contrast to that, the vortex cores behind the non-wingletted reference rotor are not seen to significantly interact for the measured range of downstream distances up to $x/D = 4.0$. In the

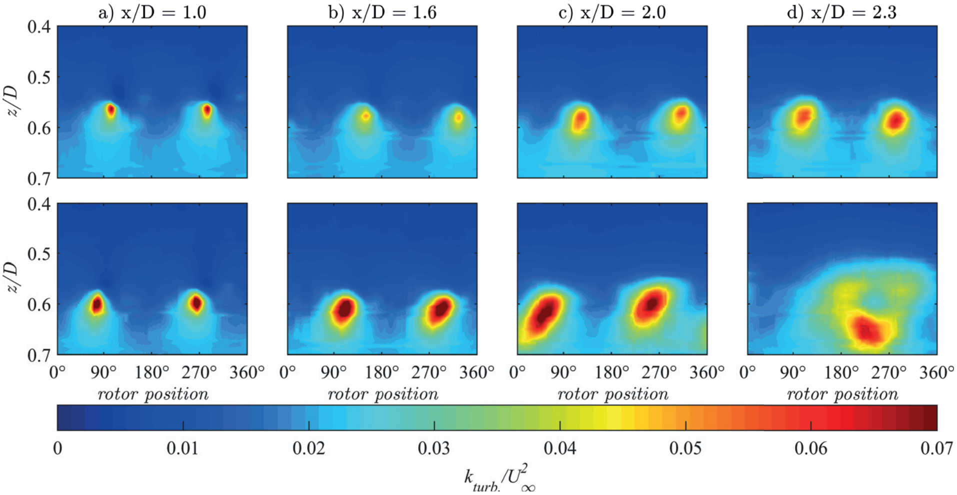

Figure 10: Phase-averaged turbulent kinetic energy k_{turb}/U_∞^2 at (a) $x/D = 1.0$, (b) $x/D = 1.6$, (c) $x/D = 2.0$ and (d) $x/D = 2.3$ for all rotor positions $0° - 360°$. Upper row: No-winglet reference case. Lower row: Winglet case.

interesting part of downstream range between $x/D = 2.0$ and $x/D = 3.0$ the vortex cores are seen to stably keep their position, while the transported turbulent kinetic energy is gradually decaying without any detectable vortex interaction. At $x/D = 4.0$, the turbulent kinetic energy is evenly distributed for both rotor tip configurations. In both cases, the energy contained in the periodic motions has at this point almost completely transferred to fully developed turbulent motions.

3.4 Phase-averaged vorticity

The interaction of the tip vortices behind the different rotor configurations is further investigated by an analysis of the phase-averaged out-of-plane vorticity component $\langle\omega_y\rangle = \langle\partial u_x/\partial z - \partial u_z/\partial x\rangle$. Since the vortices are travelling downstream in the shear layer, the streamwise convective velocity U_{conv} has to be subtracted to calculated the local vorticity. Thus, the time derivatives can be transformed to spatial derivatives using Taylor's frozen equilibrium approximation $\Delta x \approx U_{conv}\Delta\tau$. Therein, U_{conv} is approximated from the local mean velocity at the inner border of the shear layer.
The results of the phase-averaged vorticity $\langle\omega_y\rangle$ approximations downstream of the two rotor configurations are compared in Figure 12 for $x/D = 1.0$ - 2.3 and Figure 13 for $x/D = 2.6$ - 4.0, respectively. The blue arrows indicated the approximated velocity vectors in the xz-plane, while the colour scale visualizes the strength of the out-of-plane vorticity. Note that the colour scale changes from Figure 12 to Figure 13.

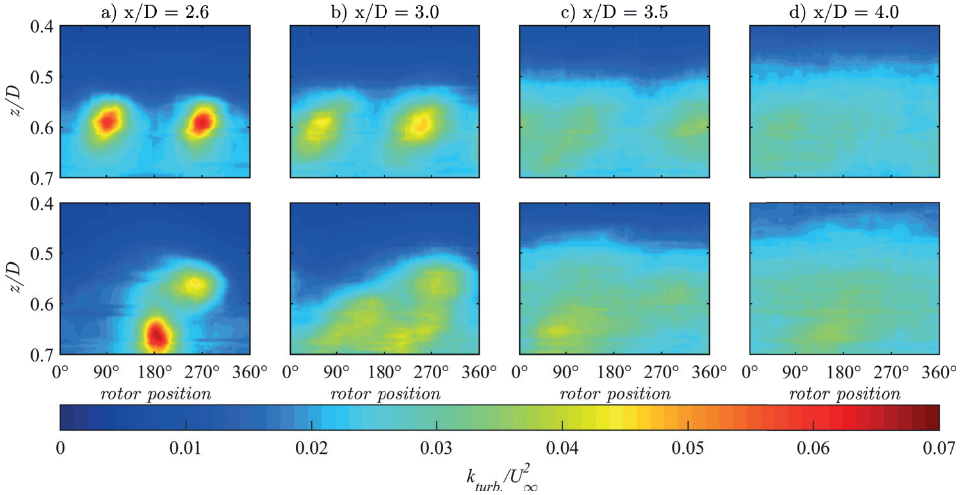

Figure 11: Phase-averaged turbulent kinetic energy k_{turb}/U_∞^2 at (a) $x/D = 2.6$, (b) $x/D = 3.0$, (c) $x/D = 3.5$ and (d) $x/D = 4.0$ for all rotor positions $0° - 360°$. Upper row: No-winglet reference case. Lower row: Winglet case.

Apart from the previously discussed lateral offset of the tip vortices in the wingletted case, the development of the vorticity $\langle \omega_y \rangle$ up to $x/D = 1.0$ is observed to be very similar for both rotor configurations. However, it has to be kept in mind that a significant portion of the data in the wake up to $x/D = 1.0$ has been filtered out due to flow angles $\theta > 45°$. From $x/D = 1.6$ and further downstream, the acquired data are almost complete and deemed to give a very reliable vorticity approximation. A significant difference in the vorticity between the two configurations is detected at $x/D = 2.0$. The vortices behind the wingletted rotor are seen to be diagonally spread along $x = z$, while the vortices behind the reference rotor still feature a circular shape with higher core vorticity levels. At $x/D = 2.3$ only one defined vortex core is detected for the wingletted configuration. The second vortex is seen to strongly interact with the first vortex at $x/D = 2.6$, riding on top of each other before finally merging into a single structure at $x/D = 3.0$. In contrast to that, evenly spaced vortex cores are still detected for the reference configuration at $x/D = 2.6$ and 3.0. A slight interaction of two significantly weaker and more spread out vortices is suspected to happen at $x/D = 3.5$ for the reference configuration, while the largest portion of the vorticity has already decayed. At $x/D = 4.0$ the phase-averaged vorticity $\langle \omega_y \rangle$ is assessed to be evenly distributed over the entire range of rotor positions for both investigated blade tip configurations, indicating a complete merging of the tip vortices in the shear layer.

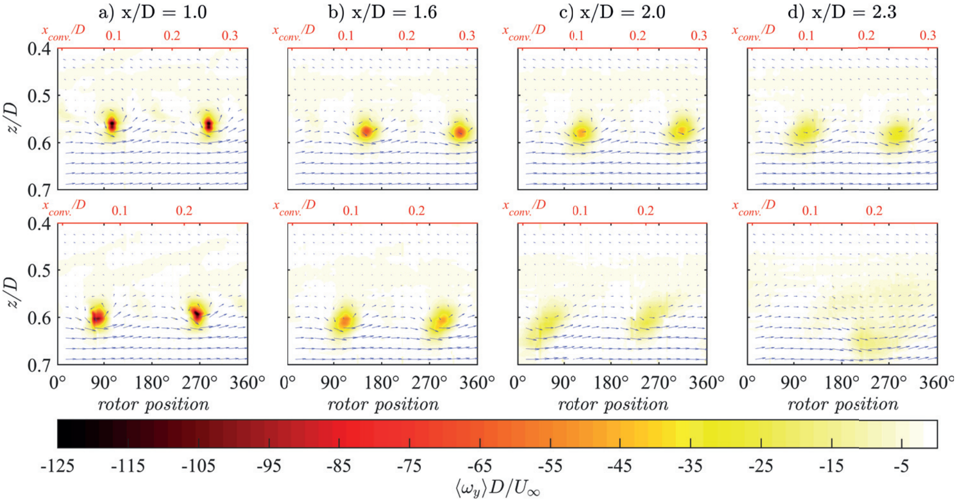

Figure 12: Normalized phase-averaged out-of-plane vorticity $\langle\omega_y\rangle D/U_\infty$ at (a) $x/D = 1.0$, (b) $x/D = 1.6$, (c) $x/D = 2.0$ and (d) $x/D = 2.3$ for all rotor positions $0° - 360°$. Upper row: No-winglet reference case. Lower row: Winglet case.

4 Discussion

The results of the study revealed a number of significant differences in the vorticity and transport of turbulent kinetic energy in the wake for the two different blade tip configurations. A previous investigation on the same rotor configurations by Hansen and Mühle (2018) disclosed significant differences of the flow in the tip region on the blade's suction side. In this region, the winglet forced the flow to be more parallel in chordwise direction on the suction side of the blade, reducing the amount of spanwise flow as observed for the non-wingletted reference case. Thus, the induced drag could be reduced by the winglets, leading to an increased power extraction and a higher thrust coefficient of the wingletted rotor at the same tip speed ratio.

The measurement of the wake flow was assessed to be restricted due to very high flow angles in the tip vortex region up to a downstream distance of about $x/D = 1.0$. As the cobra probe's operating range is limited to flow angles up to $\theta \leq 45°$, this resulted in a considerable reduction of the evaluated data in the tip vortex region up to $x/D = 1.0$. The reduced data might not depict the real vortices as the high flow angles are not resolved. For downstream distances $x/D > 1.0$, however, the major part of the acquired data is deemed to be reliable.

The time-averaged mean streamwise flow was generally seen to be very similar for both blade tip configurations, with the only significant difference being a wider initial wake extension after the wingletted rotor. This finding agrees well with observations by

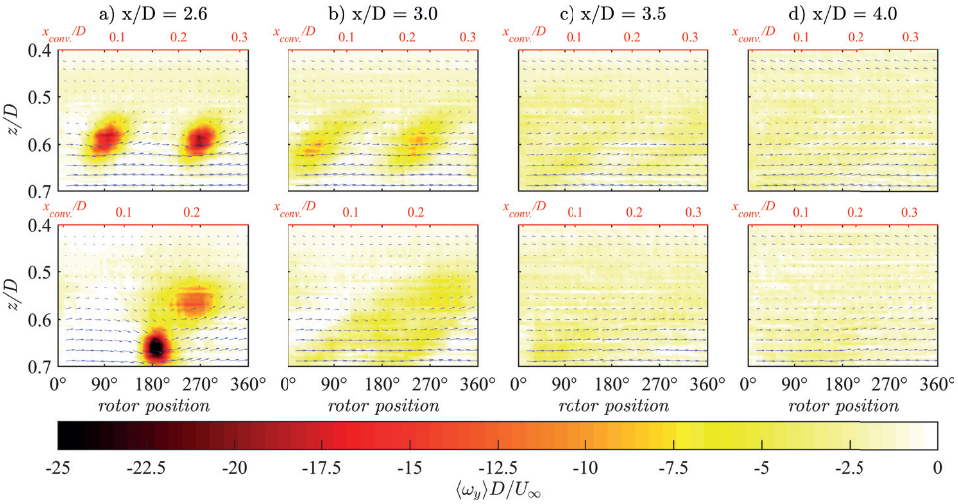

Figure 13: Normalized phase-averaged out-of-plane vorticity $\langle\omega_y\rangle D/U_\infty$ at (a) $x/D = 2.6$, (b) $x/D = 3.0$, (c) $x/D = 3.5$ and (d) $x/D = 4.0$ for all rotor positions $0° - 360°$. Upper row: No-winglet reference case. Lower row: Winglet case.

Ostovan et al. (2017), who also measured a wider wake extension and thicker mixing layer behind a three-bladed wingletted rotor. A closer look into the turbulent quantities in the wake revealed significant differences between the two investigated configurations. An evaluation of the normal and shear stresses showed a strong deviation between the two blade tip configurations of these quantities for the downstream distances x/D = 2.3 - 2.6. A detailed investigation of the phase-averaged turbulent kinetic energy k_{turb}/U_∞^2 as well as the out-of-plane vorticity $\langle\omega_y\rangle D/U_\infty$ indicated a strong interaction of the tip vortices behind the wingletted rotor tip configuration and, as a consequence, a shear layer enlargement within this downstream range. Simultaneously, the tip vortices measured behind the non-wingletted reference configuration stably kept their position without interacting. An interaction of the significantly weaker vortices was suspected around $x/D = 3.5$ for the straight cut wingtip. At $x/D = 4.0$, the turbulent kinetic energy and vorticity distributions were observed to be very similar for both configurations again. At this downstream distance, the tip vortices have almost completely broken up into purely turbulent motions for both rotor configurations, indicated by an evenly spread vorticity over the entire measurement window.

The peak levels of the time-averaged total kinetic energy measured in the wake behind both rotors are compared in Figure 14 for all downstream distances x/D = 1.0 - 4-0. The peak levels are assessed to be higher for the winglet case for all downstream distances up to $x/D = 2.0$, due to a stronger loading of the wingletted rotor in the tip region. At $x/D = 2.3$ and 2.6, the kinetic energy peak levels behind the winglet tips are lower, as the vortical structures were observed to interact in this downstream region. From about $x/D = 3.0$ the levels of peak kinetic energy was assessed to be very similar for both tip configurations, being more and more dominated by purely turbulent motions.

The decay of the total kinetic energy is furthermore compared to two reference data

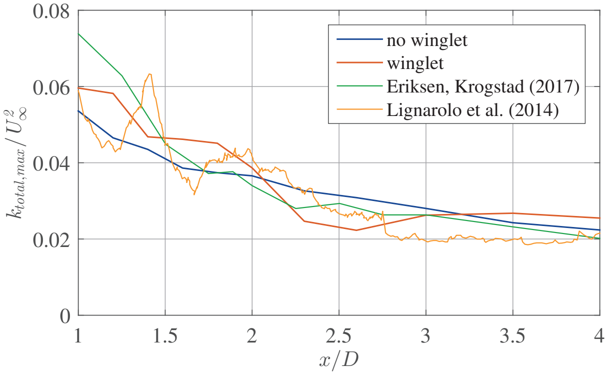

Figure 14: Streamwise decay of time-averaged total kinetic energy levels $k_{total,max}/U_\infty^2$ for the two blade tip configurations. Reference data measured behind a three-bladed non-wingletted rotor by Eriksen and Krogstad (2017) and a two-bladed rotor by Lignarolo et al. (2014).

sets measured downstream of two non-wingletted rotors by Eriksen and Krogstad (2017) and Lignarolo et al. (2014) in Figure 14. It is observed, that the decay of the time-averaged total kinetic energy in the two presented cases is generally comparable to both reference data sets. A slightly higher initial $k_{total,max}$ at $x/D = 1.0$ measured by Eriksen and Krogstad (2017) can be explained by an additional tip vortex shed off their three-bladed rotor, which is operated at the same tip speed ratio $\lambda = 6.0$. The peak total kinetic energy derived from PIV measurements by Lignarolo et al. (2014) behind a two-bladed rotor operated at $\lambda = 6.0$ is also seen to decay similarly to our data. Both reference rotors are designed with straight cut-off blade tips featuring a comparable tip chord length as our rotor. Lignarolo's two-bladed rotor has a tip chord length of $L_{c,tip} = 44$ mm, while Eriksen and Krogstad's rotor have three blades with a tip chord length of $L_{c,tip} = 26$ mm. The main parameters defining the rotor tip design, inflow conditions and downstream location of vortex interaction are compared in Table 3.

Table 3: Comparison of rotor tip design, inflow parameters and location of vortex interaction with reference studies by Eriksen and Krogstad (2017) and Lignarolo et al. (2014).

	Rotor diameter [m]	No. of blades N_B	Tip airfoil	Tip chord length [mm]	Rotor C_T [-]	Inflow TI [%]	Vortex interaction [x/D]
Mühle et al. Reference	0.90	2	R-opt	39.7	0.87	0.23	≈ 3.5
Mühle et al. Winglets	0.90	2	W-opt	20.2	0.98	0.23	2.3-2.6
Eriksen and Krogstad	0.90	3	S826	26	0.89	0.24	1.75-2.5
Lignarolo et al.	0.60	2	E387	44	0.88	0.50	1.5

A comparison of the streamwise development of the peak vorticity levels $\langle\omega_y\rangle N_B D/U_\infty$ extracted from the stronger of the two vortex cores is presented in Figure 15. Herein, N_B denotes the number of blades on the rotor and D the rotor diameter.

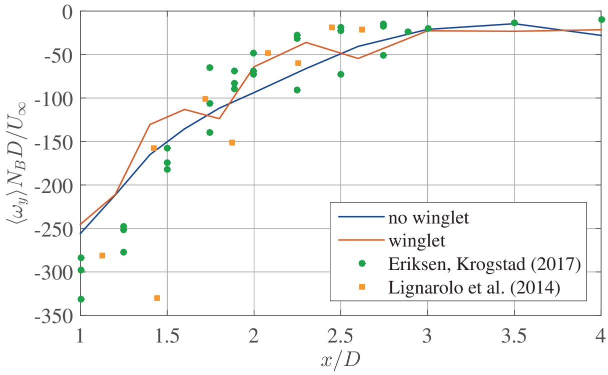

Figure 15: Comparison of the streamwise development of peak vorticity levels $\langle\omega_y\rangle N_B D/U_\infty$ for the two blade tip configurations. Peak vorticity levels are extracted from the vortex center of the stronger of the two vortices. Reference data of the three individual vortices behind a three-bladed non-wingletted rotor by Eriksen and Krogstad (2017) and the two individual vortices behind a two-bladed rotor by Lignarolo et al. (2014).

The absolute value of the peak vorticity is assessed to be higher for the non-wingletted reference configuration up to a downstream distance of approximately $x/D = 2.6$, while very similar vorticity levels are measured for $x/D = 2.6$ - 4.0. This is in agreement with results from Ostovan et al. (2017), who measured larger, but weaker vortices in the very near wake behind a wingletted blade tip. The lower absolute vorticity levels measured at x/D = 2.0 - 2.6 behind the winglet rotor, can be explained by the mutual induction of the two tip vortices observed in this downstream region. The reference data set by Eriksen and Krogstad (2017) marked with the green dots in Figure 15 initially shows significantly higher absolute vorticity levels extracted from the three individual vortex cores. The three vortices were seen to interact in a downstream region between x/D = 1.75 - 2.5, which is significantly further upstream than for both configuration of the two-bladed rotor used in this study. As the tip speed ratio of $\lambda = 6.0$, thrust coefficient $C_T = 0.89$ and the inflow turbulence level $TI = 0.23\%$ are similar in both studies, the obvious differences in the number of blades N_B is deemed to be the main reason for the different vortex strengths and interaction locations. As three vortices are shed in Eriksen and Krogstad's experiment instead of two in the present study over a very similar convective length, the spacing between the individual vortices is about 1.5 time tighter behind the three-bladed rotor, leading to an earlier vortex interaction. Considerably higher initial absolute vorticity levels have also been extracted from the vortex cores in the PIV experiment by Lignarolo et al. (2014) as indicated by the orange dots in Figure 15. As in the present study, Lignarolo et al. (2014) used a two-bladed rotor operated at a similar thrust coefficient $C_T = 0.88$ and tip speed ratio $\lambda = 6.0$. At this tip speed ratio, the maximum vortex interaction was already detected at $x/D = 1.5$. Their straight cut blade tips with a chord length of $L_{c,tip} = 44$ mm were only insignificantly longer than for the rotor used in the present study ($L_{c,tip} = 39.7$ mm). The main reason for a much earlier tip vortex interaction in Lignarolo's experiment is therefore deemed to be the increased level in inflow turbulence intensity $TI_{Inflow,Delft} = 0.50\%$ compared to $TI_{Inflow,Trondheim} = 0.23\%$ in the present experiment. The higher inflow turbulence is deemed to trigger an instability earlier, which causes the tip vortices to interact at a lower downstream distance.

5 Conclusions

An experimental study on the effect of winglets on the vortex interaction in the wake of a model wind turbine was presented. The mean streamwise velocity in the wake up to $x/D = 4$ was found not to be significantly affected by the presence of the winglets, suggesting a minor effect of blade tip extensions on the combined efficiency of a wind farm. The downstream-facing winglets created a slightly wider wake compared to a non-wingletted reference rotor with otherwise similar mean velocity. An investigation of the total kinetic energy, comprising the energy of a coherent and a turbulent motion, revealed slightly higher initial energy peaks in the tip region, when winglets were attached to the rotor tips. For a downstream range between $x/D \approx 2.0$ - 3.0 the shear layer behind the tip region was observed to be significantly broader for the wingletted configuration, indicated by bimodal peaks in two of the normal stresses at $x/D = 2.3$ and 2.6. An analysis of phase-averaged out-of-plane vorticity component indicated an instability in this downstream region, causing the tip vortices to interact before breaking around $x/D = 3.0$. In contrast to that, no interaction of the tip vortices behind the straight-cut reference tips were detected before $x/D = 3.5$, where the two significantly weaker tip vortices started to merge. A discussion of these results with existing studies on vortex interactions in a wind turbine wake disclosed the sensitivity of tip vortex stability to a number of different parameters. While this study emphasized the effect of modifications in the blade tip geometry, also the number of blades, tip speed ratio, rotor loading and turbulence characteristics in the inflow were seen to govern the tip vortex interaction behaviour in the wake.

References

Bastankhah, M. and Porté-Agel, F.: Wind tunnel study of the wind turbine interaction with a boundary-layer flow: Upwind region, turbine performance, and wake region., Physics of Fluids, 29, 065 105, doi:10.1063/1.4984078, 2017.

Benedict, L. and Gould, R.: Towards better uncertainty estimates for turbulence statistics, Experiments in Fluids, 22, 129–136, doi:10.1007/s003480050030, 1996.

Eppler, R.: Induced drag and winglets, Aerospace Science and Technology, 1, 3 – 15, doi:10.1016/S1270-9638(97)90019-5, 1997.

Eriksen, P.-E. and Krogstad, P.-Å.: Development of coherent motion in the wake of a model wind turbine, Renewable Energy, 108, 449–460, doi:10.1016/j.renene.2017.02.031, 2017.

Faye, R., Laprete, R., and Winter, M.: Blended Winglets for improved airplane performance, Aero magazine, 17, 16–31, 2002.

Gaunaa, M. and Johansen, J.: Determination of the Maximum Aerodynamic Efficiency of Wind Turbine Rotors with Winglets, Journal of Physics: Conference Series, 75, 012 006, doi:10.1088/1742-6596/75/1/012006, 2007.

Gertz, D., Johnson, D. A., and Swytink-Binnema, N.: An Evaluation Testbed for Wind Turbine Blade Tip Designs—Winglet Results, Wind Engineering, 36, 389–410, 2012.

Giuni, M. and Green, R. B.: Vortex formation on squared and rounded tip, Aerospace Science and Technology, 29, 191–199, doi:10.1016/j.ast.2013.03.004, 2013.

Hansen, T. H. and Mühle, F.: Winglet optimization for a model-scale wind turbine, Wind Energy, doi:10.1002/we.2183, 2018.

Hooper, J. and Musgrove, A.: Reynolds stress, mean velocity, and dynamic static pressure measurement by a four-hole pressure probe, Experimental Thermal and Fluid Science, 15, 375 – 383, doi:10.1016/S0894-1777(97)00005-8, 1997.

Johansen, J. and Sørensen, N. N.: Aerodynamic investigation of winglets on wind turbine blades using CFD, Denmark. Forskningscenter Risoe. Risoe-R, no. 1543(EN), iSSN 0106-2840, 2006.

Johansen, J. and Sørensen, N. N.: Numerical analysis of winglets on wind turbine blades using CFD, in: European Wind Energy Congress, Citeseer, 2007.

Lignarolo, L., Ragni, D., Krishnaswami, C., Chen, Q., Simao Ferreira, C., and van Bussel, G.: Experimental analysis of the wake of a horizontal-axis wind-turbine model, Renewable Energy, 70, 31–46, doi:10.1016/j.renene.2014.01.020, 2014.

Maniaci, D. and Maughmer, M.: Winglet design for wind turbines using a free-wake vortex analysis method, in: 50th AIAA Aerospace Sciences Meeting including the New Horizons Forum and Aerospace Exposition, p. 1158, doi:10.2514/6.2012-1158, 2012.

Ostovan, Y. and Uzol, O.: Experimental Study on the Effects of Winglets on the Performance of Two Interacting Horizontal Axis Model Wind Turbines, Journal of Physics: Conference Series, 753, 022 015, 2016.

Ostovan, Y., Akpolat, M., and Uzol, O.: Experimental Investigation of the Effects of Winglets on the Tip Vortex Behavior of a Model Horizontal Axis Wind Turbine using Particle Image Velocimetry, Journal of Solar Energy Engineering, in review, 2017.

Sarlak, H., Nishino, T., Martinez-Tossas, L. A., Meneveau, C., and Sørensen, J. N.: Assessment of blockage effects on the wake characteristics and power of wind turbines, Renewable Energy, 93, 340–352, doi:10.1016/j.renene.2016.01.101, 2016.

Sarmast, S., Dadfar, R., Mikkelsen, R. F., Schlatter, P., Ivanell, S., Sørensen, J. N., and Henningson, D. S.: Mutual inductance instability of the tip vortices behind a wind turbine, Journal of Fluid Mechanics, 755, 705–731, doi:10.1017/jfm.2014.326, 2014.

Shepherd, I. C.: A four hole pressure probe for fluid flow measurements in three dimensions, Journal of Fluids Engineering, 103, 590–594, doi:10.1115/1.3241774, 1981.

Sørensen, J. N.: Instability of helical tip vortices in rotor wakes, Journal of Fluid Mechanics, 682, 1–4, 2011.

Tobin, N., Hamed, A. M., and Chamorro, L. P.: An Experimental Study on the Effects ofWinglets on the Wake and Performance of a ModelWind Turbine, Energies, 8, 11 955–11 972, doi:doi:10.3390/en81011955, 2015.

van Dam, C. P., Holmes, B. J., and Pitts, C.: Effect of Winglets on Performance and Handling Qualities of General Aviation Aircraft, Journal of Aircraft, 18, 587–591, doi:10.2514/3.57531, 1981.

Wheeler, A. J. and Ganji, A. R.: Introduction to engineering experimentation, Upper Saddle River, NJ, USA, Pearson/Prentice Hall, XI, third edition edn., 2004.

PAPER IV

Winglet Optimisation for a Model-Scale Wind Turbine

Thomas H. Hansen[1] **and Franz Mühle**[2]

[1] Norwegian University of Science and Technology, NTNU Trondheim, Norway
and CMR Prototech, Bergen, Norway
[2] Norwegian University of Life Science, NMBU Ås, Norway

Corresponding Author: Thomas H. Hansen (thomas.hansen@ntnu.no)

Abstract. A winglet optimisation method is developed, and tested for a model-scale wind turbine. The best performing winglet shape is obtained by constructing a Kriging surrogate model which is refined using an infill criterion based on expected improvement. The turbine performance is simulated by solving the incompressible Navier-Stokes equations and the turbulent flow is predicted using the Spalart Allmaras turbulence model. To validate the simulated performance, experiments are performed in the NTNU wind tunnel. According to the simulations, the optimised winglet increases the turbine power and thrust by 7.8% and 6.3%. The wind tunnel experiments show that the turbine power and thrust increases by 8.9% and 7.4%. When introducing more turbulence in the wind tunnel to reduce laminar separation, the turbine power and thrust due to the winglet increases by 10.3% and 14.9%.

1 Introduction

To improve the performance, most modern transport and glider aircraft are built with winglets. When correctly designed, winglets create a flow-field that reduces the amount of span-wise flow in the tip region of the wing, and increases the wing's efficiency without increasing the span. For modern transport aircraft, winglets are known to reduce the block fuel consumption by 4-5%, and also moderate the noise levels at take-off (Freitag and Schulze, 2009). On span regulated gliders, the increase in performance due to winglets often surpasses the percentage score difference between the top 6 positions in a cross-country competition (Maughmer, 2003). Since the wind industry traditionally has been less concerned with span limitations, wind turbines do not normally use winglets. However, if future turbines are to be located in urban areas, or to reduce the size of floating structures, rotor span might become an important factor. This is recognised by the research community where winglets for wind turbines are given more attention. Since the flow in the tip region of the rotor blades is linked to the wake, winglets are often designed numerically using vortex lattice methods (VLM) with free wake, or with free-wake lifting line algorithms (FWLL). In Maniaci and Maughmer (2012) a winglet for a model-scale turbine is designed using a free-wake VLM code by varying the winglet shape using parameter studies. VLM calculations predict an increase in turbine power of more than 10%, and when the winglet is tested experimentally the test results showed a peak gain of 9.1%, however, this only occurs in a narrow range of conditions. In a wider applicable range, the best increase in power is about 4%. A winglet for a MW-class wind turbine is designed in Gaunaa and Johansen (2007) by optimising the circulation on the rotor using a FWLL method and a gradient algorithm. According to the FWLL calculations, the winglet increases the turbine power by 2.5%. When the winglet is analysed using the more realistic Computational Fluid Dynamics (CFD) code EllipSys3D, the increase in turbine power is reduced to 1.7%. The studies show that functional winglets for wind turbines can be designed using computational inexpensive numerical tools and simple design methods. However, in order to study the possible benefits of using winglets on wind turbines in more detail, numerical tools that predict the flow physics better and optimisation techniques that search for the global best solution should be used to design the winglet.

In this work, a winglet optimisation method for wind turbine application is developed. The tool is tested for a model-scale wind turbine. The best performing winglet shape is found by constructing a Kriging surrogate model, which is refined using an infill criterion based on expected improvement. The turbine performance is simulated by solving the incompressible Reynolds-Averaged-Navier-Stokes (RANS) equations. For the winglet optimisation, the turbulent flow is predicted using the Spalart Allmaras turbulence model, while an Elliptic Blending Reynolds-Stress model is used to analyse the design. To validate the simulated rotor performance, experiments are performed in the NTNU wind tunnel. The main purpose for the work is to develop a tool that automatically designs the best possible winglet shape when solving the computational expensive RANS equations. The work is also performed to design a test turbine for future winglet studies, and to investigate the performance and limitations of the Kriging surrogate model. To develop the wind tunnel test turbine, a new model-scale rotor geometry and new airfoils for the rotor blade and winglet are created.

2 Method

In the following, the approach used to develop the winglet optimisation tool is explained. First, the methods used to design the model-scale rotor blade and airfoils are given. Then, the surrogate model is introduced and the reasons for applying a Kriging model in combination with the expected improvement infill criterion are discussed. Finally, the CFD simulations and wind tunnel experiments are presented. In Figure 1, the optimisation method is illustrated. As can be seen, the best performing winglet shape is found by constructing and refining a Kriging surrogate model in a two stage approach. To create the initial samples, a Design of Experiment (DoE) is created using a Latin Hypercube (LHC) sampling plan. The infill points that maximise the expected improvement are obtained by optimising the Kriging model using a hybrid genetic-gradient algorithm.

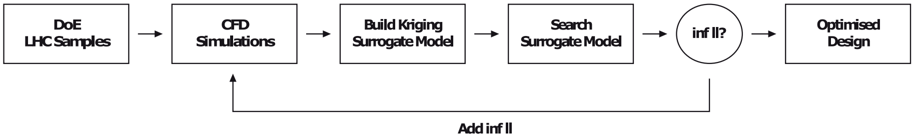

Figure 1: Winglet optimisation loop.

2.1 Rotor blade design

The rotor blade is designed by computing the chord and twist distributions according to Blade Element Momentum (BEM) theory. In this classical model the rotor blade with the best aerodynamic efficiency is obtained by optimising the rotor's axial induction factor at different stream tubes according to

$$16\ a^3 - 24\ a^2 + a(9 - 3x^2) - 1 + x^2 = 0\ . \tag{1}$$

Here, a is the axial induction and $x = \omega r / U_\infty$ is the local rotational speed at a radius r, non-dimensionalised with respect to the wind speed, U_∞. The corresponding tangential induction factor is given by

$$a' = \frac{1 - 3a}{4a - 1}\ , \tag{2}$$

and the optimal local flow angle is found from

$$\tan(\phi) = \frac{(1 - a)}{(1 + a')x}\ . \tag{3}$$

The twist distribution on the rotor blade is computed using

$$\theta = \phi - \alpha_{opt}\ , \tag{4}$$

where, α_{opt} is the airfoil angle of attack for best lift-to-drag ratio. The span-wise chord distribution is calculated according to

$$c = \frac{8\pi \ a \ x \ \sin^2(\theta)R}{(1-a)BC_n\lambda} \ , \tag{5}$$

where, R is the radius of the rotor, B is the number of blades, and λ is the tip speed ratio (TSR),

$$\lambda = \frac{\omega R}{U_\infty} \ . \tag{6}$$

The normal force coefficient is given by

$$C_n = C_{l,opt}\cos(\theta) + C_{d,opt}\sin(\theta) \ , \tag{7}$$

and is calculated using the lift and drag coefficients for the airfoil operating at its best lift-to-drag ratio (Hansen, 2008).

Due to the model-scale flow condition on the winglet and the size of the wind tunnel, both the Reynolds number at the rotor tip and the blockage in the wind tunnel are important. The Reynolds number is given by

$$Re = \frac{\lambda U_\infty c}{\nu} \ , \tag{8}$$

where ν is the kinematic viscosity of air. At low Reynolds numbers it is well known that the dominating viscous forces limit the aerodynamic performance. By increasing the rotor radius, the Reynolds number is increased, however, so is the blockage in the wind tunnel. In an effort to balance these two conflicting physical properties, a 2-bladed rotor with a radius $R = 0.45$ m and a design TSR of 5 is chosen. This rotor favours the flow conditions on the rotor tip and has a wind tunnel blockage ratio of about 13%. To check the performance of the 2-bladed rotor, the measured power and thrust is compared to an existing 3-bladed NTNU model turbine with equal rotor radius (Krogstad and Eriksen, 2013).

2.2 Airfoil design

To match the flow condition on the model-scale turbine and winglet, new airfoils are created using an optimisation method developed in earlier work (Hansen, 2017). Here, the Class-Shape-Transformation (CST) technique (Kulfan and Bussoletti, 2006) is applied to parametrise the airfoil shape, and the aerodynamic performance is computed using an adjusted version of the panel code XFOIL (Drela, 1989). Further, the derivative-free Covariance Matrix Adaptation Evolution Strategy (CMA-ES) algorithm (Hansen, 2016) is employed to find the best performing airfoil shape. The optimisation is performed by executing the XFOIL code for a range of angles of attack in each objective function evaluation. To maximise the airfoil performance, the lift-to-drag ratio for the simulated range of angles of attack is optimised. The optimisation problem is defined as

$$\begin{aligned} &\text{maximise} \quad f(\boldsymbol{x}) = \sum_{i=1}^{n} \left(\frac{C_l}{C_d} \right)_i \\ &\text{subject to} \quad b_{l,j} \leq \boldsymbol{x} \leq b_{u,j},\ j = 1, \ldots, m \end{aligned}$$

where, $\boldsymbol{x}$ is a vector with range $j = 1, .., m$ containing the CST airfoil design variables, n is the number of angles of attack where the performance is to be maximised, and C_l and C_d are the corresponding lift and drag coefficients. To symmetrically balance the shape of the lift-to-drag curve in the region of the optimum point, the computed performance in the angle of attack range $i = 1, ..., n$ is normalised with respect to the maximum value. To ensure sufficient structural stiffness for the wind tunnel models, the design space is limited using an upper and lower bound on each design variable, $b_{u,j}$ and $b_{l,j}$, where only airfoils with reasonable thickness in the trailing edge region are considered. To enable manufacturing, the wind tunnel models need to have a trailing edge thickness of 0.25%. To reduce pressure drag, the rotor and winglet airfoil thickness is set to 14% and 12%, respectively. To increase the numerical stability in XFOIL, the airfoils are optimised for a Reynolds number corresponding to a TSR of 5.5, which is slightly higher than the design TSR. The N_{crit} value in XFOIL is used to mimic the turbulence level on the airfoils (Drela and Youngren, 2014). For the rotor airfoil, an N_{crit} value of 6 is used, representing the turbulence level in the wind tunnel. To further stabilise the numerical calculations at the lower Reynolds number for the winglet airfoil, an N_{crit} value of 4 is applied. In Table 1, the design criteria for the airfoils are summarised.

Table 1: Airfoil design criteria.

Design criteria	Rotor airfoil	Winglet airfoil
Airfoil thickness	14%	12%
TE thickness	0.25%	0.25%
Reynolds number	$1.5 \cdot 10^5$	$0.8 \cdot 10^5$
N_{crit} value	6	4

The population size in CMA-ES is adjusted according to the number of CST design variables, and an optimal solution is chosen to be found when the largest change in $\boldsymbol{x}$ is smaller than $1 \cdot 10^{-3}$. The thickness of the rotor airfoil is equal to the S826 airfoil used on the 3-bladed NTNU model turbine, hence, the performance of the two airfoils can be compared.

2.3 Winglet shape optimisation

The winglet shape is optimised by constructing and refining a Kriging surrogate model using an infill criterion based on expected improvement. When using a surrogate, the number of computational expensive CFD simulations is reduced by creating an approximate model of the response when changing design variables. In Kriging, this approximate model is constructed using a Gaussian stochastic process modelling approach. This enables the calculation of an estimated error for the model's uncertainty, which is a key advantage since it allows the model to be refined by positioning infill points at locations with high uncertainty (Forrester et al., 2008). To construct the Kriging model, the MATLAB toolbox ooDACE, developed at Ghent University is applied (Couckuyt et al., 2014). The winglet shape is parametrised using 6 degrees of freedom and a normalised design space is created according to maximum and minimum values. To construct the initial Kriging model, a Latin Hypercube (LHC) sampling plan is created, and to avoid clustering and poorly sampled regions, the space-filling ability of the LHC is maximised using a genetic optimisation algorithm mat (2015). In Figure 2, the different design variables for the winglet are shown. In order to keep the total rotor radius constant at R=0.45 m, the location where the winglet is mounted to the rotor blade is adjusted according to the winglet radius. Hence, the rotor tip chord varies slightly around the value 0.04 m. Twist between the root and tip airfoil

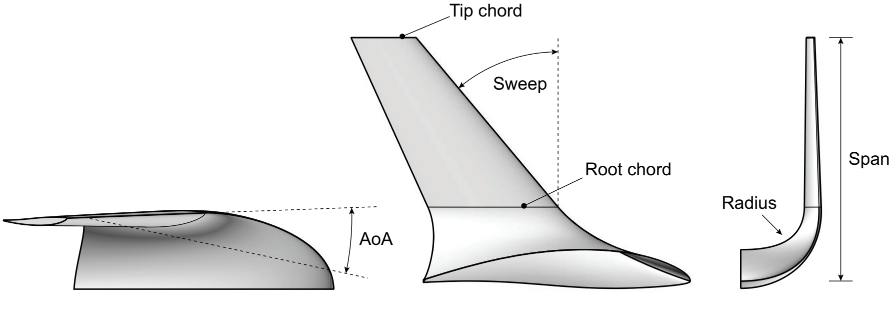

Figure 2: Winglet design variables.

on the winglet is not considered. In Table 2, the maximum and minimum values used to normalise the design variables are given.

Table 2: Winglet design variables.

Design variables	Min	Max	w.r.t
x_1 - Span	5%	12.5%	Rotor span
x_2 - Sweep	$0°$	$40°$	-
x_3 - AoA	$-2°$	$12°$	-
x_4 - Radius	2.75%	3.5%	Rotor span
x_5 - Root chord	35%	100%	Rotor tip chord
x_6 - Tip chord	50%	100%	Winglet root chord

Since the Kriging model is only an approximation, the accuracy of the surrogate is enhanced by performing more simulations in addition to the initial LHC samples. The location of these infill points are computed using the expected improvement criterion given by

$$E[I(\boldsymbol{x})] = \begin{cases} (f_{min} - \hat{f}(\boldsymbol{x}))\Phi(\frac{f_{min}-\hat{f}(\boldsymbol{x})}{\hat{s}(\boldsymbol{x})}) + \hat{s}(\boldsymbol{x})\phi(\frac{f_{min}-\hat{f}(\boldsymbol{x})}{\hat{s}(\boldsymbol{x})}), & \text{if } \hat{s} > 0 \\ 0 & \text{if } \hat{s} = 0 \end{cases}. \tag{9}$$

where, Φ and ϕ are the cumulative distribution and probability density function, respectively (Parr et al., 2010). Depending on the quality of the Kriging model, the largest improvement might exist either at under-sampled regions or in areas with improved solutions. The infill criterion thus explores and exploits the design space, and the global optimum solution is obtained when the Kriging model no longer has any expected improvement. In the expression, f_{min} and $\hat{f}$ are the current best and the predicted objective function values, respectively. The predicted mean square error is denoted $\hat{s}$. To find the infill point with the largest expected improvement, the $E[I(\boldsymbol{x})]$ criterion is maximised using a hybrid genetic-gradient algorithm. The genetic algorithm is given a population size of 200 and is allowed to evolve for 600 generations. At the end of the evolutionary search, a gradient algorithm is executed to ensure that the best local solution is found in the current global, best basin of attraction. The hybrid algorithm is stopped, and an optimal solution is chosen to be found when the largest change in $\boldsymbol{x}$ is smaller than $1 \cdot 10^{-6}$.

The performance of the rotor blade is maximised by considering the winglet as a single-point, unconstrained optimisation problem, and the power coefficient of the wind turbine operating at its best TSR is used as objective function. The power coefficient is computed from

$$C_p = \frac{P}{\frac{1}{2}\rho U_\infty^3 A} \ , \tag{10}$$

where, P is the power produced by the turbine, ρ is the density of air and A is the swept area. Since the winglet increases the amount of lift on the rotor blades, the thrust force is important. On coefficient form the thrust is given by

$$C_t = \frac{T}{\frac{1}{2}\rho U_\infty^2 A} \ , \tag{11}$$

and in this work the increase in C_t due to the winglet is monitored. If the thrust is included as a constraint, the optimisation method would allow the rotor performance to be maximised within the specified limit. The ability to include constraints is an important advantage, since the performance of more traditional design methods e.g. parameter studies, or optimising the rotor circulation, will suffer when constraints are added.

To investigate the performance of the Kriging surrogate model and the infill criterion, a 2-dimensional Branin test function is first minimised. In order to obtain a response with two local minima and one global minimum the Branin function is modified according to Parr et al. (2010).

The rotor performance with winglets is also compared to a turbine where the rotor radius is increased in order to produce the equivalent amount of power. The larger rotor span is created by extrapolating the chord and twist, using the rotor C_p with winglet as reference. The power production for the two designs are compared experimentally and the measured wind tunnel data is corrected using $\rho = 1.2$ kg/m^3.

2.4 CFD simulations and mesh

The performance of the wind turbine is simulated using the Navier-Stokes solver STAR-CCM+ from Siemens (CCM, 2017). The turbine rotation is modelled using a moving reference frame model and the air is considered incompressible. To reduce the number of cells in the mesh, periodic boundary conditions are applied and only one rotor blade is present in the model. In Figure 3, the CFD domain and boundary conditions are shown. To ensure that the flow is free to expand, the inlet and far-field boundaries are positioned 8xR from the turbine, while the outlet boundary is located 6xR behind the turbine. To reduce the amount of unsteady flow, the hub is extruded the length of the flow domain.

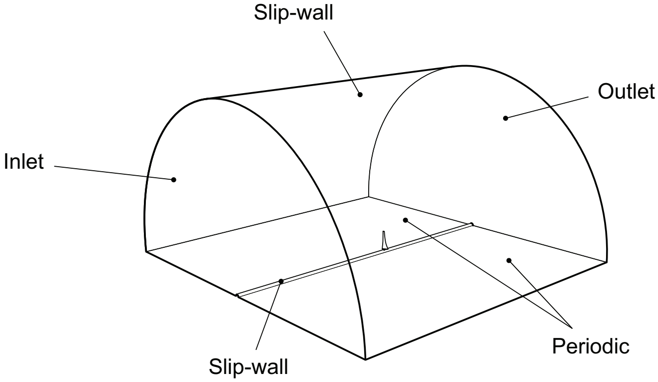

Figure 3: CFD domain and boundary conditions.

For the winglet shape optimisation, the turbulent flow is predicted using the Spalart Allmaras (SA) turbulence model. This is a one-equation, eddy viscosity turbulence model developed for the aerospace industry to predict attached boundary layers and flows with mild separation. The model solves a transport equation for the modified diffusivity $\tilde{\nu}$ to determine the turbulent viscosity, and a correction term is used to account for effects of strong streamline curvature and rapid frame-rotation.

To check the SA simulations and to analyse the transitional boundary layer flows, the rotor blade with the optimised winglet is simulated using an Elliptic Blending Reynolds-Stress Model (EB-RSM). This is a low-Reynolds number model, which solves the transport equations for each component of the Reynolds stress-tensor and, thus, accounts for the anisotropy of turbulence. The model predicts the turbulent flow more realistic than the SA turbulence model, but requires a more refined mesh and larger computational resources. When applying the EB-RSM, convergence is assumed to be reached when a drop in accuracy to the third decimal is obtained for the measured power and thrust coefficients. For the SA simulations, convergence is determined when a drop to the fourth decimal is reached.

To study the effects that the 13% blockage ratio in the NTNU wind tunnel has on the wind turbine performance, additional SA simulations are performed. Here, the distance to the far-field above the turbine is reduced to 2.78xR, a radius that corresponds to the cross-sectional area in the test section.

The turbine and flow domain is discretised using a trimmed hexahedral mesh in a Cartesian coordinate system. The mesh quality required to capture the flow on the rotor blade and wake is determined by reducing the influencing mesh sizes until the change in turbine power and thrust is less than $1 \cdot 10^{-2}$. To reduce the computation time, only the mesh in the near-wake, 1.5 m behind the rotor is refined. In Figure 4, the mesh used for the SA simulations is depicted. In the mesh, both the extruded hub and the near-wake refinement region have a cell size of 12.5 mm.

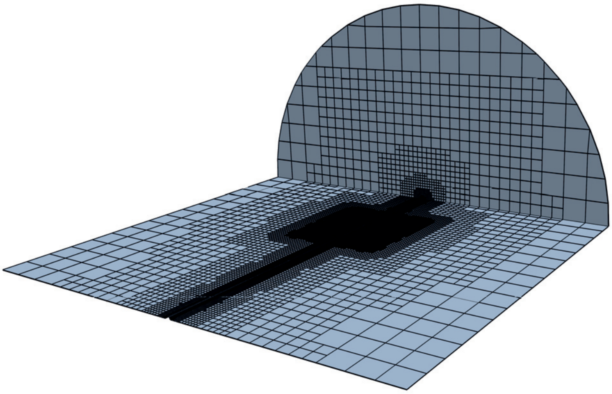

Figure 4: Flow domain mesh.

In Figure 5, a close view of the volume and surface mesh on the rotor is shown. The mesh used to capture the boundary layer flow is depicted in Figure 5a. Here, a 20 layer thick hyperbolic extruded prism layer is applied. The surface mesh depicted in Figure 5b, uses a cell size of 0.6 mm for the rotor blade. In the optimisation study, the winglet is meshed using a cell size of 0.5 mm. The final mesh without winglet has 5.5 million cells. With the winglet, the mesh size varies between 5.6 to 6.4 million cells depending on the winglet shape.

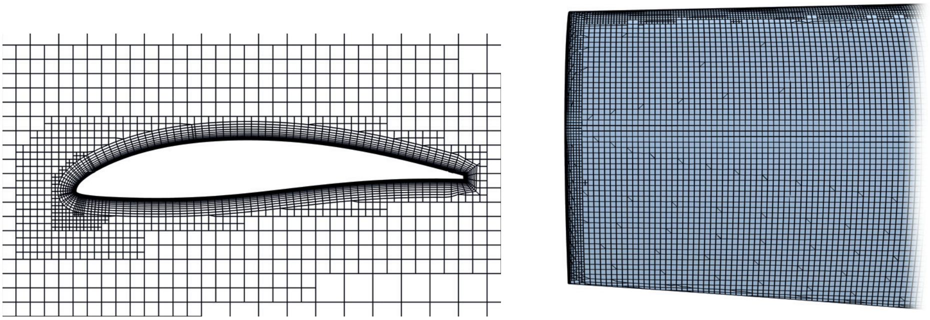

(a) (b)

Figure 5: Tetrahedral volume and surface mesh.

A refined mesh is required for the EB-RSM simulations and 25 prism layers are used to capture the boundary layer. The surface cell size on the rotor blade and winglet is reduced to 0.5 mm and 0.25 mm, respectively. The wake and the extruded hub is discretised using a mesh size of 10 mm and the total mesh has about 20.4 million cells. To resolve the flow in the boundary layer, the first cell-centroid from the wall of the rotor blade and winglet are adjusted to obtain y^+ values smaller than 1, both for the SA and the EB-RSM simulations.

2.5 Wind tunnel experiments

Experiments are performed in the closed-return wind tunnel at the Department of Energy and Process Engineering at NTNU. The wind tunnel has a test section 2.71 m wide, 1.81 m high and 11 m long, where the turbine is positioned 4.3 m from the inlet. A wind speed of $U_\infty = 10$ m/s is chosen, and the turbulence intensity in the wind tunnel is about 0.23% (Krogstad et al., 2015). The turbine torque and thrust are measured for TSR ranging from 2 to 10 using a torque transducer and a force balance. In Figure 6a, the wind turbine test model is shown in the wind tunnel. The rotor blades are 3D printed in an acrylic formulation named Verogray RGD850 (Verogray). Figure 6b shows the attachment used to mount the winglet and wing extension. In previous work, the performance of the 3-bladed NTNU turbine created in acryl and aluminium is compared (Mühle et al., 2016). The study discovered that the turbine power and thrust for the 3D printed and aluminium rotor blades compare well up to TSR 7.5. At higher TSR values, the thrust on the less stiff acrylic rotor is under predicted due to twist in the tip region. The 2-bladed wind turbine manufactured in this work is expected to have less twist, since the airfoil is designed with increased thickness in the trailing edge region and the rotor has larger chords.

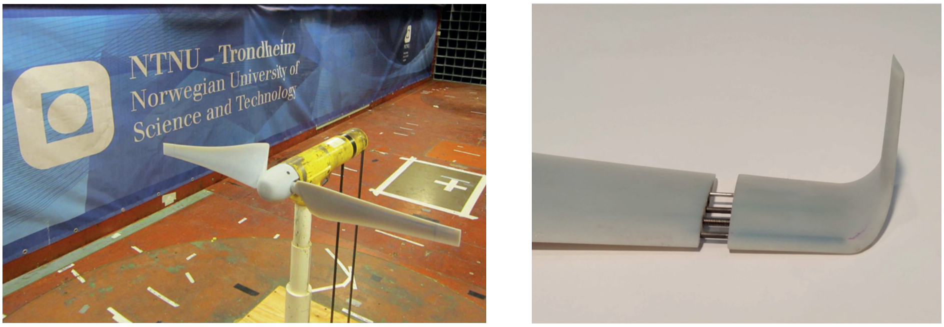

(a) (b)

Figure 6: Wind turbine in the wind tunnel and winglet attachment.

3 Results

In the following, the results of the winglet optimisation are presented. First, the shape and performance of the optimised airfoils and the model-scale wind turbine are given. Then, the performance of the winglet optimisation method is investigated by minimising the Branin function in 2-dimensions. Finally, the winglet shape is optimised and the rotor blade performance is studied.

3.1 Airfoil performance

The design space for the airfoil optimisation is created using 6 CST design variables on both suction and pressure side of the airfoil geometry. The optimisation is performed for angles of attack ranging from 4° to 8° and a population size of 24 is used in the evolutionary CMA-ES algorithm. In Figure 7, the optimised rotor airfoil (R-opt) and the optimised winglet airfoil (W-opt) are shown. The R-opt airfoil is compared to the S826 airfoil, which is used on the 3-bladed NTNU wind turbine, see Figure 7a. As can be seen, the R-opt airfoil has increased thickness in the trailing edge region. The S826 airfoil is, however, originally designed as a tip airfoil for wind turbines with rotor diameters between 20 and 40 meter, where the smaller thickness in the trailing edge region is compensated by larger chords (Somers, 2005). In Figure 7b, the shape of the W-opt and R-opt airfoil is compared. Interestingly, the smaller thickness and the lower Reynolds number on W-opt is compensated mainly by reducing the thickness on the suction side.

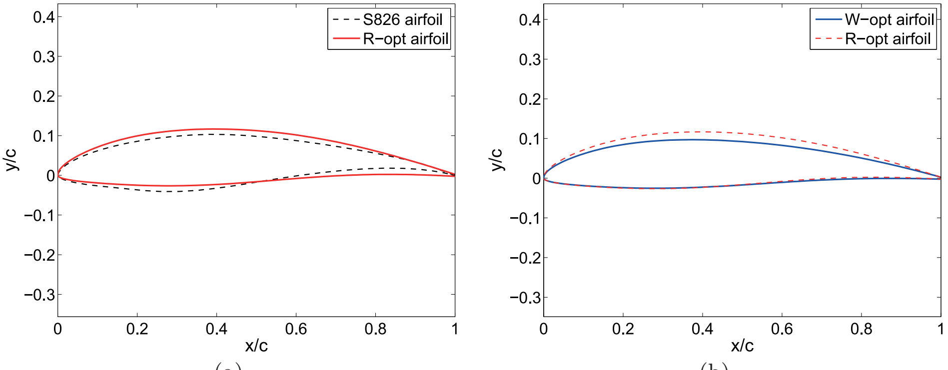

(a) (b)

Figure 7: Optimised airfoils for the rotor (R-opt) and winglet (W-opt).

In Figure 8, the performance of R-opt, W-opt and the S826 airfoil is compared. In Figure 8a, the lift coefficient at different angles of attack, α, is shown. As is seen, the lift for the R-opt airfoil compares well to the S826, except in the region of the stall, where a less abrupt reduction in C_l is predicted for R-opt. At the lower Reynolds number, the reduced thickness on the suction side of W-opt is seen to reduce the lift compared to R-opt. In Figure 8b, the lift-to-drag coefficients for the airfoils are compared. Here, the performance of the optimised R-opt airfoil outperforms the S826 at all angles of attack. The better performance of R-opt at this Reynolds number is however expected, since the S826 airfoil is designed to operate at a Reynolds number about 10 times higher (Somers, 2005). The best lift-to-drag ratio for the R-opt and S826 airfoil is 78 and 76, respectively. At the lower Reynolds number, W-opt has better performance than R-opt and the best lift-to-drag ratio is approximately 57 and 52, respectively.

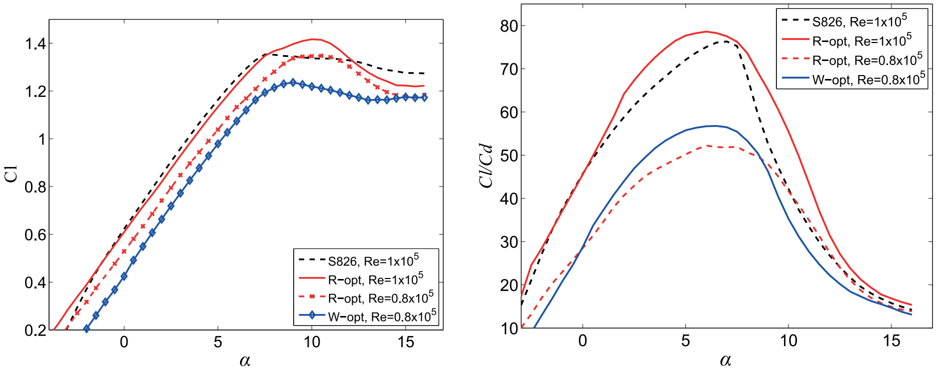

(a) (b)

Figure 8: Airfoil performance predicted using XFOIL.

3.2 Rotor blade performance

In Figure 9, the chord and twist distribution for the new 2-bladed rotor is compared to the 3-bladed NTNU model turbine. The two rotor blades are created using the same design method and the main differences are the airfoil shape and the number of blades. In Figure 9a, the chord distributions are compared. As is seen, the 2-bladed rotor has larger chords to match the solidity. In the root region, both rotors are modified according to the experimental setup. In Figure 9b, the twist is shown. Here, the difference in twist is due to the different angle of best performance for the R-opt and the S826 airfoils.

In Figure 10, the measured performance for the two wind turbines is compared. The experiments are performed for a wind velocity $U_\infty = 10$ m/s and the power and thrust are presented on coefficient form. In Figure 10a, the power coefficient for the 2-bladed rotor can be seen to outperform the 3-bladed rotor for TSR values above 4.5.

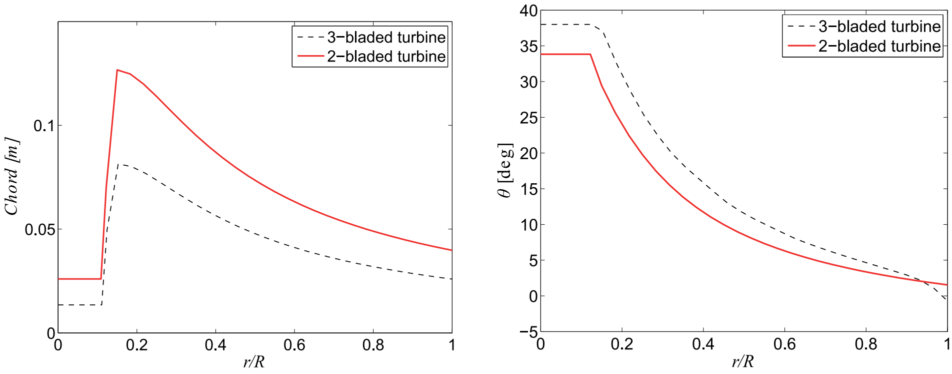

(a) (b)

Figure 9: Chord and twist distribution.

According to theory, a 2-bladed wind turbine only has slightly reduced performance

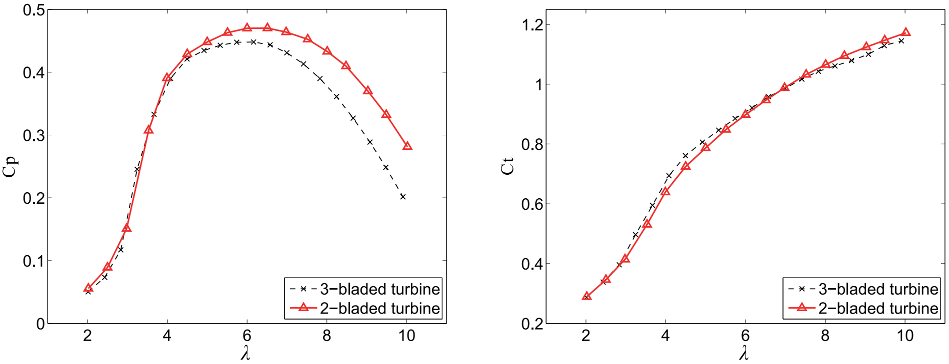

(a) (b)

Figure 10: Measured power and thrust for 2- and 3-bladed turbine.

compared to a 3-bladed wind turbine when airfoil drag is not included (Manwell et al., 2002). Hence, the better performance of the 2-bladed turbine is expected, since the optimised R-opt airfoil has better performance than S826. In Figure 10b, the thrust coefficient for the two turbines is shown. Here, the better performance for the 2-bladed turbine does not increase the thrust. For TSR values smaller than $\lambda = 7$, the C_t values on the 2-bladed turbine are about equal or slightly reduced compared to the 3-bladed turbine. At larger TSR, a small increase in thrust coefficient is observed.

3.3 CFD validation

In Figure 11, the SA simulated wind turbine performance without winglet is validated to wind tunnel experiments. In Figure 11a the simulated power coefficients at free-flow conditions can be seen to strongly underpredict the performance compared to the measured wind tunnel data. It is evident that the 13% blockage has a large effect on the power generated by the wind turbine. In the simulations where the distance to the far-field above the turbine is reduced according to the size of the wind tunnel, the predicted and the measured C_p values compare well. The increase in power for the wind turbine occurs since the energy in the wind is not free to expand, but is constricted by walls. At TSR below $\lambda = 3.5$, the simulated free-flow C_p can be seen to match the measured data very well. This is because the rotor blades are operating mostly in stall, and the free-stream wind is able to pass unaffected through the unloaded rotor system. In Sarlak et al. (2016) it is found that to be free from blockge effects, the ratio between the rotor and the size of the wind tunnel should be smaller than 5%. It is also observed that while the rotor blade is designed using BEM for $\lambda = 5$, the free-flow SA simulations predict the best performance at $\lambda = 5.5$. With wind tunnel walls, the TSR for best performance is shifted to approximately 6 in both the experimental and simulated results. It is found in Sarlak et al. (2016) that even though a large blockage ratio increases the wind turbine power, the change in flow on the rotor blades is insignificant.

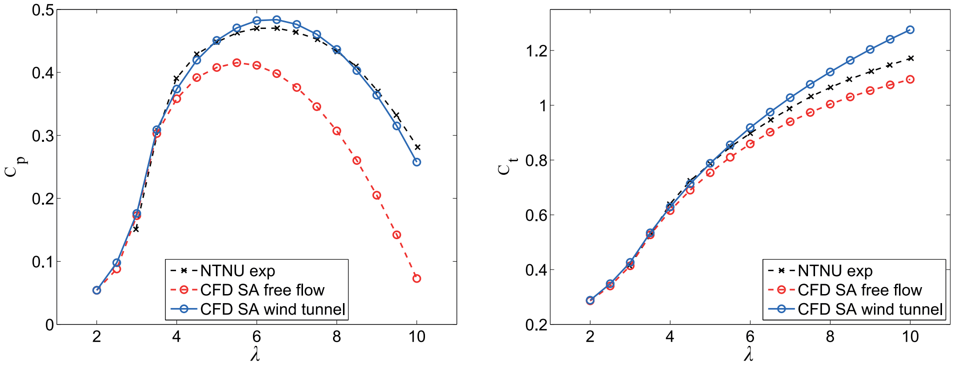

(a) (b)

Figure 11: CFD simulations and measured wind tunnel data.

In Figure 11b, the simulated and the measured thrust coefficients for the wind turbine are compared. Here, the free-flow simulations can be seen to predict lower thrust compared to the experimental data at TSR values larger than 3.5. However, when the size of the wind tunnel, and thus the blockage, is accounted for, the simulated thrust is overpredicted. This indicates that even lower C_t values should have been produced by the Spalart Allmaras turbulence model in the free-flow simulations. For TSR values below 3.5, the blockage effects are not present, and the simulated C_t values compare very well to the measured wind tunnel data.

3.4 Winglet optimisation study

To investigate the performance of the Kriging surrogate model and the expected improvement infill criterion, the 2-dimensional Branin function is minimised. In Figure 12, the Branin function and the Kriging surrogate are compared. Here, an LHC sampling plan consisting of 20 data points (triangles) is used to construct the initial Kriging model. To maximise the space-filling ability, the LHC is optimised using a genetic algorithm with a population size of 20, evolved for 200 generations. To find the best solution in the design space, the expected improvement criterion (circles) is maximised using a hybrid genetic-gradient algorithm. In the depicted example, no expected improvements exist and the global optimum is obtained (x_1=0.1216, x_2= 0.8239) after 11 infill points. As is seen, the final Kriging model represents the true Branin function very well. In the optimisation, both regions with high uncertainty (design space boundaries) and regions with improved solutions (the local and global minima) are investigated by the infill criterion. It is observed that by reducing the size of the LHC, the total number of samples required to find the global optimum is also reduced. If the LHC is increased on the other hand, the Kriging model gets saturated, and the global best solution is often found on the first iteration. Since a large LHC increases the required total number of data points, it is tempting to start the optimisation using a small LHC. However, to avoid a perceptive initial Kriging model it is recommended in Forrester et al. (2008) that approximately one-third of the total number of points should be in

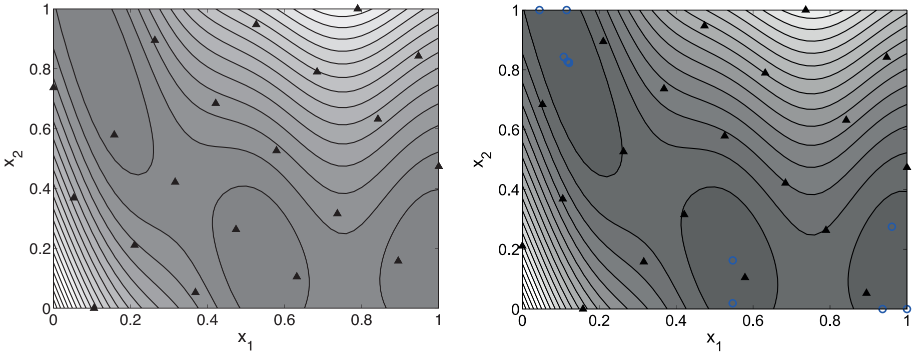

Figure 12: Branin function (left), Kriging model (right).

the sampling plan, and two-thirds determined by the infill points.

The design space for the winglet optimisation is parametrised using 6 design variables. In Figure 13, three possible winglet shapes in the design space are shown. Here, winglet **a** is given the minimum allowable values for span and sweep, while the chords are maximised. Winglet **b** uses medium values for all design parameters, and winglet **c** is created using maximum span and sweep, and minimum chords. The total number of winglet shapes investigated in the optimisation is determined according to the computational time required to reach a converged solution. The simulations are performed for $\lambda = 5.5$ on a Dell power blade cluster running 36 CPUs in parallel, and a converged solution is reached in about 3-4 hours. The simulation time limits the number of winglets, hence, 100 shapes are investigated. Here, 30 winglets are simulated in the LHC, while 70 shapes are determined by maximising $E[I(\boldsymbol{x})]$.

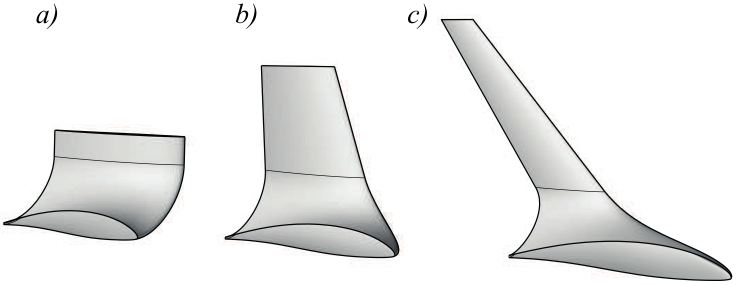

Figure 13: Examples of winglets in the design space.

In Figure 14, the percentage increase in power and thrust coefficient due to the winglet shapes obtained in the optimisation study are presented. As can be seen, the initial LHC simulation samples the design space well and winglets that both reduce and improve the rotor performance are tested. The infill points continue to explore the design space and as the Kriging model is refined, most winglet shapes improve the turbine performance. At the end of the optimisation, expected improvement still exists in the 6-dimensional, multi-modal solution space, i.e. the global optimum might not have been obtained. Hence, more winglet shapes should be tested. Nevertheless, 8 shapes are found in the Kriging model, which increase the turbine performance by

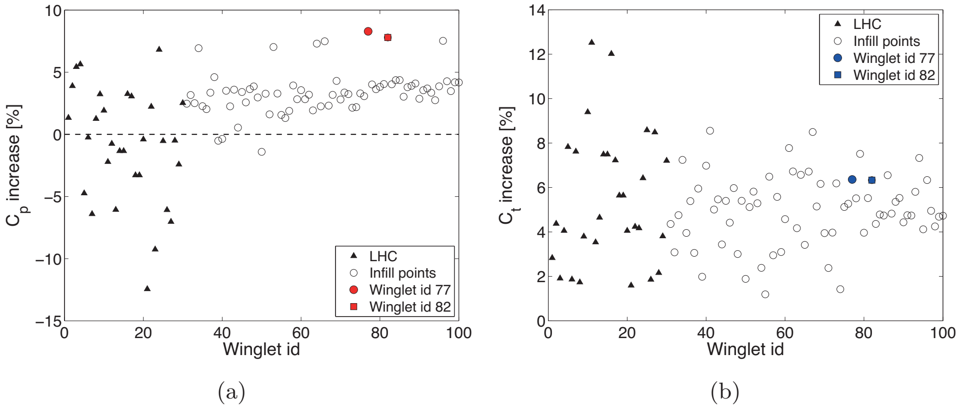

(a) (b)

Figure 14: Winglet optimisation study.

more than 6%. The best solutions are winglet id 77 and 82, which increase the turbine C_p by 8.28% and 7.80%, respectively. In Figure 14b, the corresponding increase in C_t is shown. Here, the largest differences in thrust are seen in the LHC, while the increase is less for the winglets investigated using the infill criterion. For winglet id 77 and 82 the increase in thrust is 6.36% and 6.33%, respectively. In Table 3, the five best performing winglet (WL) shapes are listed. It can be seen that winglet id 77 has the largest increase in power. However, this winglet also has the largest physical span,

Table 3: Best performing winglet shapes with increase in C_p and C_t.

WL id	x_1	x_2	x_3	x_4	x_5	x_6	C_p	C_t
64	0.6456	0.4299	0.1142	0.5025	0.4144	0.7446	7.30%	6.57%
66	0.6689	0.1289	0.0671	0.4991	0.4499	0.7552	7.49%	6.71%
77	0.8960	0.4508	0.0258	0.3973	0.3445	0.7772	8.28%	6.36%
82	0.7683	0.4465	0.0592	0.4381	0.3585	0.7629	7.80%	6.33%
96	0.6739	0.2510	0.0300	0.7918	0.4239	0.8426	7.52%	6.33%

$x_1 = 0.896$. In order to validate the acrylic 3D printed winglet in the wind tunnel, winglet id 82 is chosen to be the best solution. This winglet has slightly reduced C_p and a smaller span, $x_1 = 0.7683$. In Figure 15 the winglet is depicted and its un-normalised design values are listed in Table 4.

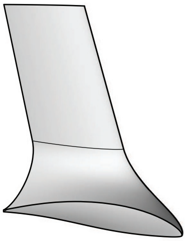

Figure 15: Winglet id 82.

Parameters	Value	w.r.t
Span	10.76%	Rotor span
Sweep	17.86°	-
AoA	-1.17°	-
Radius	3.09%	Rotor span
Root chord	58%	Rotor tip chord
Tip chord	88%	Winglet root chord

Table 4: Winglet design parameters.

3.5 Winglet analysis

The performance of the rotor blade with the optimised winglet is investigated numerically and experimentally for TSR values ranging from 2 to 10. In Figure 16, the simulated vorticity at $\lambda = 6$, with the SA and the EB-RSM turbulence models is depicted. As can be seen, the EB-RSM simulations provide a more detailed description of the wake. In Figure 17, the simulated wind turbine performance with and without winglets is compared. The increase in power coefficient due to the winglet is shown in Figure 17a. Here, the SA simulations predict a symmetrical increase in turbine C_p around the design point at $\lambda = 5.5$ with the winglet. At TSR lower than 3.5 and for TSR larger than 8.5, the simulated turbine performance is unaffected by the winglet. Since the EB-RSM simulations increase the computational time by a factor of 10-15 compared to the SA simulations, only TSR values with steady flow are investigated. As shown in the same figure, EB-RSM predicts a slightly better performance, both with and without winglet, compared to the SA simulations. With the EB-RSM, the

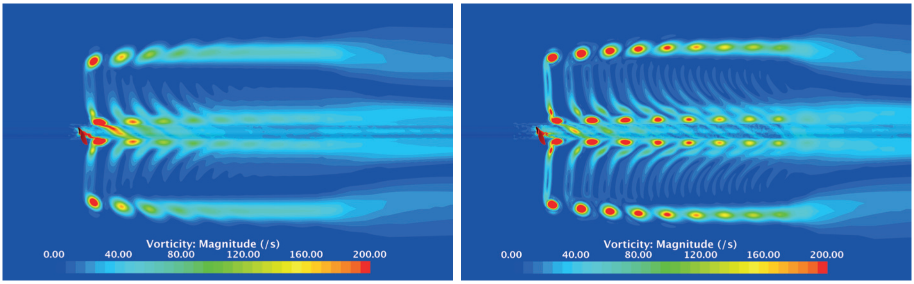

Figure 16: SA wake (left), EB-RSM wake (right).

best winglet performance is predicted at $\lambda = 6$, where the winglet increases the turbine C_p by 5.8%. In Figure 17b, the SA simulated thrust coefficients with winglet do not increase at TSR values below $\lambda = 3.5$ compared to the turbine without winglets. At values above, the difference in thrust coefficients steadily increases. In the EB-RSM simulations the C_t values are slightly reduced, compared to the SA turbulence model for $\lambda = 5$. At $\lambda = 6$, the EB-RSM predicts an increase in turbine C_t of 5.9% due to the winglet. In Figure 18, the experimental results for the wind turbine with and without winglet are shown. Here, it is found that the wind tunnel blockage effect changes the flow on the winglet slightly. Based on additional CFD simulations and experimental parameter studies, a modified winglet is created to compensate for the different flow. This winglet has an increased angle of attack, $\alpha = 1.2°$. In Figure 18a, the turbine power with and without winglet is shown. As can be seen, compared to the simulated predictions the performance with winglet is worse. The best increase in power is 8.9%, however, it occurs at $\lambda = 7$. The improvement is not symmetrical and at lower TSR values, only a small increase in performance exists. In Figure 18b, the thrust force can be seen to resemble the CFD simulations better, and at $\lambda = 7$ the winglet increases the thrust by 7.4%.

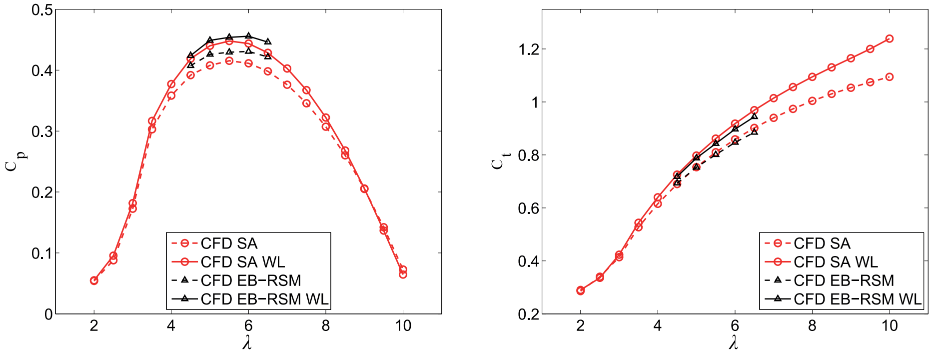

(a) (b)

Figure 17: Simulated winglet performance.

The low increase in performance found in the experimental results can be explained by laminar separation of the boundary layer on the model-scale winglet. In order to reduce laminar separation, the turbulence intensity in the wind tunnel flow is increased using a grid. With the grid, the turbulence intensity in the test section is about 5% (Krogstad et al., 2015).

In Figure 19, the measured turbine power and thrust with the grid is compared to the winglet and to the extended tip, where the rotor radius is increased by 3.64%. In Figure 19a, the increased turbulence level can be seen to improve the winglet

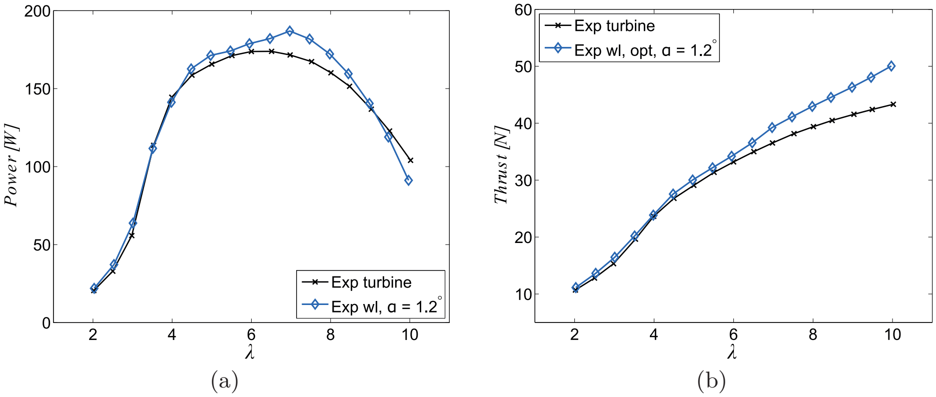

(a) (b)

Figure 18: Measured winglet performance.

performance. The best increase in power with the winglet is 10.3% at $\lambda = 6.5$. At TSR

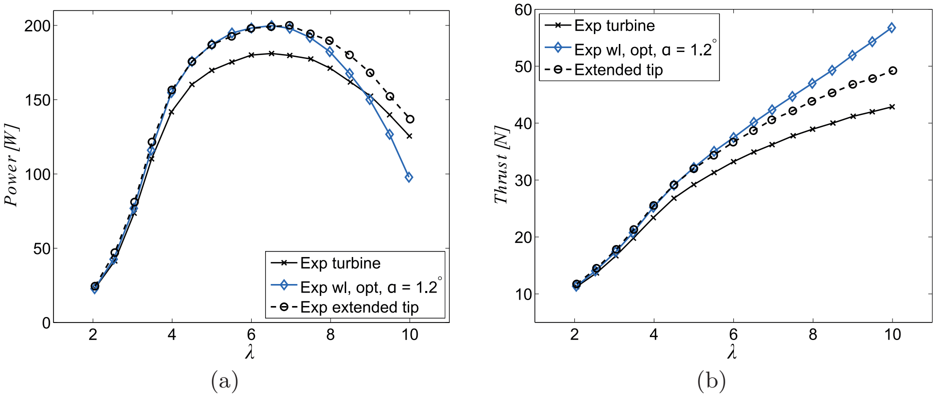

(a) (b)

Figure 19: Measured winglet and extended tip performance, with grid.

values larger than about 9 however, the rotor with winglet produces less power than the turbine without winglet. With the extended tip, the rotor power compares very well to the winglet for TSR values below 6.5. At higher TSR values, the extended tip has better performance. However, the larger rotor radius also increases the blockage ratio in the wind tunnel and this could explain the better performance.

In Figure 19b, the thrust is compared. Here, the thrust for the turbine with winglets and extended tip is seen to compare well for TSR values below 5. At higher values, the thrust forces on the rotor with winglet grow faster than the rotor blade with extended tip. This is unexpected, since the increased thrust is not measured in the experiments without the grid. The increase in rotor thrust is investigated further using a high-speed camera. It is found that for TSR values above 6 the acrylic winglet increasingly twists and bends, hence the performance is reduced.

To understand how the winglet increases the power production for the wind turbine, the EB-RSM simulations are investigated in detail at $\lambda = 6$. In Figure 20, the flow on the suction side of the rotor blades with and without winglet are compared. Here, the flow is visualised using constrained streamlines of the relative velocity and turbulent kinetic energy (TKE). The figures are created using a perspective projection mode in order to show the flow on the winglet. As seen, the flow on the rotor blades is similar, except locally at the tip, where the streamlines for the blade with winglet are more parallel to the chord-wise direction. On the rotor blade without winglet, the flow at the tip is skewed due to the pressure difference between the suction and pressure side on the blade, and when the two flows meet at the tip a vortex is created. This phenomenon is known as induced drag, or drag due to lift, and increases the drag and reduces the lift on the rotor blade. For the wind turbine studied in this work, the main contribution to the reduced performance is found to be the loss in lift.

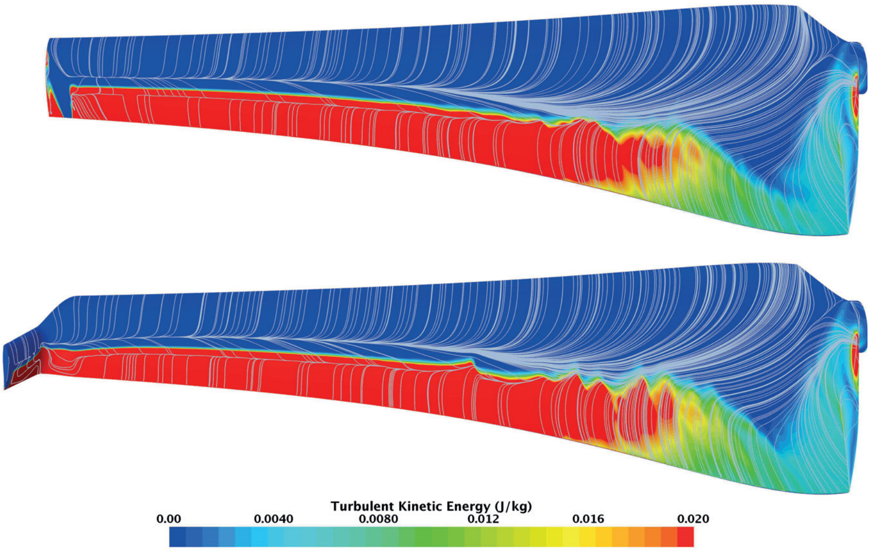

Figure 20: Rotor blade flow comparison, suction side.

In the root region of the blades, in the same Figure 20, the flow is strongly affected by the rotation and the streamlines follow the rotors in the span-wise direction. Further out on the blades, the rotational velocity is higher and the flow is more parallel to the chord-wise direction. Here, a laminar separation bubble is created at about half chord. The start of the bubble is seen where the streamlines form a stagnation line in the laminar region of the TKE. Transition to turbulence then occurs where turbulent kinetic energy is created, and the flow re-attaches as turbulent flow at a stagnation line, which can be seen behind the transition point.

In Figure 21, the constrained streamlines and the turbulent kinetic energy on the pressure side of a rotor blade with and without winglets is compared. Here, only laminar flow is predicted by the EB-RSM. In the root region, the flow on the blades is less affected by the rotation than on the suction side, and the main difference in flow occurs at the tip. As is seen, the flow on the rotor without winglet is more skewed due to the induced drag. In Figure 22, the pressure on the suction side of the rotor blade with winglet, without winglet, and with the extended tip is shown. In the figure, the pressure is scaled to better visualise the lift in the tip region. As can be seen, the rotor blade with winglet has a larger and stronger region of negative pressure, compared to the rotor without winglet. The improved lift is generated since the flow-field on the winglet interacts with the flow-field on the rotor blade and reduces the amount of span-wise flow in the tip region of the blade. The winglet thus shifts the pressure difference from the rotor blade to the winglet, and the induced drag on the rotor is reduced. The presence of the winglet introduces additional drag, however, the larger lift on the rotor blade compensates the extra drag, and the power coefficient for the wind turbine is increased. As is seen, induced drag now exists on the winglet, and the lift generated in the tip region of the winglet is therefore reduced. Hence, if the design space is expanded to include refinement of the winglet tip shape, it is believed that a

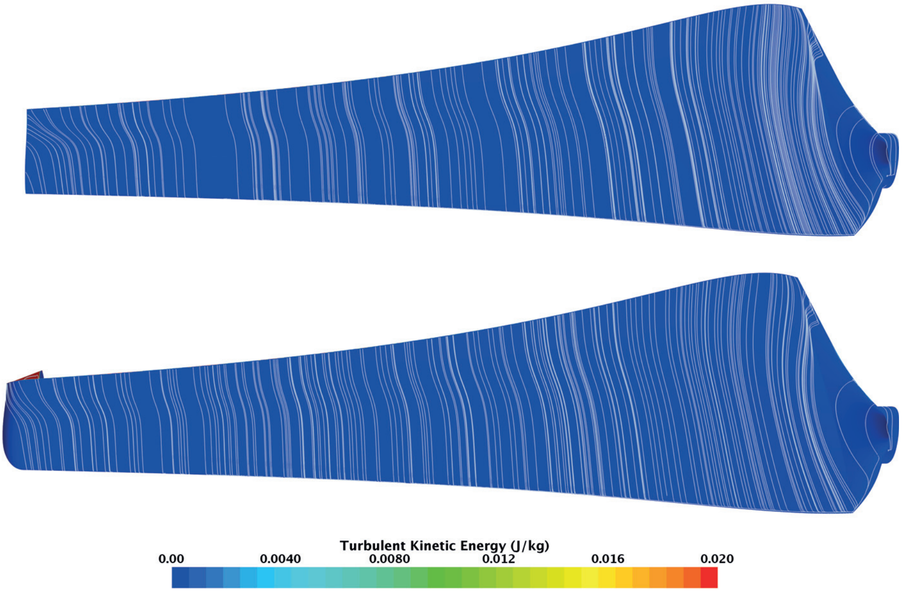

Figure 21: Rotor blade flow comparison, pressure side.

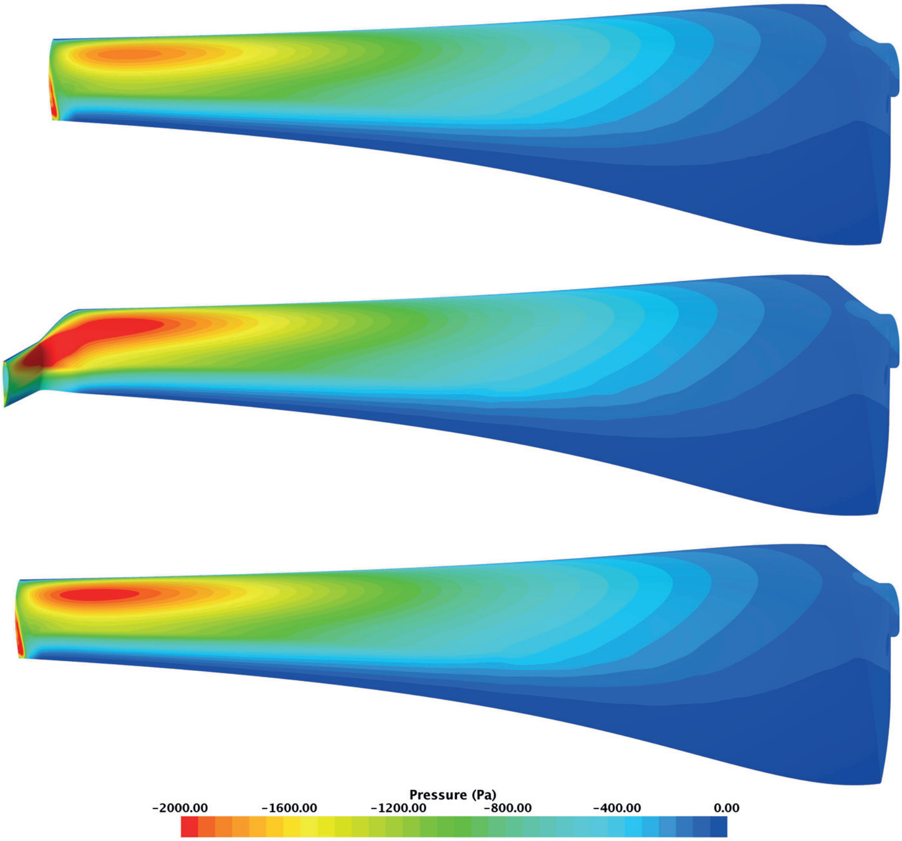

Figure 22: Rotor blade pressure comparison.

more efficient winglet could be optimised. Also for the rotor with extended tip, a larger and stronger region of negative pressure is obtained. Here, the better lift is created by shifting the local induced drag phenomena further out on the rotor blade, and thereby expanding the region where lift is created. Since the new tip is an extension, also the aspect ratio is increased slightly. The better performance is, thus, the combined result of capturing more wind energy using a larger rotor radius and reducing the induced drag by using smaller tip chords. As can be seen, a pressure difference at the tip of the blade still exists. Hence, by applying a winglet also on the blade with extended tip, the induced drag would be reduced and the rotor performance could be increased further.

4 Conclusions

In this study, a winglet optimisation method is developed and tested for a model-scale wind turbine. The best performing winglet shape is obtained by constructing and refining a Kriging surrogate model using an infill criterion based on expected improvement. The turbine performance is simulated by solving the incompressible RANS equations and the turbulent flow is predicted using the Spalart Allmaras turbulence model. The winglet is parametrised using 6 design variables, and 100 shapes are tested in the optimisation. To validate the simulated results, experiments are performed in the NTNU wind tunnel, using 3D printed test models.
It is found that the method performs well, and the optimised winglet increases the power coefficient for the turbine by 7.8%, while increasing the trust by 6.3%. In the optimisation, however, the infill criterion is not fully converged, and a better winglet shape might exist in the design space. The wind tunnel experiments show that the winglet increases the power and thrust by 8.9% and 7.4%. However, due to the small scale, the winglet performance is influenced by laminar separation and the increase in performance only occurs in a small range of operational conditions. To eliminate laminar separation, additional wind tunnel tests are performed using a grid to increase the turbulence intensity. With the grid, the winglet increases the turbine power in a wider range of conditions, and the largest increase in power and thrust is 10.3% and 14.9% at a tip speed ratio of 6.5. It is found that the winglet improves the turbine power mainly by increasing the lift locally in the tip region of the rotor blades. Here, the induced drag is reduced since the pressure difference on the rotor blades is shifted to the winglet. However, since induced drag exists on the winglet, a slightly better solution could be obtained by including an extra design variable for the winglet tip shape. Future studies should include constraints in the Kriging optimisation and simulate the wind turbine using a turbulence model that captures the flow physics even better.

5 Acknowledgments

This project is financially supported by the Research Council of Norway and CMR Prototech. The authors wish to thank Professor Per-Åge Krogstad and Professor Lars Sætran at the Department of Energy and Process Engineering at the Norwegian University of Science and Technology (NTNU) as well as Professor Muyiwa S. Adaramola from the faculty of Environmental Sciences and Natural Resource Management at the Norwegian University of Life Sciences (NMBU) for supervising this work. Also, thanks to Dr. Sonia Faaland at CMR Prototech for her support throughout this study.

References

Verogray RGD850, Stratasys, safety data sheet, revision A, 2nd March 2016.

Global Optimization Toolbox User's Guide, R2015b, MathWorks Inc., 2015.

Introducing STAR-CCM+, CD-Adapco, user guide, STAR-CCM+ version 12.02.010, 2017.

Couckuyt, I., Dhaene, T., and Demeester, P.: ooDACE Toolbox: A flexible object-oriented Kriging implementation, Journal of Machine Learning Research, 15, 3183–3186, 2014.

Drela, M.: XFOIL: An Analysis and Design System for Low Reynolds Number Airfoils. Low Reynolds Number Aerodynamics, Springer-Verlag, lecture notes in Eng. 54., 1989.

Drela, M. and Youngren, H.: XFOIL 6.9 User Primer, http://web.mit.edu/drela/Public/web/xfoil/, 2014.

Forrester, A., Sóbester, A., and Keane, A.: Engineering design via surrogate modelling, John Wiley & Sons, 1st edn., 2008.

Freitag, W. and Schulze, E. T.: Blended Winglets Improve Performance, AERO-MAGAZINE, 35, 2009.

Gaunaa, M. and Johansen, J.: Determination of the maximum aerodynamic efficiency of wind turbine rotors with winglets, Journal of Physics, doi:10.1088/1742-6596/75/1/012006, 2007.

Hansen, M. O. L.: Aerodynamics of Wind Turbines, Earthscan, London, UK, 2nd edn., 2008.

Hansen, N.: The CMA Evolution Strategy: A Tutorial, Research Centre Saclay-Île-de-France, Université Paris-Saclay, 2016.

Hansen, T. H.: Airfoil optimisation for wind turbine application, submitted to *Wind Energy* January 2017.

Krogstad, P.-Å. and Eriksen, P. E.: "Blind test" calculations of the performance and wake development for a model wind turbine, Renewable Energy, 50, 325–333, 2013.

Krogstad, P.-Å., Sætran, L., and Adaramola, M. S.: "Blind test 3" calculations of the performance and wake development behind two in-line and offset model wind turbines, Journal of Fluids and Structures, 52, 65–80, 2015.

Kulfan, B. M. and Bussoletti, J. E.: Fundamental Parametric Geometry Representation for Aircraft Component Shapes, in: 11th AIAA/ISSMO Multidisciplinary Analysis and Optimization Conference, Portsmouth, VA USA, aIAA 2006-6948, 2006.

Maniaci, D. C. and Maughmer, M. D.: Winglet Design for Wind Turbines Using a Free-Wake Vortex Analysis Method, in: 50th AIAA Aerospace Sciences Meeting including the New Horizons Forum and Aerospace Exposition, AIAA 2012-1158, Nashville, Tennessee, 2012.

Manwell, J. F., McGowan, J. G., and Rogers, A. L.: Wind Energy Explained, John Wiley & Sons, 2002.

Maughmer, M. D.: The Design of Winglets for High-Performance Sailplanes, Technical Soaring, XXVII, 44–51, 2003.

Mühle, F., Adaramola, M. S., and Sætran, L.: Alternative production methods for model wind turbine rotors – is the 3D printing technology suited?, in: 12th EAWE PhD Seminar on Wind Energy in Europe, DTU Lyngby, Denmark, 2016.

Parr, J. M., Holden, C. M. E., Forrester, A. I. J., and Keane, A. J.: Review of Efficient Surrogate Infill Sampling Criteria with Constraint Handling, in: 2nd International Conference on Engineering Optimization, Lisbon, Portugal, 2010.

Sarlak, H., Nishino, T., Martinez-Tossas, L. A., Meneveau, C., and Sørensen, J. N.: Assessment of blockage effects on the wake characteristics and power of wind turbines, Renewable Energy, 93, 340–352, 2016.

Somers, D. M.: The S825 and S826 Airfoils Period of Performance: 1994 - 1995, Report SR-500-36344, National Renewable Energy Lab, Golden, Colorado USA.

PAPER V

Wind tunnel experiments on wind turbine wakes in yaw: Effects of inflow turbulence and shear

Jan Bartl[1], Franz Mühle[2], Jannik Schottler[3], Lars Sætran[1], Joachim Peinke[3,4], Muyiwa S Adaramola[2] and Michael Hölling[3]

[1] Department of Energy and Process Engineering, Norwegian University of Science And Technology, Trondheim, Norway

[2] Faculty of Environmental Sciences and Natural Resource Management, Norwegian University of Life Sciences, Ås, Norway

[3] ForWind, Institute of Physics, University of Oldenburg, Oldenburg, Germany

[4] Fraunhofer IWES, Oldenburg, Germany

Corresponding Author: Jan Bartl (jan.bartl@ntnu.no)

Abstract. The wake characteristics behind a yawed model wind turbine exposed to different customized inflow conditions are investigated. Laser Doppler Anemometry is used to measure the wake flow in two planes at x/D=3 and x/D=6 while the turbine yaw angle is varied from $\gamma = [-30°, 0°, +30°]$. The objective is to assess the influence of grid-generated inflow turbulence and shear on the mean and turbulent flow components.

The wake flow is observed to be asymmetric with respect to negative and positive yaw angles. A counter-rotating vortex pair is detected creating a kidney-shaped velocity deficit for all inflow conditions. Exposing the rotor to non-uniform highly turbulent shear inflow changes the mean and turbulent wake characteristics only insignificantly. At low inflow turbulence the curled wake shape and wake center deflection are more pronounced than at high inflow turbulence. For a yawed turbine the rotor-generated turbulence profiles peak in regions of strong mean velocity gradients, while the levels of peak turbulence decrease at approximately the same rate as the rotor thrust.

1 Introduction

In the light of a steadily increasing worldwide use of wind energy, optimized control for wind farms has become a focus area of research. The reduced wind speeds in the wake leave significantly less energy for downstream turbines causing wind farm power losses up to 20% (Barthelmie et al., 2010). At the same time increased turbulence levels in the wake lead to higher fatigue loads on downstream rotors, which experience an increased probability for component failure (Thomsen and Sørensen, 1999). In order to mitigate these unfavorable consequences of wake impingement, different wind farm control methods have been suggested for optimizing the total power output and minimizing loads on a wind farm's individual turbines (Gebraad et al., 2015; Knudsen et al., 2014).

These methods include the reduction of the upstream turbine's axial-induction by varying its torque or blade pitch angle (Annoni et al., 2016; Bartl and Sætran, 2016) as well as wake redirection techniques, which intentionally apply a tilted thrust vector on the front row rotors. In Fleming et al. (2015) different wake deflection mechanisms have been discussed with respect to higher wind farm power production and rotor loads. As individual pitch control has been shown to cause high structural loads and current turbine designs do not feature a degree of freedom in tilt direction, yaw actuation has been concluded to be a very promising technique.

For the development of wake deflection strategies by yaw misalignment, the characteristics of the mean and turbulent wake flow behind a yawed turbine have to be understood in detail. Besides the turbine's geometry and operational state, the wake flow is strongly dependent on the atmospheric conditions which represent the inflow state to the turbine. The stability of the atmospheric boundary layer can be described by height-dependent distributions of potential temperature, wind direction (veer), velocity distribution (shear) and turbulence intensity (Vollmer et al., 2016). As it is rather impossible to simulate realistic atmospheric conditions in a wind tunnel environment, these parameters have to be investigated separately. Therefore, the present study investigates the dependency of the wake flow behind yawed turbines for different customized inflow conditions. The wind tunnel study intends to shed light on the effects of non-uniform shear and inflow turbulence levels on the wake characteristics. Wind tunnel wake experiments have the advantage of being conducted in controlled laboratory environment. Thus, intentional variations of inflow conditions and turbine operating points can help to gain a deeper understanding of the effects on the wake flow. They furthermore can serve as validation data of numerical results and a base for the fine-tuning of engineering wake models.

An early set of experimental studies on the wake of a yawed turbine was reported by Grant et al. (1997), in which they used optical methods in the wake behind a model turbine of D=0.90 m to track the tip vortices and calculate wake deflection and expansion. In a follow-up study, Grant and Parkin (2000) presented phase-locked particle image velocimetry (PIV) measurements in the wake. The measured circulation in the wake showed clear asymmetries in the wake shape for positive and negative yaw angles. An asymmetric wake was also reported by Haans et al. (2005), who found non-symmetric tip vortex locations behind a yawed model turbine of D=1.20 m. Another yaw experiment was conducted by Medici and Alfredsson (2006) on a small model turbine of D=0.12 m. They reported a clear cross-stream flow component deflecting the wake laterally. These experimental results were later used by Jiménez et al. (2010) as verification data for a wake deflection model for yawed turbines. Based on large eddy simulations (LES) around a yawed actuator disc they developed a simple analytical model that is able to predict the wake skew angle and wake velocity deficit in the far wake. An engineering model for the axial induced velocity on a yawed turbine was developed by Schepers (1999), which was based on inflow measurements in front of different yawed turbines.

An extensive study of flow and load characteristics on a yawed wind turbine rotor on a D=4.50 m rotor was presented by Schepers et al. (2014). In the so-called Mexnext project, a comparison of twenty different computations with detailed PIV and load measurements revealed modeling deficiencies while simultaneously shedding light on complex instationary flow at the rotor. The topic of utilizing yaw misalignment for improved wind farm control was thoroughly investigated by Fleming et al. (2015) and Gebraad et al. (2016). They analyzed wake mitigation strategies by using both a parametric wake model and the advanced computational fluid dynamics (CFD) tool SOWFA. A recent follow-up study by Fleming et al. (2017) focused on large-scale flow structures in the wake behind one and multiple aligned turbines and addresses a wake deflection behind a non-yawed downstream impinged by a partial wake of a yawed upstream turbine. In another LES investigation Vollmer et al. (2016) studied the influence of three atmospheric stability classes on the wake characteristics behind a yawed turbine rotor. A strong dependency of the wake shape and deflection on the stability is found, showing significantly higher wake deflection for a stable atmosphere than for neutral or convective conditions. Another LES study on yaw misalignment was performed by Wang et al. (2017), who highlighted the importance of including nacelle and tower structures in the computational model when comparing with experimental results.

Yaw angle dependent turbine performance and near-wake measurements were performed by Krogstad and Adaramola (2012). They found a power decrease proportional to $cos^3(\gamma)$ and showed that the near-wake deflection is dependent on the turbine's tip speed ratio. A combined experimental and computational wake study for a larger range of downstream distances was recently reported by Howland et al. (2016). The wake behind a yawed small drag disc of D=0.03 m was analyzed, describing the formation of a curled wake shape by a counter-rotating vortex pair. The influence of wake swirl, ground effect and turbulent diffusion on the formation mechanisms of this counter-rotating vortex pair was systematically investigated by Berdowski et al. (2018) using a free-wake vortex filament method. An extensive contribution to the field of yawed turbine wakes was recently made by Bastankhah and Porté-Agel (2016). In an experimental PIV study on a model turbine of D=0.15 m an asymmetric flow entrainment in the wake by both mean and turbulent momentum fluxes was shown.

Moreover, an analytical model for the far wake of a yawed turbine was developed based on self-similar velocity and skew angle distributions.
An experimental study on the interaction of two model wind turbines was conducted by Schottler et al. (2016) showing clear asymmetries of the downstream turbine power output with respect to the upstream turbine's positive or negative yaw angle. In a follow-up study the asymmetry was ascribed to a strong shear in the inflow, which caused an asymmetry in the opposite direction when the sheared inflow was vertically inverted (Schottler et al., 2017a). These studies encouraged a more detailed investigation of the inflow-dependent wake flow behind a yawed turbine. As for the present study, we aim to close the gap between turbine interactions for yaw-controlled wind farms by presenting high-fidelity wake measurement data at controlled inflow conditions. The influence of turbulence and shear in the inflow on the wake's shape, deflection and symmetry with respect to yaw angle is quantified. This work is part of a joint experimental campaign by the NTNU Trondheim and ForWind in Oldenburg. While this paper examines the influence of varying inflow conditions on the wake of one model wind turbine, a second paper by Schottler et al. (2018) compares the wake characteristics behind two different model wind turbines exposed to one inflow only while also adding two-point statistics to the evaluation.

2 Experimental setup

2.1 Turbine model, inflow & operating conditions

Turbine model

The wind turbine model used for this study has a rotor diameter of D=0.90 m with a hub diameter of D_{hub}=0.090 m. The tower and nacelle structure of the turbine is a slimmer re-design of the turbines previously used in Bartl and Sætran (2017). The tower thickness and the nacelle length have been significantly reduced in size in order to minimize their impact on the wake flow behind the yawed rotor. Photographs of the turbine exposed to different inflow conditions are shown in Figure 1. The blades are milled in aluminum and based on an NREL S826 airfoil, which was originally designed at the National Renewable Energy Laboratory (NREL). The rotor turns in counter-clockwise direction when observed from an upstream point of view. The rotation is controlled via an electric servo motor of the type 400W Panasonic LIQI, which is located inside the nacelle. The frequency-controlled motor ensures a rotation at constant rotational speed, while the excessive power is burned off in an external resistor. The blade pitch angle was fixed to $\beta = 0°$ for the entire experiment.

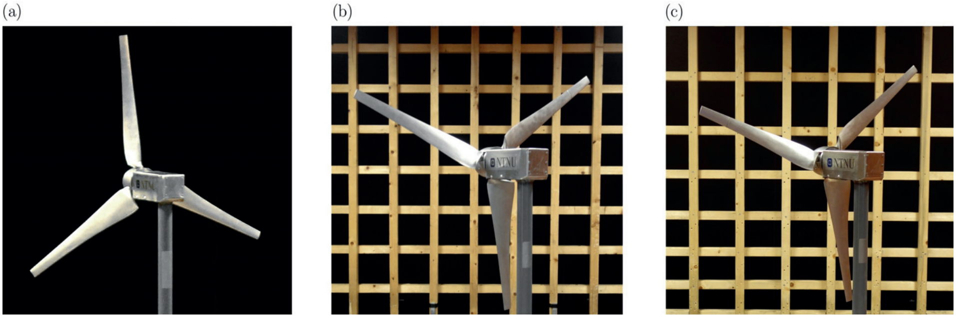

Figure 1: Yawed model wind turbine exposed to different inflow conditions: **(a)** TI_A=0.23%, uniform **(b)** TI_B=10.0%, uniform **(c)** TI_C=10.0%, non-uniform shear.

Scaling and blockage

The experiments were performed at the low-speed wind tunnel at the Norwegian University of Science and Technology (NTNU) in Trondheim, Norway. The test section is 11.15 m long with an inlet cross-section of 2.71 m × 1.81 m (width × height). Compared to a full scale wind turbine, the model size is scaled down at a geometrical scaling ratio of approximately 1:100 resulting in a mismatch in Reynolds number in the model experiment. The turbine is operated at a Reynolds number of approximately $Re_{\text{tip}} \approx 10^5$ at the blade tip, which is more than one full order of magnitude lower than for full scale turbines. Re_{tip} is based on the chord length at the blade tip and the effective velocity during turbine operation.

Furthermore, the rotor swept area of the turbine model blocks 12.8 % of the wind tunnel's cross sectional area. The wind tunnel height is approximately twice the rotor diameter while its width measures about three times the diameter. Consequently, there is about one full diameter of space for lateral wake deflection on each side behind the rotor. However, an influence of the wind tunnel walls on the wake expansion and deflection cannot be completely excluded.

Inflow conditions

The measurements are performed for three different stationary inflow conditions as listed in Table 1. As shown in Figure 1 inflows B and C are generated by static grids at the inlet. The streamwise mean velocities and turbulence intensity levels measured in the empty wind tunnel at the turbine position (x/D=0) and wake measurement locations (x/D=3 and x/D=6) are presented in Figure 4.

Table 1: Characteristics of the three different investigated inflow conditions.

Inflow	TI [%]	spatial uniformity	power law coeff. α
A	0.23	uniform	0
B	10.0	uniform	0
C	10.0	non-uniform	0.11

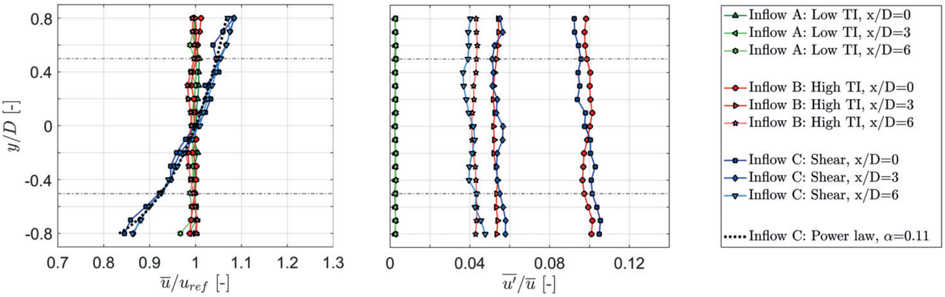

Figure 2: Normalized mean velocity $\overline{u}/u_{ref}$ and turbulence intensity $\overline{u'}/\overline{u}$ measured in the empty wind tunnel at the turbine position $x/D = 0$ and wake measurement positions $x/D = 3$ and $x/D = 6$.

Inflow A can be characterized as a typical laboratory flow, in which the turbine is exposed to the uniform, low turbulence inflow of the wind tunnel (TI_A=0.23%). The low turbulence level in test case A is considered to be far below the intensities present in the real atmospheric boundary layer. Nevertheless, test case A is considered an extreme test case for the performance of computational prediction models. In order to generate a higher turbulence level for inflow B, a custom-made turbulence grid with evenly spaced horizontal and vertical bars is placed at the test section inlet x/D=-2 upstream of the turbine. At the turbine position (x/D=0) a mean streamwise turbulence level of TI_B=10.0% is measured, which decays to 5.5% at x/D=3. Test case B represents turbulence conditions that are comparable to those of a neutral atmospheric boundary layer, although the inevitable decay of the grid-generated turbulence in the experiment is not representative for real conditions. Over the rotor swept area, inflow A is measured to be uniform within ±0.8% in y- and z-direction for all downstream distances. For inflow B, wakes of the single grid bars are still observed at x/D=0, causing a spatial mean velocity variation within ±2.5%, while already at x/D=3 the grid-generated turbulent flow is uniform within ±1.0%.

The non-uniform shear inflow C is created by a grid with non-uniformly spaced horizontal bars, which is described in more detail in Bartl and Sætran (2017). The vertical flow profile establishes for all streamwise positions and can be approximated by the power law

$$\frac{u}{u_{ref}} = \left(\frac{y}{y_{ref}}\right)^{\alpha} \tag{1}$$

in which α describes the strength of the shear profiles gradient du/dy. The grid generated shear flow is approximated by a shear coefficient of $\alpha = 0.11$. Combined with a turbulence intensity of TI_C=10.0%, inflow C resembles conditions measured at an onshore site for a neutral atmospheric boundary layer (Wharton and Lundquist, 2012). In the z-direction, inflow C is measured to be spatially uniform within ±1.0% over the rotor-swept area. The v-component of the flow is observed to be slightly negative for inflow C ranging from v/u_{ref}=[-0.005 -0.080] for all measurement positions. The influence of the negative v-component in the inflow is deemed insignificant for the streamwise velocity u/u_{ref} in the wake. For the analysis of three-dimensional flow effects in the wake the v-component from the inflow is subtracted. All presented mean velocity profiles and turbulence levels are measured in the empty wind tunnel at the reference velocity of $u_{ref} = 10.0 m/s$.

Operating conditions

Figure 3 shows the turbine's measured power and thrust curves for different inflow conditions and yaw angles γ=0° and γ=+30°. In general, power and thrust measurements show very similar behavior for all three inflow conditions as shown in Table 2. Minor differences in the performance curves occur in the transition from stall around λ=3 as previously discussed in Bartl and Sætran (2017).

Performance curves measured for γ=-30° match well with those of γ=+30°, but are not plotted for clarity. For this study, the turbine tip speed ratio is kept constant at its design point at $\lambda_{opt} = 6.0$ for all yaw angles and inflow conditions. For the investigated yaw angles $\gamma = \pm 30°$ the power reduces about 30% compared to the maximum power of the non-yawed turbine. An approximation of this reduction can be obtained with sufficient accuracy by multiplying the maximum power of the non-yawed turbine by $C_{P,A} \cdot cos^3(30°) \approx 0.304$. An adequate estimate of the thrust coefficient of the yawed rotor can be obtained assuming a reduction by $C_{T,A} \cdot cos^2(30°) \approx 0.670$ on the thrust of the non-yawed rotor. This corresponds well to previous measurements by Krogstad and Adaramola (2012).

2.2 Measurement techniques

Power and force measurements

In order to assess the rotor power characteristics, the rotor was installed at another

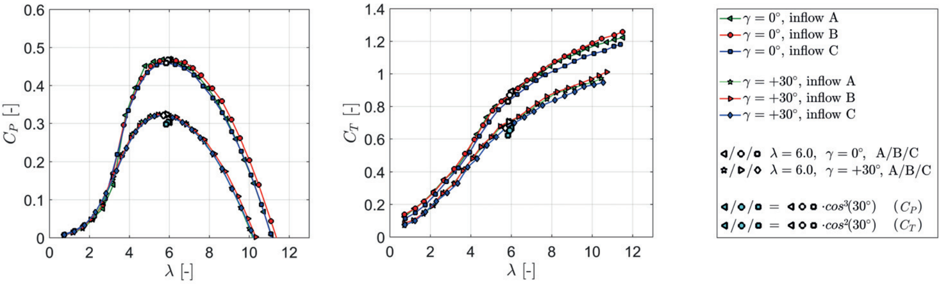

Figure 3: Operating conditions of the model wind turbine: **(a)** power coefficient C_P and **(b)** thrust coefficient C_T for different turbine yaw angels and inflow conditions. The white points indicate the operational conditions, at which wake measurements are performed. Cyan colored points indicate a theoretical power and thrust reduction by yawing of $C_{P,\gamma=0} \cdot cos^3(30°)$ respectively $C_{T,\gamma=0} \cdot cos^2(30°)$.

Table 2: Turbine performance (C_P and C_T) at the optimal operating point ($\lambda = 6.0$) for different yaw angles and inflow conditions.

	Inflow A		Inflow B		Inflow C	
γ [°]	C_P [−]	C_T [−]	C_P [−]	C_T [−]	C_P [−]	C_T [−]
0	0.468	0.893	0.467	0.870	0.459	0.830
+30	0.322	0.707	0.324	0.706	0.321	0.667
-30	0.328	0.711	0.331	0.713	0.327	0.679

test rig equipped with an HBM torque transducer of the type T20W-N/2-Nm. Flexible couplings connect the torque transducer to the rotor shaft. An optical photo cell is installed on the shaft enabling to measure the rotor rotational speed. The friction in the ball bearing between the rotor and torque sensor is measured without the rotor and thereafter subtracted from the total mechanical power. For the wake measurements the rotor is then installed on a smaller nacelle, which interacts less with the flow. The rotational speed is controlled via a servo motor, ensuring the same power characteristics. For measurements of rotor thrust the model turbine is installed on a six-component force balance produced by Carl Schenck AG.

Flow measurements

The wake flow was measured with a two-component DANTEC FiberFlow Laser Doppler Anemometer (LDA) system used in Differential Doppler Mode. The laser was set up to record the streamwise flow component u as well as the vertical flow component v. In order to obtain results for the lateral flow component w, the laser was turned in $u - w$ direction for one wake measurement. The reference coordinate system and measurement grid is shown in Figure 4. 5×10^4 samples are taken for each measurement point over a period of approximately $30s$, resulting in an average sampling frequency of $1666Hz$. A grid consisting of 357 points is scanned for one full wake contour. For that purpose the LDA system is traversed from -1.0D to +1.0D in z-direction and from -0.8D to +0.8D in y-direction. The distance between two measurement points is 0.1D. For further analysis, these values are interpolated to a finer grid of $401 \times 321 \approx 129000$ grid points. The natural neighbor interpolation method is used, which gives a smoother interpolation of the value distribution according to Sukumar (1997).

2.3 Measurement uncertainties

The uncertainty of the measured mean velocity is assessed for every sample following the procedure described in Wheeler and Ganji (2004). The LDA manufacturer Dantec Dynamics specifies the uncertainty on measured velocity by 0.04%. Random errors are computed from repeated measurements of various representative measurement points based on a 95 % confidence interval. In the freestream flow as well as in the wake center the calculated uncertainties are below 1%, while increased uncertainties of up to 4% are calculated in the shear layers. Small inaccuracies in the adjustment of the traversing system are deemed to be the main contributor. The uncertainty in turbulent kinetic energy is computed according to the method proposed by Benedict and Gould (1996). Corresponding to the mean velocity the highest uncertainties up to 5% are found in the shear layer between wake and free stream flow.

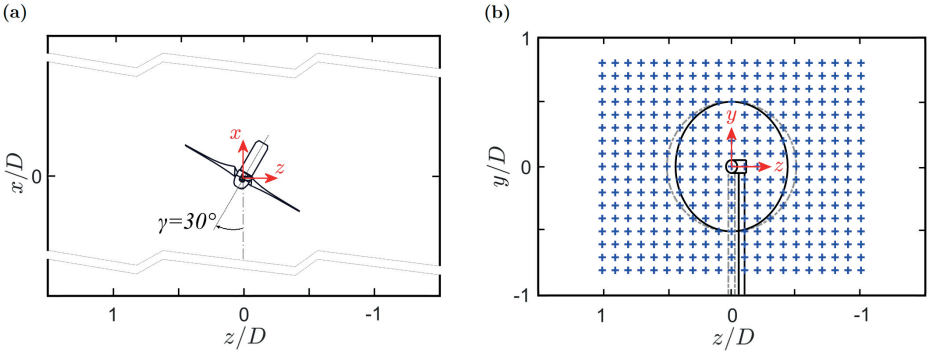

Figure 4: Reference coordinate system in the wind tunnel: **(a)** top view of yawed turbine setup and **(b)** grid for wake measurements.

3 Methods

3.1 Wake shape parametrization

In order to compare the shape of the mean wake for different inflows, the velocity contours are parametrized. The wake contours are therefore sliced into horizontal profiles for each of the 321 interpolated vertical positions. 201 of these 321 velocity profiles are located behind the rotor swept area from y/D=-0.5 to y/D=0.5. These profiles are fitted with an eighth order polynomial to smoothen out local unsteadinesses. Then, an algorithm is applied to locate the z-position of the minimum fitted velocity for each profile. When plotting the z-positions of all these minima versus their y-position, an arc shaped curve is obtained. The curves allow for a direct wake shape comparison depending on inflow condition and yaw angle.

3.2 Wake deflection assessment

As intentional yaw misalignment could possibly be utilized for optimized wind farm control, an exact quantification of the inflow-dependent wake deflection is an important input parameter. However, several methods to quantify the wake deflection have been used in the past, showing a large method-dependent variation in the deflection. Some of these methods are discussed in Section 5. In the present study an available power approach is used, which is deemed to give a solid assessment of the wake deflection. In order to assess the deflection of the wake, the potential power of an imaginary downstream turbine for various lateral offset positions is calculated. The z-position, at which the available power P^* is minimum, is then defined as the position of wake center deflection $\delta(z/D)$. In this study the available power P^* is calculated for 50 different locations ranging from $-0.5 \leq$ z/D ≤ 0.5. The details of the method including an illustration are described in Schottler et al. (2017a).

4 Results

4.1 Mean wake flow

At first the mean wake flows for all three yaw angles $\gamma = [-30, 0, +30]°$, both downstream distances x/D=[3, 6] and all three inflow conditions [A, B, C] are analyzed. Full cross-sectional wake measurements are presented in Figure 5. At the top, the wake flow for inflow A (TI_A=0.23%) is presented. The velocity deficit in the wake is observed to reduce significantly when the turbine is yawed. As the rotor thrust is reduced, a smaller amount of streamwise momentum is lost in x-direction. For a yawed rotor, a cross-stream momentum in z-component is induced. Due to this lateral force component, the wake flow is deflected sideways. This is clearly observed at x/D=3, where the wake is seen to be deflected. Comparing the wake contours at γ=-30° and γ=+30°, an asymmetry in the mean velocity distribution is obvious. The asymmetry between positive and negative wake deflection is even more pronounced at x/D=6, where the wakes are seen to form a kidney shape. Both wake deflection and location of maximum velocity deficit are not symmetric, which is analyzed in more detail in the following sections.

Effects of inflow turbulence

In the center of Figure 5 the mean velocity results of test case B, in which the inflow turbulence level is increased to TI_B=10.0%, are shown. Due to a faster wake recovery the velocity deficits are observed to be smaller for all yaw angles. Increased turbulent mixing smoothened out the gradients between wake and freestream flow compared to test case A. The general wake shape and its lateral deflection for $\gamma = \pm 30°$ is seen to be similar as for the low turbulence inflow. A curled kidney-shaped velocity deficit is also observed at x/D=6 for test case B; however, the curl is not as pronounced as in test case A. Increased mixing might have smoothened the strong gradients in cross-flow direction in this case. The wake behind a positively and negatively yawed turbine appears to feature a higher degree of symmetry than in test case A. Yet an asymmetry of the minimum wake velocity is still obvious for the increased background turbulence level in test case B.

Effects of inflow shear

The wake results for a turbine exposed to inflow shear are shown at the bottom of

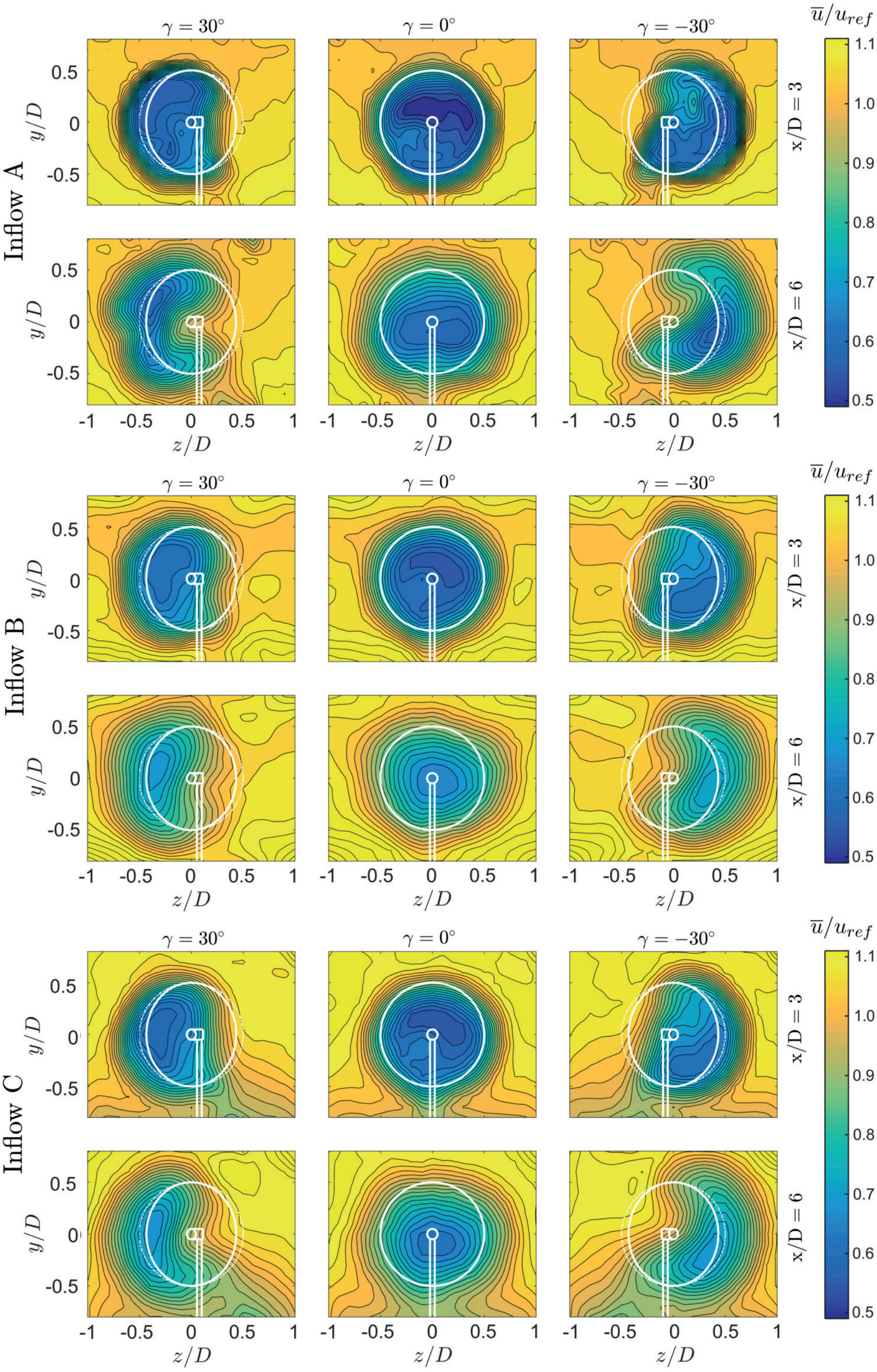

Figure 5: Normalized mean velocity components $\overline{u}/u_{ref}$ for all measured yaw angles $\gamma = [-30, 0, +30]^\circ$, downstream distances x/D=[3, 6] and inflow conditions [A, B, C].

Figure 5. The turbulence level TI_C=10.0% is the same as in test case B, but shear is present in the inflow. Despite the sheared inflow the wake shapes for all three yaw angles and both downstream distances are observed to be very similar to those of test case B. The normalized velocity levels as well as the inner structure of the wake are almost identical. The influence of shear is however only investigated at high inflow turbulence levels, which does not allow for any conclusions at lower inflow turbulence levels. In the freestream region outside the wake the shear is clearly visible, especially the lower half. Compared to test case B, the wake of the tower is detectable in test case C. The tower wake recovery seems to be slower as the freestream fluid near the tunnel floor contains less kinetic energy in test case C.

Curled wake shape

At x/D=6 a kidney-shaped velocity deficit is observed (Figure 5), showing a higher local velocities behind the rotor center. In other words, the maximum wake deflection is found at hub height. The curled kidney shape of the wake can be explained by the formation of a counter-rotating vortex pair, which was previously discussed by Howland et al. (2016) as well as Bastankhah and Porté-Agel (2016). Bastankhah and Porté-Agel also presented a comprehensive explanation by the means of the differential form of the continuity equation. An illustration of the counter-rotating vortex pair at x/D=6 is presented in Figure 6, where the velocity vector $\overrightarrow{u_{yz}}$ as well as the mean streamwise vorticity $\overline{\omega_x}$ are calculated from all three velocity components. The velocity vector in the yz-plane is defined as $\overrightarrow{u_{yz}} = (v, w)$, while the streamwise time-averaged vorticity is defined as $\overline{\omega_x} = \partial v/\partial z - \partial w/\partial y$. As shown in terms of $\overrightarrow{u_{yz}}$ the two vortex centers are formed approximately at the lower and upper boundary of the rotor swept area. The clockwise rotating vortex meets the counter-clockwise rotating vortex in the center behind the wake, leading to strong lateral velocities deflecting the wake sideways.

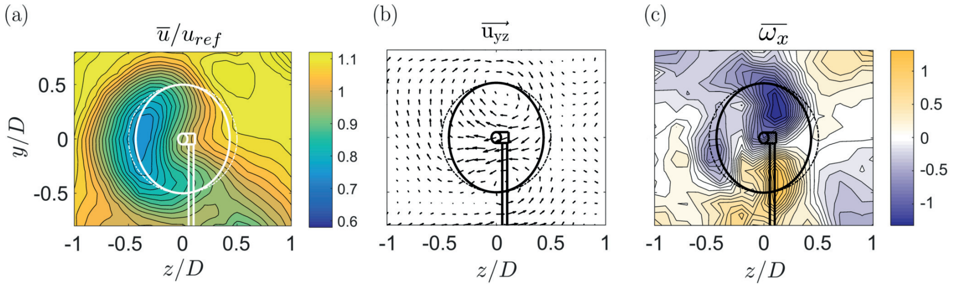

Figure 6: **(a)** Streamwise mean velocity $\overline{u}/u_{ref}$, **(b)** velocity vector $\vec{u_{yz}}$ in the yz-plane and **(c)** streamwise mean vorticity $\overline{\omega_x}$ at $\gamma = 30°$ and $x/D = 6$ at inflow C.

The locations of high rotation are furthermore visualized by increased levels of vorticity $\overline{\omega_x}$ around the vortex centers. The phenomenon of a counter-rotating vortex pair is not limited to rotating wind turbines. Howland et al. (2016) detected the similar large-scale vortices behind a non-rotating drag disc. Counter-rotating vortex pairs have previously been investigated for jet flows exposed to a cross-flow e.g. by Cortelezzi and Karagozian (2001), a phenomenon which can be interpreted is the inverse to the wake flow behind a skewed rotor. In both phenomena the free shear flow, i.e. a wake or a jet, is superimposed with a strong lateral cross-flow, leading to the formation of a counter-rotating vortex pair at higher downstream distances.

Tower wake deflection

On the bottom of the wake contour plot in Figure 6 (a), the wake of the turbine tower is indicated. The tower wake is observed to be deflected in the opposite direction than the rotor wake when the turbine is yawed. The deflection of the tower wake in the opposite direction is believed to have two reasons. Firstly, the turbine tower has a slight offset from z/D=0 as the center of yaw-rotation was set to the rotor midpoint and not the tower. Therefore, a minor offset from the central position is expected for the tower wake. Secondly and more importantly, the tower wake experiences an additional deflection in opposite direction due to an adversely directed cross-flow component outside near the wind tunnel floor as depicted in the vector plot in Figure 6 (b). This cross-flow balances the counter-rotating vortex pair above and possibly deflects the tower wake further to the side.

Wake curl symmetry

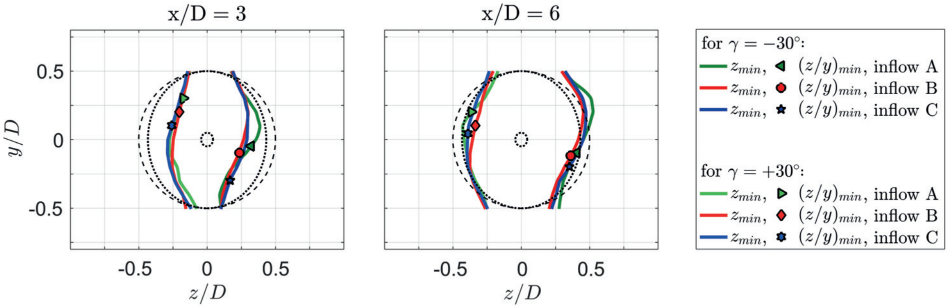

Figure 7: Minimum values in streamwise velocity $\overline{u}/u_{ref}$. Curl shapes and minimum positions are presented at x/D=3 (left) and x/D=6 (right) for the three different inflow conditions.

In order to compare the three-dimensional wake shapes behind a positively versus negatively yawed turbine more quantitatively, the curled shapes of the velocity deficit area are parametrized to a two-dimensional line. For this purpose, the minimum values in streamwise velocity $\overline{u}/u_{ref}$ are extracted from the fitted wake contours for each vertical position ranging from y/D=[-0.5, ..., 0.5]. The detailed method is described in Section 3.1. This results in the z_{min} lines as presented in Figure 7, which indicate the inflow-dependent wake curl. In addition to that, the position of the minimum velocity $(z/y)_{min}$ in both y- and z-direction is extracted and depicted in the plot by different symbols. The z_{min} lines for all inflow conditions are observed to be slightly tilted in clockwise direction for both downstream distances x/D=3 and x/D=6. The counter-clockwise rotating turbine induces an initial clockwise rotation to the wake flow. Superimposing the clockwise wake rotation with the counter-rotating vortex pair thus results in a slightly tilted curled wake shape. As previously mentioned the wake curl is seen to be more asymmetric for the low background turbulence test case A. A significant bulge is visible for γ=-30° in the upper half of the wake for both downstream positions. For inflow conditions B and C the curl parametrization lines are almost coinciding, confirming the insignificant influence of the moderately sheared inflow on the wake shape. Analyzing the locations of minimum velocities $(z/y)_{min}$ in the wake contours, a deviation from the horizontal centerline y/D=0 for both positive and negative yaw angles is obvious. For γ=-30° the minimum velocities $(z/y)_{min}$ are deflected to the lower half of the wake, while an upward deflection happens for positive yaw angles γ=+30°. In agreement with Bastankhah and Porté-Agel (2016), the wake rotation is assumed to turn the velocity minimum in clockwise direction initially. The deflection from the wake centerline is observed to be larger for x/D=3 than for x/D=6, where mixing processes already have smoothened the gradients. In the case of sheared inflow of test case C, the locations of minimum wake velocity $(z/y)_{min}$ are found to be lower than for test cases A and B.

Overall wake deflection

The three-dimensional Available power method is used to quantify the overall deflection of the kinetic energy contained in the wake. As explained in Section 3.2 the minimum available power in a circular area in the wake is located, which is reducing the full wake flow field to a single parameter representing the overall wake deflection. A comparison of the minimum available power in the wakes behind a positively versus negatively yawed turbine enables a comparison of symmetry in the deflection of the energy contained in the wake with respect to the yaw angle. Additionally, a two-dimensional Gaussian fit method for the wake center detection at the turbine's hub-height is used to demonstrate systematic differences in the deflection quantification methods. In order to judge possible blockage effects, another rotor of a smaller diameter ($D_{Rot,small}$=0.45 m, $\sigma_{Blockage,small} = \frac{A_{Rot,small}}{A_{Tunnel}}$=3.3%) was used in addition to the 0.90 m ($\sigma_{Blockage,large}$=12.8%) rotor. The details of the experimental setup featuring the smaller 0.45 m rotor are described in Bartl et al. (2018). Further, the results are compared with two different wake models by Jiménez et al. (2010) (JCM) and Bastankhah and Porté-Agel (2016) (BPA). The recommended default model-parameters were used in the implementation of both wake deflection models. For the JCM-model a linear wake expansion factor of $\beta = 0.125$ was applied, while $k_y = 0.022$, $k_z = 0.022$, $\alpha^* = 2.32$ and $\beta^* = 0.154$ were used in the case of the BPA-model. The comparisons of the wake deflections are shown in Figure 8. At x/D=3 the wake deflection for γ=+30° of the smaller rotor and the original rotor match very well. At x/D=6 a small deviation in the wake deflection after the rotors of different sizes and blockage is calculated. It can be assumed that blockage by the wind tunnel walls influences the wake deflection; however, the difference in deflection between the different rotors is observed to be rather small. Comparing the measured deflection with the prediction models discloses larger deviations. The deflection predicted by the JCM-model is generally observed to be larger than the one predicted by the BPA-model. The calculated wake deflection by the available power method at x/D=3 is still well predicted by the BPA-model, while more significant deviations are observed at x/D=6. Obviously larger differences in wake deflection are predicted by the JCM-model, both at x/D=3 and x/D=6. A number of reasons are possible to cause the significant deviations between measured and modeled deflection results. Besides the discussed wind tunnel blockage, a major source of uncertainty in this comparison arises from the method used to calculate the wake deflection. Quantifying the wake deflection by he minimum of a fitted Gaussian on the hub height velocity profiles results in a better match with the BPA-model at x/D=6 as shown by the red curve in Figure 8. However, using the hub height profile only for the wake center deflection does not take the total mean kinetic energy content in the wake into account. Due to the complex three dimensional shape of the velocity deficit, a reduction of the wake deflection to one single value has been shown to be difficult A number of different methods have been proposed, resulting in many different deflection quantifications (Vollmer et al., 2016). Further, the wake deflection $\delta(z/D)$ for all three inflow conditions is compared. These results are shown in Figure 9 and compared to the BPA-model. In contrast to the JCM-model, the inflow turbulence intensity is an input variable in the BPA-model. It can be observed that the BPA-model predicts a higher wake deflection for a smaller inflow turbulence level. Bastankhah and Porté-Agel (2016) argue that smaller inflow turbulence reduces the flow entrainment in the far wake and thus increases the wake deflection. The calculated lateral deflection

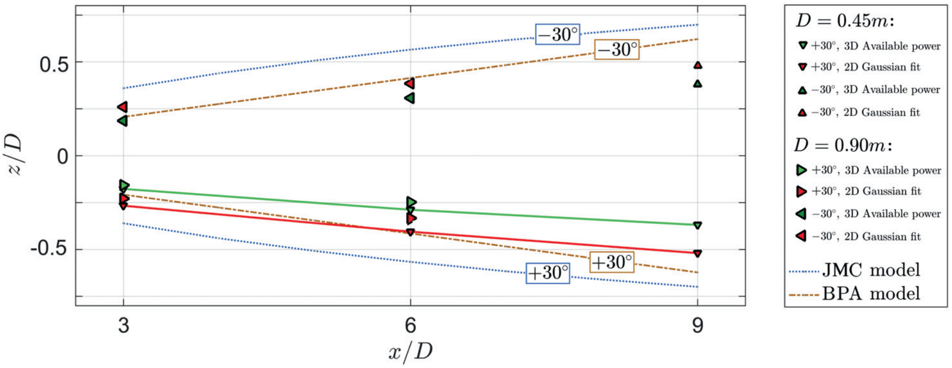

Figure 8: Calculated wake deflection $\delta(z/D)$ for the NTNU rotor ($D = 0.90m$), a downscaled NTNU rotor ($D = 0.45m$) as well as Jiménez et al.'s and Bastankhah and Porte-Agél's wake deflection model. The inflow turbulence level is $TI_A = 0.23\%$.

values $\delta(z/D)$ and the associated wake skew angle ξ are furthermore listed in Table 3.

In general, a very similar wake deflection is observed for all three inflow conditions at both downstream distances. A systematic asymmetry in the wake deflection represented by the minimum available power behind a turbine yawed γ=-30° and γ=+30° is observed. The wake shows a higher deflection for negative yaw angles in all inflow cases. Also the wake behind the non-yawed turbine is seen to be slightly deflected in positive z-direction, which is assumed to stem from the interaction of the rotating wake with the turbine tower. As discussed by Pierella and Sætran (2017) who performed experiments on the same rotor with a larger tower, the tower-wake-interaction leads to an uneven momentum entrainment in the wake. For a non-yawed setup, they observed both a lateral and vertical displacement of the wake vortex center, induced by an interaction with the tower wake. It can therefore be assumed that also the interaction of the counter-rotating vortex pair with the tower wake slightly displaced wake vortex in the yawed cases might be influence by an interaction with the tower wake, which is the only source of asymmetry in an otherwise perfectly symmetrical setup. Increasing the turbulence level from TI_A=0.23% to TI_B=10.00% is found to only have a small influence on the wake deflection. In fact, no difference is detected for γ=-30°. For γ=+30°, however, a slightly smaller wake deflection is calculated for the lower inflow turbulence. This can also be interpreted as a higher degree of asymmetry for low background turbulence. Adding shear to the inflow is not observed to change the wake deflection significantly. This confirms the above-mentioned similarity in wake shapes measured for test cases B and C.

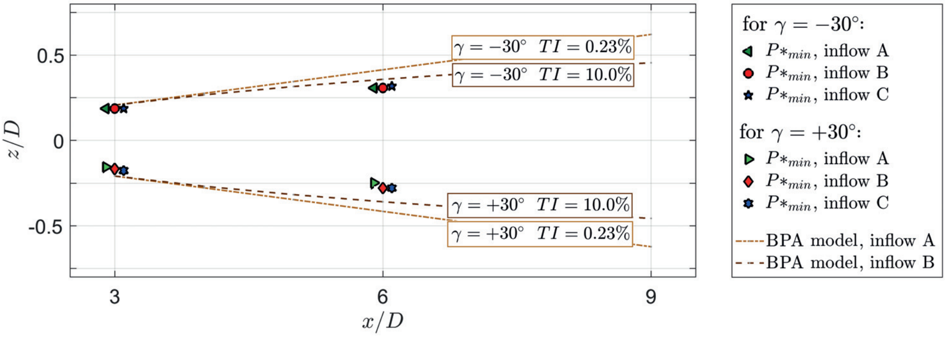

Figure 9: Calculated wake deflection $\delta(z/D)$ at x/D=3 and x/D=6 for three different inflow conditions A, B and C compared to TI-dependent deflection predictions by Bastankhah and Porte-Agél's wake deflection model. Note that a small offset in x/D of the measured values was chosen for better visibility.

Table 3: Lateral deflection $\delta(z/D)$ [−] and wake skew angle ξ [°] calculated with the available power method.

		Inflow A		Inflow B		Inflow C	
γ [°]	x/D [−]	$\delta(z/D)$	ξ [°]	$\delta(z/D)$	ξ [°]	$\delta(z/D)$	ξ [°]
0	3	0.015	0.29	0.005	0.10	0.015	0.29
+30	3	-0.157	-2.99	-0.167	-3.18	-0.177	-3.38
-30	3	0.187	3.57	0.187	3.57	0.187	3.57
0	6	0.026	0.24	0.036	0.34	0.036	0.34
+30	6	-0.248	-2.36	-0.278	-2.65	-0.278	-2.65
-30	6	0.308	2.94	0.308	2.94	0.318	3.03

4.2 Rotor-generated turbulence

For the measurements presented in the this study the kinetic energy is considered to be fully dominated by turbulent motions from $x/D \geq 3$ for inflow A, as Eriksen and Krogstad (2017) recently showed that the production of rotor-generated turbulent kinetic energy is finished at x/D=3 for measurements on the same rotor and inflow condition. For inflow conditions B and C, the transition to fully turbulent motions is expected to take place at even smaller downstream distances.

Effects of yawing on turbulent kinetic energy distributions

At the top of Figure 10 the TKE levels in the wake are presented for test case A (TI_A=0.23%). As observed in earlier studies (Bartl and Sætran, 2017; Eriksen and Krogstad, 2017) a ring of high turbulence levels is formed behind the tips of the rotor blades for a non-yawed turbine. In this region the tip vortices decayed into turbulent motions. With increasing downstream distance the sharp peaks decrease in magnitude and blur out to their surrounding. For a yawed turbine, the ring of peak turbulence is laterally deflected and deformed accordingly. For x/D=3 the peaks are clearly separated by an area of low turbulence in the center of the deflected wake. For x/D=6, this area is observed to be significantly smaller. The peaks are still distinct, but it is expected that they start merging into one peak for higher downstream distances. The strongest TKE levels are observed for locations of the highest gradient in mean streamwise velocity. Thus, the TKE-ring's extension is observed to be slightly larger than the contours of the mean streamwise velocity, emphasizing the need to take the parameter TKE into account in wind farm site planning or yaw control studies.

Effects of inflow turbulence and shear

The TKE contours for increased inflow turbulence of test case B are shown in the center of Figure 10 as well as the red lines in Figure 11. At x/D=3, slightly smaller TKE peaks and higher centerline turbulence are measured for test case B than for test case A. The higher TKE levels in the freestream lead to an increased mixing, which is reducing the TKE peaks in the tip region. At x/D=6 the TKE peaks are observed to be at about the same level for both inflow conditions. For the yawed cases also the turbulence level in the wake center has evened out between inflow cases A and B. The TKE levels for the sheared inflow in test case C are observed to be very similar to those of test case B for all investigated yaw angles. These findings suggest that the presence of a moderate shear flow in a highly turbulent boundary layer does not influence the production of rotor-generated turbulent kinetic energy significantly.

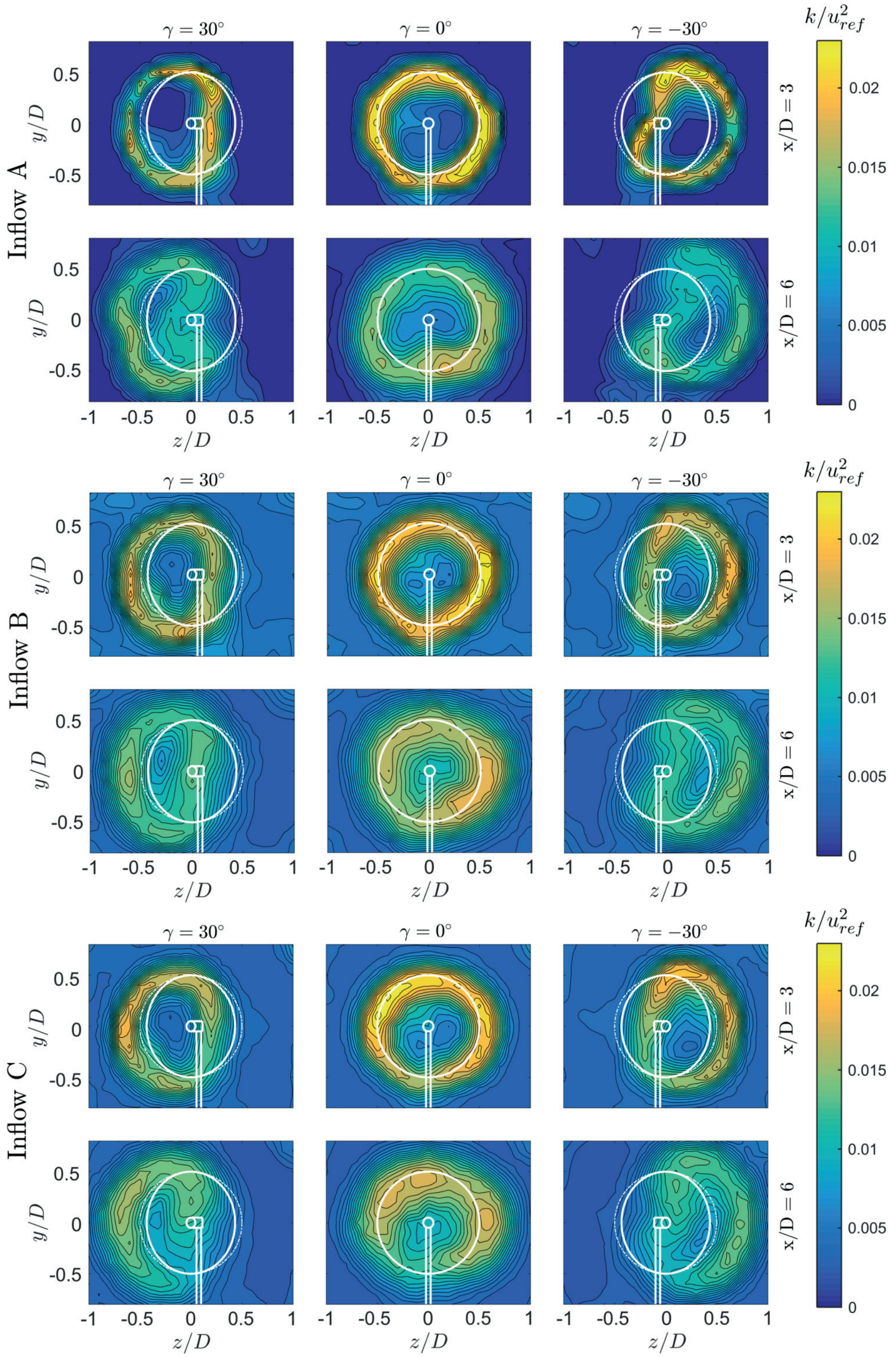

Figure 10: Turbulent kinetic energy k/u_{ref}^2 for all measured yaw angles $\gamma = [-30, 0, +30]^\circ$, downstream distances $x/D = [3, 6]$ and inflow conditions [A, B, C].

Approximation for turbulent kinetic energy distributions in yaw

The levels of peak turbulence are observed to decrease considerably when the rotor is yawed. For a direct case-to-case comparison, TKE-profiles at hub height y=0 at x/D=6 are presented for $\gamma = 0°$ and $\gamma = -30°$ in the lower plots of Figure 11. For a yawed turbine, the rotor thrust reduces with approximately $cos^2(\gamma)$ as previously shown in Figure 3. Multiplying also the TKE levels generated by the non-yawed rotor with $cos^2(\gamma)$ is observed to result in a decent first order approximation of the turbulence levels behind the yawed rotor. The reduced TKE levels for $\gamma = -30°$ are indicated by the chain-dotted lines in the lower left plot of Figure 11. For an approximation of the lateral deflection of the turbulence peaks for yawed rotors, their location can be estimated as proposed by Schottler et al. (2018). In this approach the expected value and standard deviation of a Gaussian fit of the velocity profile behind a yawed rotor is calculated. Adding the standard deviation to the expected value $\mu \pm \sigma_u$ gives a rough estimate of the locations of the corresponding TKE peaks, as shown by the vertical lines in Figure 11. Thus, it is possible to approximate both TKE peak locations and levels by knowing TKE and mean velocity for the now-yawed case. This might be a useful addition for modeling the rotor-generated turbulence in yawed wakes. For a complete assessment of mean velocity and turbulent kinetic energy in a yawed wind turbine wake, the model for streamwise velocity profiles by Bastankhah and Porté-Agel (2016) could be extended by the proposed relations for the rotor generated turbulence.

5 Discussion

The present wind tunnel investigation showed detailed flow measurements in the wake of a yawed model turbine for different inflow conditions. A number of modeling techniques and turbine sizes were used in previous yaw wake studies in the literature, resulting in a significant variation in wake shapes and their deflection. However, a number of general flow effects in the wake behind a yawed turbine seem to be reproducible
Our results indicated minor asymmetries in the wake flow behind positively and negatively yawed turbines. The interference of the modified flow field around the tower and wake rotation is deemed to be the source for this asymmetry. This explanation is consistent with findings by Grant and Parkin (2000), who reported clear asymmetries in the tip vortex shedding and circulation in the wake for positive and negative yaw angles. Our experimental measurements showed a kidney shaped mean velocity deficit at x/D=6 for all inflow conditions. These results agree well with recently discussed experimental results by Howland et al. (2016). Although the wake shape was not

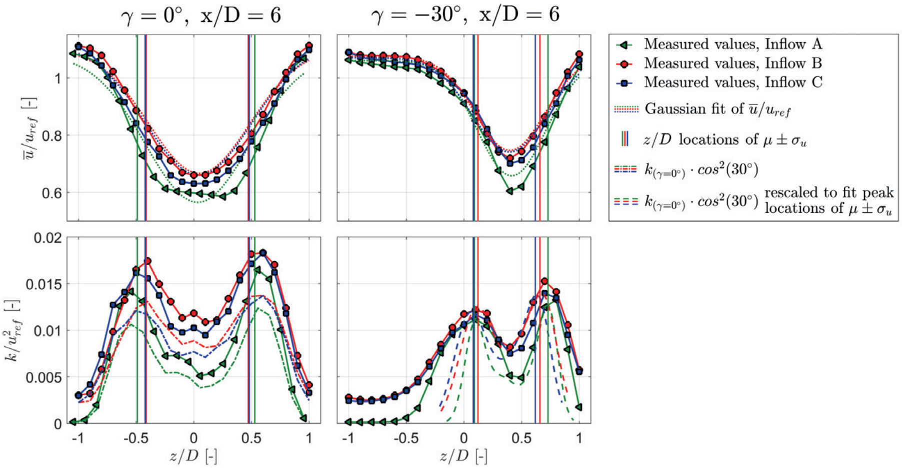

Figure 11: Normalized mean velocity and turbulent kinetic energy k/u_{ref}^2 profiles at hub height $y = 0$ and x/D=6. The yaw angles are set to $\gamma = 0°$ and $\gamma = -30°$. Vertical lines indicate the borders of standard deviations of Gaussian-fitted velocity profiles $\mu \pm \sigma_u$. Chain-dotted lines indicate a TKE profiles at $\gamma = 0°$ multiplied by $cos^2(-30°)$. Dashed lines in the lower right subplot have the same magnitude as the chain-dotted lines, but are linearly scaled in z to fit the peak locations of $\mu \pm \sigma_u$.

specifically discussed, a curled wake shape was already indicated in the results presented by Medici and Alfredsson (2006). The results presented by Bastankhah and Porté-Agel (2016) offer a good comparison as wakes were measured at a number of yaw angles and downstream distances. The wake shape and velocity deficit at $\gamma = \pm 30°$ and x/D=6 match qualitatively well with our results, when an opposite sense of turbine rotation is taken into account. A direct comparison of the wakes at x/D=3 and x/D=6 of the here presented results of test case B with an equivalent setup for a slightly smaller model turbine of different rotor geometry was performed by Schottler et al. (2017b) and Schottler et al. (2018). These results show a more distinct curl in the wake already at x/D=3 while velocity deficit and wake deflection are generally found to be very similar for both model turbines.

Our study moreover indicates that the wake shape and deflection is affected by inflow turbulence. The overall wake deflection was observed to be similar for both investigated turbulence levels. For a more detailed investigation of diffusion mechanisms in the wake, however, a vorticity analysis in the wake of a turbine exposed to low and high turbulence is motivated for future studies. The inflow turbulence is furthermore implemented as an input parameter in the recently developed wake model by Bastankhah and Porté-Agel (2016). The influence of the inflow turbulence seems to be slightly overpredicted by their model, although a more thorough analysis for different yaw angles and downstream distances on a smaller, unblocked rotor are needed for a solid assessment of the model's sensitivity to inflow turbulence. Furthermore, the comparison of the model-predicted deflection and experimentally obtained results is not straightforward. Due to the various different calculation methods used the assessment of the wake center deflection is found to be equivocal. Gaussian fitting to locate the minimum wake velocity was amongst others used by Jiménez et al. (2010) as well as Fleming et al. (2014), while Luo et al. (2015) and Howland et al. (2016) calculated the center of mass of the three-dimensional velocity contour. A comparison of different wake deflection methods was presented by Vollmer et al. (2016), showing the significant method-related variation in deflection quantification.

Another focus of the present study was to assess whether the wake's properties are significantly influenced by sheared inflow. Shear is present in most atmospheric boundary layer flows and highly dependent on stability and the terrain's complexity and roughness. The strength of the investigated shear in test case C is rather moderate and considered typical for a neutral atmospheric boundary layer (Wharton and Lundquist, 2012). As the study investigated only two different shear flows (α_B=0.0 and α_C=0.11), solid statements about the wake flow's sensitivity to this parameter cannot be made. The results do however indicate a rather insignificant effect of such a moderate shear on the wake flow. Possibly, a considerably stronger shear at lower inflow turbulence would have resulted in more distinguishable wake characteristics. In contrast to a recent full-scale LES study by Vollmer et al. (2016), our results seem to shown a rather small dependency of the wake characteristics on the inflow conditions. However, Vollmer et al. (2016) varied four different inflow parameters (turbulence intensity, potential temperature wind shear and veer) simultaneously, which made direct conclusions on the sensitivity to a single inflow parameter difficult. In conclusion, our results do not contradict with their findings as the inflow conditions in both setups were modeled very differently.

6 Conclusions

An experimental study on the inflow-dependent wake characteristics of a yawed model wind turbine was realized. In accordance with previous studies, it is confirmed that intentional turbine yaw misalignment is an effective method to laterally deflect the velocity deficit in the wake and thus offers a large potential for power optimization in wind farms. For the equally important optimization of downstream turbine fatigue loads, a careful planning of wind farm layout and control strategy should thus also take the strength and expansion of rotor-generated turbulence footprints into account. We show that the rotor-generated turbulence distributions are deflected in the same degree as the mean velocity profiles, but feature a slightly wider expansion. Further analysis demonstrated that an increasing yaw angle reduces the levels of the peak turbulence, which is decreasing at a similar rate as the rotor thrust.

The study moreover recommends a consideration of the inflow turbulence level as an important parameter for deflection models implemented in wind farm controllers, as it is affecting the yaw-angle dependent symmetry in shape and deflection. The degree of asymmetry was observed to be higher for lower inflow turbulence. The recently proposed wake deflection model by Bastankhah and Porté-Agel (2016) proved to deliver good approximations of inflow-turbulence-dependent wake deflection. However, more wake measurements at different yaw angles and various downstream distances should be performed to fully assess the model's sensitivity to inflow turbulence. As the influence of a gentle inflow-shear on the wake characteristics was found to be insignificant, an inclusion of this parameter in wake models is thus not considered to be essential at this stage. The experimental results revealed very similar velocity deficit and rotor-generated turbulence distributions to those measured for an uniform inflow.

References

Annoni, J., Gebraad, P., Scholbrock, A., Fleming, P., and van Wingerden, J.-W.: Analysis of axial-induction-based wind plant control using an engineering and a high-order wind plant model, Wind Energy, 19, 113–1150, doi:10.1002/we.1891, 2016.

Barthelmie, R. J., Pryor, S. C., Frandsen, S. T., Hansen, K. S., Schepers, J. G., Rados, K., Schlez, W., Neubert, a., Jensen, L. E., and Neckelmann, S.: Quantifying the impact of wind turbine wakes on power output at offshore wind farms, Journal of Atmospheric and Oceanic Technology, 27, 1302–1317, doi:10.1175/2010JTECHA1398. 1, 2010.

Bartl, J. and Sætran, L.: Experimental testing of axial induction based control strategies for wake control and wind farm optimization, Journal of Physics: Conference Series, 753, 032 035, doi:10.1088/1742-6596/753/3/032035, 2016.

Bartl, J. and Sætran, L.: Blind test comparison of the performance and wake flow between two in-line wind turbines exposed to different turbulent inflow conditions, Wind Energy Science, 2, 55–76, doi:10.5194/wes-2-55-2017, 2017.

Bartl, J., Müller, A., Landolt, A., Mühle, F., Vatn, M., Oggiano, L., and Sætran, L.: Validation of the real-time-response ProCap measurement system for full wake scans behind a yawed model-scale wind turbine, Manuscript submitted to Journal of Physics: Conference Series, DeepWind 2018 Conference, 2018.

Bastankhah, M. and Porté-Agel, F.: Experimental and theoretical study of wind turbine wakes in yawed conditions, Journal of Fluid Mechanics, 806, 506–541, doi: 10.1017/jfm.2016.595, 2016.

Benedict, L. and Gould, R.: Towards better uncertainty estimates for turbulence statistics, Experiments in Fluids, 22, 129–136, doi:10.1007/s003480050030, 1996.

Berdowski, T., Ferreira, C., van Zuijlen, A., and van Bussel, G.: Three-Dimensional Free-Wake Vortex Simulations of an Actuator Disc in Yaw, AIAA SciTech Forum, Wind Energy Synopsium 2018, doi:10.2514/6.2018-0513, 2018.

Cortelezzi, L. and Karagozian, A.: On the formation of the counter-rotating vortex pair in transverse jets, Journal of Fluid Mechanics, 446, 347–373, doi:10.1017/S0022112001005894, 2001.

Eriksen, P. E. and Krogstad, P.-Å.: Development of coherent motion in the wake of a model wind turbine, Renewable Energy, 108, 449–460, doi:10.1016/j.renene.2017.02.031, 2017.

Fleming, P., Gebraad, P., Lee, S., van Wingerden, J.-W., Johnson, K., Churchfield, M., Michalakes, J., Spalart, P., and Moriarty, P.: Evaluating techniques for redirecting turbine wakes using SOWFA, Renewable Energy, 70, 211–218, doi:10.1016/j.renene.2014.02.015, 2014.

Fleming, P., Gebraad, P., Lee, S., van Wingerden, J.-W., Johnson, K., Churchfield, M., Michalakes, J., Spalart, P., and Moriarty, P.: Simulation comparison of wake mitigation control strategies for a two-turbine case, Wind Energy, 18, 2135–2143, doi:10.1002/we.1810, 2015.

Fleming, P., Annoni, J., Churchfield, M., Martinez, L., Gruchalla, K., Lawson, M., and Moriarty, P.: From wake steering to flow control, Wind Energ. Sci. Disc., doi:10.5194/wes-2017-52, 2017.

Gebraad, P. M. O., Fleming, P. A., and van Wingerden, J. W.: Comparison of Actuation Methods for Wake Control in Wind Plants, American Control Conference, doi:10.1109/ACC.2015.7170977, 2015.

Gebraad, P. M. O., Teeuwisse, F. W., van Wingerden, J. W., Fleming, P. A., Ruben, S. D., Marden, J. R., and Pao, L. Y.: Wind plant power optimization through yaw control using a parametric model for wake effects-a CFD simulation study, Wind Energy, 19, 95–114, doi:10.1002/we.1822, 2016.

Grant, I. and Parkin, P.: A DPIV study of the trailing vortex elements from the blades of a horizontal axis wind turbine in yaw, Experiments in Fluids, 28, 368–376, doi:10.1007/s003480050, 2000.

Grant, I., Parkin, P., and Wang, X.: Optical vortex tracking studies of a horizontal axis wind turbine in yaw using laser-sheet, flow visualisation, Experiments in Fluids, 23, 513–519, doi:10.1007/s003480050, 1997.

Haans, W., Sant, T., van Kuik, G., and van Bussel, G.: Measurement of Tip Vortex Paths in the Wake of a HAWT Under Yawed Flow Conditions, Journal of Solar Energy Engineering, 127, 456–463, doi:10.1115/1.2037092, 2005.

Howland, M. F., Bossuyt, J., and Mart, L. A.: Wake Structure of Wind Turbines in Yaw under Uniform Inflow Conditions, Journal of Renewable and Sustainable Energy, 8, 043 301, doi:10.1063/1.4955091, 2016.

Jiménez, Á., Crespo, A., and Migoya, E.: Application of a LES technique to characterize the wake deflection of a wind turbine in yaw, Wind Energy, 13, 559–572, doi:10.1002/we.380, 2010.

Knudsen, T., Bak, T., and Svenstrup, M.: Survey of wind farm control—power and fatigue optimization, Wind Energy, 18, 1333–1351, doi:10.1002/we.1760, 2014.

Krogstad, P.-Å. and Adaramola, M. S.: Performance and near wake measurements of a model horizontal axis wind turbine, Wind Energy, 15, 743–756, doi:10.1002/we.502, 2012.

Luo, L., Srivastava, N., and Ramaprabhu, P.: A Study of Intensified Wake Deflection by Multiple Yawed Turbines based on Large Eddy Simulations, AIAA SciTech Forum, (AIAA 2015-0220), doi:10.2514/6.2015-0220, 2015.

Medici, D. and Alfredsson, P. H.: Measurements on a wind turbine wake: 3D effects and bluff body vortex shedding, Wind Energy, 9, 219–236, doi:10.1002/we.156, 2006.

Pierella, F. and Sætran, L.: Wind tunnel investigation on the effect of the turbine tower on wind turbines wake symmetry, Wind Energy, doi:10.1002/we.2120, 2017.

Schepers, J. G.: An Engineering Model For Yawed Conditions, Developed On Basis Of Wind Tunnel Measurements, American Institute of Aeronautics and Astronautics, 99-0039, 164–174, doi:10.2514/6.1999-39, 1999.

Schepers, J. G., K. Boorsma, K., and Munduate, X.: Final Results from Mexnext-I: Analysis of detailed aerodynamic measurements on a 4.5 m diameter rotor placed in the large German Dutch Wind Tunnel DNW, Journal of Physics: Conference Series, 555, 012 089, doi:10.1088/1742-6596/555/1/012089, 2014.

Schottler, J., Hölling, A., Peinke, J., and Hölling, M.: Wind tunnel tests on controllable model wind turbines in yaw, AIAA 34th Wind Energy Symposium, p. 1523, doi:10.2514/6.2016-1523, 2016.

Schottler, J., Hölling, A., Peinke, J., and Hölling, M.: Brief communication: On the influence of vertical wind shear on the combined power output of two model wind turbines in yaw, Wind Energy Science, 2, 439–442, doi:10.5194/wes-2-439-2017, 2017a.

Schottler, J., Mühle, F., Bartl, J., Peinke, J., Adaramola, M. S., Sætran, L., and Hölling, M.: Comparative study on the wake deflection behind yawed wind turbine models, Journal of Physics: Conference Series, 854, 012 032, doi:10.1088/1742-6596/854/1/012032, 2017b.

Schottler, J., Bartl, J., Mühle, F., Sætran, L., Peinke, J., and Hölling, M.: Wind tunnel experiments on wind turbine wakes in yaw: Redefining the wake width, In review in Wind Energ. Sci. Discuss., doi:10.5194/wes-2017-58, 2018.

Sukumar, N.: A Note on Natural Neighbor Interpolation and the Natural Element Method (NEM), Theoretical and Applied Mechanics, Northwestern University, IL 60208, (last access: 25 February 2017), 1997.

Thomsen, K. and Sørensen, P.: Fatigue loads for wind turbines operating in wakes, Journal of Wind Engineering and Industrial Aerodynamics, 80, 121–136, doi:10.1016/S0167-6105(98)00194-9, 1999.

Vollmer, L., Steinfeld, G., Heinemann, D., and Kühn, M.: Estimating the wake deflection downstream of a wind turbine in different atmospheric stabilities: an LES study, Wind Energy Science, 1, 129–141, doi:10.5194/wes-1-129-2016, 2016.

Wang, J., Foley, S., Nanos, E. M., Yu, T., Campagnolo, F., Bottasso, C. L., Zanotti, A., and Croce, A.: Numerical and Experimental Study of Wake Redirection Techniques in a Boundary Layer Wind Tunnel, Journal of Physics: Conference Series, 854, 012 048, doi:10.1088/1742-6596/854/1/012048, 2017.

Wharton, S. and Lundquist, J. K.: Assessing atmospheric stability and its impacts on rotor-disk wind characteristics at an onshore wind farm, Wind Energy, 15, 525–546, doi:10.1002/we.483, 2012.

Wheeler, A. J. and Ganji, A. R.: Introduction to engineering experimentation, Upper Saddle River, NJ, USA, Pearson/Prentice Hall, XI, third edition edn., 2004.

PAPER VI

Wind tunnel study on power and loads optimization of two yaw-controlled model wind turbines

Jan Bartl[1], **Franz Mühle**[2] **and Lars Sætran**[1]

[1] Department of Energy and Process Engineering, Norwegian University of Science And Technology, Trondheim, Norway
[2] Faculty of Environmental Sciences and Natural Resource Management, Norwegian University of Life Sciences, Ås, Norway

Corresponding Author: Jan Bartl (jan.bartl@ntnu.no)

Abstract. In this experimental wind tunnel study the effects of intentional yaw misalignment on the power production and loads of a downstream turbine are investigated for full and partial wake overlap situations. Power, thrust force and yaw moment are measured on both the upstream and downstream turbine. The influence of inflow turbulence level and streamwise turbine separation distance are analyzed for full wake overlap situations. For partial wake overlap the concept of downstream turbine yawing for yaw moment mitigation is examined for different lateral offset positions.

Results indicate that upstream turbine yaw misalignment is able to increase the combined power production of the two turbines for both partial and full wake overlap setups. For aligned turbine setups the combined power is increased between 3.5% and 11% depending on the inflow turbulence level and turbine separation distance. The increase in combined power is at the expense of increased yaw moments on both upstream and downstream turbine. For partial wake overlap situations, yaw moments on the downstream turbine can be mitigated through upstream turbine yawing, while simultaneously increasing the combined power production. A final test case demonstrates the concept of opposed downstream turbine yawing in partial wake situations, which is shown to reduce its yaw moments and increasing its power production by up to 5%.

1 Introduction

In wind farms the individual wind turbines interact aerodynamically through their wakes. Besides significant power losses, rotors exposed to upstream turbines' wakes experience higher unsteady loading (Kim et al., 2015). The reduced power and increased rotor loads are dependent on the downstream turbine's lateral and streamwise location in the wake, the upstream turbine's control settings and the characteristics of the incoming wind. The inflow characteristics are governed by the atmospheric stability, in which the turbulence level as well as the degree of shear and veer are important parameters. In combination with the wind farm layout, the site dependent wind statistic, such as wind speed and direction distributions, define the occurrence for downstream turbines to be fully or partially exposed to the upstream turbine's wake. In order to mitigate power losses and wake induced loads on downstream turbines, different upstream turbine control strategies have recently been suggested (Gebraad et al., 2015; Knudsen et al., 2014). These include methods to reduce the axial-induction of an upstream turbine and thus also mean and turbulent gradients in the wake (Annoni et al., 2016; Bartl and Sætran, 2016) as well as wake redirection techniques (Fleming et al., 2015). The most discussed wake deflection mechanisms include individual pitch angle control, tilt angle variation and yaw angle actuation. In a computational fluid dynamics (CFD) study Fleming et al. (2015) compare these techniques with regards to power gains and blade out-of-plane bending loads on a two turbine setup. Individual pitch control was observed to cause high structural loads. Most current turbine designs do not feature tilt mechanisms, while yaw actuation is concluded to be a promising technique due to its simple implementability. As all modern wind turbines are equipped with yaw actuators, intentional yaw misalignment can be used to laterally deflect the wake flow and potentially increase the wind farm power output.

A number of recent research focused on the wake characteristics behind a yawed wind turbine. In a combined experimental and computational study Howland et al. (2016) measured the wake of yawed small drag disc and conducted a Large-Eddy-Simulation (LES) behind an actuator disc/line modeled rotor. They discussed different quantifications for wake deflection and characterized the formation of a curled wake shape due to a counter-rotating vortex pair. A similar wake shape was found in a LES study by Vollmer et al. (2016), who found a significant variation of wake shape and deflection depending on the atmospheric stability. The yawed wake characteristics' dependency on inflow turbulence and shear were investigated in an experimental study by Bartl et al. (2018). The inflow turbulence level was observed to influence the shape and deflection of the wake, in contrast to a moderate shear in the inflow. Schottler et al. (2018) highlight the importance of considering non-Gaussian distributions of velocity increments in wind farm control and layout optimizations. A ring of strongly intermittent flow is shown to surround the mean velocity deficit locations, suggesting a much wider wake expansion as based on the mean velocity. An extensive theoretical and experimental study on yaw wakes was performed by Bastankhah and Porté-Agel (2016). They presented a theoretical description for the formation of the counter-rotating vortex pair in the wake and developed a sophisticated analytical model for the far wake of a yawed turbine. Including inflow turbulence as an additional input parameter makes Bastankhah and Porté-Agel's model a favorable alternative to the wake deflection model by Jiménez et al. (2010).

Moreover, various research investigated the potential of overall wind farm power gains through intentional yaw misalignment. An experimental study by Adaramola and Krogstad (2011) on two aligned model wind turbines ($x/D = 3$) demonstrated an increase in combined efficiency with increasing upstream turbine yaw angle. For a yaw angle of 30°, they measured an increase of 12% in combined power compared to the reference case at 0°. For the same separation distance Schottler et al. (2015) measured a combined power increase of about 4% for an upstream turbine yaw angle of $-18°$. Their experimental study on two aligned model turbines furthermore pointed out clear asymmetries of the downstream turbine power output with regards to the upstream turbine yaw angle. Another experimental study on three model wind turbines was presented by Campagnolo et al. (2016), who measured a combined power increase of 21% for an lateral offset of $\Delta z/D = 0.45$ between the turbines. Comprehensive studies on yaw misalignment for optimized full wind farm control haven been presented by Fleming et al. (2014) and Gebraad et al. (2016). They analyzed wake mitigation strategies by using both the LES code SOWFA as well as a parametric wake model. A dedicated full-scale study by McKay et al. (2013) investigated the connection of yaw alignment and power output of a downstream turbine operated in the wake of an upstream turbine. They found an independent yaw alignment for the purpose of individual power increase of downstream turbines operated in partial wake situations. Most of these studies focus on the possibilities for power optimization through yaw control; however, the discussion of increased structural loads is often left open. Yet, yaw misalignment of an undisturbed turbine was observed to create increased unsteady loading on the yawed rotor. In a simulation by Kragh and Hansen (2014) these loads are quantified for different inflow conditions. It is furthermore shown that load variations due to wind shear can potentially be alleviated by yaw misalignment. Load characteristics on a yawed model turbine rotor were compared to various computational approaches by Schepers et al. (2014). The so-called Mexnext project revealed modeling deficiencies while shedding light on complex unsteady flow phenomena during yaw. In a recent paper by Damiani et al. (2017) damage equivalent loads and extreme loads under yaw misalignment are measured and predicted for a fully instrumented wind turbine. They observed rather complex, inflow-dependent load distributions for yaw angle offsets. In a computational setup of ten aligned, non-yawed wind turbines Andersen et al. (2017) recently investigated the influence of inflow velocity, turbulence intensity and streamwise turbine spacing on the yaw moments and other equivalent loads on downstream turbines operated in the wake. The study shows up unexpected load peaks for every second or third downstream turbine in below-rated operating conditions. A way to utilize measured rotor loads such as yaw moments to estimate rotor yaw misalignment, inflow shear or partial wake rotor operation is investigated by

Schreiber et al. (2016). Using a computational framework of a wake model, BEM model for power and loads and a gradient-based optimizer van Dijk et al. (2017) investigated the effects of yaw misalignment on power production and loads in full and partial wake overlap situations. They found that upstream turbine yaw-misalignment is able to increase the total power production of their modeled wind farm, while reducing the loads in partial wake overlap situations.

The objective of the present study is to analyze potentials of yaw control for the often contradicting goals of combined power gains and load mitigation. Balancing the benefits of power gains and costs of increased rotor loads is of utmost importance for the design of cost-effective wind farm control strategies. For this purpose the parameters turbine separation distance x/D, lateral turbine offset $\Delta z/D$ and turbine yaw settings γ_{T1} and γ_{T2} are systematically varied in this wind tunnel experiment. Special focus is given to the concept of downstream turbine yawing in partial wake situations for the purpose of load reduction and combined power gains. Together with the inflow-dependent wake flow measurements on the same experimental setup presented in Bartl et al. (2018), this study completes the link between detailed wake flow characteristics and power, yaw moments and thrust forces on a turbine operated in the wake.

2 Experimental setup

2.1 Wind turbine models

Two wind turbine models of the exactly same rotor geometry were used for this study. The rotor was designed based on the NREL S826 aifoil and has a total diameter of $D = 0.894\,m$. The tower and nacelle structure of the upstream turbine (T1) is slightly slimmer than that of the downstream turbine (T2), in order to minimize the effect on the wake flow behind the yawed upstream turbine. The maximum power point of both turbines is reached at a tip speed ratio of $\lambda_{T1} = \lambda_{T2} = 6.0$ in undisturbed inflow. In this experiment T2 is controlled to its optimum power point, which strongly varies for different positions and upstream turbine operational parameters. The exact geometry and detailed performance curves of T1 are described in Bartl et al. (2018), while T2's characteristics can be found in Bartl and Sætran (2017). In contrast to most other turbines, the investigated model turbines rotate counter-clockwise. Positive yaw is defined as indicated in Figure 2.

The experiments were performed in the closed-loop wind tunnel at the Norwegian University of Science and Technology (NTNU) in Trondheim, Norway. The tunnel's cross-section measures $2.71\,m$ in width, $1.81\,m$ in height and $11.15\,m$ in length. The turbine models are operated at a blade tip Reynolds numbers of approximately

$Re_{\text{tip}} \approx 10^5$.

Moreover, about 12.8% of the wind tunnel's cross sectional area are blocked by the turbines' rotor swept area. The wind tunnel width measures about three times the turbine's rotor diameter, which leaves sufficient space for lateral wake deflection and offset positions for T2. However, a speed-up of the flow in free-stream areas around the rotors is observed due to blockage effects as described in detail in Bartl et al. (2018).

2.2 Inflow conditions

The influence of different inflow turbulence levels is investigated in this study. For this purpose the turbines are exposed to an inflow of very low turbulence intensity $TI_A = 0.23\%$ (Inflow A) as well as high turbulence intensity $TI_B = 10.0\%$ (Inflow B). Inflow B is generated by a static grid at the wind tunnel inlet. The grid-generated turbulence decays with increasing downstream distance to about $TI_B = 5.5\%$ at $x/D = 3$ and to $TI_B = 4.0\%$ at $x/D = 6$. The profiles of streamwise mean velocity and turbulence intensity measured in the empty wind tunnel for different downstream positions are presented in Bartl et al. (2018). Inflow A is assessed to be uniform within ±0.8% over the rotor swept area. A velocity variation of ±2.5% is measured at $x/D = 0$ for Inflow B, as the footprint of the grid's single bars are still detectable At $x/D = 3$, however, the grid-generated turbulent flow is seen to be uniform within ±1.0%. Both test cases were performed at the constant reference velocity of $u_{ref} = 10.0 m/s$.

2.3 Measurement techniques

The mechanical power on both rotors was measured in separate steps with a HBM torque transducer of the type T20W-N/2-Nm, which is installed in the nacelle of the downstream turbine T2. The transducer is connected to the rotor shaft through flexible couplings. An optical photo cell inside the nacelle makes the rotor's rotational speed assessable. On the test rig of T1 the rotational speed is controlled via a servo motor, ensuring the same power and load characteristics as for T2.

For the purpose of thrust force and yaw moment measurements the model turbines are separately installed on a six-component force balance by Carl Schenck AG. By constantly recording signals obtained from the three horizontal force cells, the yaw moments referred to the rotor center can be calculated. For the assessment of the rotor thrust, the drag force on tower and nacelle is measured isolated and then subtracted from the total thrust. No such correction is applied for the assessment of the yaw moments.

2.4 Statistical measurement uncertainties

The statistical measurement uncertainties for power coefficients, thrust coefficient and normalized yaw moments have been calculated following the procedure described by Wheeler and Ganji (2004). Random errors are computed from repeated measurements of various representative measurement points based on a 95 % confidence interval. Furthermore, the match of power and thrust values of the baseline cases (e.g. $\gamma_{T1} = 0°$, $x/D = 3$, $\Delta z/D = 0$) with previous results e.g. by Bartl and Sætran (2016, 2017) has been checked for consistency.

For the purpose of clarity, errorbars are not shown in the resulting graphs in Section 3. Instead, a short overview of uncertainties for the different measures is given here. The total uncertainty in T1's power coefficient is 0.011 (1.9%) for non-yawed operation, rising up to about 0.017 (3.9%) for a yaw angle of $\gamma_{T1} = 30°$. The uncertainty in T1's thrust coefficient is assessed to be very similar, varying from 0.013 (1.4%) to 0.018 (3.1%) for yaw angles 0° and ±40°, respectively. The uncertainty in normalized yaw moments M_y^* is 0.0032, which corresponds to almost 15% of the absolute measurement value at $\gamma_{T1} = 30°$. Due to very small absolute values of the yaw moments, the relative uncertainty is rather high. In the case of T2, the uncertainties are presented representatively for the aligned test case, in which the upstream turbine is operated at $\gamma_{T1} = 30°$ and T2 located at $x/D = 3$ and operated at $\gamma_{T2} = 0°$. The total uncertainties in power and thrust coefficient are 0.006 (2.5% of the absolute C_P-value) respectively 0.007 (0.9% of the absolute C_T-value). The normalized yaw moment of the downstream turbine for this case is amounts 0.0019 (about 8% of the absolute value).

2.5 Test case definition

Three main test cases are investigated in this study. In a first test case the two model turbines are installed in an aligned arrangement in the wind tunnel, i.e. T2 is immersed in the full wake of T1 (for $\gamma_{T1} = 0°$). The upstream turbine's yaw angle is then systematically varied at nine different values γ_{T1} = [-40°, -30°, -20°, -10°, 0°, +10°, +20°, +30°, +40°]. Moreover, the streamwise separation distance between the turbines is varied from x/D=3 to x/D=6. Finally, the inflow turbulence intensity is varied from $TI_A = 0.23\%$ (Inflow A) to $TI_B = 10.0\%$ (Inflow B).

In a second test case, the effect of the lateral offset position $\Delta z/D$ of the downstream turbine T2 in the wake of an upstream turbine T1 is investigated. That means that T2 is in most cases exposed to partial wake situations. For this purpose, the lateral

Table 1: Overview of test cases.

Test case		**Parameter variation**	**Inflow turbulence**	**Yaw angle γ_{T1}**
1 (a)	Aligned turbines	γ_{T1} & x/D	0.23%	[-40°,..., +40°]
1 (b)	Aligned turbines	γ_{T1} & x/D	10.0%	[-40°,..., +40°]
2 (a)	Offset turbines	$\Delta z/D$	10.0%	0°
2 (b)	Offset turbines	$\Delta z/D$	10.0%	+30°
3 (a)	Downstream turbine yaw	$\Delta z/D$ & γ_{T2}	10.0%	0°
3 (b)	Downstream turbine yaw	$\Delta z/D$ & γ_{T2}	10.0%	+30°
		Streamwise separation x/D	**Lateral offset $\Delta z/D$**	**Yaw angle γ_{T2}**
1 (a)		3 & 6	0	0°
1 (b)		3 & 6	0	0°
2 (a)		3	[-0.5,...+0.5]	0°
2 (b)		3	[-0.5,...+0.5]	0°
3 (a)		3	[-0.5,...+0.5]	[-30°,...,+30°]
3 (b)		3	[-0.5,...+0.5]	[-30°,...,+30°]

offset is set to seven different positions ranging from $\Delta z/D$ = [-0.50, -0.33, -0.16, 0, +0.16, +0.33, +0.50]. This is done for two upstream turbine yaw angles $\gamma_{T1} = 0°$ and $\gamma_{T1} = +30°$. The turbine separation distance is kept constant at $x/D = 3$ and only the highly turbulent inflow condition (Inflow B) is investigated.

In a third and final test case the downstream turbine yaw angle γ_{T2} is varied as an additional parameter while it is operated at different lateral offset positions $\Delta z/D$. This concept intends to demonstrate the possibility for yaw moment mitigation in partial wake situations by opposed yawing of the downstream turbine. In this test case T2 is therefore operated at 13 different yaw angles ranging from $\gamma_{T2} = [-30°, ..., +30°]$. An overview of all investigated test cases is presented in Table 1.

For all test cases the power coefficient C_P, thrust coefficient C_T and normalized yaw moment M_y^* are assessed on T1 and T2. The power coefficient is the measured mechanical power normalized with the kinetic power of the wind in a streamtube of the same diameter:

$$C_P = \frac{P}{1/8\,\rho\,\pi\,D^2\,U_{ref}^3}. \qquad (1)$$

The thrust coefficient is defined as the thrust force normal to the rotor plane normalized with the momentum of the wind in a streamtube:

$$C_T = \frac{F_T}{1/8\,\rho\,\pi\,D^2\,U_{ref}^2}. \tag{2}$$

The yaw moment M_y is normalized in a similar way as the thrust force with an additional rotor diameter D to account for the normalization of the yaw moment's lever:

$$M_y^* = \frac{M_y}{1/8\,\rho\,\pi\,D^3\,U_{ref}^2}. \tag{3}$$

3 Results

3.1 Operating characteristics of T1

At first the yaw-angle dependent operating characteristics of the upstream wind turbine are presented for two inflow conditions in Figure 1. The model turbine is operated at a tip speed ratio of $\lambda_{T1} = 6.0$ for all yaw angles. The downstream turbine shows the exactly same operating characteristics when operated in undisturbed inflow. For measurements showing the power and thrust coefficient depending on the tip speed ratio λ_{T1} it is referred to Bartl et al. (2018).

At $\gamma_{T1} = 0$ the upstream turbine reaches a power coefficient of about $C_{P,T1} = 0.460$ for both inflow conditions. It is observed that an increase in inflow turbulence results in the same performance characteristics. As discussed by Bartl et al. (2018), the decrease in power coefficient can be approximated $C_{P,\gamma_{T1}=0} \cdot cos^3(\gamma_{T1})$ when the turbine yaw angle is varied. The thrust coefficient's reduction through yawing is observed to match well with $C_{T,\gamma_{T1}=0} \cdot cos^2(\gamma_{T1})$. The normalized yaw moment shows an almost linear behavior around the origin. However, minor asymmetries between positive and corresponding negative yaw angles are observed. These asymmetries are slightly stronger for inflow A ($TI_A = 0.23\%$).

3.2 Test case 1: Aligned turbines

In the first test case both rotors are installed in the center of the wind tunnel at $(y, z) = (0, 0)$ aligned with the main inflow direction. The downstream turbine position is varied from $x/D = 3$ to $x/D = 6$, while the upstream turbine yaw angle is systematically changed in steps of $\Delta\gamma_{T1} = 10°$ from $\gamma_{T1} = [-40°, ..., +40°]$. Figure 2 shows two example cases, in which the downstream turbine is operated in the upstream turbine's wake for $\gamma_{T1} = 0°$ and $\gamma_{T1} = 30°$. The sketched wake flow contours in the xz-plane at

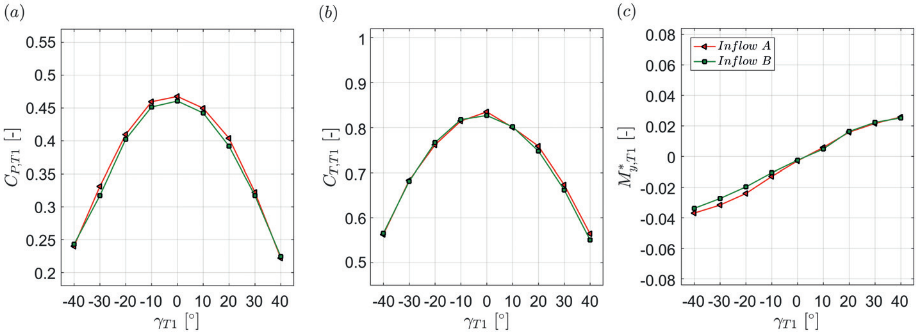

Figure 1: **(a)** Power coefficient $C_{P,T1}$ **(b)** thrust coefficient $C_{T,T1}$ and **(c)** normalized yaw moment $M^*_{y,T1}$ of the undisturbed upstream turbine T1 for different inflow conditions. The turbine is operated at $\lambda_{opt,T1} = 6.0$ for all yaw angles.

hub height are Laser Doppler Anemometry (LDA) measurements of an example case and are only included for illustrative purposes. An exact quantification of the wake can be obtained from cross-sectional measurements in the yz-plane as presented in Bartl et al. (2018).

The results for the downstream turbine $C_{P,T2}$, $C_{T,T2}$ and $M^*_{y,T2}$ at inflow B in dependency of its tip speed ratio λ_{T2} are shown in Figure 3. The downstream turbine's power is observed to increase with an increasing absolute value of the upstream turbine yaw angle. As the wake is laterally deflected, the downstream turbine is partly exposed to higher flow velocities in the freestream. The power recovery of the downstream turbine is observed to be asymmetric with respect to the upstream turbine yaw angle. Higher downstream turbine power coefficients are measured for negative upstream turbine yaw angles. Obviously, the optimum downstream turbine T2's operating point shifts to higher tip speed ratios λ_{T2} the more kinetic energy is available in the wake. A corresponding asymmetry between positive and negative upstream turbine yaw

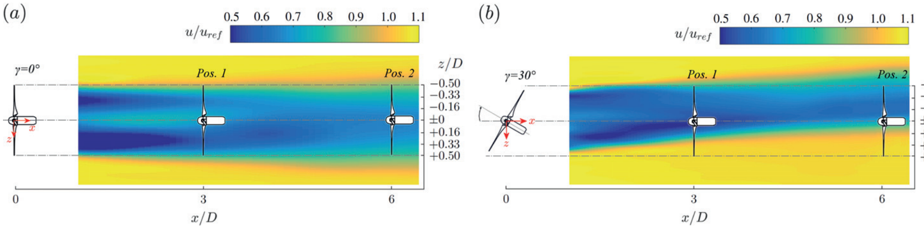

Figure 2: Topview of the aligned downstream turbine operated in the wake of an upstream turbine at the two different positions $x/D = 3$ and $x/D = 6$. The wake flow is indicated by measured example cases for **(a)** $\gamma_{T1} = 0°$ and **(b)** $\gamma_{T1} = 30°$.

angles is also observed in T2's thrust coefficient, showing higher values for negative upstream turbine yaw angles. The yaw moments experienced by the downstream turbine are observed to grow with increasing upstream turbine yaw angle. As expected, downstream turbine yaw moments are positive for positive upstream turbine yaw angles and vice versa. For low tip speed ratios, i.e. during stall the yaw moments are seen to be small and below 0.01. As soon as the flow is attached the absolute value of the yaw moments is observed to strongly rise. Again, an asymmetry between negative and positive upstream turbine yaw angles is observed. The asymmetric wake deflection is considered to be the main reason for the asymmetric distribution of T2's yaw moments.

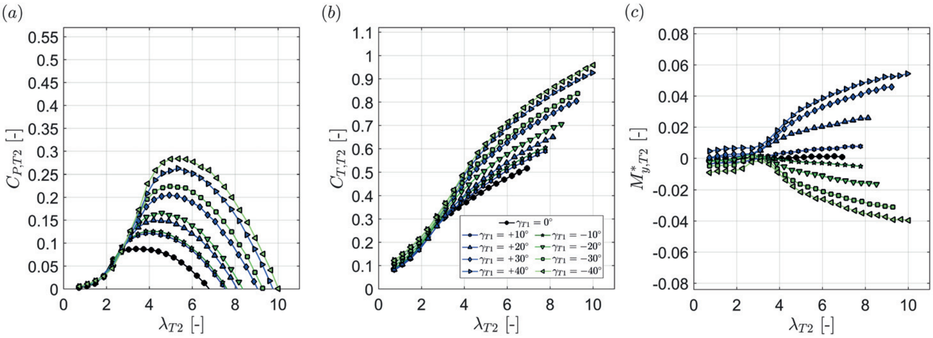

Figure 3: Downstream turbine **(a)** power coefficient, **(b)** thrust coefficient and **(c)** normalized yaw moment as a function of its tip speed ratio λ_{T2} for different upstream turbine yaw angles γ_{T1}. The downstream turbine T2 is located at $x/D = 3$. The turbines are exposed to inflow B.

The effect of a variation in inflow turbulence level ($TI_A = 0.23\%$ versus $TI_B = 10.0\%$) on the downstream turbine's $C_{P,T2}$, $C_{T,T2}$ and $M^*_{y,T2}$ is shown in Figure 4. The results are presented for varying upstream turbine yaw angle γ_{T1}. The downstream turbine T2 is operated at a λ_{T2}, for which $C_{P,T2}$ was maximum for the specific conditions. Note that for $x/D = 6$ neither thrust nor yaw moments were measured.

The downstream turbine's power coefficient $C_{P,T2}$ is in general observed to be higher for a higher inflow turbulence (Inflow B). The wake flow recovers at a higher rate leaving more kinetic energy for the downstream turbine to extract. The difference in T2's power extraction between the two inflow turbulence levels is observed to be highest at small upstream turbine yaw angles γ_{T1}. At high yaw angles $\gamma_{T1} \geq 30°$, however, the power coefficient $C_{P,T2}$ is very similar for the two different inflow turbulence levels. For these high yaw angles the wake's mean velocity deficit has the largest lateral deflection, exposing about half of T2's rotor swept area to the freestream. The kinetic energy content in the freestream is about the same for both inflows, which brings T2's power levels closer together. Moreover, the downstream turbine's power output at low

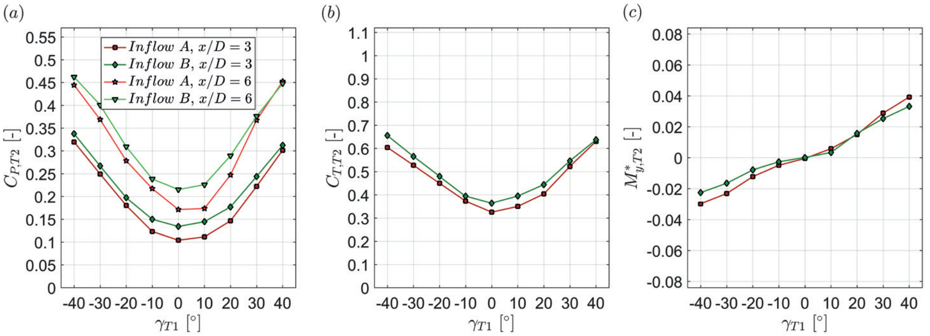

Figure 4: Downstream turbine **(a)** power coefficient, **(b)** thrust coefficient and **(c)** normalized yaw moment as a function of the upstream turbine's yaw angle γ_{T1}. The downstream turbine T2 is located at $x/D = 3$ and $x/D = 6$ respectively. The turbines are exposed to inflows A and B.

inflow turbulence (inflow A) is observed to be more asymmetric with respect to γ_{T1} than at high inflow turbulence (B). Especially for $x/D = 6$, the downstream turbine power $C_{P,T2}$ is strongly asymmetric for inflow A. For extreme yaw angles $\gamma_{T1} = \pm 40°$, T2's power coefficient reaches levels of $C_{P,T2} = 0.45 - 0.46$, which is about the same magnitude of $C_{P,T1}$ at $\gamma_{T1} = 0°$. Although a considerable part of the downstream turbine rotor is impinged by T1's wake, blockage-increase freestream velocity levels of $\overline{u}/u_{ref} = 1.10$ lift the downstream turbine's power to these levels.

Similar trends are observed for the downstream turbine thrust coefficient $C_{P,T2}$ (Figure 4 (b)), where higher thrust forces are measured for the higher turbulence level in Inflow B. Inflow A implicates a higher asymmetry in $C_{T,T2}$ with respect to γ_{T1}. As previously discussed, the downstream turbine yaw moments $M^*_{y,T2}$ are observed to increase with larger upstream turbine yaw angles γ_{T1}. For both inflow cases, the yaw moments' absolute values are seen to be higher for positive γ_{T1} than for negative γ_{T1}. Larger yaw moments are measured for Inflow A than for Inflow B, which possibly stems from stronger mean velocity gradients in the wake flow in Inflow A. The yaw moments $M^*_{y,T2}$ on the downstream turbine located at $x/D = 3$ have approximately the same magnitude as the yaw moments measured on the upstream turbine $M^*_{y,T1}$. Consequently, an intentional upstream turbine yaw misalignment implicates significant yaw moments on the upstream turbine it self as well as an aligned downstream turbine.

A main goal of this study is to find out if upstream turbine yawing can positively affect the total power output. As observed in Figure 1 yawing the upstream turbine reduces its power output, while Figure 4 shows that the downstream turbine's power increases simultaneously. In order to quantify if the gain in T2 power can make up for the losses in T1, we define the combined relative power output of the two turbine array

$$P^{*}_{T1+T2} = \frac{P_{T1}(\gamma_{T1}) + P_{T2}(\gamma_{T1})}{P_{T1,\gamma_{T1}=0} + P_{T2,\gamma_{T1}=0}}. \tag{4}$$

The results for the combined relative power are presented in Figure 5 for both inflow conditions and two turbine separation distances. In all of these four setups an increase in combined power between 3.5% and 11% was measured for upstream turbine yawing. For both turbine spacings, the maximum combined efficiencies were measured for $\gamma_{T1} = -30°$. The combination of a larger wake deflection and a progressed wake recovery at higher separation distances are seen to shift the optimum of the energy balance between T1 and T2 to higher yaw angles γ_{T1}. Moreover, the combined relative power is seen to be asymmetric with higher values for negative yaw angles γ_{T1}. Both, upstream turbine power $C_{P,T1}$ and downstream turbine power $C_{P,T2}$ have seen not to be perfectly symmetrical, the larger portion can however be subscribed to the power extraction of downstream turbine exposed to asymmetric wake flow fields for positive and negative yaw angles. Furthermore, the relative power gains are observed to be significantly larger for lower inflow turbulence levels (Inflow A). Relative power gains of about 11% were measured at Inflow A, while only 8% were obtained for Inflow B at the same yaw angle of $\gamma_{T1} = -30°$.

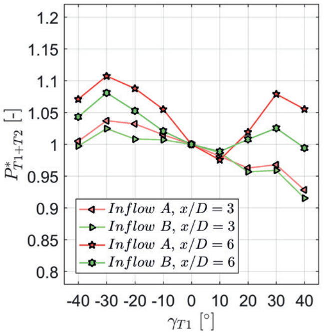

Figure 5: Combined relative power P^{*}_{T1+T2} of two turbines for different upstream turbine yaw angles γ_{T1}. The downstream turbine T2 is located at $x/D = 3$ and $x/D = 6$ respectively. The turbines are exposed to inflows A and B.

3.3 Test case 2: Offset turbines

The power and loads of the downstream turbine T2 are dependent on many different parameters, such as the inflow conditions, the operating point of the upstream turbine

T1, its relative streamwise and lateral position with respect to T1 as well as its operating point. In a second test case we therefore investigate the downstream turbine's performance in lateral offset. That means that T2 experiences partial wake situations. The turbine separation distance is in this test case fixed to $x/D = 3$, while different offset positions $\Delta z/D = [-0.50, -0.33, -0.16, \pm 0, +0.16, +0.33, +0.50]$ are investigated. This is done for Inflow B ($TI_B = 10.0\%$) only, while upstream turbine yaw angles of $\gamma_{T1} = 0°$ and $\gamma_{T1} = +30°$ are investigated. In Figure 6 two example positions of the downstream turbine are sketched, illustrating two different wake impingement situations.

Figure 7 shows the downstream turbine's $C_{P,T2}$, $C_{T,T2}$ and $M^*_{y,T2}$ while operated in the wake of the upstream turbine at $\gamma_{T1} = 0°$ in dependency of its tip speed ratio λ_{T2} and lateral offset position $\Delta z/D$. As expected, the power coefficient is seen to increase with increasing lateral offset $\Delta z/D$ as the downstream turbine is partly exposed to a flow of higher kinetic energy. T2's power coefficient is observed not to be entirely symmetric with respect to its lateral position in the wake. Slightly higher power coefficients are measured for negative offset positions. The reason for this is deemed to be a not perfectly axis-symmetric velocity deficit at $x/D = 3$ as indicated in Figure 6 (a) and Bartl et al. (2018). As observed earlier, T2's optimum operating point shifts to higher tip speed ratios λ_{T2} with increasing kinetic energy being available in the wake. Similar trends are observed for the downstream turbine thrust coefficient $C_{T,T2}$, which was measured to be slightly higher for negative offset positions. The yaw moments experienced by the downstream turbine are seen to increase for larger lateral offsets as the rotor is impinged by stronger mean velocity gradients. The largest increases are detected for a change from $\Delta z/D = \pm 0$ to ± 0.16 and from ± 0.16 to ± 0.33, while a position change from ± 0.33 to ± 0.50 only causes a small increase in yaw moment. The curves are generally observed to be almost symmetric with respect to the offset position, but also show slightly higher absolute values for negative offset positions.

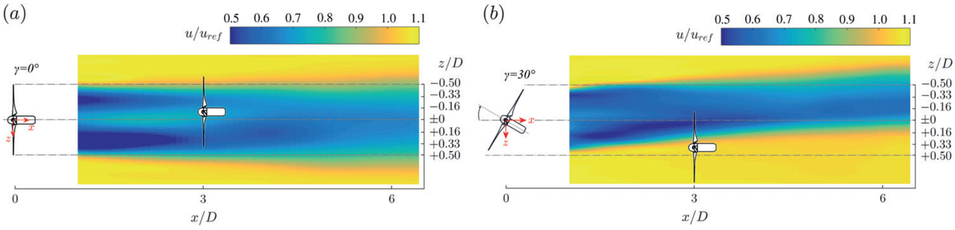

Figure 6: Topview of two lateral offset positions ((**a**) $\Delta z/D = -0.16$ and (**b**) $\Delta z/D = +0.33$) of the downstream turbine while operated in the wake of an upstream turbine at $x/D = 3$. The upstream turbine is operated at (**a**) $\gamma_{T1} = 0°$ and (**b**) $\gamma_{T1} = 30°$.

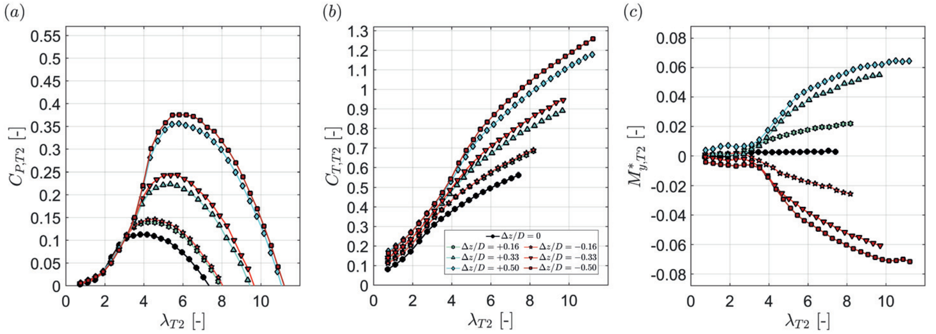

Figure 7: Downstream turbine **(a)** power coefficient, **(b)** thrust coefficient and **(c)** normalized yaw moment as a function of its tip speed ratio λ_{T2} for different lateral offset positions $\Delta z/D$. The upstream turbine yaw angle is kept constant at $\gamma_{T1} = 0°$. The downstream turbine T2 is located at $x/D = 3$. The turbines are exposed to inflow B.

The effect of a variation in upstream turbine yaw angle from $\gamma_{T1} = 0°$ to $\gamma_{T1} = 30°$ on the downstream turbine's characteristics in different lateral offset positions is presented in Figure 8. For the shown results the downstream turbine T2 is operated at a its optimum λ_{T2}, which differs for each offset position.

The red curves summarize the results for $\gamma_{T1} = 0°$ already shown in Figure 7 for their optimum operating point, while the blue curves represent a setup, in which T1 is operated at $\gamma_{T1} = 30°$ (see Figure 6). For this upstream turbine yaw angle, the wake center is shifted to $\Delta z/D = -0.167$ (Bartl et al., 2018) and correspondingly the blue curves minima in $C_{P,T2}$ and $C_{T,T2}$ are shifted to $\Delta z/D = -0.16$ (Figure 8 (a) and (b)). The yaw moment $M^*_{y,T2}$ as depicted in Figure 8 (c) is observed to be around zero for this offset position, as the rotor is approximately impinged by a full wake. For an offset position around $\Delta z/D = +0.16$ to $\Delta z/D = +0.33$ the yaw moments reach a maximum level, as roughly half the rotor swept area is impinged by the low velocity region of the wake, while the other have is impinged by the high velocity freestream flow. At a lateral offset of $\Delta z/D = +0.50$ the yaw moments on T2 are observed to decrease again. A large part of the rotor is exposed to the freestream flow; however, the wake is not yet entirely deflected away from T2. For this offset position the power and thrust coefficient are seen to reach very high levels as the rotor is exposed to a large portion of high kinetic energy freestream flow. A power coefficient of $C_{P,T2} > 0.50$ can be explained by increased freestream velocity levels of $\overline{u}/u_{ref} = 1.10$ (Bartl et al., 2018) caused by wind tunnel blockage. The power and thrust coefficient still are referred to u_{ref} measured $x/D = -2$ upstream of T1.

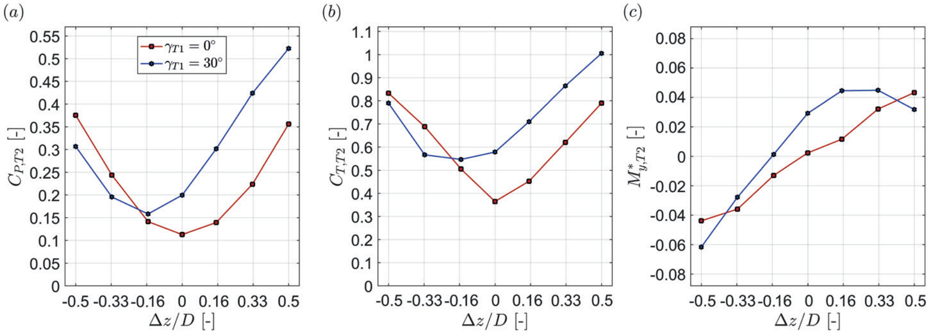

Figure 8: Downstream turbine **(a)** power coefficient, **(b)** thrust coefficient and **(c)** normalized yaw moment as a function of its lateral offset position $\Delta z/D$. The upstream turbine yaw angle is kept constant at $\gamma_{T1} = 0°$. The downstream turbine T2 is located at $x/D = 3$. The turbines are exposed to inflow B.

The combined relative power output of the two-turbine array is in this case calculated for a change of upstream turbine yaw angle from $\gamma_{T1} = 0°$ to $+30°$. It has to be kept in mind, that the upstream turbine power is constant, independent of the downstream turbine position. The combined power for each offset position is calculated as

$$P^*_{T1+T2} = \frac{P_{T1,\gamma_{T1}=30} + P_{T2,\gamma_{T1}=30}(z/D)}{P_{T1,\gamma_{T1}=0} + P_{T2,\gamma_{T1}=0}(z/D)}. \tag{5}$$

Figure 9 shows the resultant combined relative power output. For an offset position of $\Delta z/D = +0.33$ a maximum combined power increase of 13% is measured, as a major part is deflected away from the downstream rotor. Surprisingly, the relative power gains measured for an offset $\Delta z/D = +0.50$ are measured to be smaller, amounting about 6%. This can be explained by significantly larger $C_{P,T2}$-values in the non-yawed case for $\Delta z/D = +0.50$ than for $\Delta z/D = +0.33$, allowing smaller relative gains. For zero lateral offset, about 5% in combined power are lost when yawing T1 to $\gamma_{T1} = +30°$ as previously observed in Figure 5. In the case of the downstream turbine being located at negative offset positions $\Delta z/D$, the wake is deflected directly on T2's rotor, significantly reducing its power output and consequently also the combined power.
In conclusion, is has been demonstrated that intentional upstream turbine yaw control is favorable in offset situations when considering both, the power output and yaw moments on a downstream turbine. Depending on the downstream turbine's streamwise and lateral position, the wake can be partly or even fully deflected away from its rotor swept area.

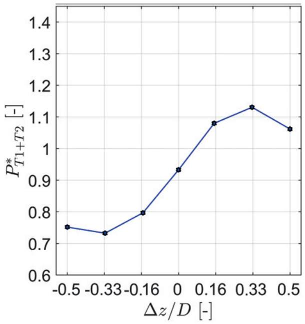

Figure 9: Combined relative power P^*_{T1+T2} of the two-turbine-array for different lateral offset positions $\Delta z/D$. The combined power is calculated for a change of upstream turbine yaw angle from $\gamma_{T1} = 0°$ to $+30°$ for each position. The downstream turbine T2 is located at $x/D = 3$. The turbines are exposed to inflow B.

3.4 Test case3: Downstream turbine yawing

The third and final test case investigates whether a variation in downstream turbine yaw angle γ_{T2} contributes to a yaw-load mitigation and power optimization. As previously seen, both partial wake impingement and turbine yaw misalignment are possible sources for increased yaw moments. An intentional yaw misalignment opposed to the partial wake impingement is therefore considered to cancel out yaw loading on the turbine. For this purpose, the downstream turbine yaw angle is systematically varied from γ_{T2}=$[-30°, ..., +30°]$ in steps of 5° for all seven lateral offset positions and upstream turbine yaw angles γ_{T1}=$[0°, +30°]$. A sketch of two downstream turbine yaw angles at two offset positions is presented in Figure 10.

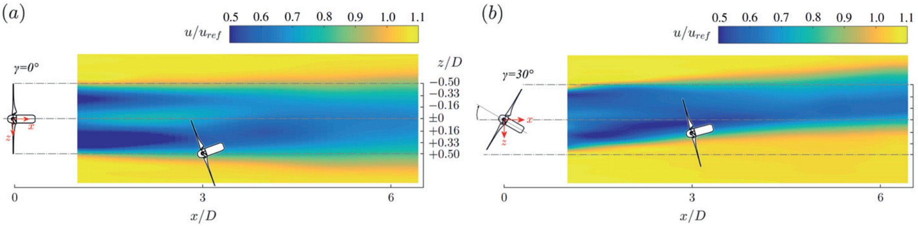

Figure 10: **(a)** Topview of the downstream turbine T2 operated at a lateral offset position $\Delta z/D = +0.50$ and a yaw angle of $\gamma_{T2} = -20°$ in the wake of an upstream turbine T1 operated at $\gamma_{T1} = 0°$. **(b)** Topview of the downstream turbine T2 operated at a lateral offset position ($\Delta z/D = +0.16$) and a yaw angle of $\gamma_{T2} = -15°$ in the wake of an upstream turbine T1 operated at $\gamma_{T1} = 30°$.

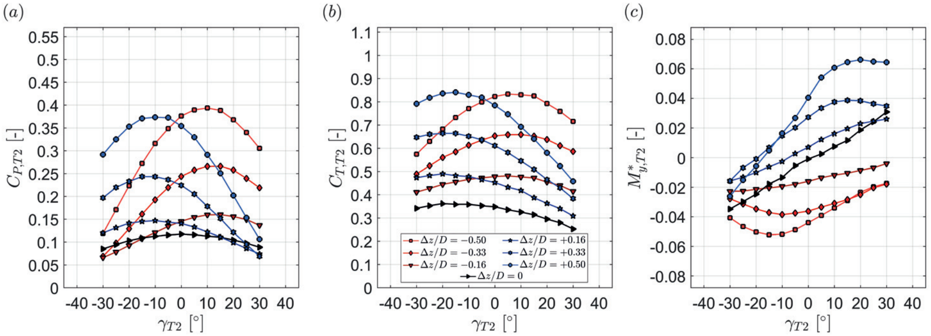

Figure 11: Downstream turbine **(a)** power coefficient, **(b)** thrust coefficient and **(c)** normalized yaw moment as a function of its yaw angle γ_{T2} for different lateral offset positions $\Delta z/D$. The upstream turbine yaw angle is kept constant at $\gamma_{T1} = 0°$. The downstream turbine T2 is located at $x/D = 3$. The turbines are exposed to inflow B.

The resulting $C_{P,T2}$, $C_{T,T2}$ and $M^*_{y,T2}$ of the downstream turbine in dependency of its yaw angle γ_{T2} and lateral offset position $\Delta z/D$ for a constant upstream turbine yaw angle of $\gamma_{T1} = 0°$ are shown in Figure 11. The points for $\gamma_{T2} = 0°$ correspond to the previously shown red lines in Figure 8. In case the downstream turbine rotor is fully impinged by the upstream turbine's wake, i.e. $\Delta z/D = 0$, a variation of its yaw angle γ_{T2} reduces its power output and increases uneven yaw moments. During a lateral offset however, the maximum power output and minimum yaw moments are found for yaw angles $\gamma_{T2} \neq 0°$. At a lateral offset position of $\Delta z/D = +0.16$, for instance, the maximum $C_{P,T2}$ is assessed for $\gamma_{T2} = -10°$. Simultaneously, the yaw moment is measured to be around zero at this yaw angle. The downstream turbine is exposed to a strong shear flow in the partial wake situation, mitigating yaw moments by actively yawing opposed to that shear. The simultaneous power increase for the oppositely yawed downstream rotor is a positive side effect, although the exact reasons for the power increase are not entirely clear at this stage. Higher power outputs and decreased yaw moments are also measured for moderate yaw angles around $\gamma_{T2} = -10°$ at larger lateral offsets of $\Delta z/D = +0.33$ and $\Delta z/D = +0.50$. The slope of the power curves in Figure 11 (a) and yaw moment curves in Figure 11 (c) are observed to be even steeper for larger lateral offsets. The power gains when yawing the turbine from $\gamma_{T2} = 0°$ to $\gamma_{T2} = -10°$ are larger for higher lateral offsets. At the same time, the relative yaw moment reduction is larger, implying that opposed downstream yawing is deemed to be even more effective for higher lateral offsets.

For negative lateral offset positions, obviously the opposite trends are observed, i.e. maximum power and smallest absolute yaw moments are measured for positive downstream turbine yaw angles γ_{T2}. The power output and yaw moment distribution is however not completely symmetrical with respect to yaw angle γ_{T2} and offset position $\Delta z/D$.

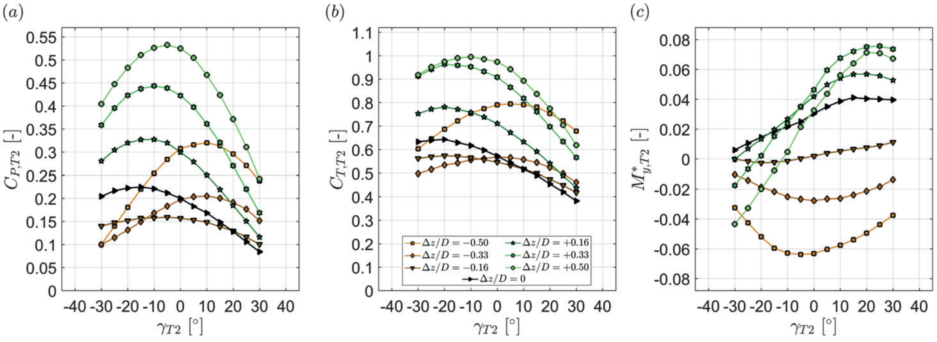

Figure 12: Downstream turbine **(a)** power coefficient, **(b)** thrust coefficient and **(c)** normalized yaw moment as a function of its yaw angle γ_{T2} for different lateral offset position $\Delta z/D$. The upstream turbine yaw angle is kept constant at $\gamma_{T1} = 30°$. The downstream turbine T2 is located at $x/D = 3$. The turbines are exposed to inflow B.

The concept of downstream turbine yawing in partial wake impingement situations is moreover investigated for an upstream turbine yaw angle of $\gamma_{T1} = +30°$. The wake flow features a significantly higher asymmetry in this case. The results for $C_{P,T2}$, $C_{T,T2}$ and $M^*_{y,T2}$ are shown in Figure 12. As previously observed, an offset of $\Delta z/D = -0.16$ approximately corresponds to an impingement of the full wake. Thus, the power coefficient has an almost symmetric distribution with respect to downstream turbine yaw angle γ_{T2}. The yaw moments are observed to be rather low for this offset position and around zero for $\gamma_{T2} = 0$. For partial wake impingement situations at $\Delta z/D \geq 0$, negative downstream turbine yaw angles are again seen to reduce the yaw moments acting on the rotor. The gradients in yaw moment reduction per degree of yaw angle are observed to be steeper for larger lateral offsets. The maximum power coefficients are again measured for moderate downstream turbine yaw angles around $\gamma_{T2} \pm 10°$. Power gains by downstream turbine yawing are assessed by a relative combined power of the two-turbine array

$$P^*_{T1+T2} = \frac{P_{T1} + P_{T2}(\gamma_{T2}, z/D)}{P_{T1,\gamma_{T1}=0,z/D=0} + P_{T2,\gamma_{T1}=0,\gamma_{T2}=0,z/D=0}}. \tag{6}$$

As a reference the power measured for the non-yawed upstream turbine, a non-yawed downstream turbine in an aligned setup ($\Delta z/D = 0$) is used. The results are shown in Figure 13. For an upstream turbine yaw angle of $\gamma_{T1} = 0°$ (Figure 13 (a)) combined power gains of approximately 3% are measured for a moderate downstream turbine yaw angles ($\gamma_{T2} \pm 10 - \pm 15°$). The combined power characteristics are observed to be quite symmetrical with respect to downstream turbine offset and its yaw angle. Slightly higher relative power gains are obtained for the case of an upstream turbine yaw angle of $\gamma_{T1} = +30°$ (Figure 13 (b)). A maximum power gain of about 5% is measured for offset positions $\Delta z/D = 0$ and $+0.16$ and a downstream turbine yaw angle between $\gamma_{T1} = -10°$ and $-15°$.

In conclusion, this third test case demonstrates that moderate downstream turbine yawing can be an effective method to mitigate yaw moments acting on the rotor in partial wake situations, while simultaneously obtaining slight power gains.

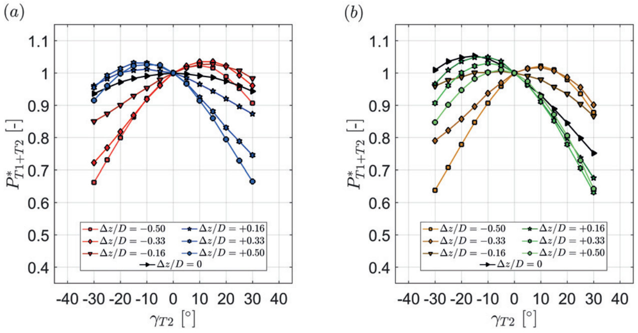

Figure 13: Combined relative power P^*_{T1+T2} of two turbines as a function of the downstream turbine yaw angle γ_{T2} for different lateral offset positions $\Delta z/D$. The upstream turbine yaw angle is kept constant at **(a)** $\gamma_{T1} = 0°$ and **(b)** $\gamma_{T1} = 30°$ respectively. The downstream turbine T2 is located at $x/D = 3$. The turbines are exposed to inflow B.

4 Discussion

When assessing the operational characteristics of the upstream turbine in dependency of its yaw angle, some asymmetries were apparent. While the power and thrust curves only showed slight deviations for positive and the corresponding negative yaw angle, higher asymmetries were found for the yaw moment. Although it is not entirely clear where these stem from, the only reasonable source for an asymmetric load distribution in an uniform inflow is the rotor's interaction with the turbine tower. In the course of a revolution, the blades of a yawed turbine experience unsteady flow conditions, i.e. fluctuations in angle of attack and relative velocity. When superimposing an additional low-velocity zone, tower shadow or shear for example, the yaw-symmetry is disturbed. Asymmetric load distributions for turbines exposed to sheared inflow were recently reported by Damiani et al. (2017). They showed that vertical wind shear causes asymmetric distributions of angle of attack and relative flow velocity in the course of a blade revolution. They link these to rotor loads and conclude further consequences on wake characteristics and wind farm control strategies.

Moreover, our study emphasized even stronger asymmetries in loads and power on an aligned downstream turbine. The combined power output of a two turbine setup consequently also featured an asymmetric distribution, which has been previously observed in an computational study Gebraad et al. (2016) and a similar experimental setup by Schottler et al. (2015). In a recent follow-up study, Schottler et al. (2017) attributed the asymmetry to a strong shear in the inflow to the two-turbine setup. As the inflow in the present study was measured to be spatially uniform, inflow shear is not a reason for the observed asymmetries. The major contributor to an asymmetric combined power distribution was seen to be the downstream turbine power. The yaw angle dependency of downstream turbine power is in direct relation to an asymmetric wake deflection observed on the same setup by in Bartl et al. (2018). Therein, the wake deflection is slightly larger for negative yaw angles than for the corresponding positive yaw angles, a trend which is seen to directly affect the downstream turbine power, thrust and yaw moment distribution.

The present results further demonstrate a significant influence of the inflow turbulence level on the effectiveness of wake steering by yaw. The relative power gains were observed to be significantly larger for lower inflow turbulence levels (11% versus 8%). The reason might to a small degree be differences in wake deflection (Bartl et al., 2018), but can mostly be subscribed to lower average kinetic energy levels in wakes for turbines exposed to low inflow turbulence. When deflecting a kinetic energy sink away from the downstream rotor, the relative gains in combined power are higher. Alongside with combined power increases, the results demonstrated a linear increase in the upstream turbine's yaw moments with its yaw angle. For wake steering behind an upstream turbine, partial wake impingement situations arise for an aligned downstream turbine, resulting in increased yaw moments also on the downstream turbine.

In a real wind farm exposed to varying wind directions, however, partial wake situations, in which the downstream turbine is laterally offset are just as important as the aligned case. For a lateral offset of half a rotor diameter, for instance, it is demonstrated, that upstream turbine yaw control is able to steer most of the wake flow away from an offset downstream turbine. Consequently, both the combined power increases and yaw moments on the downstream turbine are significantly mitigated. This finding experimentally confirms results of a similar test case recently computed with a model-framework by van Dijk et al. (2017). For an offset of $\Delta z/D = +0.33$, we measured a maximum power increase of about 13% for when yawing the upstream turbine from

$\gamma_{T1} = 0°$ to $+30°$. Although not directly comparable, this result is estimated to be at the same order of magnitude as power gains experimentally obtained by Campagnolo et al. (2016), who measured a combined power increase of 21% for a setup of three model turbines with an lateral offset of $\Delta z/D = +0.45$. Furthermore, our results indicated a not perfectly symmetrical distribution of the downstream turbine power and thrust coefficients with respect to its positive or negative offset position, as slightly higher power coefficients were obtained for negative offset positions. The reason for this is deemed to be an asymmetric velocity deficit in the non-yawed wake as indicated in Pierella and Sætran (2017) and Bartl et al. (2018).

In a final test case, we introduced the concept of downstream turbine yawing in partial wake overlap situations for the purpose of load mitigation. The concept suggests that yawing a downstream turbine opposed to a strong horizontally sheared flow is able to mitigate rotor's yaw moments while simultaneously increasing the rotor's power output. The horizontally sheared flow is in this case the transition zone between the low- velocity wake flow to the high-velocity freestream flow. A mitigation of yaw moments by yawing the rotor opposed to the shear is intuitively imaginable, while the simultaneous power increase might be surprising. Similar effects have, however, been reported in full-scale data evaluation by McKay et al. (2013), who found an offset in the downstream turbine's yaw alignment for the purpose of optimized power output when operated in a partial wake of an upstream turbine. The downstream turbine yaw angle was observed to adjust itself opposed to the velocity gradient in the partial wake impinging the downstream rotor. These findings are in total agreement with the optimal downstream turbine yaw angle measured in our wind tunnel experiment. The potential of load reductions of a single turbine by yawing has been previously discussed by Kragh and Hansen (2014), in situations where the rotor was exposed to vertically sheared inflows. In the present test case, however, the partial wake impingement on the rotor represents a situation of a strongly horizontally sheared flow. Whether the shear in the incoming wind field is horizontal or vertical obviously makes a big difference, but mitigation of loads and maximization of power might be possible with yaw adjustments in both cases.

The power output and yaw moment distribution was however not completely symmetrical with respect to yaw angle γ_{T2} and offset position $\Delta z/D$. Besides the slightly asymmetric streamwise wake flow, also the interaction of the downstream turbine with respect to the wake rotation of the upstream turbine might cause this asymmetry. A characterization of the wake rotation and asymmetric freestream flow entrainment in the wake behind the same rotor is given by Pierella and Sætran (2017). As a yawed operation of a downstream rotor in a partial wake of an upstream turbine is highly complex, a combination of a number of different factors are assumed to influence wake-rotor interaction, making a clear conclusion difficult at this stage.

5 Conclusions

A wind tunnel experiment studying the effects of intentional yaw misalignment on the power production and yaw moments of a downstream turbine was presented. Both, full wake impingement and partial wake overlap situations were investigated. For partial wake overlap the concept of downstream turbine yawing for yaw moment mitigation was investigated for different lateral offset positions.
It is demonstrated that upstream turbine yaw misalignment is able to increase the combined power production of the two turbines for both partial and full wake overlap setups. For aligned turbines the combined array power was increased up to 11% for a separation distance of $x/D = 6$ and low inflow turbulence levels ($TI_A = 0.23\%$). At a higher inflow turbulence of $TI_B = 10.0\%$, however, the relative power increase was assessed to be only 8%. For smaller turbine separation distances, combined power gains were assessed to be even smaller. The distribution of combined power gains in dependency of the upstream turbine yaw angle was observed to be rather asymmetrical. The formation of not entirely symmetric velocity deficit shapes in the wake was deemed to be the main reason for that finding.
The obtained power gains were assessed to be at the cost of increased yaw moments on the upstream rotor. The yaw moments on the upstream rotor are observed to increase roughly linearly with increasing yaw angle, but are not entirely symmetrical distributed. Upstream turbine yaw control is moreover seen to directly influence the yaw moments on a downstream rotor. For aligned turbine positions, the downstream turbine yaw moments are observed to increase to similar magnitudes as for the upstream turbine. These results highlight the importance of also taking loads into account when optimizing layout and control of a wind farm.
Further, we demonstrate advantages of upstream turbine yaw control for load reduction and power increases on an offset downstream turbine. For situations, in which the downstream turbine is impinged by a partial wake, upstream turbine yaw control can redirect the wake either on or away from the downstream rotor. In case the wake is directed onto the downstream turbine's rotor swept area, its yaw moments and power production reduce. If the lateral offset between the turbines is large enough, the wake can be deflected entirely away from the downstream turbine, maximizing its power and canceling out yaw moments.
Moreover, a final test case proved the concept of yaw control for yaw moment mitigation on a downstream turbine operated in a partial wake overlap situation. While yaw

moments are observed to decrease when yawing the rotor opposed to the shear layer in the incoming wake flow, also the turbine's power output is seen to increase. These results illustrate the importance for combined power and load optimization on all turbines in a wind farm.

References

Adaramola, M. and Krogstad, P.-Å.: Experimental investigation of wake effects on wind turbine performance, Renewable Energy, 36, 2078–2086, doi:10.1016/j.renene.2011.01.024, 2011.

Andersen, S., Sørensen, J., and Mikkelsen, R.: Performance and Equivalent Loads of Wind Turbines in Large Wind Farms, Journal of Physics: Conference Series, 854, 012 001, doi:10.1088/1742-6596/854/1/012001, 2017.

Annoni, J., Gebraad, P., Scholbrock, A., Fleming, P., and van Wingerden, J.: Analysis of axial-induction-based wind plant control using an engineering and a high-order wind plant model, Wind Energy, 19, 1135–1150, doi:10.1002/we.1891, 2016.

Bartl, J. and Sætran, L.: Experimental testing of axial induction based control strategies for wake control and wind farm optimization, Journal of Physics: Conference Series, 753, 032 035, doi:10.1088/1742-6596/753/3/032035, 2016.

Bartl, J. and Sætran, L.: Blind test comparison of the performance and wake flow between two in-line wind turbines exposed to different turbulent inflow conditions, Wind Energy Science, 2, 55–76, doi:10.5194/wes-2-55-2017, 2017.

Bartl, J., Mühle, F., Schottler, J., Hölling, M., Peinke, J., Adaramola, M., and Sætran, L.: Wind tunnel experiments on wind turbine wakes in yaw: Influence of inflow turbulence and shear, In review in Wind Energ. Sci. Discuss., doi:10.5194/wes-2017-59, 2018.

Bastankhah, M. and Porté-Agel, F.: Experimental and theoretical study of wind turbine wakes in yawed conditions, Journal of Fluid Mechanics, 806, 506–541, doi:10.1017/jfm.2016.595, 2016.

Campagnolo, F., Petrović, V., Bottasso, C., and Croce, A.: Wind Tunnel Testing of Wake Control Strategies, American Control Conference, doi:10.1109/ACC.2016.7524965, 2016.

Damiani, R., Dana, S., Annoni, J., Fleming, P., Roadman, J., van Dam, J., and Dykes, K.: Assessment of Wind Turbine Component Loads Under Yaw-Offset Conditions, Wind Energy Science Discussions, doi:10.5194/wes-2017-38, 2017.

Fleming, P., Gebraad, P., Lee, S., van Wingerden, J.-W., Johnson, K., Churchfield, M., Michalakes, J., Spalart, P., and Moriarty, P.: Evaluating techniques for redirecting turbine wakes using SOWFA, Renewable Energy, 70, 211–218, doi:10.1016/j.renene.2014.02.015, 2014.

Fleming, P., Gebraad, P. M., Lee, S., van Wingerden, J.-W., Johnson, K., Churchfield, M., Michalakes, J., Spalart, P., and Moriarty, P.: Simulation comparison of wake mitigation control strategies for a two-turbine case, Wind Energy, 18, 2135–2143, doi:10.1002/we.1810, 2015.

Gebraad, P. M. O., Fleming, P. A., and Wingerden, J. W. v.: Comparison of Actuation Methods for Wake Control in Wind Plants, American Control Conference, doi: 10.1109/ACC.2015.7170977, 2015.

Gebraad, P. M. O., Teeuwisse, F. W., van Wingerden, J. W., Fleming, P. A., Ruben, S. D., Marden, J. R., and Pao, L. Y.: Wind plant power optimization through yaw control using a parametric model for wake effects-a CFD simulation study, Wind Energy, 19, 95–114, doi:10.1002/we.1822, 2016.

Howland, M., Bossuyt, J., Martinez-Tossas, L., Meyers, J., and Meneveau, C.: Wake Structure of Wind Turbines in Yaw under Uniform Inflow Conditions, Journal of Renewable and Sustainable Energy, 8, 043 301, doi:10.1063/1.4955091, 2016.

Jiménez, Á., Crespo, A., and Migoya, E.: Application of a LES technique to characterize the wake deflection of a wind turbine in yaw, Wind Energy, 13, 559–572, doi: 10.1002/we.380, 2010.

Kim, S.-H., Shin, H.-K., Joo, Y.-C., and Kim, K.-H.: A study of the wake effects on the wind characteristics and fatigue loads for the turbines in a wind farm, Renewable Energy, 74, 536–543, doi:10.1016/j.renene.2014.08.054, 2015.

Knudsen, T., Bak, T., and Svenstrup, M.: Survey of wind farm control—power and fatigue optimization, Wind Energy, 18, 1333–1351, doi:10.1002/we.1760, 2014.

Kragh, K. A. and Hansen, M. H.: Load alleviation of wind turbines by yaw misalignment, Wind Energy, 17, 971–982, doi:10.1002/we.1612, 2014.

McKay, P., Carriveau, R., and Ting, D. S.-K.: Wake impacts on downstream wind turbine performance and yaw alignment, Wind Energy, 16, 221–234, doi:10.1002/we.554, 2013.

Pierella, F. and Sætran, L.: Wind tunnel investigation on the effect of the turbine tower on wind turbines wake symmetry, Wind Energy, 20, 1753–1769, doi:10.1002/we.2120, 2017.

Schepers, J. G., K. Boorsma, K., and Munduate, X.: Final Results from Mexnext-I: Analysis of detailed aerodynamic measurements on a 4.5 m diameter rotor placed in the large German Dutch Wind Tunnel DNW, Journal of Physics: Conference Series, 555, 012 089, doi:10.1088/1742-6596/555/1/012089, 2014.

Schottler, J., Hölling, A., Peinke, J., and Hölling, M.: Wind tunnel tests on controllable model wind turbines in yaw, AIAA 34th Wind Energy Symposium, p. 1523, doi: 10.2514/6.2016-1523, 2015.

Schottler, J., Hölling, A., Peinke, J., and Hölling, M.: Brief communication: On the influence of vertical wind shear on the combined power output of two model wind turbines in yaw, Wind Energy Science, 2, 439–442, doi:10.5194/wes-2-439-2017, 2017.

Schottler, J., Bartl, J., Mühle, F., Sætran, L., Peinke, J., and Hölling, M.: Wind tunnel experiments on wind turbine wakes in yaw: Redefining the wake width, In review in Wind Energ. Sci. Discuss., doi:10.5194/wes-2017-58, 2018.

Schreiber, J., Cacciola, S., Campagnolo, F., Petrovic, V., Mourembles, D., and Bottasso, C. L.: Wind shear estimation and wake detection by rotor loads - First wind tunnel verification, Journal of Physics: Conference Series, 753, 032 027, doi:10.1088/1742-6596/753/3/032027, 2016.

van Dijk, M., van Wingerden, J.-W., Ashuri, T., and Li, Y.: Wind farm multi-objective wake redirection for optimizing power production and loads, Energy, 121, 561–569, doi:10.1016/j.energy.2017.01.051, 2017.

Vollmer, L., Steinfeld, G., Heinemann, D., and Kühn, M.: Estimating the wake deflection downstream of a wind turbine in different atmospheric stabilities: an LES study, Wind Energy Science, 1, 129–141, doi:10.5194/wes-1-129-2016, 2016.

Wheeler, A. J. and Ganji, A. R.: Introduction to engineering experimentation, Upper Saddle River, NJ, USA, Pearson/Prentice Hall, XI, third edition edn., 2004.

PAPER VII

Blind test comparison on the wake behind a yawed wind turbine

Franz Mühle[1], **Jannik Schottler**[2], **Jan Bartl**[3], **Romain Futrzynski**[4], **Steve Evans**[4], **Luca Bernini**[5], **Paolo Schito**[5], **Martín Draper**[6], **Andrés Guggeri**[6], **Elektra Kleusberg**[7], **Dan S. Henningson**[7], **Michael Hölling**[2], **Joachim Peinke**[2,8], **Muyiwa S Adaramola**[1] **and Lars Sætran**[3]

[1] Faculty of Environmental Sciences and Natural Resource Management, Norwegian University of Life Sciences, Ås, Norway
[2] ForWind - Center for Wind Energy, Institute of Physics, University of Oldenburg, Oldenburg, Germany
[3] Department of Energy and Process Engineering, Norwegian University of Science and Technology, Trondheim, Norway
[4] Siemens PLM Software, London, United Kingdom
[5] Department of Mechanical Engineering, Politecnico di Milano, Milan, Italy
[6] Facultad de Ingeniería, Universidad de la República, Montevideo, Uruguay
[7] Linné FLOW Centre and Swedish e-Science Research Centre (SeRC), Department of Mechanics, KTH Royal Institute of Technology, Stockholm, Sweden
[8] Fraunhofer IWES, Oldenburg, Germany

Corresponding Author: Franz Mühle (franz.muhle@nmbu.no)

Abstract. This article summarizes the results of a fifth Blind test workshop, which was held in Visby, Sweden, in May 2017. This study compares the numerical predictions of the wake flow behind a model wind turbine operated in yaw to experimental wind tunnel results. Prior to the work shop, research groups were invited to predict the turbines' performances and wake flow properties using computational fluid dynamics (CFD) methods. For this purpose, the power, thrust and yaw moments for a 30 ° yawed model turbine as well as the wake's mean and turbulent streamwise and vertical flow components were measured in the wind tunnel at the Norwegian University of Science and Technology (NTNU). In order to increase the complexity, a non-yawed downstream turbine was added in a second test case, while a third test case challenged the modelers with a new rotor and turbine geometry.

Four participants submitted predictions using different flow solvers, three of which were based on Large Eddy Simulations (LES) while another one used an Improved Delayed Detached Eddy Simulation (IDDES) model. The performance of a single yawed turbine was fairly well predicted by all simulations, both in the first and third test case. The scatter in the downstream turbine's performance predictions in the second test case, however, was found to be significantly larger. The complex asymmetric shape of the mean streamwise and vertical velocity was generally well predicted by all the simulations for all test cases. The largest improvement with respect to previous Blind tests is the good prediction of the levels of turbulent kinetic energy in the wake, even for the complex case of yaw misalignment. These very promising results confirm the mature development stage of LES/DES simulations for wind turbine wake modeling, while competitive advantages might be obtained by faster computational methods.

1 Introduction

Wind turbine wake interaction has become a major topic in wind energy research during the last decades. The power drop between the first and second turbine can be up to 35% in an offshore installation, when the turbines are aligned with the wind direction, while the averaged losses due to wake interactions are estimated to range between 10 - 20% (Barthelmie et al., 2009). Furthermore, wind turbine wakes show increased levels of turbulent kinetic energy, which potentially affects fatigue loads of downstream turbines. Consequently, the prediction of the wake's mean and turbulent characteristics is highly important in the wind farm planning process in order to optimize farm layout and control. For this purpose, the development of simple analytical wake models started already 40 years ago and is still ongoing. However, these models give only predictions of the mean velocity deficit (Polster et al., 2017). For a more accurate simulation of the wake flow, advanced CFD tools based on Navier-Stokes solvers are used. It is necessary to validate these numerical tools against experimental data sets to determine their accuracy. Therefore, a series of Blind tests providing detailed flow measurement data was initiated at NTNU in 2011. In the first Blind test the performance of a single turbine as well as the mean streamwise velocity and turbulent kinetic energy in the wake for distances up to $5D$ behind the turbine were compared, D being the rotor diameter. Eight different research groups participated in the workshop, contributing various types of simulations ranging from Reynolds-Averaged-Navier-Stokes (RANS) simulations to LES. The performance predictions showed a considerable spread around the experimental results while the prediction of wake turbulence was scattered by several orders of magnitude, as summarized by Krogstad and Eriksen (2013). For the next Blind test the complexity was increased by adding a second turbine operating in the wake of the first turbine. Modelers were asked to simulate the performance of both turbines and the wake formed behind the downstream turbine. For this Blind test nine predictions were submitted by eight organizations. The results reported by Pierella et al. (2014) still showed a large spread in performance and also the predictions of the wake properties varied significantly. To further investigate the difference between experimental results and numerical simulations a third Blind test was realized, in which the complexity was again increased by applying a lateral offset of half a rotor diameter to the same turbine array. While the performance was predicted fairly well, the simulations of the asymmetric wake showed large uncertainties in predicting turbulence (Krogstad et al., 2015). The focus of the fourth Blind test was the influence of different inflow conditions. Therefore, the wake behind a single turbine was investigated at three different downstream distances for a low-turbulent, a high-turbulent and a turbulent shear inflow. Furthermore the modelers were asked to predict the performance of an aligned turbine array. This Blind test attracted five groups, who all managed to predict the performance of the upstream turbine fairly well. Nevertheless, the scatter in the downstream turbine's performance was still significant. The mean wake properties were generally predicted well, while the turbulence predictions still showed a large spread, as shown by Bartl and Sætran (2017).

During the last years CFD models were constantly improved, both by increasing their accuracy and by reducing computational costs. In order to give the model developers the possibility to test their CFD models in a complex wake flow, a fifth Blind test was initiated, challenging the modelers with the dynamic flow situation of a yawed wind turbine. The wakes behind two different turbines and two inline turbines were investigated. Yaw misalignment is currently a widely discussed topic in wind energy research. Intentional yaw misalignment of an upstream turbine in a wind farm is deemed to have a large potential for increasing the farm's efficiency (Fleming et al., 2014). A first comparison of CFD results to experimental data on yawed wind turbines was part of the so called Mexnext project (Schepers et al., 2014), in which blade loads and wake data were measured on a model wind turbine of $D = 4.5\,\mathrm{m}$ operated in yaw. Even though the analysis investigated numerical flow predictions of a yawed rotor, there is need for a deeper investigation of wake properties behind yawed wind turbines. By increasing the complexity with respect to previous Blind tests, the wake behind a yawed wind turbine is considered to be a challenging task for simulations.

2 Experimental setup

2.1 Model wind turbines

In this Blind test experiment three different turbine geometries were used. For the purpose of yaw experiments, a new turbine test rig was constructed at NTNU, which is called Laterally Angled Rotating System 1 (LARS1). It features a shorter nacelle and slimmer tower compared to the turbines used in previous Blind tests in order to minimize the effects on the wake, as shown in Fig. 1a. A detailed description and technical drawings of all turbines are presented in the invitation document to the Blind test (Sætran et al., 2018). The 3-bladed rotor is milled from aluminum and is based on the NREL S826 airfoil. It has a diameter of $D_{LARS1} = 0.984\,\mathrm{m}$ and is identical to the rotor used in previous Blind tests, a detailed description of the rotor can be found in Krogstad and Lund (2012). At its design tip speed ratio $\lambda = 6$ and $u_{ref} = 10.0\,\mathrm{m/s}$

the turbine experiences a chord based Reynolds number at the blade tips of around $Re_{tip,NTNU} = 1.1 \cdot 10^5$.

NTNU's model wind turbine called T2 was already used in previous Blind test experiments. The sketch in Fig. 1b shows that T2 has exactly the same rotor as LARS1, while the nacelle and tower structures are significantly bigger and of different shape. The turbine is used as a non-yawed downstream turbine in the investigation of an aligned turbine array.

The third turbine used in this Blind test is the model wind turbine designed by ForWind at the University of Oldenburg. For the experiments in the NTNU wind tunnel the turbine's hub height was increased with four cylindrical rods, in order to be operated at a height, comparable to the NTNU turbines. The turbine has a smaller rotor diameter of $D_{ForWind} = 0.580\,\text{m}$ and is sketched in Fig. 1c. The rotor is based on the SD7003 airfoil and is manufactured using a synthetic compound. A detailed description can be found in Schottler et al. (2016). It has the same design tip speed ratio $\lambda = 6$ as the NTNU turbines. For safety reasons, it was operated at a lower inflow velocity of $u_{ref} = 7.5\,\text{m/s}$, which results in a chord based Reynolds number at the tips of around $Re_{tip,ForWind} = 6.4 \cdot 10^4$.

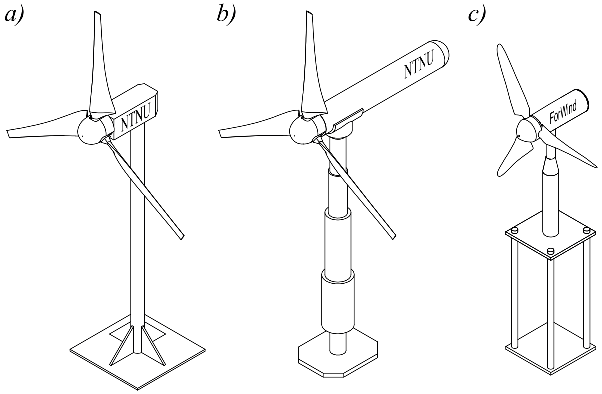

Figure 1: Sketches of the model wind turbines, (a) NTNU turbine LARS1, (b) NTNU turbine T2, (c) ForWind turbine.

The NTNU and ForWind rotors are based on two different airfoils. The NREL S826 airfoil, which is used from root to tip for the NTNU rotor is originally designed for the application in the tip region of full scale wind turbines, a detailed description can be found in Somers (2005). It is designed for Reynolds numbers of $Re \approx 1.0 \cdot 10^6$, which is around one order of magnitude higher as the Reynolds number at the rotor tip in the experiments. Nevertheless, experimental data sets for airfoil performance were measured for lower Reynolds numbers at Denmark's Technical University (DTU)

(Sarmast and Mikkelsen, 2012) and NTNU (Bartl et al., 2018b). In Fig. 2 the airfoil polars from the DTU experiments at $Re = 1.0{\cdot}10^5$ are compared to a standard set of lift and drag coefficients calculated for $Re = 1.0{\cdot}10^5$ in XFoil, which was provided in the invitation document (Sætran et al., 2018). It can be seen that the drag coefficient C_D is slightly different and lift coefficient C_L is diverging significantly from an angle of attack α of approximately 4°between the experimental and XFoil data. This difference is very distinct for high angles of attack that may occur close to stall.

The ForWind rotor is based on the SD7003 airfoil that is defined in detail in Selig et al. (1995). It is specifically designed for low Reynolds numbers and is thus well suited for wind tunnel experiments. In Selig et al. (1995) two experimental data sets for $Re = 6.4{\cdot}10^4$ and $Re = 1.02{\cdot}10^5$ are presented. They are in good agreement with XFoil data sets for $Re = 5.0{\cdot}10^4$ and $Re = 1.0{\cdot}10^5$ which were provided to the participants.

2.2 Wind tunnel and inflow condition

All the experimental data were measured in the closed-loop wind tunnel at the Department of Energy and Process Engineering at NTNU in Trondheim. The wind tunnel has a test section length of 11.5 m, a width of 2.7 m and a height of 1.8 m. The reference coordinate system is pictured in Fig. 3 and a detailed description can be found in Sætran et al. (2018).

For all test cases a non-uniform shear flow was generated by a grid at the inlet of the test section. The grid is built from wooden bars with a cross section of 0.047 m x 0.047 m. In the horizontal direction the bars are evenly distributed with a distance of 0.24 m between the edges of the bars. In the vertical direction the mesh size increases with increasing height from a clearance of 0.016 m close to the floor to an opening of 0.30 m underneath the roof. The grid has a total solidity of about 34% in the wind tunnel cross section. The shear profile can be described by the power law,

$$\frac{\bar{u}}{u_{ref}} = \left(\frac{y}{y_{ref}}\right)^{\alpha}. \tag{1}$$

The power law describes the wind speed $\bar{u}$ as a function of the height y provided that the reference wind speed u_{ref} is known at a reference height y_{ref}. The strength of the shear is described by the power law coefficient α. The shear grid used in the experiments was designed to obtain an exponent of α 0.11.

As the velocities of the shear profile vary in height and are non-uniform over the rotor area, the reference wind speed u_{ref} is defined at the turbine hub height as shown in Fig. 4a. Furthermore, the velocity profile approximated by Eq. (1) matches well with the measured velocities, having a maximum deviation of ±1.0%. Fig. 4b shows the

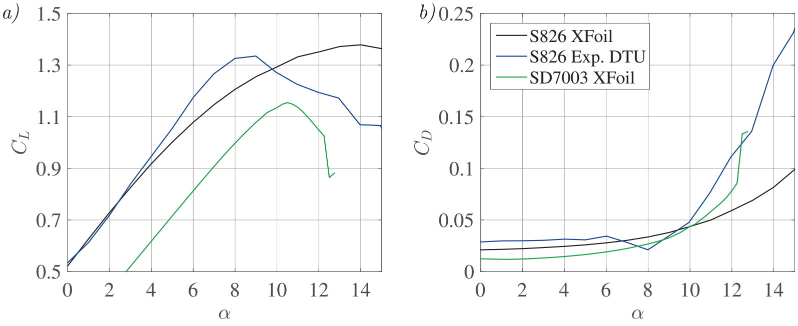

Figure 2: (a) lift coefficient and (b) drag coefficient for $Re = 1.0{\cdot}10^5$ for NREL S826 from XFoil, NREL S826 from experiments DTU and SD7003 from XFoil.

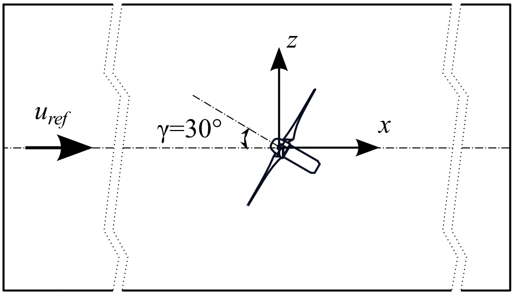

Figure 3: Reference coordinate system in the wind tunnel and definition of positive yaw angle γ, top view.

normalized vertical velocity component of the inflow for the NTNU turbine. It can be seen that the vertical flow component v is negative, which creates a slight down flow in the wind tunnel. The deviations in v from zero were not known at the time the Blind test invitation was sent out, in which a zero velocity component for v was assumed. In order to take this into account, in the comparison, v at the inlet is subtracted from the vertical velocity component that is measured in the wake at the same y-position.

The turbulence intensity (TI) of the inflow is shown in Fig. 4c. As expected, the turbulence decays with increasing downstream distance. At the position of the NTNU turbine the turbulence intensity is measured to be $TI = 10.0\%$ at hub height. The integral length scales L_{uu} are calculated from hot-wire measurements of the streamwise velocity fluctuation u' and the dissipation rate of the turbulent kinetic energy E, by applying $E = {}^{3}\!/_{2} A \frac{u'^3}{L_{uu}}$, where $A \approx 1$, taken from Krogstad and Davidson (2010). This results in $L_{uu} = 0.097\,\mathrm{m}$ at the position of the NTNU turbine. The ForWind turbine was placed $5D$ ($D = D_{LARS1}$) behind the shear grid and thus experienced a lower turbulence intensity of TI = 5.2%. The integral length scale however increased to $L_{uu} = 0.167\,\mathrm{m}$ at this position. The third investigated streamwise position is $6D$ behind the NTNU turbine. At this position the turbulence has further decayed to $TI = 4.1\%$. The corresponding integral length scale at this position is $L_{uu} = 0.271\,\mathrm{m}$.

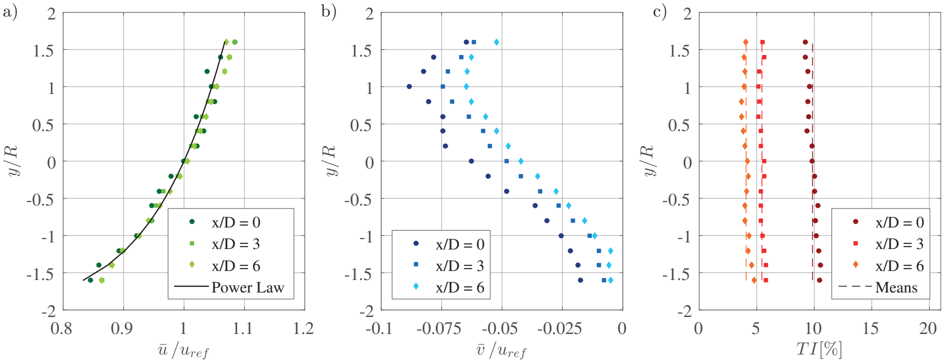

Figure 4: Inflow at different wind tunnel positions, in which $x/D = 0$ refers to the position of the NTNU turbine: (a) normalized streamwise velocity u^*, (b) normalized vertical velocity v^*, (c) turbulence intensity $TI[\%]$. The radius R and diameter D refer to the NTNU turbine.

2.3 Test cases description

In this Blind test experiment the modelers were asked to simulate three test cases. In test case 1 the flow $3D$ and $6D$ behind the yawed turbine LARS1 and its performance, thrust force and yaw moment are investigated. The grid at the inlet is located -$2D$ upstream of the turbine location at x = -$2D$. The inflow velocity is adjusted to $u_{ref} = 10.0\,\mathrm{m/s}$ and the turbulence intensity is $TI = 10.0\%$ at the turbine's position. The turbine's hub height is in the center of the wind tunnel at $h_{hub} = 0.89\,\mathrm{m}$. LARS1 is yawed to $\gamma_{LARS1} = +30°$ and operated at its design tip speed ratio of $\lambda_{LARS1} = 6$ throughout all measurements. In test case 2 a turbine operating in the wake of a yawed upstream turbine is investigated. Therefore, the setup of test case 1 is extended with the turbine T2 located $3D$ behind the upstream turbine LARS1. In contrast to LARS1, T2 is not yawed ($\gamma_{T2} = 0°$). As the downstream turbine is impinged by a partial wake of the upstream turbine, its optimum tip speed ratio is reduced to $\lambda_{T2} = 5$, taking into account that the tip speed ratio is based on the constant reference velocity $u_{ref} = 10.0\,\mathrm{m/s}$ upstream of the two-turbine array. This test case investigates to which degree a partial wake impact can deflect the wake behind a non-yawed downstream turbine. This has recently been investigated in a LES study by Fleming et al. (2017). In test case 3, similar to test case 1, the flow $3D$ and $6D$ ($D = D_{ForWind}$) behind the

ForWind turbine is investigated. The turbine is located at $x = 3D$ ($D = D_{LARS1}$), which resulted in a lower turbulence intensity of $TI = 5.2\%$ at the turbine position. The hub height is set to $h_{hub} = 0.89\,\mathrm{m}$ and the inflow velocity is reduced to $u_{ref} = 7.5\,\mathrm{m/s}$. Corresponding to test case 1 the turbine is yawed for $\gamma_{ForWind} = 30°$ and is operated at its optimum tip speed ratio of $\lambda_{ForWind} = 6$. All setup parameters for test cases 1-3 are summarized in Table 1 and a detailed description can be found in (Sætran et al., 2018).

Table 1: Summary of the parameters that are varied for the three investigated test cases, *up* refers to the upstream and *down* to the downstream turbine position.

Test case	u_{inf}	TI at turbine position	Upstream turbine	λ_{up}	γ_{up}	Downstream turbine	λ_{down}	γ_{down}	Wake scan locations
TC1	10.0 m/s	10.0%	LARS1	6.0	30°	-	-	-	3D, 6D
TC2	10.0 m/s	10.0%	LARS1	6.0	30°	T2	5.0	0°	6D
TC3	7.5 m/s	5.2%	ForWind	6.0	30°	-	-	-	3D, 6D

3 Methods

3.1 Measurements techniques

The u- and v- velocity components in the wake were measured using a 2-component FiberFlow Laser Doppler Velocimetry (LDV) system from DANTEC dynamics. The LDV probe was placed inside the wind tunnel on a traverse system. For each measurement point $5.0 \cdot 10^4$ samples were recorded. The sampling frequency was adjusted by controlling the particles in the flow, ranging from 1500 - 2000 Hz which resulted in an average sampling time of approximately 25 - 33 s.

The thrust force and yaw moments acting on the upstream and downstream turbine were measured separately using a Schencker six-component force balance, which was installed under the wind tunnel floor. The balance also served as a turning table allowing an exact adjustment of the yaw angle. For the rotor thrust only the load cell parallel to the flow was taken into account. The yaw moment was calculated from a moment equilibrium of three measured forces in the horizontal plane (referred to the rotor center).

The aerodynamic power P of the NTNU rotors was measured using the test rig of turbine T2. This turbine is equipped with an optical RPM sensor and a torque transducer in the hub. Thus, the torque T and the rotational speed ω of the turbine could be measured simultaneously so that $P = \omega \cdot T$.

3.2 Measurement uncertainties

The experimentally measured values feature several uncertainties. The statistical uncertainties of every sample of the mean velocity, power, thrust and yaw moments are calculated based on a 95% confidence level according to the procedure described in Wheeler and Ganji (2010). The uncertainty for the power measurements is calculated to be within ±3% while the force measurements' uncertainty is slightly lower (±2%). The exact values for all measured points are presented as error bars in the plots for the power coefficients C_P, the thrust coefficients C_T and the yaw moments ${M_y}^*$. The uncertainties for the mean streamwise velocities u in the wake are calculated to be smaller than ±1%. The uncertainties for the vertical velocity component v are slightly higher due to the correction by the inlet component. In order to determine the inaccuracy in the turbulent kinetic energy measurements, the method proposed by Benedict and Gould (1996) was applied. The uncertainties for a 95% confidence level are found to be below ±2% in the wake. It should be noted that the coarse measurement grid slightly influences the position of the turbulent kinetic energy (TKE) peaks.

3.3 Participants and computational methods

Siemens PLM software from the United Kingdom (Siemens), the Department of Mechanical Engineering of the Politecnico di Milano in Italy (POLIMI), the Facultad de Ingeniería of the Universidad de la República in Uruguay (UdelaR) and KTH Mechanics from the Royal Institute of Technology in Sweden (KTH) participated in the Blind test and submitted computational results. For clarity, only the abbreviations will be used in the following. A summary of the simulation methods and mesh properties is presented in Table 2.

Table 2: Overview of simulation methods and parameters. Abbreviations: Improved Delayed Detached Eddy Simulation (IDDES), Large Eddy Simulation (LES), Actuator Line (ACL), Fully Resolved (FR).

Participant	Simulation code	Flow solver type	Rotor model	Airfoil polars	Tower, nacelle	Mesh properties	Number of cells
Siemens	Star-CCM+	IDDES	FR	-	FR	Hexah./polyh.	$\approx 30.0\cdot 10^6$
POLIMI	ALEVM	LES	ACL	X-Foil	No	Cartesian	$\approx 4.1 \cdot 10^6$
UdelaR	caffa3d	LES	ACL	X-Foil	Yes	Cartesian	$\approx 0.7 \cdot 10^6$
KTH	Nek5000	LES	ACL	Experiments	Yes	Uniform	$\approx 58.0\cdot 10^6$

Siemens PLM Software (Siemens)

Siemens, who previously participated in Blind test experiments as CD-adapco, used the finite volume code STAR-CCM+ v12.04 to mesh and solve all three test cases. Each simulation resolved the rotor, nacelle and tower structure completely, and used the hybrid method Improved Delayed Detached Eddy Simulation (IDDES), which resolves the energy-carrying eddies in the free stream and solves the boundary layer flow with RANS. The Spalart-Allmaras model was used for closure of the turbulence equations, and the fluid was considered incompressible. Convective fluxes used a MUSCL 3$^{\mathrm{rd}}$ order scheme, while time was discretized using a 2$^{\mathrm{nd}}$ order implicit scheme. Each set of blades and hub was contained inside a cylindrical, rotating volume which was meshed with polyhedral cells, whereas the main domain used trimmed cells, resulting in a hexahedral dominant mesh in which a small proportion of cells was trimmed near the boundaries. Due to the rotation of the cylindrical volumes, the mesh was not conformal at the interface between the two regions, and flow quantities were interpolated from one volume to another. All wall surfaces, including the wind turbine bodies and the wind tunnel walls, were covered in several layers of prismatic cells to improve the resolution of boundary layers. The resulting y^+ values were below 1 on the turbine bodies, and around 30 on the wind tunnel walls. The smallest cell size on the surface of the turbine bodies was 0.3 mm, typically found at the leading edge of the blades. The characteristic cell size in the rotating regions was 10 mm, which was also the cell size used in the wake of the rotors. The rest of the domain had a characteristic cell size of 20 mm. This resulted in meshes of $29{\cdot}10^6$, $35{\cdot}10^6$, and $17{\cdot}10^6$ cells for cases 1, 2, and 3 respectively. All simulations were run with a time step of $10{\cdot}10^{-4}$ s. As inflow the given analytical mean velocity profile $U_{inlet} = u_{ref}{\cdot}(y\text{-}y_{ref})^{\alpha}$ was used. Furthermore, the Synthetic Eddy Method was used to superpose time-dependent eddies with the characteristic length scale of 10 mm, and a turbulence intensity $TI = 5\%$. All cases were run for 1.6 s to establish the flow prior to sampling, and then mean values were sampled over a period of 2 to 3 s. An example using STAR-CCM+ can be found in (Mendonça et al., 2012).

Politecnico di Milano (POLIMI)

POLIMI submitted a LES that was computed using the ALEVM code. It is an aerodynamic turbine simulation tool written in C++ and based on pisoFoam, which is an incompressible transient solver included in the OpenFOAM framework. The standard PISO (Pressure-Implicit with Splitting of Operators) solver was modified to include the effect of the turbine blades that are represented using the lifting line approach. The blade lines are discretized in segments based on the intersections with the numerical mesh grid, in which an actuation point acts on each segment. Each point of the Actuator Line (ACL) acts as an isolated blade section. More information about the ACL method can be found in Sørensen and Shen (2002). The wind velocity is numerically sampled for every blade point and used to compute the relative wind speed and the angle of attack. Thereafter, the aerodynamic forces are obtained through a lookup table, in which the blades' geometrical and aerodynamic properties are listed. In ALEVM the wind velocity is not sampled on a single point but averaged over a line, which is placed upstream of the blade point position with a distance proportional to the mesh cell dimension. The wind velocity is estimated using the mean of the velocity probed across the line. The main purpose of the relative wind speed estimation is in the angle of attack calculation. The wind velocity direction is then corrected to account for the local up wash due to the lifting line force. Based on the lifting line approach, the ALEVM code includes the turbine blade effect as an external momentum source term in the Navier-Stokes equations solved by the PISO algorithm.

ALEVM employs the well know solution of the Regularization kernel, smearing the line forces on the multiple cells following a Gaussian distribution and thus avoiding abrupt variation of the source term strength between adjacent cells. The turbulence in the wake region is modeled using a LES, adopting the Smagorinsky sub-grid scale model. For the time discretization scheme a first order implicit approximation is used, while the divergence discretization scheme and the gradient discretization scheme are approximated by second order. The wind tunnel walls are included as no-slip-boundaries, while also the inlet turbulence grid is geometrically modeled. The total cell count for the simulations is approximately $4.1 \cdot 10^6$. Further details about the code can be found in (Schito and Zasso, 2014).

Universidad de la República (UdelaR)

UdelaR submitted another LES using their in-house developed caffa3d code. It is an open source, finite volume code, with second order accuracy in space and time, parallelized with a Message Passing Interface (MPI), in which the domain is divided in unstructured blocks of structured grids. Complex geometries are represented by a combination of body fitted grids and the immersed boundary method over both, Cartesian and body fitted grid blocks. The properties of the geometry and the flow are expressed as primitive variables in a Cartesian coordinate system, using a collocated arrangement. An ACL approach is used to discretize the turbine blades in the simulations. The aerodynamic forces on the blade elements are computed using the provided XFoil data. The forces then are projected onto the computational domain. In order to compute the additional source term, a Gaussian smearing function is used, taking into account one smearing factor for each direction: normal, tangential and radial to the rotor plane. The domain, representing the wind tunnel, is uniformly divided into 192 x 72 x 48 grid cells in the streamwise, spanwise and vertical directions, resulting in a total cell count of approximately $0.7\cdot10^6$. A zero velocity gradient is imposed at the outlet, while a logarithmic law is used to compute the stress at the bottom wall and the symmetry boundary condition is used at the lateral and top boundaries. A Crank-Nicolson time scheme is used with a time step of $2.5\cdot10^{-3}$ s. The scale dependent dynamic Smagorinsky model is used to compute the subgrid scale stress, using a local averaging scheme. The inflow condition is obtained from a precursor simulation with a similar numerical setup. More information about the application of caffa3d for wind energy simulations can be found in (Guggeri et al., 2017; Mendina et al., 2014; Usera et al., 2008).

Royal Institute of Technology (KTH)

A third LES was submitted by KTH. The spectral element code Nek5000 (Fischer et al., 2008), which was developed to solve the dimensionless, incompressible Navier–Stokes equations, was used. Each spectral element is discretized using Gauss–Lobatto–Legendre quadrature points on which the solution is expanded using Legendre polynomials. The LES applies a spatial filtering technique to the two highest modes to remove a part of the energy in the smallest scales and redistribute it to the lower modes thus stabilizing the numerical simulation. The domain is discretized using $7.98\cdot10^4$ uniformly distributed spectral elements with 9th order polynomials in each element, resulting in a total cell count of approximately $58\cdot10^6$. The numerical domain size corresponds to the dimensions of the wind tunnel. In the case of the NTNU turbine this mesh size corresponds to 45 grid points along each blade, when the blades are aligned with the mesh. The wind turbine blade geometry is represented by body forces according to the ACL method with the lift and drag forces being computed using tabulated airfoil data. For the NTNU turbines the experimental airfoil data set from DTU (Sarmast and Mikkelsen, 2012) is used. It provides lift and drag coefficients over a range of Reynolds numbers. The ForWind turbine lift and drag forcing was computed using airfoil polars generated by Xfoil that were provided in the invitation. At the blade tips the Prandtl tip correction is applied. The forces computed at each actuator line are distributed using a three-dimensional Gaussian distribution. The Gaussian width is selected to be 2.5 times the average grid spacing. The tower is also modeled using a body force approach. Both an oscillating lift component and a constant and oscillating drag component are included. The lift and drag coefficients for the mean drag and root-mean-squared lift and drag of a cylinder are taken from Summer and Fredsøe (2011). The line forces are then distributed using the three-dimensional Gaussian approximately in the volume occupied by the tower. This setup has been previously validated against experimental data from the NTNU turbine (Kleusberg et al., 2017). In the case of the ForWind turbine only the actual tower of the support structure is included. The turbulence at the inlet is modeled using sinusoidal modes with random phase shifts and they are scaled with a von Kármán energy spectrum. It is superimposed to the desired uniform inflow condition. The turbulence is calibrated to give a turbulence intensity at hub height of approximately $TI = 10.0\%$ at the upstream turbine LARS1 and $TI = 4.8\%$ at the downstream turbine T2. At the outlet a zero-stress boundary condition is used while the symmetry boundary condition is imposed laterally to avoid resolving the wall boundary layer. More details about the the computational setup can be found in (Kleusberg et al., 2017).

Wind turbine performance, forces and moments

The modelers were asked to predict the power coefficients C_P (Eq. 2), where P is the mechanical power of the turbine, ρ is the air density and A the rotor swept area, as well as the thrust coefficients C_T (Eq. 3), where T is the thrust force acting on the whole test rig, including rotor and tower, perpendicular to the rotor plane. Furthermore, the normalized yaw moments ${M_y}^*$ (Eq. 4), were required, where M_y is the yaw moment that is calculated by a moment equilibrium of the horizontal forces taking the distances of the load cells according to the center of the rotor plane into account. In test case 1 the power coefficient $C_{P,LARS1}$, the thrust coefficient $C_{T,LARS1}$ and the normalized yaw moment ${M_{y,LARS1}}^*$ are compared. For the aligned turbine array in test case 2, the predictions for the upstream turbine are similar to test case 1. However, additional predictions of $C_{P,T2}$, $C_{T,T2}$ and ${M_{y,T2}}^*$ for the downstream turbine were compared. Due to a high uncertainty in the power and thrust force measurements of the ForWind turbine, $C_{P,ForWind}$, $C_{T,ForWind}$ and ${M_{y,ForWind}}^*$ are not compared in test case 3. The performance characteristics of the NTNU turbines are listed in Table 1.

$$C_P = \frac{2P}{\rho \cdot A \cdot {u_{ref}}^3} \tag{2}$$

$$C_T = \frac{2T}{\rho \cdot A \cdot {u_{ref}}^2} \tag{3}$$

$$M_y^* = \frac{M_y}{\rho \cdot A \cdot {u_{ref}}^2 \cdot D} \tag{4}$$

Mean and turbulent wake flow

The modelers were asked to provide predictions of the velocities and turbulent kinetic energy in full wake planes in the ranges -1.0 $\leq z/D \leq$ +1.0 and -0.8 $\leq y/D \leq$ +0.8. The grid points are separated by $0.1D$ resulting in a grid consisting of 357 points, which is sketched in Fig. 5. The streamwise and vertical velocities u and v for all points are normalized by u_{ref} so that $u^* = u/u_{ref}$ and $v^* = u/u_{ref}$ respectively. The same procedure is applied for the turbulent kinetic energy k, which is normalized to $k^* = k/{u_{ref}}^2$. The turbulent kinetic energy in a three dimensional flow is defined as

$$k = {}^1\!/_2 \left(\overline{u'^2} + \overline{v'^2} + \overline{w'^2}\right). \tag{5}$$

However, in the experiments only the two velocity components u and v were measured. Comparing *u'* and *v'* showed that the TKE is not perfectly isotropic. Therefore, additional measurements of the third velocity component w for one wake scan were performed to investigate whether the fluctuations *v'* and *w'* were in the same range. The results confirmed the assumption, allowing an approximation of the turbulent kinetic energy as

$$k = {}^1\!/_2 \left(\overline{u'^2} + 2\overline{v'^2}\right). \tag{6}$$

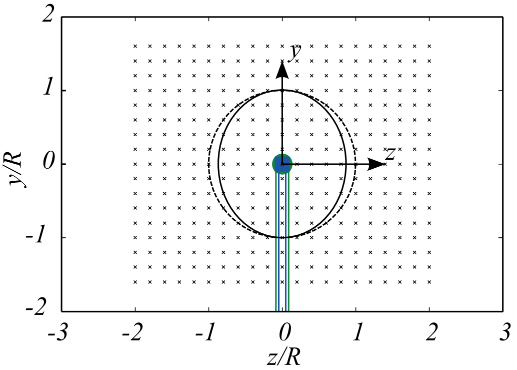

Figure 5: Measurement grid in the wake consisting of 357 points, the blue tower and nacelle represents the NTNU turbine LARS1, the green tower and nacelle represents the ForWind turbine, the dashed line corresponds to the projection of the rotor diameter $\gamma = 0°$, the solid line corresponds to the projection of the rotor area $\gamma = 30°$ and the outline corresponds to the cross section of the wind tunnel with the NTNU turbine installed.

3.4 Comparative methods

Two-dimensional wake contours are difficult to compare quantitatively as they cannot be plotted in the same diagram. However, they provide valuable insight into the shape and position of the wake. Therefore, the wake shapes are in a first iteration compared qualitatively. To obtain quantitative measures of comparison, different methods to compute the wake position, the energy content in the wake and the magnitudes of the wake parameters are applied. These are described below.

Available power method for wake deflection and energy content

In order to quantify the wake deflection, a method approximating the available power is used, which was previously described by Schottler et al. (2017). This method is deemed to be an appropriate approach to analyze the wake deflection of a yawed wind turbine, as it takes the full wake scans into account. To find the wake center deflection an imaginary rotor is traversed laterally in the wake while the wake center is defined as the position where the available power in the wake is the lowest. To get information about the energy content in the wake, the minimum of available power of the deflected wake is normalized by the available power found in the free stream of the experiment. With the resulting normalized minimum available power (${P_{wake}}^*$) possible deviations in the location and magnitude of the energy content can be directly quantified.

Statistical methods for wake properties

The predictions of C_P, C_T and ${M_y}^*$ are directly compared to the experimental results. The deviations of the predictions from the measurements are presented as a percentage of the experimental reference value in supplementing tables.

From the statistical error measures proposed by Chang and Hanna (2004) the normalized mean square error (*NMSE*) and the correlation coefficient (r) are used to quantify the differences between simulations and experiments regarding u^*, v^* and k^*. For this purpose, all 357 points in the yz-plane of the CFD predictions are compared to the corresponding measurement points. Perfect predictions would result in $NMSE = 0.0$ and $r = 1.0$. They are calculated according to

$$NMSE = \frac{\overline{(x_e - x_s)^2}}{\overline{x_s} - \overline{x_e}}, \tag{7}$$

$$r = \frac{\overline{(x_e - \overline{x_e}) \cdot (x_s - \overline{x_s})}}{\sigma_{x_e} \cdot \sigma_{x_s}}, \tag{8}$$

where x_e represents the experimentally measured values and x_s are the simulated values. $\overline{x}$ indicates the average of all 357 points of the full wake scans. The standard deviation of all points of the whole wake scan is given in σ_x. *NMSE* is a measure of mean relative scatter and thus reflects both systematic and random errors (Chang and Hanna, 2004), as the difference of every data point is squared, outliers are emphasized, which is not considered to be significant as no major outliers are expected. *NMSE* is used to analyze the predictions of u^* and k^*. The method is however not suited to evaluate the discrepancy of v^*, because v^* fluctuates around 0. Consequently the denominator of Eq. (7) also ranges around 0 which results in unrealistically high values for the *NMSE*. The correlation coefficient r represents a linear relationship between the measurements and predictions. It directly compares the measured and predicted values at a certain point. The predictions of all three investigated wake properties u^*, v^* and k^* are analyzed using the coefficient r.

4 Results

4.1 Test case 1

Power, thrust and yaw moment

The results of $C_{P,LARS1}$, $C_{T,LARS1}$ and $M_{y,LARS1}{}^*$ for test case 1, in which the turbine is operated at $\gamma = 30°$, are depicted in Fig. 6. For $\lambda = 6$ the differences between the experimental and numerical results are summarized in Table 3. Comparing the values of $C_{P,LARS1}$ in Fig. 6a it can be seen that the simulation results deviate from the measurements by up to 19%. This is a larger scatter compared to the previous Blind tests eg. (Bartl and Sætran, 2017). However, it should be kept in mind that the complexity is increased by the yawed turbine operation. Siemens, who fully resolved the rotor, overpredict $C_{P,LARS1}$ by 14.2%, which is almost in the same range as UdelaR and POLIMI who used ACL with the provided polars from XFoil and showed deviations of 18.5% and 16.8%, respectively. KTH also applied an ACL model, but used the experimentally generated data set of airfoil polars from DTU (Sarmast and Mikkelsen, 2012). Using this data results in a good agreement with the experimental data with only a slight underprediction of 2.3%.

The BEM tool Ashes (Thomassen et al., 2012) was used to analyze the blade loads. The calculations showed that the angle of attack for the yawed turbine is fluctuating during one rotation for approximately 2.0°in the outer third of the blade, causing very high angles of attack to occur on the blade. From Fig. 2 can be seen that the lift and drag coefficient from the DTU experiments and XFoil are very different for such high angles of attack. The experimental polars from DTU seem to be more accurate as the polars predicted with XFoil for such high angles of attack, what explains the better predictions of C_P by the simulations using the experimental polars.

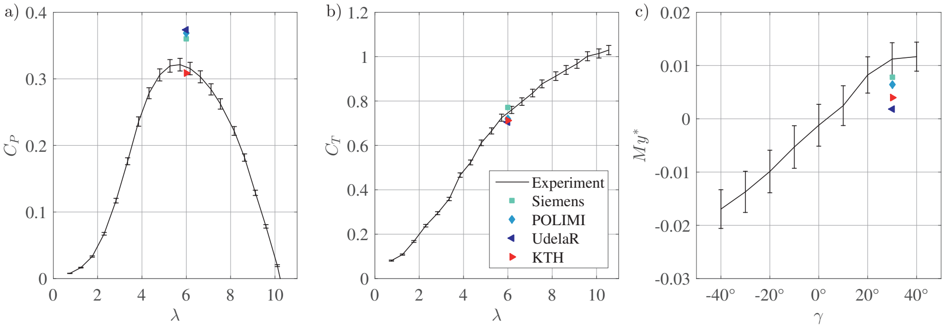

Figure 6: Power coefficient $C_{P,LARS1}$ (a) and thrust coefficient $C_{T,LARS1}$ (b) for the upstream turbine LARS1 operated at $\gamma_{LARS1} = 30°$ and normalized yaw moment $M_{y,LARS1}{}^*$ (c) for the upstream turbine LARS1 operated at $\lambda_{LARS1} = 6$ for γ = -40° to +40°.

The thrust coefficients $C_{T,LARS1}$ for the single yawed turbine LARS1 are presented in Fig. 6b and only show a small scatter of up to 7.0% around the experimental results and thus are almost all within the measurement uncertainty. Consequently, for C_T predictions the experimental polars do not yield better results with respect to the polars generated by XFoil. The yaw moment $M_{y,LARS1}{}^*$ is presented in Fig. 6c, over a range of yaw angles from γ = -40° to γ = +40°. All simulations underestimate the experimental value of $M_{y,LARS1}{}^*$ while the deviations ranging from about 30% to 80% are rather large. Nevertheless it should be kept in mind that the values of $M_{y,LARS1}{}^*$ are very small and thus small deviations result in large differences in percentage.

Table 3: Numerical values of power coefficient C_P, thrust coefficient C_T and normalized yaw moment $M_y{}^*$ and deviations of predictions to measurements in percent for test cases 1 and 2.

	Upstream turbine LARS1						Downstream turbine T2					
Inst.	$C_{P,LARS1}$		$C_{T,LARS1}$		$M_{y,LARS1}{}^*$		$C_{P,T2}$		$C_{T,T2}$		$M_{y,T2}{}^*$	
		diff		diff		diff		diff		diff		diff
Exp.	0.32		0.76		0.011		0.19		0.63		0.011	
Siemens	0.36	14.2%	0.77	1.7%	0.008	30.5%	0.21	10.5%	0.56	-10.7%	0.022	101.4%
POLIMI	0.37	16.8%	0.72	-5.2%	0.006	42.5%	0.27	43.6%	0.60	-4.6%	0.016	43.4%
UdelaR	0.37	18.5%	0.71	-7.0%	0.002	84.1%	0.28	48.9%	0.56	-10.6%	0.005	-50.6%
KTH	0.31	-2.3%	0.71	-6.1%	0.004	65.1%	0.19	0.0%	0.53	-15.3%	0.011	1.5%

Wake characteristics

Fig. 7 shows a comparison of the predictions of the streamwise velocity u^* at $x = 3D$, with line profiles at hub height are added to the full wake contours. The wake contours as presented in Fig. 7b show a slightly curled wake shape, which is generally well predicted by three of the simulations. Only the wake predicted by UdelaR has a rather oval shape. As expected, the wake is not only curled, but also clearly deflected in negative z-direction. This is very well predicted by all the simulations. POLIMI and KTH match the deflection whereas UdelaR and Siemens slightly underestimate it. This is not consistent with the predictions of C_T in which all institutions except Siemens estimate a lower C_T. The tower shadow is also clearly visible in all simulations. By fully resolving the rotor and turbine geometry Siemens matches the experimental results almost perfectly. UdelaR and KTH, who both modeled tower and nacelle with a line of drag forces, simulate a fairly accurate tower shadow. Even though POLIMI did not model nacelle and tower, their results show a strong velocity deficit in the area where the tower shadow is expected. This effect is considered to be caused by the flow velocities modeled near the wind tunnel floor, whose influence is pronounced in all simulations by POLIMI. In the free stream, the shear flow can be clearly seen in the experimental results. Siemens, UdelaR and KTH apply a user defined shear function at the inlet and thus predict a smooth shear profile, while POLIMI, who fully resolved the turbulence grid at the inlet, simulate a shear profile with a too strong shear and very low velocities close to the floor. Fig. 7a shows that POLIMI generally predicts lower velocities in the free stream, as the normalized velocity u^* at hub height does not reach 1.0 in the free stream. Nevertheless, the velocities behind the rotor are represented very well, while a poor $NMSE_u$ of 0.017 and a r_u of 0.878 show the discrepancy in the free stream to the measurements. All in all, it can be seen that u^* is predicted well by all simulations. Siemens' results for this test case are almost perfectly in accordance with the experiments, which results in a very low $NMSE_u$ of 0.002 and a large r_u of 0.964. Good statistical performance values are also achieved by KTH ($NMSE_u = 0.002$, $r_u = 0.957$), even though the velocity deficit in the wake center is slightly underestimated. An even clearer under prediction of the velocity deficit in the wake center can be observed for the UdelaR simulations, which result in a $NMSE_u$ of 0.005 and a r_u of 0.914. These observations are confirmed by comparing the available power levels in the wake (Table 4). In case of Siemens' accurate simulations of u^*, ${P^*}_{wake}$ only deviates by -2.7% from the experiments. UdelaR underestimates the velocity deficit in the center significantly, resulting in an overprediction of ${P^*}_{wake}$ by 42.7%. KTH also overestimates ${P^*}_{wake}$ by 15.6%, which confirms the higher velocities observed in the wake center. The available power method shows a good agreement of

POLIMI's simulations with the experiments, deviating only 11.2%. This is because the method takes only the area in the wake center into account and thus is not affected by the deviating velocity levels in the free stream.

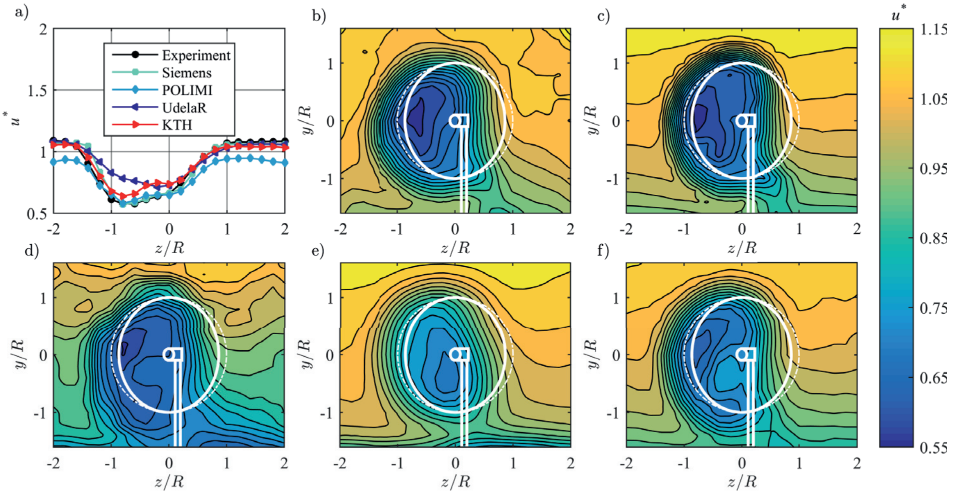

Figure 7: (a) Line plot and (b-f) contour plots for normalized streamwise mean velocity u^* in the wake $3D$ behind turbine LARS1, from (b) experiments, (c) Siemens, (d) POLIMI, (e) UdelaR and (f) KTH. The white lines represent the turbine rotor, nacelle and tower, solid lines $\gamma = 30°$, dashed lines $\gamma = 0°$.

Next, Fig. 8 shows the normalized vertical flow component v^*. In general the velocity contours are dominated by two major flow patterns: A larger scale bi-pole, characterized by flow from the ceiling to the center ($v^* < 0$) and from the bottom to the center ($v^* > 0$); and a smaller bi-pole at the rotor edge at z/D = -0.8, where v^* is positive outside the rotor swept area and negative in the rotor swept area featuring strong gradients between the peaks. These structures are generally predicted fairly well. Siemens, POLIMI and KTH match the flow pattern very accurately, which is confirmed by the line plots at hub height (Fig. 8a). High values of the correlation coefficient r_v for these three simulations range from 0.819 to 0.866 and confirm the observations. The simulation by UdelaR (Fig. 8e) does not show very strong gradients and thus does not capture the detailed flow patterns. This is assumed to be due to a rather coarse mesh resolution for this simulation and can be seen in the low r_v-value of 0.383. Nevertheless, the general shape showing the large scale structures on the right is captured well.

The normalized turbulent kinetic energy k^* is presented in Fig. 9. The contours show a clear ring of turbulence located around the rotor area. Similar to the shape of u^* the ring is slightly compressed at the right side. Fig. 9a shows that all simulations

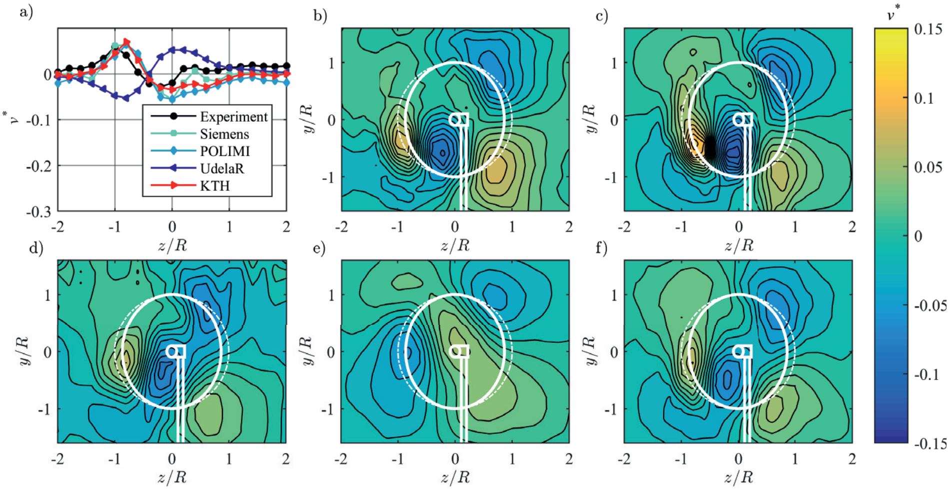

Figure 8: (a) Line plot and (b-f) contour plots for normalized vertical mean velocity v^* in the wake $3D$ behind turbine LARS1, from (b) experiments, (c) Siemens, (d) POLIMI, (e) UdelaR and (f) KTH. The white lines represent the turbine rotor, nacelle and tower, solid lines $\gamma = 30°$, dashed lines $\gamma = 0°$.

predict the position and magnitude of the turbulence peaks very well. Larger differences between measurement and simulations can be found outside of the ring. Here, Siemens predicts a very low turbulent kinetic energy close to $k^* = 0$ in the free stream and in the wake center. This underprediction of k^* is assumed to be due to the rather large cell size in the free stream that is too coarse to sustain the free stream turbulence. It results in a rather large $NMSE_k$ of 0.663 whereas r_k with 0.873 suggests a good correlation of the shapes. POLIMI's prediction of k^* shows a higher background turbulence, especially below the rotor area in positive z-direction. These discrepancies result in poor statistical performance values of $NMSE_k = 0.332$ and $r_k = 0.583$. UdelaR's results show a clear shear profile of k^* with increasing turbulence towards the wind tunnel floor. This is quite different from the experimental results, therefore the values of $NMSE_k = 1.045$ and $r_k = 0.333$ are observed to be far off. The simulations of KTH are in very good agreement with the experiments which is confirmed by a low $NMSE_k$ of 0.085 and high r_k of 0.924.

The comparisons of u^*, v^* and k^* $6D$ behind LARS1 show similar trends as already observed at a distance of $3D$. Therefore, the results at $6D$ are not shown. The comparison parameters summarized in Table 4 confirm these observations. A major difference to the wake at $3D$ is a more distinct curled wake shape, which is generally well predicted by all simulations. The wake is further deflected, while the skew angle is lower compared to the observations at $x = 3D$ (Table 4). This is expected to be

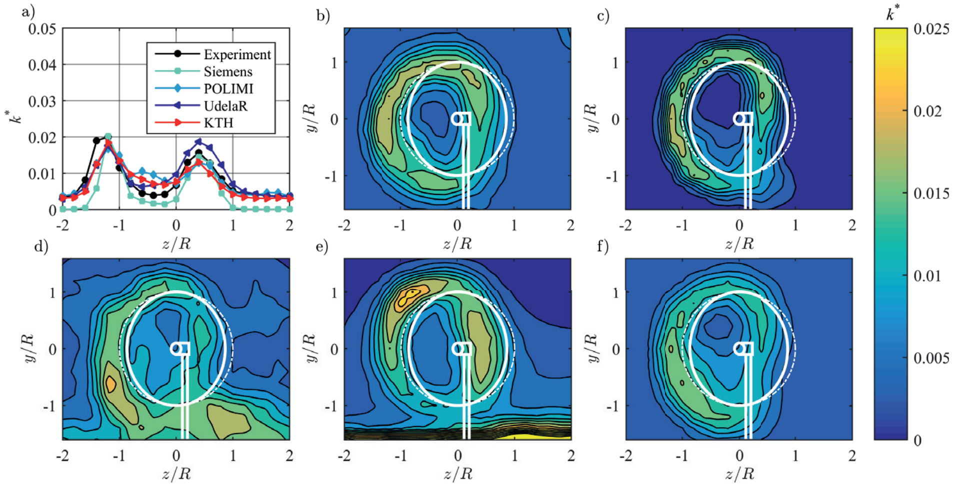

Figure 9: (a) Line plot and (b-f) contour plots for normalized turbulent kinetic energy k^* in the wake $3D$ behind turbine LARS1, from (b) experiments, (c) Siemens, (d) POLIMI, (e) UdelaR and (f) KTH. The white lines represent the turbine rotor, nacelle and tower, solid lines $\gamma = 30°$, dashed lines $\gamma = 0°$.

due to the large blockage ratio of the NTNU turbine and the interference of the wake with the wind tunnel walls. The experimental results of the wake at $x = 6D$ are also documented by Bartl et al. (2018a).

4.2 Test case 2

Power, thrust and yaw moment

In test case 2 an aligned turbine array with both NTNU turbines LARS1 and T2 is investigated. The upstream turbine LARS1 is operated at $\gamma_{LARS1} = 30°$ and $\lambda_{LARS1} = 6.0$. Consequently, $C_{P,LARS1}$, $C_{T,LARS1}$ and $M_{y,LARS1}{}^*$ are identical to test case 1 (Fig. 6, Table 3) and are therefore not further discussed here. The downstream turbine T2 is operated at $\gamma_{T2} = 0°$ and the tip speed ratio $\lambda_{T2} = 5.0$ is computed using $u_{ref} = 10.0$ m/s. It is located $3D$ behind the yawed upstream turbine, meaning that the wake flow of test case 1 represents the inflow for T2. Previous Blind tests discussed the higher spread in prediction results of a downstream turbine's performance. This is confirmed by comparing $C_{P,T2}$, $C_{T,T2}$ and $M_{y,T2}{}^*$ of T2, which show a significantly larger spread of performance than for test case 1 (Fig. 10, Table 3). The simulation results of the downstream turbine's power coefficient $C_{P,T2}$ (Fig. 10a) deviate between 0% and 48.9% from the experimental results. KTH matches the experimental value exactly and thus confirms the good forecast from test case 1. Siemens predicts the

Table 4: Comparison parameters: Skew angle (ξ), wake deflection (δ) and available power in the wake (${P^*}_{wake}$) and their differences to the measurements. Statistical performance measures: $NMSE$ and r for u^*, v^* and k^* at $3D$ and $6D$ behind upstream turbine LARS1.

	Institution	Skew angle	Deflection (z/R)	Diff. (z/R)	${P^*}_{wake}$ [-]	Diff. [%]	$NMSE_u$	r_u	r_v	$NMSE_k$	r_k
$3D$	Experiments	3.31 °	-0.347		0.383						
	Siemens	2.53 °	-0.265	0.082	0.372	-2.7%	0.002	0.964	0.819	0.663	0.873
	POLIMI	3.31 °	-0.347	0.000	0.340	-11.2%	0.017	0.878	0.830	0.332	0.583
	UdelaR	2.92 °	-0.306	0.041	0.546	42.7%	0.005	0.914	0.383	1.045	0.333
	KTH	3.31 °	-0.347	0.000	0.443	15.6%	0.002	0.957	0.866	0.085	0.924
$6D$	Experiments	2.63 °	-0.551		0.489						
	Siemens	2.24 °	-0.469	0.082	0.476	-2.7%	0.002	0.949	0.810	0.477	0.898
	POLIMI	2.44 °	-0.510	0.041	0.441	-9.9%	0.012	0.860	0.781	0.164	0.758
	UdelaR	2.05 °	-0.429	0.122	0.691	41.2%	0.006	0.795	0.463	0.946	0.192
	KTH	2.63 °	-0.551	0.000	0.527	7.7%	0.002	0.955	0.805	0.125	0.970

available power in the wake fairly accurately and thus overestimates $C_{P,T2}$ by only 10.5%. POLIMI and UdelaR over estimate $C_{P,T2}$ significantly by 43.6% and 48.9%, respectively. This trend could already be seen for the upstream turbine power coefficient $C_{P,LARS1}$ and is enhanced by overpredicting the available power in the wake for UdelaR. POLIMI prognosticates less available power in the wake. The simulation results of the downstream turbine thrust coefficient $C_{T,T2}$ (Fig. 10b) show smaller deviations than those for $C_{P,T2}$. Nevertheless, they are slightly larger than those of $C_{T,LARS1}$ in test case 1. All simulations underestimate $C_{T,T2}$ while KTH's result shows the largest deviation of -15.3% compared to their accurate prediction of $C_{P,T2}$. Siemens and UdelaR show a similar thrust that deviates from the experimental value by -10.7% and -10.6%, respectively. POLIMI underpredicts $C_{T,T2}$ by 4.6%.

A larger spread is again observed for the simulations of ${M_{y,T2}}^*$ (Fig. 10c) as the values for ${M_{y,T2}}^*$ are very small and consequently more difficult to predict. Siemens and POLIMI are observed to overestimate ${M_{y,T2}}^*$ by 101.4% and 43.3%, respectively. UdelaR under predicts ${M_{y,T2}}^*$ for 50.6% while KTH matches the experimental results very accurately with only 1.5% difference.

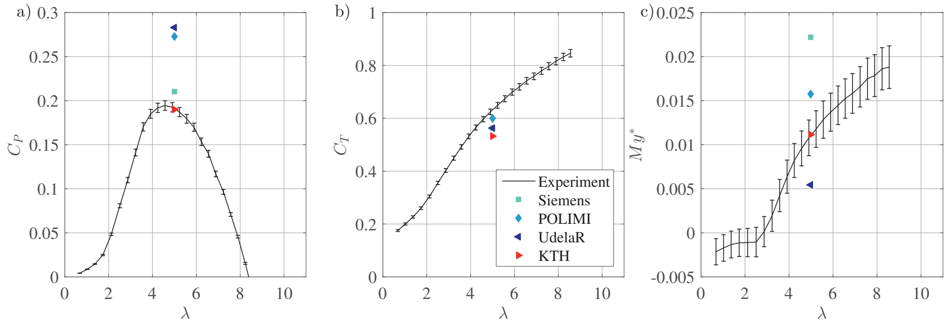

Figure 10: Power coefficient $C_{P,T2}$ (a), thrust coefficient $C_{T,T2}$ (b) and normalized yaw moment ${M_{y,LARS1}}^*$ (c) for the downstream turbine T2 operated in the wake of LARS1 at $\gamma_{T2} = 0°$ for $\lambda_{T2} = 1-12$.

Wake characteristics

This section discusses the wake characteristics $3D$ behind the two-turbine array. The wake is clearly deflected in the negative z-direction. However, the deflection is not as big as $6D$ behind the single yawed turbine, but rather in the same range as $3D$ behind the single yawed turbine. This suggests that a further wake deflection is restricted by the non-yawed downstream turbine and maintained at approximately the same level at which it hits the downstream turbine. Moreover, the wake shape does not show a curled shape, instead being rather oval (Fig. 11). The tower shadow, which is mainly formed by the downstream turbine T2's tower, is more centered than in test case 1 and is well-predicted in all simulations. The shear profile in the free stream is well-captured by all simulations. However, all predictions show a slightly lower velocity level than in the experiment. POLIMI's simulations indicate a rather strong velocity gradient again, with very low velocities close to the wind tunnel floor. However, the gradient is better established than in test case 1 as it develops further downstream. The line plot in Fig. 11a confirms that all the simulations underestimate the additional speed-up around the downstream turbine rotor.

Siemens overpredicts the velocity deficit in the wake center which is confirmed by the available power that is 19.5% lower as the one resulting from the experiments. Considering the whole wake scan, the statistical performance parameters $NMSE_u = 0.006$ and $r_u = 0.976$ on the other hand suggest better agreement. POLIMI predicts the velocities in the wake very accurately and estimates ${P^*}_{wake}$ only 12.1% lower than in the experiments. The statistical measures however do not confirm the good match of the energy level, resulting in a $NMSE_u$ of 0.025 and a r_u of 0.925. The too low velocities in the free stream, that are not considered in ${P^*}_{wake}$, are deemed to impair

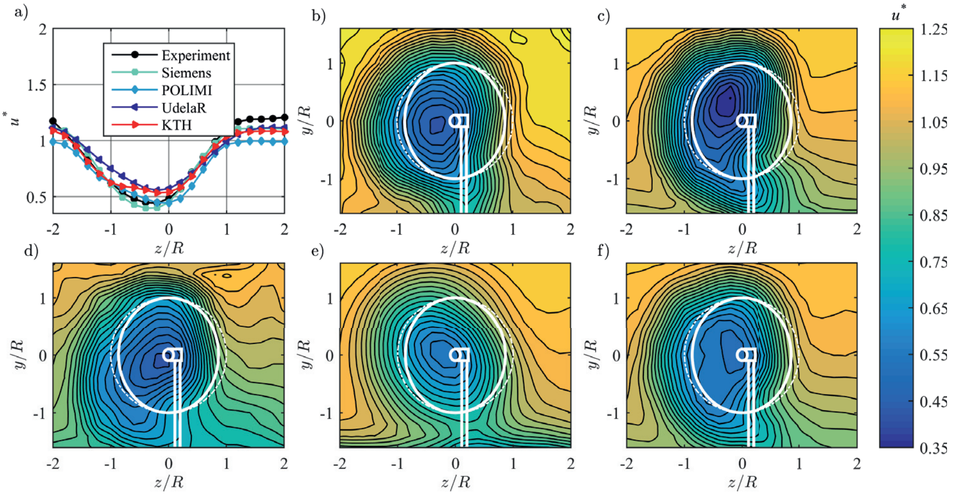

Figure 11: (a) Line plot and (b-f) contour plots for normalized streamwise mean velocity u^* in the wake $3D$ behind downstream turbine T2, from (b) experiments, (c) Siemens, (d) POLIMI, (e) UdelaR and (f) KTH. The white lines represent the turbine rotor, nacelle and tower, solid lines $\gamma = 30°$, dashed lines $\gamma = 0°$.

the correlation coefficients here. The available power of UdelaR exceeds that of the experiments clearly by 51.1% which is mainly due to an under prediction of the velocity deficit in the wake center. Nevertheless, the statistical parameters that take the whole measurement grid into account, suggest a good agreement with $NMSE_u = 0.010$ and $r_u = 0.928$ as the lower velocities in the free stream counterbalance the higher velocities in the wake center. The velocity levels in the wake center are overpredicted by KTH, however, the available power is in good agreement with the experiments and only deviates 4.1%. This is confirmed by good statistical values of $NMSE_u = 0.007$ and $r_u = 0.976$. The wake deflection is predicted well by all simulations. POLIMI and KTH match it accurately, whereas Siemens underpredicts it by $z/R = 0.041$ and UdelaR by $z/R = 0.082$.

The contours of the vertical velocity component v^* behind the turbine array show a similar flow pattern as the one behind the single yawed turbine (Fig. 12). Nevertheless, the magnitudes of v^* are smaller compared to test case 1. The flow pattern is described fairly accurately by all simulations. However, Siemens, POLIMI and KTH have average correlation values r_v ranging from 0.452 to 0.586. The predictions by UdelaR are again rather coarse and thus reveal less details, which results in an even lower linear correlation coefficient of only $r_v = 0.091$.

The turbulent kinetic energy k^* in the wake behind the turbine array as shown in Fig. 13 is characterized by a ring of higher TKE that is deflected in the same way

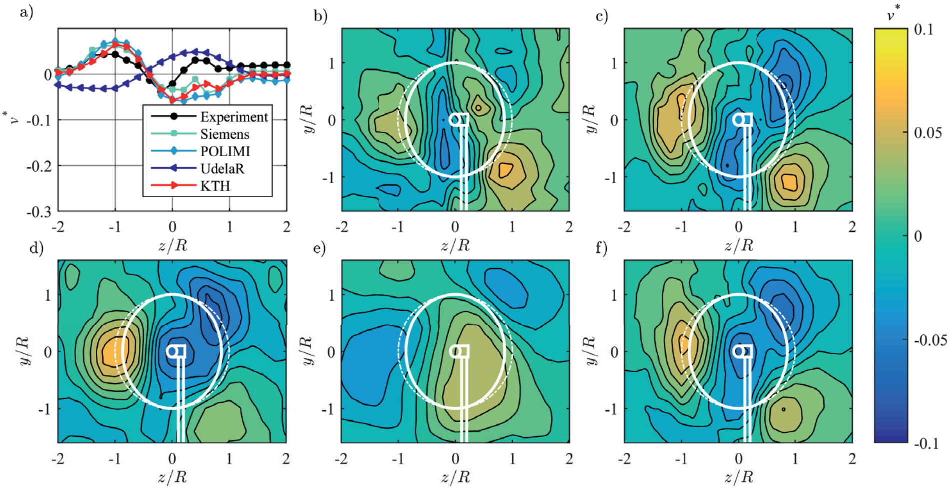

Figure 12: (a) Line plot and (b-f) contour plots for normalized vertical mean velocity v^* in the wake $3D$ behind downstream turbine T2, from (b) experiments, (c) Siemens, (d) POLIMI, (e) UdelaR and (f) KTH. The white lines represent the turbine rotor, nacelle and tower, solid lines $\gamma = 30°$, dashed lines $\gamma = 0°$.

as u^* and thus is similar to test case 1. Compared to the single turbine wake, the ring of high TKE is observed to be broader and flattened out (Fig. 13a). The peak locations are prognosticated very well by all simulations. However, Siemens and KTH underpredict the levels of k^*, while UdelaR overpredicts the turbulence in the ring, especially on the right hand side of the wake. POLIMI seems to match the turbulence in the ring fairly accurately which results in a low $NMSE_k$ of 0.087 and r_k of 0.915. Good r_k values are also obtained by Siemens and KTH with $r_k = 0.947$ and $r_k = 0.976$, respectively. However, their $NMSE_k$ values of $NMSE_k = 0.345$ and $NMSE_k = 0.153$, respectively, suggest some deviations. The overprediction of TKE by UdelaR results in slightly poorer statistical performance values of $NMSE_k = 0.709$ and $r_k = 0.784$.

4.3 Test case 3

Wake characteristics

In the third test case the wake behind the yawed ForWind turbine is investigated. It was simulated by three of the modelers, while POLIMI did not submit predictions for this test case. The contours of the streamwise velocity $3D$ ($D = D_{ForWind}$) behind the ForWind turbine are presented in Fig. 14b-e. They show a more distinct curled wake shape than that observed for the NTNU turbine. In contrast to the NTNU turbine the ForWind turbine rotates in clockwise direction when observed from upstream.

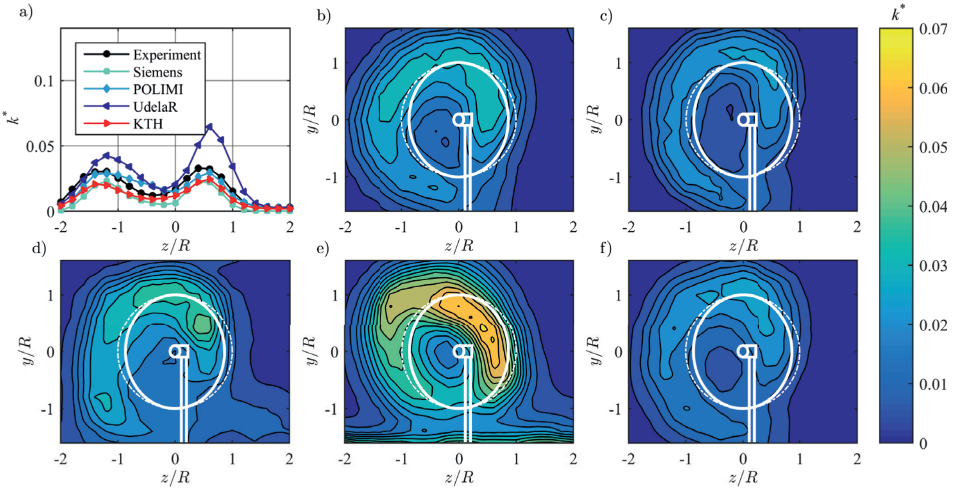

Figure 13: (a) Line plot and (b-f) contour plots for normalized turbulent kinetic energy k^* in the wake $3D$ behind downstream turbine T2, from (b) experiments, (c) Siemens, (d) POLIMI, (e) UdelaR and (f) KTH. The white lines represent the turbine rotor, nacelle and tower, solid lines $\gamma = 30°$, dashed lines $\gamma = 0°$.

Table 5: Comparison parameters: Skew angle (ξ), wake deflection (δ) and available power in the wake (P^*_{wake}) and their differences to the measurements. Statistical performance measures: $NMSE$ and r for u^*, v^* and k^* at $3D$ behind downstream turbine T2.

	Institution	Skew angle	Deflection (z/R)	Diff. (z/R)	P^*_{wake} [-]	Diff. [%]	$NMSE_u$	r_u	r_v	$NMSE_k$	r_k
$3D$	Experiments	3.71 °	-0.388		0.251						
	Siemens	3.31 °	-0.347	0.041	0.202	-19.5%	0.006	0.976	0.586	0.345	0.947
	POLIMI	3.71 °	-0.388	0.000	0.220	-12.1%	0.025	0.925	0.452	0.087	0.915
	UdelaR	2.92 °	-0.306	0.082	0.379	51.1%	0.010	0.928	0.091	0.709	0.784
	KTH	3.71 °	-0.390	0.000	0.261	4.1%	0.007	0.976	0.561	0.153	0.976

A counter-clockwise wake rotation deflects the wake center to the lower half behind the rotor as described in detail by Schottler et al. (2018). Furthermore, it can be seen that due to the smaller rotor diameter there is less blockage which reduces the speed up around the rotor significantly (Fig. 14a). Thus, a smooth shear profile is observed in the free stream. The velocity deficit as well as the curled wake shape are predicted very well by all simulations with only UdelaR's simulations showing a less distinct curl. The position of the largest velocity deficit is consistent for all simulations.

Nevertheless, most participants overestimate the magnitude of the velocity deficit. Siemens has the largest deviations from the experiments, which results in an available power that is 49.4% lower compared to the measurements. However, when not only taking the imaginary rotor area into account but considering the whole wake scan, the statistical performance values $NMSE_u = 0.012$ and $r_u = 0.968$, indicate a good agreement. UdelaR predicts velocities that result in only 27.6% less available power for a potential downstream turbine, but $NMSE_u = 0.007$ and $r_u = 0.953$ are in the same range as the Siemens predictions and indicate a good match of the whole wake scan. The KTH simulation matches the experimental results best and shows the smallest deviation of available power and with $NMSE_u = 0.005$ and $r_u = 0.960$ their statistical performance values confirm the good agreement. The wake of the ForWind turbine is slightly stronger deflected than $3D$ behind the NTNU turbine (Table 6). Siemens again under predicts the deflection, whereas UdelaR and especially KTH predict a stronger deflection of the wake than observed in the experiments.

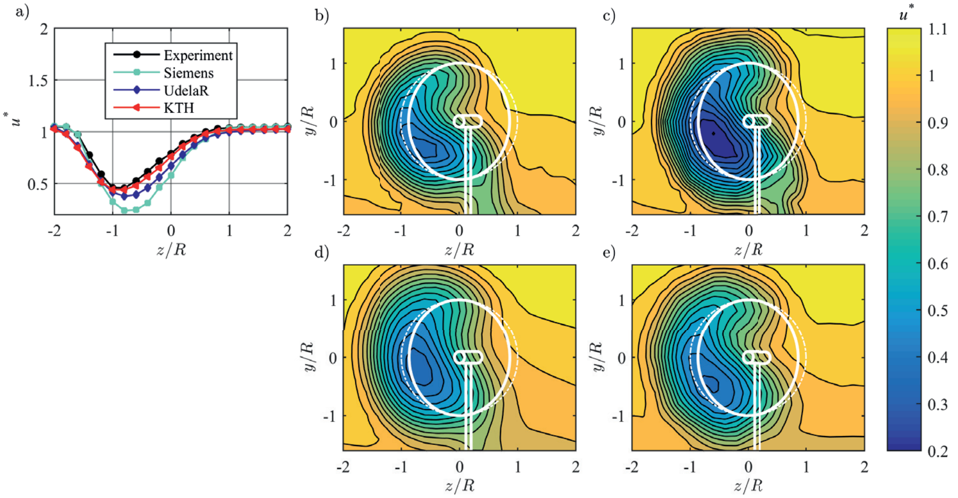

Figure 14: (a) Line plot and (b-e) contour plots for normalized streamwise mean velocity u^* in the wake $3D$ behind ForWind turbine, from (b) experiments, (c) Siemens, (d) UdelaR and (e) KTH and. The white lines represent the turbine rotor, nacelle and tower, solid lines $\gamma = 30°$, dashed lines $\gamma = 0°$.

The contours of the normalized vertical velocity v^* (Fig. 15b-e) are similar to those observed $3D$ behind LARS1. The flow field is dominated by the same major flow patterns as already observed in test case 1. The major difference is that the peaks in positive z-direction are more centered and that the dipole at the left rotor edge are not as distinct. All simulations of v^* match the experiment fairly accurately , which results in similar r_v values ranging from 0.802 to 0.851. Siemens however predicts slightly higher positive peaks, but the distribution of v^* is captured very well. The same applies for KTH and UdelaR, who again predicts smoother gradients due to a coarse mesh resolution.

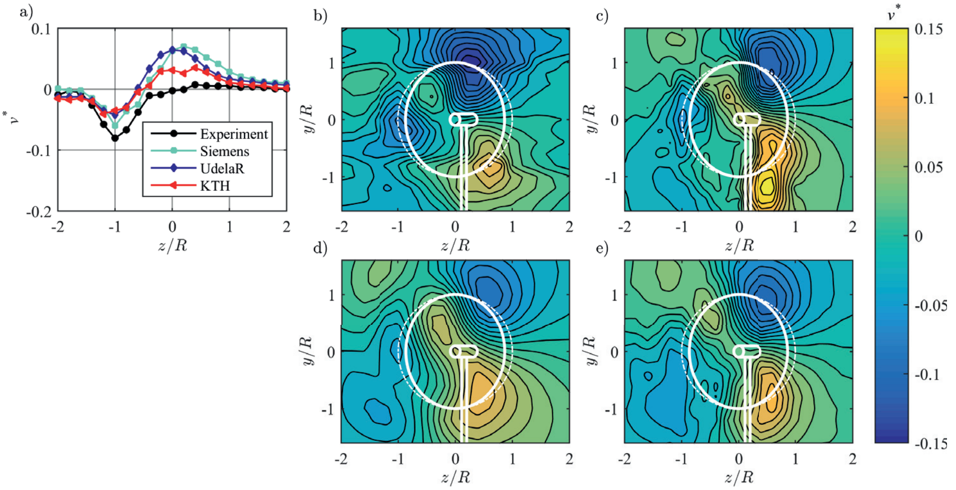

Figure 15: (a) Line plot and (b-e) contour plots for normalized vertical mean velocity v^* in the wake $3D$ behind ForWind turbine, from (b) experiments, (c) Siemens, (d) UdelaR and (e) KTH and. The white lines represent the turbine rotor, nacelle and tower, solid lines $\gamma = 30°$, dashed lines $\gamma = 0°$.

The turbulent kinetic energy contours presented in Fig. 16b-e also indicate a clear curled shape. The k^* values behind the ForWind turbine are observed to result in a significantly wider peak in positive z-direction (Fig. 16a) than observed behind LARS1. In contrast to the previous test cases, k^* is distributed more smoothly over the wake which results in higher turbulence levels in the wake center. The shape of the turbulent kinetic energy contours is represented accurately by all simulations. Siemens and UdelaR, however, over estimate the peak magnitudes significantly, while Siemens predicts the peak location in the upper half accurately. UdelaR's simulation is observed to result in higher TKE values in the whole ring. The simulations of KTH are in closest agreement with the experiments. The linear correlation coefficients are in the same range ($r_k = 0.878 - 0.905$) for all three predictions. Larger deviations can be observed in $NMSE_k$ that ranges from 0.202 to 0.734.

The comparison of the wake characteristics $6D$ behind the yawed ForWind turbine results in conclusions similar to those at $3D$. Therefore, the figures comparing u^*, v^* and k^* $6D$ behind the ForWind turbine are not shown here, but the comparison parameters and statistical performance measures are listed in Table 6. The streamwise

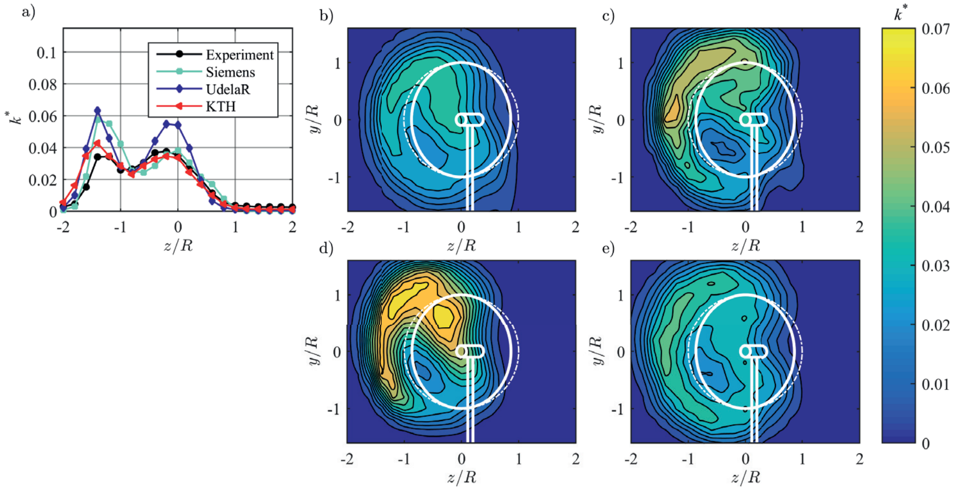

Figure 16: (a) Line plot and (b-e) contour plots for normalized turbulent kinetic energy k^* in the wake $3D$ behind ForWind turbine, from (b) experiments, (c) Siemens, (d) UdelaR and (e) KTH and. The white lines represent the turbine rotor, nacelle and tower, solid lines $\gamma = 30°$, dashed lines $\gamma = 0°$.

velocity u^* and the vertical velocity v^* are generally predicted accurately, which is represented by better comparison parameters and statistical performance values at $6D$ than at $3D$ for all simulations.

5 Discussion and conclusions

The results of four different computational contributions were compared to experimental wind tunnel results in this Blind test experiment. The modelers submitted predictions for the performance of two single yawed turbine models and an aligned turbine array where only the upstream turbine is yawed. Furthermore, they predicted the mean and turbulent wake flow behind two different model turbines and the turbine array.

The power of a single yawed turbine $C_{P,LARS1}$ was predicted with a scatter of ±19%, which was slightly bigger than in the two previous Blind test experiments. A bigger scatter of ±49% is observed in the predictions of the power coefficient $C_{P,T2}$ for a downstream turbine operating in partial wake conditions of the yawed upstream turbine. This variation is significantly larger than the scatter for an aligned downstream turbine operated in a full wake in Blind test 4 (Bartl and Sætran, 2017), in which a scatter of only ±15% was observed for the same distance. For a downstream turbine with a lateral offset operated in a partial wake in Blind Test 3 (Krogstad et al., 2015), however, a similar variation in power prediction was observed (±50%). These results

Table 6: Comparison parameters: Skew angle (ξ), wake deflection (δ) and available power in the wake (${P^*}_{wake}$) and their differences to the measurements. Statistical performance measures: *NMSE* and r for u^*, v^* and k^* at $3D$ and $6D$ behind upstream ForWind turbine.

	Institution	Skew angle	Deflection (z/R)	Diff. (z/R)	${P^*}_{wake}$ [-]	Diff. [%]	$NMSE_u$	r_u	r_v	$NMSE_k$	r_k
$3D$	Experiments	4.10 °	-0.429		0.285						
	Siemens	3.71 °	-0.388	0.041	0.141	-49.4%	0.012	0.968	0.813	0.383	0.889
	UdelaR	4.88 °	-0.510	-0.082	0.207	-27.6%	0.007	0.953	0.802	0.734	0.878
	KTH	5.27 °	-0.551	-0.122	0.233	-18.%	0.005	0.960	0.851	0.202	0.905
$6D$	Experiments	3.80 °	-0.796		0.533						
	Siemens	3.41 °	-0.714	0.082	0.430	-19.3%	0.002	0.960	0.845	0.047	0.961
	UdelaR	4.00 °	-0.837	-0.041	0.540	1.2%	0.001	0.963	0.799	0.067	0.956
	KTH	4.19 °	-0.878	-0.082	0.475	-11.0%	0.002	0.950	0.884	0.052	0.947

indicate a more difficult prediction of turbine performance for an operation in a partial wake situation, due to the increased complexity of highly unsteady blade loading over the course of a rotation.

The predictions of the thrust coefficients $C_{T,LARS1}$ and $C_{T,T2}$ show a smaller scatter of ±7% and ±15%, respectively, which is in the same range as observed in Blind test 4. Consequently, the thrust predictions are not influenced as strongly by yawing the turbine as the power predictions. Three of the simulations modeled the rotor by an actuator line approach, two of which used XFoil generated polars while one simulation used an experimentally measured data set. The power, thrust and yaw moment predictions of the simulations using an experimental data set consistently performed best. As the rotor was operated in yaw (test case 1) or a partial wake inflow (test case 2) the angle of attack varied during one rotor rotation, reaching high values. The experimental airfoil polars might be more realistic for such large angles of attack, which result in better performance predictions. The fourth simulation fully resolved the rotor geometry and directly calculated the forces on the rotor. The time step in these simulations was chosen to be rather large in order to save computational time which might have negatively influenced the accuracy of the blade forces. The parameters of the wake flow, however, were not impaired by this large time step.

When comparing CFD predictions to experimental measurements it is important to quantify the differences. Therefore, different techniques have been applied to analyze the wake properties. The statistical methods *NMSE* and r were in good agreement with each other and gave an acceptable indication of how well the simulations performed.

However, they analyzed the whole wake scan and did not reveal specific discrepancies. The statistical methods were not always in accordance with the available power method, which only considered an area around the wake center for comparison. The available power method thus provided a good quantification of the wake deflection and the energy content in the wake. However, it only compared a certain section of the wake scan and accordingly could not quantify the overall performance of the simulations. Comparing the wake contours visually resulted in a qualitative comparison, revealing flow patterns and differences in the wake shape for each simulation in comparison to the experiments . Combining the outcome from all methods provided a good overall picture of how well the wake properties from CFD predictions and measurements agree.

The comparison of the mean streamwise velocity u^* in the wake generally shows a very good agreement between the experimental data and the numerical predictions. The general features such as the wake shape and deflection were predicted well by all the simulations using IDDES as well as LES. The velocity in the wake was also predicted fairly accurately by all simulations. The high mesh resolution of the IDDES simulations by Siemens was seen to reveal exact flow details and thus resulted in a high statistical correlation for u^*. A similarly high statistical correlation was obtained by KTH's u^* predictions using their LES-ACL simulation. The rather coarse mesh of UdelaR saved computational time, but also smeared flow details, nevertheless the velocity and turbulence levels were predicted accurately. Modeling the grid at the inlet as done in POLIMI's simulation was observed to not perfectly predict the inflow, which was not as smooth at the position of the first turbine as in the measurements. Applying a user-defined shear profile at the inlet, as performed by the other institutions, resulted in better predictions of the free stream flow. Despite its low magnitude, the complex patterns in vertical velocity component v^* were in general accurately predicted by all simulations. The details of the flow were well captured by both LES and IDDES simulations. One of the most positive results of this Blind test experiment were the very accurate predictions of the turbulent kinetic energy in the wake behind a single turbine and the two-turbine array. The prediction of wake turbulence was seen to be difficult in previous Blind test comparisons. This workshop, however, confirms the strength of LES and IDDES simulations to accurately predict rotor generated turbulence.

Furthermore, the good results of the simulations based on a lower cell-count indicate a new trend towards CFD codes, that are able to perform accurate wake flow predictions at significantly lower computational cost. This becomes especially important for wake predictions of full scale turbines in which the dimensions and Reynolds numbers exceed those of the experiments. Consequently, simulations with a fine grid may be very hard to realize in such a case. Nevertheless, the good performance of the coarse-grid simulations in the Blind test shows that they are a promising tool for full scale wake predictions.

Overall, the results of this Blind test comparison confirm a continuous improvement in performance and wake flow predictions from Blind test 1 to Blind test 5. LES-ACL approaches as well as the hybrid IDDES technique were confirmed to be able to perform accurate predictions, also for complex setups featuring highly unsteady flow in yawed and partial wake operation.

References

Barthelmie, R. J., Hansen, K., Frandsen, S. T., Rathmann, O., Schepers, J. G., Schlez, W., Phillips, J., Rados, K., Zervos, a., Politis, E. S., and Chaviaropoulos, P. K.: Modelling and measuring flow and wind turbine wakes in large wind farms offshore, Wind Energy, 12, 431–444, doi:10.1002/we.348, 2009.

Bartl, J. and Sætran, L.: Blind test comparison of the performance and wake flow between two in-line wind turbines exposed to different turbulent inflow conditions, Wind Energy Science, 2, 55–76, doi:10.5194/wes-2-55-2017, 2017.

Bartl, J., Mühle, F., Schottler, J., Sætran, L., Peinke, J., Adaramola, M., and Hölling, M.: Wind tunnel experiments on wind turbine wakes in yaw: Effects of inflow turbulence and shear, Wind Energy Science Discussions, 2018, 1–22, doi:10.5194/wes-2017-59, 2018a.

Bartl, J., Sagmo, K., Bracchi, T., and Sætran, L.: Performance of the NREL S826 airfoil at low to moderate Reynold numbers - A reference experiment, submitted to European Journal of Mechanics B/Fluids, 2018b.

Benedict, L. H. and Gould, R. D.: Towards better uncertainty estimates for turbulence statistics, Experiments in Fluids, 22, 129–136, doi:10.1007/s003480050030, 1996.

Chang, J. C. and Hanna, S. R.: Air quality model performance evaluation, Meteorology and Atmospheric Physics, 87, 167–196, doi:10.1007/s00703-003-0070-7, 2004.

Fischer, P. F., Lottes, J. W., and Kerkemeier, S. G.: Nek5000, URL http://nek5000.mcs.anl.gov, 2008.

Fleming, P., Annoni, J., Churchfield, M., Martinez, L., Gruchalla, K., Lawson, M., and Moriarty, P.: From wake steering to flow control, Wind Energy Science Discussions, 2017, 1–17, doi:10.5194/wes-2017-52, 2017.

Fleming, P. a., Gebraad, P. M. O., Lee, S., van Wingerden, J. W., Johnson, K., Churchfield, M., Michalakes, J., Spalart, P., and Moriarty, P.: Evaluating techniques for redirecting turbine wakes using SOWFA, Renewable Energy, 70, 211–218, doi:10.1016/j.renene.2014.02.015, 2014.

Guggeri, A., Draper, M., and Usera, G.: Simulation of a 7.7 MW onshore wind farm with the Actuator Line Model, Journal of Physics: Conference Series, 854, 012 018, doi:10.1088/1742-6596/854/1/012018, 2017.

Kleusberg, E., Mikkelsen, R. F., Schlatter, P., Ivanell, S., and Henningson, D. S.: High-order numerical simulations of wind turbine wakes, Journal of Physics: Conference Series, 854, 012 025, doi:10.1088-1742-6596-854-1-012025, 2017.

Krogstad, P.-Å. and Davidson, P. A.: Is grid turbulence Saffman turbulence?, Journal of Fluid Mechanics, 642, 373–394, doi:10.1017/S0022112009991807, 2010.

Krogstad, P.-Å. and Eriksen, P. E.: “Blind test” calculations of the performance and wake development for a model wind turbine, Renewable Energy, 50, 325 − 333, doi:10.1016/j.renene.2012.06.044, 2013.

Krogstad, P. Å. and Lund, J.: An experimental and numerical study of the performance of a model turbine, Wind Energy, 15, 443–457, doi:10.1002/we.482, 2012.

Krogstad, P.-Å., Sætran, L., and Adaramola, M. S.: “Blind Test 3” calculations of the performance and wake development behind two in-line and offset model wind turbines, Journal of Fluids and Structures, 52, 65–80, doi:10.1016/j.jfluidstructs.2014.10.002, 2015.

Mendina, M., Draper, M., Kelm Soares, A. P., Narancio, G., and Usera, G.: A general purpose parallel block structured open source incompressible flow solver, Cluster Computing, 17, 231–241, doi:10.1007/s10586-013-0323-2, 2014.

Mendonça, F., Baris, O., and Capon, G.: Simulation of radial compressor aeroacoustics using CFD, ASME Turbo Expo 2012: Turbine Technical Conference and Exposition, Volume 8: Turbomachinery, Parts A, B, and C, 1823–1832, doi: 10.1115/GT2012-70028, 2012.

Pierella, F., Krogstad, P.-Å., and Sætran, L.: Blind Test 2 calculations for two in-line model wind turbines where the downstream turbine operates at various rotational speeds, Renewable Energy, 70, 62 − 77, doi:10.1016/j.renene.2014.03.034, special issue on aerodynamics of offshore wind energy systems and wakes, 2014.

Polster, F., Bartl, J., Mühle, F., Thamsen, P. U., and Sætran, L.: Experimental validation of analytical wake and downstream turbine performance modelling, manuscript submitted for publication, 2017.

Sætran, L., Mühle, F., Bartl, J., Schottler, J., Hölling, M., and Adaramola, M. S.: Invitation to the 2017 "Blind test 5" workshop - The wake behind a yawed wind turbine, doi:10.5281/zenodo.1218555, 2018.

Sarmast, S. and Mikkelsen, R. F.: The experimental results of the NREL S826 airfoil at low Reynolds numbers, URL l{http://www.diva-portal.org/smash/record.jsf?pid=diva2%3A615785&dswid=-528}, (last access: 9 February 2017), 2012.

Schepers, J. G., Boorsma, K., and Munduate, X.: Final results from Mexnext-I: Analysis of detailed aerodynamic measurements on a 4.5 m diameter rotor placed in the large German Dutch Wind Tunnel DNW, Journal of Physics: Conference Series, 555, 012 089, doi:10.1088/1742-6596-555-1-012089, 2014.

Schito, P. and Zasso, A.: Actuator forces in CFD: RANS and LES modeling in OpenFOAM, Journal of Physics: Conference Series, 524, 012 160, doi:10.1088/1742-6596/524/1/012160, 2014.

Schottler, J., Hölling, A., Peinke, J., and Hölling, M.: Design and implementation of a controllable model wind turbine for experimental studies, Journal of Physics: Conference Series, 753, 072 030, doi:10.1088/1742-6596/753/7/072030, 2016.

Schottler, J., Mühle, F., Bartl, J., Peinke, J., Adaramola, M. S., Sætran, L., and Hölling, M.: Comparative study on the wake deflection behind yawed wind turbine models, Journal of Physics: Conference Series, 854, 012 032, doi:10.1088/1742-6596/854/1/012032, 2017.

Schottler, J., Bartl, J., Mühle, F., Sætran, L., Peinke, J., and Hölling, M.: Wind tunnel experiments on wind turbine wakes in yaw: Redefining the wake width, Wind Energy Science Discussions, 2018, 1–22, doi:10.5194/wes-2017-58, 2018.

Selig, M., Guglielmo, J., Broeren, A., and Giguere, P.: Summary of low-speed airfoil data, SoarTech Publications, URL http://m-selig.ae.illinois.edu/uiuc_lsat/Low-Speed-Airfoil-Data-V1.pdf, last access 03.11.2017, 1995.

Somers, D. M.: The S825 and S826 airfoils, National Renewable Energy Laboratory, Subcontractor Report, last access 03.11.2017, 2005.

Sørensen, J. N. and Shen, W. Z.: Numerical Modeling of Wind Turbine Wakes, 124, 393, doi:10.1115/1.1471361, 2002.

Summer, B. M. and Fredsøe, J.: Forces on a cylinder in regular waves, pp. 123–209, WORLD SCIENTIFIC, revised edn., doi:10.1142/9789812772770_0004, 2011.

Thomassen, P. E., Bruheim, P. I., Suja, L., Frøyd, L., et al.: A novel tool for FEM analysis of offshore wind turbines with innovative visualization techniques, in: The Twenty-second International Offshore and Polar Engineering Conference, International Society of Offshore and Polar Engineers, 2012.

Usera, G., Vernet, A., and Ferré, J. A.: A parallel block-structured finite volume method for flows in complex geometry with sliding interfaces, Flow, Turbulence and Combustion, 81, 471, doi:10.1007/s10494-008-9153-3, 2008.

Wheeler, A. and Ganji, A.: Introduction to Engineering Experimentation, Pearson Education, Upper Saddle River, New Jersey, USA, third edition edn., 2010.

ISBN: 978-82-575-1762-5
ISSN: 1894-6402

Norwegian University
of Life Sciences

Postboks 5003
NO-1432 Ås, Norway
+47 67 23 00 00
www.nmbu.no

99564 / ANDVORDGRAFISK.NO